# Äspö Hard Rock Laboratory

## Äspö Pillar Stability Experiment, Final report

## Rock mass response to coupled mechanical thermal loading

J Christer Andersson

Svensk Kärnbränslehantering AB

January 2007

**SKB**

# Äspö Hard Rock Laboratory

## Äspö Pillar Stability Experiment, Final report

## Rock mass response to coupled mechanical thermal loading

J Christer Andersson

Svensk Kärnbränslehantering AB

January 2007

A pdf version of this document can be downloaded from www.skb.se

# Preface

This report has been published as a Doctoral Thesis in Soil and Rock Mechanics at the Royal Institute of Technology in Stockholm, Sweden 2007, by the same author (J.C. Andersson). The title of the PhD thesis is "Rock Mass Response to Coupled Mechanical Thermal Loading. Äspö Pillar Stability Experiment, Sweden."

This report is focused on the design and execution of, and observations made during, the Äspö Pillar Stability Experiment. Particular attention has been given to studies of the yield strength of the rock mass and the effect of a confining pressure. The experiment has generated a large quantity of data. Studying all the data in detail and trying to couple all the different processes involved would require the efforts of several PhD students. The ambition of this report is therefore to present the experiment in such detail that further studies are encouraged.

The work has been carried out at Äspö Hard Rock Laboratory in Oskarshamn, a research facility operated by SKB, Svensk Kärnbränslehantering AB (the Swedish Nuclear Fuel and Waste Management Co). The author is employed by SKB and has carried out the study as an industrial PhD student with full funding by SKB.

The experiment and evaluation of the results have been supervised by Prof. Håkan Stille at KTH, Prof. Derek Martin at the University of Alberta, Canada, and Mr. Rolf Christiansson, responsible for the rock mechanics programme at SKB. Internationally recognized experts have reviewed parts of the project on an as-needed basis.

The Äspö Pillar Stability Experiment has been quite an extensive undertaking, requiring the contributions of a large number of people. The author's main contributions have been to I) manage the design and execution of the experiment to produce a high-quality set of data, and II) document, analyze and discuss observations and findings made in the course of the experiment.

# Notations

σ   Stress, compression positive

$\sigma_c$   Unconfined compressive strength

$\sigma_{ci}$   Crack initiation stress

$\sigma_{cd}$   Crack damage stress

$\sigma_1$   Major principal stress

$\sigma_2$   Intermediate principal stress

$\sigma_3$   Minor principal stress

ε   Strain

$\varepsilon_v$   Volumetric strain

$\varepsilon_{v,e}$   Elastic volumetric strain

ν   Poisson's ratio


AE   Acoustic emission

E   Young's modulus

UCS   Uniaxial compressive strength

EDZ   Excavation damaged zone

LAN   Local area network

LVDT  Linear variable differential transformer

# Summary

The Äspö Pillar Stability Experiment (APSE) was carried out to examine the failure process in a heterogeneous and slightly fractured rock mass when subjected to coupled excavation-induced and thermal-induced stresses.

The pillar was created by the excavation of two large boreholes (ø 1.75 m, 6.5 m deep) so that a rock web of ~ 1 m was left in between them. The experiment was located in a tunnel excavated for the experiment. The floor was arched to concentrate the excavation-induced stresses in the centre of the floor. Acoustic emission, displacement and thermal monitoring systems were installed to follow the yielding of the pillar as the temperature was increased. The pillar was heated by electrical heaters so that thermal stresses were induced which caused the pillar wall in the open hole to yield gradually and in a controlled manner. The yielding propagated down along the pillar wall and created a v-shaped notch.

The first of the two large holes was confined with a water pressure before the excavation of the second hole commenced. This was done to enable the effect of a confinement pressure on the response of the rock mass to increased loading to be studied.

The main objectives of this study are to:

1. Provide an estimate of the yield strength of the rock mass and compare that with laboratory results on cores.

2. Describe the effect of the confining pressure, the observations during the de-stress drilling and the removal of the blocks.

3. Thoroughly describe the experiment, monitoring results and observations.

Because there was very limited experience of rock mass yielding associated with the excavations at the Äspö HRL, the findings from AECL's URL were used to guide the design of the Äspö Pillar Stability experiment. It should be noted, however that while the mean uniaxial laboratory compressive strength (UCS) of Äspö diorite is approximately equal to the UCS of Lac du Bonnet granite, the magnitude of the maximum principal stress at the 450 m level of the Äspö HRL was only 50% (approximately 30 MPa) of the maximum principal stress in the AECL's URL (60 MPa). Hence, a major challenge for the experiment was to develop a design that would increase the excavation-induced stresses in a controlled manner, similar to that used in a laboratory environment, so that the failure process could be controlled. This would facilitate data collection and visual observations at all stages of the experiment. The most practical way to achieve these objectives was to use the observational design approach for the experiment. The major steps in the experiment were:

1. Literature review and scoping calculations. The scoping calculations were used to establish the geometries of the experiment tunnel.

2. Selection of site at Äspö and preliminary predictive modelling. The blind predictions were made to permit comparison of their results with the observed response of the rock mass.

3. Excavation, characterization and final predictive modelling. Special care was taken to minimize the excavation-induced damage. An extensive characterization programme was carried out to support the numerical models with relevant data.

4. Installations and heating.

5. Post-experimental characterization, compilation of the predictive modelling results and evaluation of the outcome of the experiment.

The experiment commenced in 2002 and ended in 2006. A timetable of the main stages is provided in Figure 0-1.

When the second of the large-diameter holes had been excavated an initial verification of the accuracy of the scoping calculations was obtained. The rock in the second hole had yielded from a depth of approximately 0.5 m down to 2 m. It was now obvious that the excavation induced stresses were enough to initiate yielding in the upper part of the hole and that a modest increase of the pillar

temperature would propagate the yielded surface further down the hole. Figure 0-2 shows the yielded area after excavation and the yielded area at the end of the experiment. It is evident that the yielding took place close to the centre of the pillar where the tangential stress was highest.
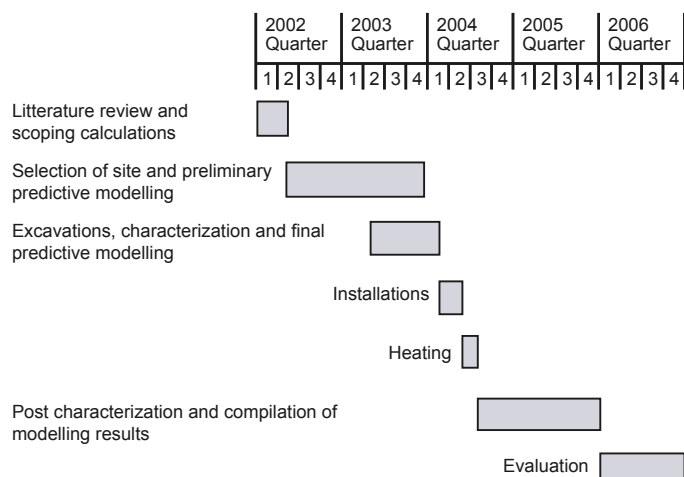


*Figure 0-1. General timetable for the Äspö Pillar Stability Experiment.*
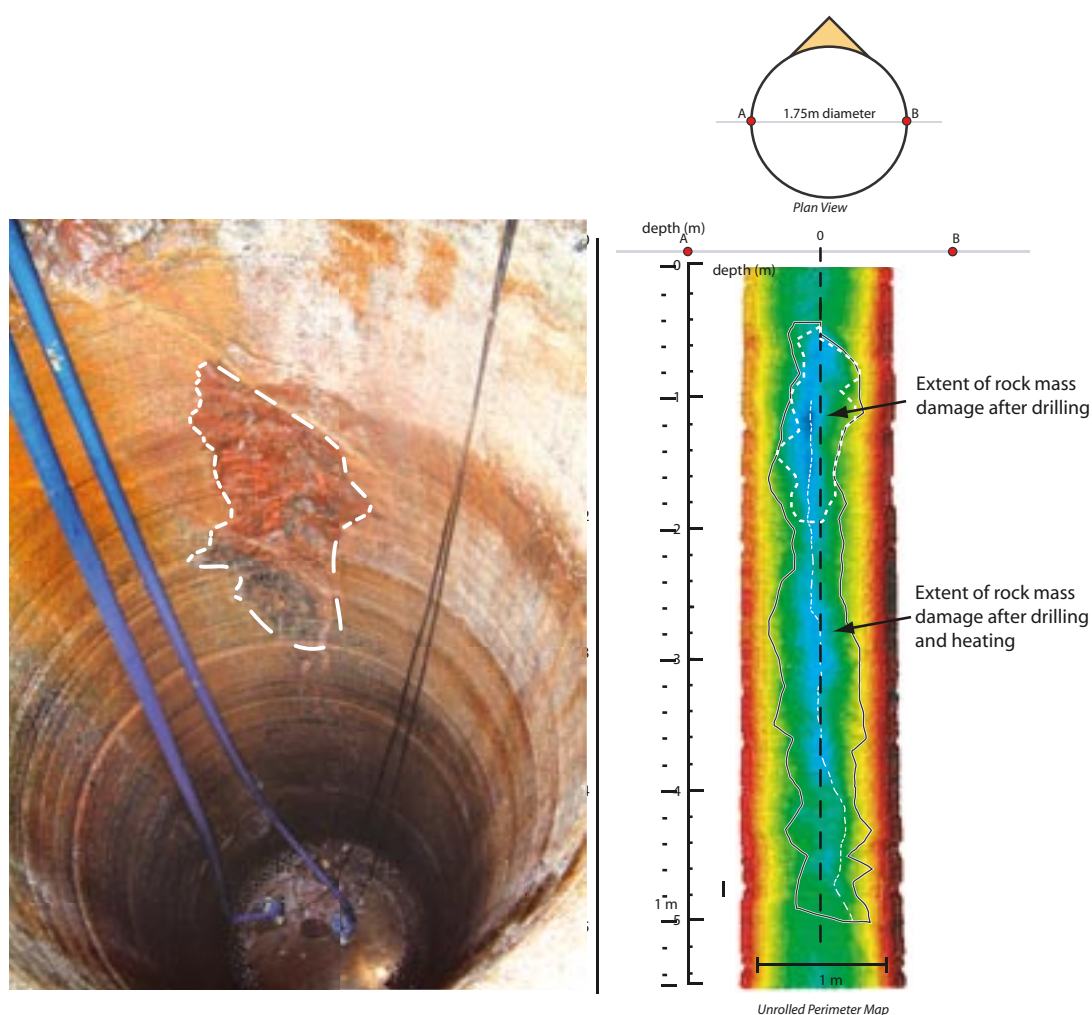


*Figure 0-2. Photograph of the rock volume that yielded during the excavation of the second large hole. The total yielded area after heating derived from a laser scanning of the pillar wall is presented in the right part of the figure.*

The effect of the confinement pressure was obvious as soon as the excavation of the second hole started. Acoustic Emission, AE, events were recorded in the unconfined hole but not in the confined one. During the hole heating period of the experiment the AEs in the confined hole were only a fraction of those in the unconfined hole.

The yielding of the rock as the v-shaped notch propagated down the hole wall could be closely followed by the AE system. Heating started on day 0. The ambient temperature was then 14.5°C. At day two the temperature reached 15°C, and shortly thereafter the acoustic frequency increased. Figure 0-3 shows the accumulated AEs per day together with the temperature at the centre of the pillar wall in the open hole at a depth of 3.03 m. A clear correlation can be seen between increasing temperature (which induces the thermal stress component) and AE frequency.

Acoustic emissions provided a good approximation of the general yielding rate in the pillar. However, it was found during the analysis of the data that the AEs could not be correlated to the amount of damage to the rock or to the monitored displacements. It was concluded that fracturing and displacements in many cases occurred without being registered by the AE system.

Visits were made in the open hole about once a week. The pillar wall was then photographed and sketches were made of the fracturing and yielding. After the experiment, the yielded rock was removed and the full extent of the v-shaped notch could be studied. One important conclusion could be drawn from the hole visits and the removal of the yielded rock. The vast majority of the fracturing seemed to be initiated and propagated in extension. The only evidence of shearing was found in the deepest part of the notch, where rock flour was present on the surfaces.

The displacement measurements indicated that the hole wall contracted (radial expansion) as the notch approached the displacement transducers. The phenomena are probably due to stress re-distributions as the rock yields. Efforts have been made to back-calculate these deformations without success; only one-tenth of the measured displacements could be modelled.

The monitored temperatures were used to back-calculate the temperature in the experimental volume, and coupled modelling was used to determine the increase in thermal stress in the pillar. By combining these stresses with the excavation-induced ones, the total stress in the pillar could be determined at all times. When correlated with these data, observations of when and where the rock yielded gave the yield strength of the rock. This strength was determined at 18 different locations on the pillar wall. The mean value was $0.59\sigma_c$, with a standard deviation of $0.03\sigma_c$. This value was correlated to the crack initiation
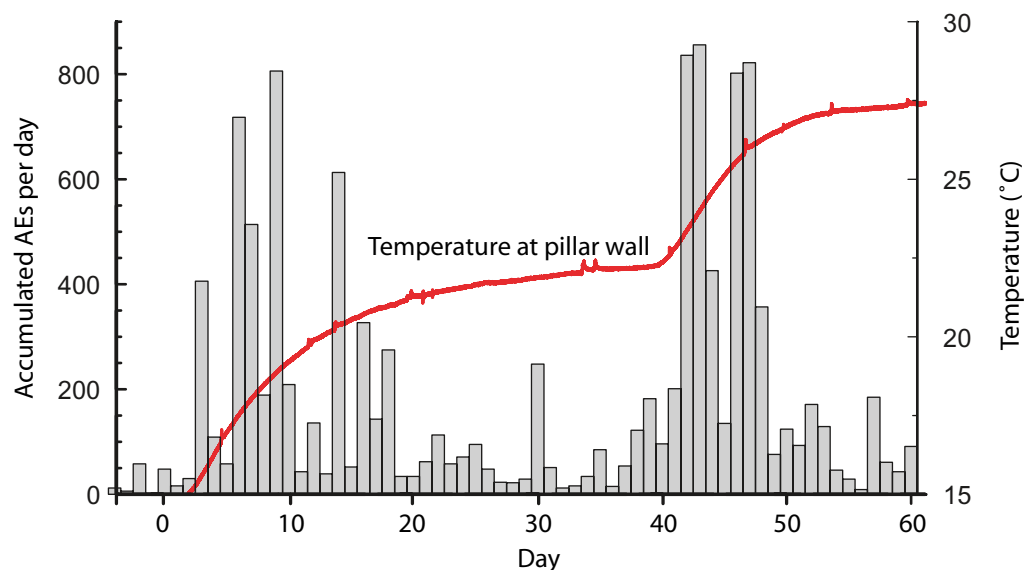


*Figure 0-3. Accumulated acoustic emission events per day and the temperature at the pillar wall of DQ0063G01 at a depth of 3.03 m.*

stress (CIS) determined by the volumetric strain method on core samples taken from the experimental volume. The mean value of the CIS was $(0.45 \pm 0.03)\sigma_c$. It is recommended that the crack volumetric strain method be used to estimate the yield strength of a rock mass in the absence of in situ data.

When the notch had propagated close to the bottom of the open hole, the temperature increase in the pillar stopped and a steady state was reached. At this time the confinement pressure was gradually released. During the pressure release, approximately one-third of the recorded acoustic events were located in the confined hole. Further yielding only occurred at a few locations with small areas. In practice, the previously confined hole was unaffected by the removal of the confinement pressure. The reason for this is probably that micro fractures not picked up the AE system were formed during the heating phase of the experiment. The fracturing softened the rock at the hole wall and re-distributed the stresses so that yielding did not occur.

After removal of the confinement pressure, the pillar was allowed to cool before it was sawn into five blocks which were removed from the experimental site. The pillar had to be de-stressed to permit sawing of the blocks. This was done by drilling a slot on the left side of the pillar. Stress re-distribution during this drilling caused failed zone along the pillar wall of the open hole. The blocks were geologically mapped after removal to permit a 3D geological visualisation of the pillar.

# Sammanfattning

Äspö Pillar Stability Experiment (APSE) genomfördes för att studera brottprocesserna i en något uppsprucken heterogen bergmassa. Brottprocessen initierades genom att koncentrera bergspänningar genom dels tunnelns geometri och dels genom värmeinducerade laster.

Pelaren skapades genom borrning av två stora borrhål med diametern 1,75 m och ett djup på cirka 6,5 m. Borrhålens centrumavstånd valdes så att bergplinten dem emellan blev cirka 1 m tjock. Experimentet utfördes i en tunnel som tillretts speciellt för experimentets syften. Sulan gavs en rundad form så att de geometriskt inducerade lasterna skulle koncentreras i dess centrum. Akustisk emission, deformations och temperaturövervakning var de metoder som användes för att följa brotts-processen i pelaren allteftersom temperaturen ökades. Elektriska värmare användes för att inducera termiska laster i pelaren på ett sådant sätt att en kontrollerad spjälkprocess i det öppna hålet erhölls. Spjälkningen propagerade nedför pelarväggen och skapade en v-formad kil.

Det först borrade av de två stora hålen utsattes för ett invändigt mothållande vattentryck innan borrningen av det andra stora hålet påbörjades. Detta genomfördes för att möjliggöra studier av det mothållande tryckets effekt på bergmassans respons på den termiskt inducerade lastökningen.

Huvudmålsättningarna med denna studie har varit att:

1. Göra en uppskattning av bergets spjälkhållfasthet och jämföra detta med resultat från laboratorie-resultat på borrkärnor.

2. Beskriva effekten av det mothållande trycket, observationer gjorda under avlastningsborrningen samt upptaget av blocken.

3. Ge en detaljerad beskrivning av experimentet, insamlad data samt gjorda observationer.

Väldigt få fall av spjälkning eller andra typer av spänningsinducerade brott har uppträtt i Äspös tunnel-system. Erfarenheter från AECL:s URL har därför till stor del använts vid designen av försöket. Den enaxiella tryckhållfastheten av Äspödiorit och Lac du Bonnet granit är i stort sett likvärdig. En viktig skillnad mellan experimentplatserna är dock att magnituden på den största huvudspänningen på 450 m nivån vid Äspölaboratoriet är bara ca 50 % (30 MPa) av huvudspänningen vid AECL:s URL (60 MPa). En stor utmaning för experimentet var därför att utveckla en design som skulle öka de geometriskt inducerade spänningarna på ett kontrollerat sätt. Spjälkningen kan då kontrolleras likt vid ett laboratorie-försök. Genom att kontrollera spjälkförloppet förenklas datainsamlingen och kvalitén på de visuella observationerna under experimentets alla faser höjs. För att klara detta användes observationsmetoden som förebild vid designen. De viktigaste delarna av experimentet var:

1. Litteratursökning och överslagsberäkningar. Överslagsberäkningarna användes för att slå fast experimenttunnelns geometri.

2. Val av experimentplats på Äspö samt genomförande av prediktiv modellering. Blindprediktioner gjordes för att kunna jämföras med bergmassans observerade respons.

3. Tillredning, karakterisering och slutlig prediktiv modellering. Särskilda åtgärder vidtogs för att minimera den störda zonen i berget runt tunneln. De numeriska modellerna försågs med relevant data genom ett ambitiöst karakteriseringsprogram av experimentvolymen.

4. Installationer och värmning.

5. Slutkarakterisering, sammanställning av prediktionerna samt utvärdering av experimentet.

Experimentet påbörjades år 2002 och slutfördes under 2006. En översiktlig tidsplan av experimentets viktigaste delar presenteras i figur 0-1.

En första verifiering av noggrannheten i överslagsberäkningarna erhölls när det andra stora borrhålet var färdigställt. Pelarväggen i det hålet hade då spjälkat från cirka 0,5 m djup till 2 m djup. Detta faktum bevisade att de geometriskt inducerade spänningarna var tillräckligt stora för att initiera spjälkning i den övre delen av hålet, samt, att en relativt liten temperaturhöjning av pelaren skulle

propagera spjälkbrottet djupare ned i borrhålet. Figur 0-2 visar den spjälkade arean efter både slutförandet av det andra hålet och efter hela försöket. Ur figuren framgår tydligt att spjälkningen skedde närmast pelarcentrum där tangentialspänningen var som högst.
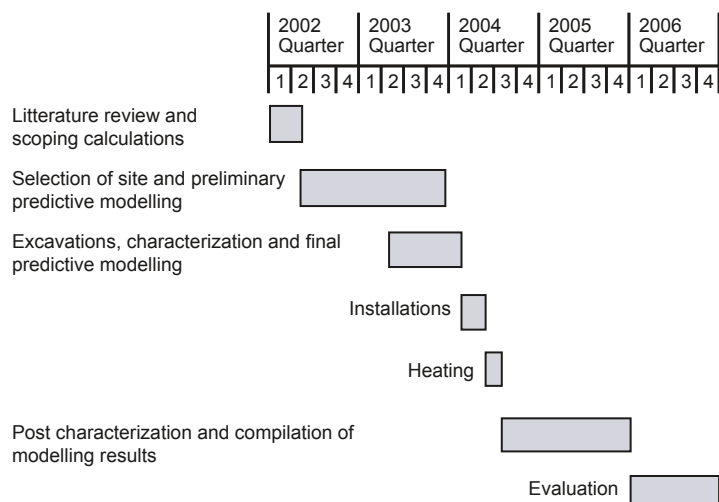


**Figur 0-1.** *Översiktlig tidplan för Äspö Pillar Stability Experiment.*
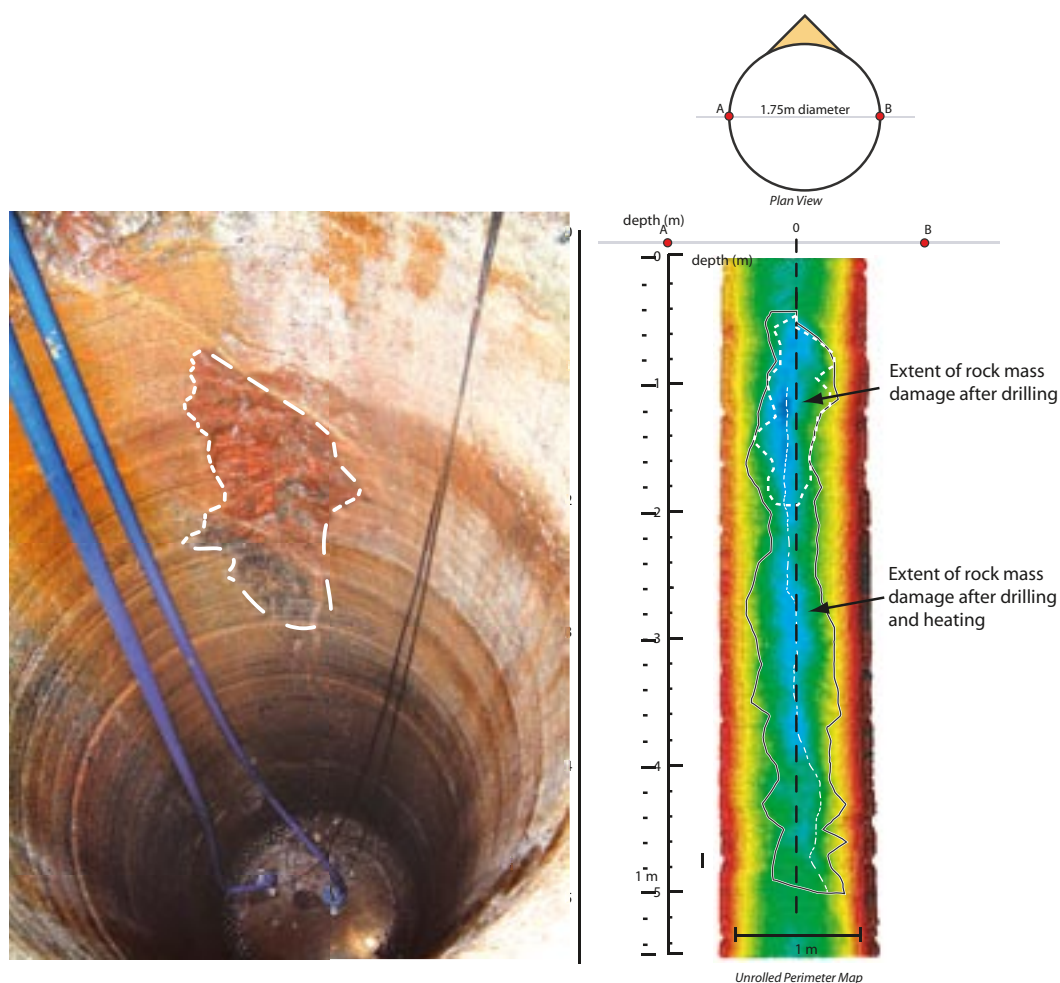


**Figur 0-2.** *Fotografi av bergvolymen som spjälkade under borrningen av det andra stora hålet. Den totala spjälkade arean efter uppvärmningen bestämd med laserskanning av pelarväggen redovisas i figurens högra del.*

12

Effekten av det mothållande trycket blev uppenbar så snart som borrningen av det andra hålet började. Akustisk Emission, AE, registrerades i det öppna hålet men inte i det trycksatta. Under hela försökets uppvärmningstid var de AE som registrerades i det trycksatta hålet bara en bråkdel av de registrerade i det öppna hålet.

Spjälkningen av berget när den v-formade kilen propagerade nedför pelarväggen var noggrant övervakad av AE-systemet. Värmningen av pelaren startade dag 0. Temperaturen i bergmassan var då cirka 14,5°C. Dag två var temperaturen 15°C. och kort därefter ökade antalet registrerade akustiska signaler snabbt. Figur 0-3 redovisar den ackumulerade mängden AE per dygn tillsammans med temperaturen i centrum pelarvägg på 3,03 m djup. En klar korrelation mellan ökande temperatur (ökande temperaturinducerade laster) och antalet AE framgår ur figuren.

Akustisk registrering gav en god uppskattning av pelarens generella spjälkning men kunde inte korreleras mot skadan i berget eller de deformationer som mättes upp. En slutsats är att sprickbildning och förskjutningar i många fall skedde utan att bli registrerade av det akustiska systemet.

Besök i det öppna hålet gjordes ungefär en gång i veckan. Pelaren fotograferades och skisser på sprickpropagering och spjälkning ritades. I slutfasen av experimentet plockades det spjälkade berget bort och den v-formade kilen kunde studeras i detalj. En viktig slutsats kunde dras utifrån de regelbundna besöken i hålet och bortplockandet av det spjälkade berget. Den överväldigande delen av de inducerade sprickorna verkar ha blivit både initierade och propagerade genom dragspänningar. Den enda indikationen för skjuvning fanns i kilens djupaste centrala delar bergmjöl förekom.

Deformationsmätarna indikerade att pelarväggen kontrakterade (hålradien ökade) när kilen närmade sig givarna. Detta fenomen beror troligen på spänningsomlagringar i berget i samband med spjälkningen. Försök att återberäkna denna kontraktion har gjorts men misslyckades. Bara en tiondel av den uppmätta kontraktionen kunde återskapas i de numeriska modellerna.

Temperaturmoneteringen användes för att kunna återberäkna temperaturfördelningen i pelarvolymen vilket gjorde att den termiskt inducerade lasten kunde bestämmas. Genom att kombinera denna last med de geometriskt inducerade blir totalspänningen i pelaren känd för varje tidpunkt. Genom att jämföra totalspänningen med observationerna om när och var berget i pelaren spjälkade kunde spjälkhållfastheten bestämmas. Spjälkhållfastheten bestämdes i 18 olika punkter i pelarväggen. Medelvärdet är $0,58\sigma_c$ med en standardavvikelse på $0,04\sigma_c$. Detta värde jämförs sedan i sin tur med sprickinitieringslasten (CIS) som bestämts genom att studera volymtöjningarna på borrkärnor från
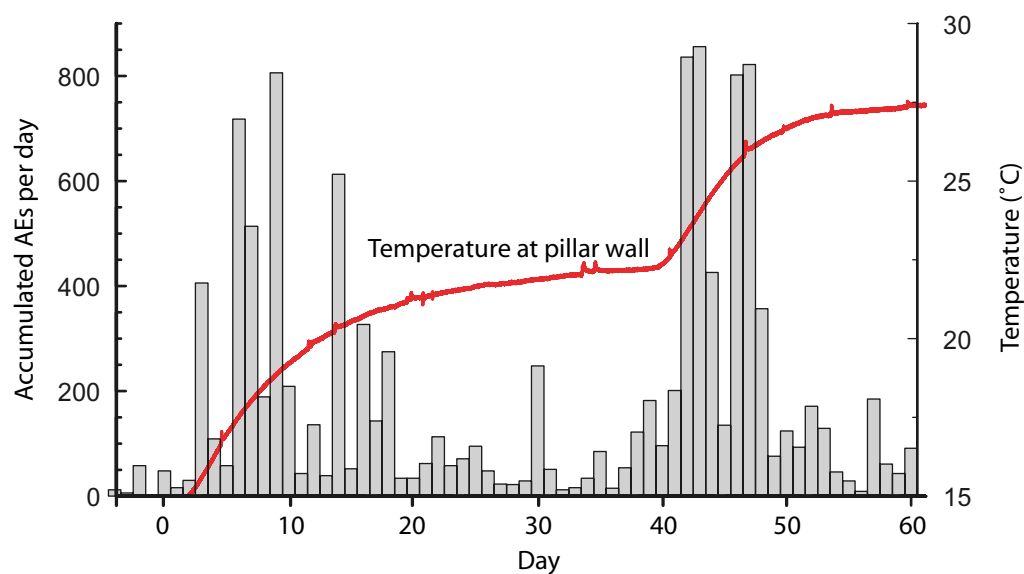


*Figur 0-3.* *Ackumulerade akustiska händelser per dygn tillsammans med temperaturen mätt i pelarväggen i DQ0063G01 på 3,03 m djup.*

13

experimentområdet. CIS medelvärdet är $(0,45 \pm 0,03)\sigma_c$. Om inte platsspecifika data på spjälkhåll-fastheten finns tillgängliga rekommenderas att metoden med volymtöjningar används för att bedöma spjälkhållfastheten.

När kilen nästan hade propagerat till botten av det öppna borrhålet inträffade ett termalt jämvikts-läge. Det var nu dags att gradvis sänka det mothållande trycket i det första hålet. Under trycksänk-ningen registrerades endast cirka en tredjedel av de akustiska emissionerna i den trycksatta pelar-väggen. Spjälkning i det hålet skedde i en mycket begränsad omfattning på små ytor. I praktiken blev det ingen påverkan i det trycksatta hålet trots i samband med tryckreduceringen. En orsak till detta kan vara att mikrosprickor som inte detekterades av AE-systemet bildades under uppvärmningen. Sprickorna sänktes bergets ytnära E-modul och omfördelade tangentialspänningen inåt i pelaren så att spjälkning inte initierades när trycket sänktes.

När sänkningen av mottrycket slutförts fick pelaren kallna och sågades sedan upp i fem stora block. För att kunna genomföra sågningen var pelaren tvungen att avlastas. Detta gjordes genom att borra en slits på pelarens vänstra sida. Spänningsomvandlingen som skedde under denna borrning orsakade en brottzon i pelarväggen. Efter upptaget karterades pelarblocken. Karteringen låg som underlag för en geologisk 3D visualisation av pelaren.

# Contents

# 1 Introduction

The construction of nuclear waste repositories and prediction of their long-term behaviour require a more detailed understanding of certain rock mechanics problems than has previously been needed by the industry. The nuclear waste repository will be located at great depth. The stresses at that depth increase the risk of stress-induced yielding in parts of the repository. Due to the stringent safety requirements, this may cause a problem in designing the facility. The actual initiation point for yielding should therefore be determined as precisely as is practically possible. Large rock volumes will be excavated and all excavated volumes will be backfilled. Small increases in the spacing between deposition holes and/or deposition tunnels greatly increase the costs. The use of unnecessarily large safety factors should therefore be avoided. It is, however, not only the stress level at the onset of damage that is of interest. Knowledge of fracturing and the final geometry of the yielded volume may be important information for the safety assessment of the repository.

Problems with spalling and pillar stability have been studied to a great extent in the mining industry, but they take a different approach to the safety factor for their underground openings. Localized yielding or failure is a natural part of the process, since the extraction ratio has to be as large as possible. Different empirical methods have been developed, but very few people have taken a more theoretical look at the problem and verified the theories with controlled field experiments. If, for example, the APSE pillar is compared with empirical relationships found in the literature, quite different results can be found. If a width/height ratio of 0.6 is used for the APSE pillar, /Hoek and Brown 1980/ indicate that the pillar strength could be up to ~ $1.1\sigma_c$. /Martin and Maybee 2000/ compiled six different empirical strength formulas which indicate that the APSE pillar would have a safety factor of one for a pillar stress of ~ $0.3\sigma_c$. From a nuclear waste repository point of view, these empirical results are not accurate enough and the problem has to be further studied on a more both empirical and theoretical basis.

/Ortlepp 1997/ presents a comprehensive illustrative study of rock fracturing and rock bursts in South African mines. Ortlepp concludes that it is likely that all fracturing in the observed deep underground mines is extensional in nature. This is indicated by a fracture surface that tends to be macroscopically planar where pebbles or grains are cleaved or split right through. The original rounded surface of the grain or pebble does not protrude above the plane. Ortlepp further states that if this is not seen, but a whitened abraded surface with striation is seen instead, these are almost certainly secondary effects resulting from subsequent differential movements of the original fracture surface. Accumulation of white rock dust from abrasion due to fracture propagation is reported to occur close to the notch tip of yielded volumes.

In this report the term "yielding" is used for the localized brittle failure that was induced in the experimental pillar. In the literature (in example: /Ortlepp 1997, Bergman and Stille 1983/, terms like "micro-slabbing", "spalling" and "popping" are used for similar phenomenon.

Quite a lot of material has been published about yielding in hard rocks during the years. The ambition in this report has not been to compile those findings. In most cases the geology and stress field is not described in such detail that the results can be compared with the APSE findings. /Edelbro 2006/ has compiled field data and observations from rock mass failures in mines and civil engineering projects in Scandinavia. The cases presented have been selected because detailed information about type of failure, geology and stresses has been available. Where failures in hard granitic rocks with limited fracturing are described those stress, strength ratios corresponds reasonably well with the stress, strength ratio for at which the Äspö diorite yields.

/Bergman and Stille 1983/ describes rock mass yielding in a storage facility excavated in very good granite at shallow depth. Despite relatively low stresses problems with spalling was encountered. The paper concludes that the yielding likely was influenced by rock mass structures invisible for the naked eye, rock petrography and residual stresses. This illustrates how important it is to have detailed information about the rock mass when predictions are to be made.

The first well documented full-scale experimental approach to studying the yielding of a rock mass was preformed at the Underground Research Laboratory (URL), Pinawa, Manitoba, Canada where the Mine-by Experiment (MBE) was carried out. In conjunction with the MBE borehole, breakouts were studied and heated failure tests were performed /Read 2004/ to enhance the understanding of the yielding process in massive rock.

To verify that the findings from the URL, where the rock is in principle fracture-free, could be applied to the rock in the Fennoscandian shield, which includes fractures, SKB conducted the Äspö Pillar Stability Experiment (APSE) in order to: 1) demonstrate our current capability to predict yielding in a rock mass containing fractures, 2) demonstrate the effect of a confining pressure, and 3) compare the 2D and 3D mechanical and thermal predicting capabilities of existing numerical codes.

APSE was located at the 450 m level of the Äspö Hard Rock Laboratory. The experimental layout consisted of two 1.75-m-diameter boreholes separated by a 1-m-thick pillar of Äspö diorite containing fractures (Figure 1-1). Because of the relatively low in situ stress magnitudes, compared with the intact rock strength, specially designed excavation-induced and thermally-induced stresses were required to ensure stress magnitudes sufficient to induce yielding of the rock mass. This meant that the experiment was able to track both the elastic and non-elastic rock mass response as the excavation-induced and thermally-induced stress magnitudes were gradually increased.

The experiment was carried out in several steps: (1) excavate the tunnel geometry, (2) excavate the first 1.75-m-diameter borehole, (3) install the confining system (4) drill the 2nd 1.75-m-diameter borehole to form the 1-m thick pillar and (5) apply the thermal stresses. To enable the experiment to be properly designed, the Mine-by Experiment was studied in great detail. The important conclusions of that study are presented below.

## 1.1    Experiments at the URL

This section provides a brief summary of the experiments at the URL that were important for the design of the APSE.

### 1.1.1    Mine-by Experiment

The Mine-by Experiment was conducted between 1989 and 1995 in Canada to study the processes involved in excavation-induced damage and progressive failure around an underground opening subjected to high differential stress under ambient temperature conditions. The circular experimental tunnel was excavated at a depth of 420 m using the non-explosive hydraulic splitting technique in 1-m rounds. It was aligned nearly perpendicular to the major principal stress direction to maximize
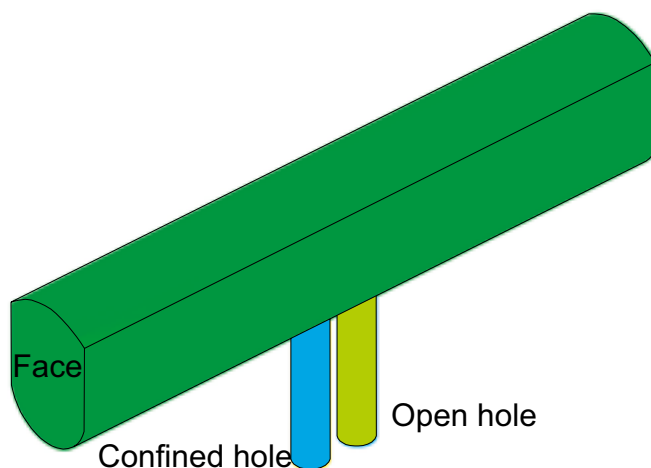


**Figure 1-1.** *General layout of the Äspö Pillar Stability Experiment.*

the tangential stress at the boundary and thereby promote rock mass failure. The best estimate of the three principal stress magnitudes is 60, 45 and 11 MPa with plunges of 11, 08 and 77 degrees, respectively.

The test tunnel was excavated in a volume of mixed Lac du Bonnet granite and granodiorite, whose properties are similar to Äspö diorite. The rock mass at the URL at the 420-m level is fracture-free.

The excavation-induced stress initiated spalling, and v-shaped notches formed at the locations of the highest stress concentration, Figure 1-2. /Martin 1997/ observed four stages during the process of notch development:

1. Initiation: Microcracking of the rock ahead of the tunnel face. The location of these small-scale cracks was determined by the microseismic monitoring system, and they are concentrated in a narrow region near the tunnel face. The deviator stress ($\sigma_1$–$\sigma_3$) at this stage is estimated to 70 MPa ($0.33\sigma_c$).

2. Process zone: Crushing in a very narrow (5 to 10 cm wide) process zone on the tunnel periphery, approximately 0.5 to 1 m back from the tunnel face, where the maximum tangential stress exceeds the strength of the rock. Crushing first occurs in the region where the microcrack density, i.e. microseismic events, is the greatest. Dilatation and small-scale (10 to 100 mm) flaking in this process zone results in the formation of thin slabs that are typically as thick as the grain size of the granite (2–5 mm). This zone is analogous to the classical process zone discussed in the fracture mechanics literature, as it is the zone of damage that forms in advance of the notch.

3. Slabbing and spalling: Formation of larger slabs (1 to several centimetres thick) on the flanks of the notch as the tunnel advances. These slabs form in an unstable manner. This stage represents the strength of the rock around the test tunnel, which is estimated to 120 MPa ($0.55\sigma_c$).

4. Stabilization: When the notch geometry provides sufficient confinement to stabilize the process zone at the notch tip, failure is halted. This occurs when the geometry takes on a teardrop-like shape. The teardrop-like geometry of the notch re-orients the principal stresses locally and results in high values of $\sigma_1$ and associated high confinement.

It also became evident that the v-shaped notches did not form diametrically opposite to one another. It was expected that the notches would be initiated at the points of maximum tangential stress concentration. In the case of a circular test section in an elastic medium subjected to an anisotropic stress field, the points of maximum tangential stress concentration would be located diametrically opposite to one another. /Read 2004/ concluded that three-dimensional stress history effects can result in nonuniform preconditioning of the rock mass near the tunnel periphery. This preconditioning could lead to the asymmetric notch development observed. The 3D history effects would originate from the fact that the tunnel was not excavated parallel to a principal stress direction.

Another important observation made during the MBE was that the yielding process was very sensitive to small confining pressures. During the excavations the notch located in the roof could develop freely as the spalled off slabs fell down. There were no indications, including from AE surveying, of yielding close to the tunnel floor. It was not until an approximately 0.5-m-thick layer of tunnel muck was removed from the floor that spalling was initiated at the floor. The notch that formed here was not as deep as the one in the roof where the slabs could fall off freely. The confinement pressure effect of the slabs remaining in the notch is hence probably enough to partly control the yielding process.

## 1.1.2 Borehole breakouts and the heated failure tests

A number of boreholes with diameters ranging from 150 to 1,240 mm were excavated. Observations of the borehole breakouts revealed that they did not form diametrically opposite to one another. The boreholes shared the characteristic that they were not excavated parallel to a principal stress direction. During excavation of an opening not aligned with one principal stress direction the 3D-stress field in front of the excavation will rotate as it is re-distributed around the excavation. During this process, stress increases and decreases in different directions, which can precondition the rock in front of the excavations if the stresses are large enough in relation to the rock strength. To verify a hypothesis that this was the reason for the breakouts not being diametrically opposite, 600-mm-diameter boreholes were drilled parallel to the $\sigma_3$ direction at the 420-m-level. In these holes the

asymmetry in the borehole breakouts was practically eliminated. It was concluded that this verified the theory of preconditioning of a rock mass due to rotating stress fields. The test was carried out in five different stages which included heating of the rock mass in different sequences and application of a confining pressure /Read 2004/.
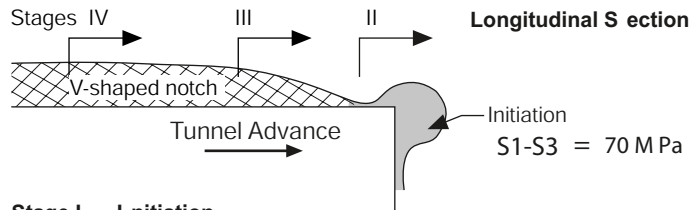


**Stage I - Initiation**
Cracking initiates ahead of the tunnel face in the region defined by the deviatoric stress exceeding a critical value.
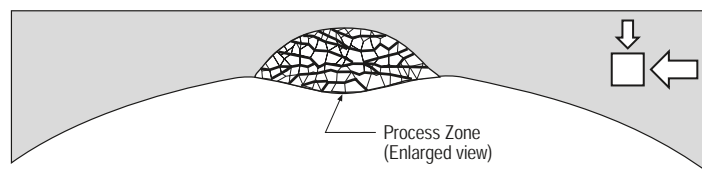
**Stage II - Process Zone**
Critically oriented flaws are exploited in the zone of maximum tangential stress. This process initiates at the boundary of the tunnel. Shearing and crushing occurs in a very narrow process zone about 5 - 10 cm wide. Extensive dilation, at the grain-size scale, occurs in this process zone.
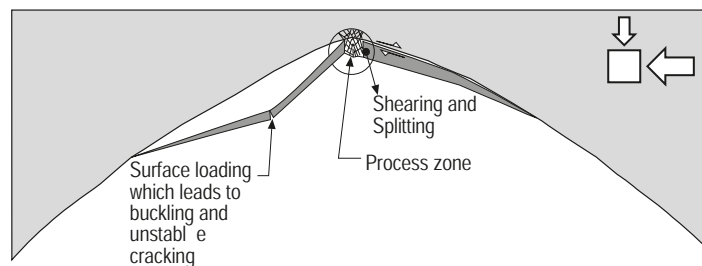
**Stage III - Slabbing & Spalling**
Development of the process zone leads to the formation of thin slab. These thin slabs form by: 1) shearing, 2) splitting, and 3) buckling. The thickness of the slabs varies from 1 to 5 cm. The thickest slabs form as the notch reaches its maximum size. Near the notch tip the slabs are curved.
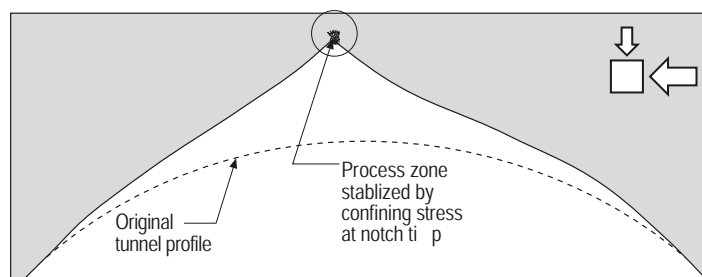
**Stage IV - Stabilization**
The development of the notch stops when the notch geometry provides sufficient confinement to stabilize the process zone at the notch tip. This usually means there is a slight "tear-drop" like curvature to the notch shape.

*Figure 1-2. Illustration of the major processes involved in the initiation, development and stabilization of the v-shaped notch in the Mine-by Experiment. Modified from /Martin 1997/.*

Among the monitoring equipment used was an AE system. From the different stages it was found that damage development as indicated by AE activity occurred primarily during periods of drilling and heating. AE activity occurred to a lesser extent during cooling and tended to decrease during periods of constant temperature. The water pressure in the vinyl liner suppressed AE activity during the heating phase. When the pressure was removed, AE activity increased, indicating the effect of a 100 kPa confinement pressure on the yielding process in the rock.

### 1.1.3 Experiences from laboratory testing of Lac du Bonnet granite

/Martin and Chandler 1994/ investigated the progressive failure of Lac du Bonnet granite in unconfined laboratory tests. They identified three different stress stages in their study of these tests: crack initiation stress ($\sigma_{ci}$), crack damage stress ($\sigma_{cd}$) and peak strength ($\sigma_c$). $\sigma_{ci}$ is caused by stable tensile cracking and $\sigma_{cd}$ by crack sliding. The two stress levels thus have a completely different origin related to the type of damage they represent.

Martin and Chandler also tested the scale effect on $\sigma_{ci}$ and $\sigma_{cd}$ in samples ranging in diameters from 33 to 300 mm. The sample volume did not affect the stress levels for $\sigma_{ci}$ and $\sigma_{cd}$. Furthermore, the data indicated that the peak strength trended towards the crack damage stress as the sample size was increased.

The crack initiation damage stress parameter was further studied by running damage controlled tests. This testing revealed that $\sigma_{ci}$ still was fairly constant and apparently independent of the accumulated damage in the sample. On the other hand, $\sigma_{cd}$ was sensitive to the initial damage of the sample and was quickly reduced to a threshold value in the early stages of the tests.

Damage-controlled tests were also performed in a tri-axial testing apparatus. It was found that the observed drop in $\sigma_{cd}$ was reduced with higher confining pressures and reached a threshold value greater than $\sigma_{ci}$. In unconfined tests, the crack damage stress threshold was close to the crack initiation stress. When the crack damage threshold was plotted in the $\sigma_1$–$\sigma_3$ interval it followed a linear relationship which was close to the residual friction angle of Lac du Bonnet granite.

### 1.1.4 Relevance to APSE

The findings from the experiments at the URL were very important for the planning and design of the pillar stability experiment. The ability to predict $\sigma_{ci}$ and $\sigma_{cd}$ from compression tests on cores and then be able to estimate the appropriate level of excavation-induced stress in the pillar was applied with success. The low confining pressures needed to suppress fracture growth were also an important finding. The confining pressure for the APSE could therefore be set to a reasonable level from the beginning.

General observations of the yielding in the Mine-by Experiment confirmed that it would be possible to cause gradually yielding of parts of an experimental pillar without the risk that it would suddenly collapse in a violent manner.

## 1.2 Observational method

The novelty in the design and execution of the Äspö Pillar Stability Experiment required close observation. The detailed study of the rock yielding process that was to be performed required that the process had to be controlled to as large an extent as possible. Unexpected observations had to be prepared for, and modification of the design had to be possible to guide the process in the desired direction. A great deal of the successful outcome of the experiment origins from running it in strong resemblance with the observational method recommended by /Peck 1969/.

## 1.3    Hypotheses

Mainly based on the illustrative study by /Ortlepp 1997/ and the observations and interpretations of the Mine-by Experiment, the following hypotheses were derived. The hypotheses served as a basis for the design work.

1. Äspö diorite is expected to yield in a manner similar to the Lac du Bonnet granite at the URL, despite the fact that the diorite is fractured. The yield strength should therefore be approximately 0.6 $\sigma_c$ and the depth of the breakout should be between 1.1a and 1.4 a (9 to 35 cm), where "a" is the radius of the large hole).

2. Elastically calculated temperature-induced stresses can be superimposed on the excavation-induced stresses at locations where the rock has not yielded. A good approximation of the actual stress state at those locations can then be derived.

3. Small confining pressures significantly influence the yield strength of rock. A clear difference in the behaviour of the rock mass in the two holes was therefore expected to be observed.

## 1.4    Limitations and objectives

This report focuses on an experimental study of the response of the rock mass to a coupled mechanical thermal loading. A great deal of attention has been devoted to the planning, design and execution of the experiment and documentation of the results. This report therefore provides a detailed description of the work done and presents the results in such a way that further research on the experimental data is encouraged. The objective is that the reader should be convinced that the documentation is of such good quality that the data sets acquired can be used for different studies.

In addition to the description of the experiment, an effort has been made to estimate the yield strength of the rock mass studied and verify those results. Elastic and plastic numerical codes have been used to estimate the yield strength.

The objectives of this report can be summarized as:

1. Estimate of the yield strength of the rock mass, compare it with results of laboratory tests and compare this with results obtained from the URL to validate the APSE findings.

2. Describe the observations of the effect of the confining pressure.

3. Describe and model rock mass response to the drilling of the de-stress slot.

4. Thoroughly describe the experiment, monitoring and observations to ensure the relevance of the data and the observations to the reader.

# 2 Design of experiment

Rock mass yielding has only been associated with a few locations in the deeper parts of the Äspö HRL. The findings from the URL were, as previously described, used to guide the design of the Äspö Pillar Stability Experiment. It should be noted, however, that while the mean uniaxial laboratory compressive strength (UCS) of Äspö diorite is approximately equal to the UCS of Lac du Bonnet granite, the magnitude of the maximum principal stress at the 450 m level of the Äspö HRL is only 50% (approximately 30 MPa) of the maximum principal stress in the AECL's URL (60 MPa). Hence, a major challenge for the experiment was to develop a design that would increase the excavation-induced stresses in a controlled manner, similar to that used in a laboratory environment, so that the failure process could be controlled. This would facilitate data collection and visual observations at all stages of the experiment. The most practical way to achieve the objectives was to use the observational design approach for the experiment, similar to that proposed by /Peck 1969/. The experiment contained the following major steps:

1) Determine a suitable site for the experiment on the 450 m level of the Äspö Hard Rock laboratory (Figure 2-1).

2) Determine the largest practical tunnel geometry for elevating the stresses in the floor of the tunnel to an optimum magnitude.

3) Conduct scoping calculations and predict the pillar response.

4) Excavate the tunnel and carry out site characterization.

5) Determine the optimum width of the deposition-hole pillar based on scoping calculations and site characterization.

6) Design and test the confining system that was to be installed after the drilling of the first hole.

7) Select the location for the pillar, and install the instrumentation.
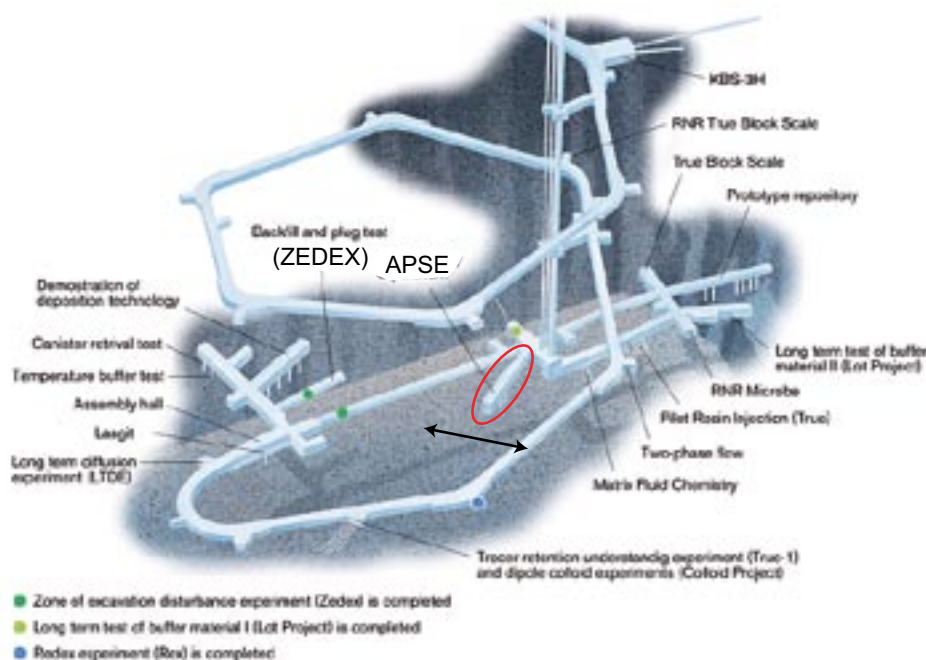


*Figure 2-1.* *Location of APSE in relation to the deeper parts of Äspö HRL. The arrow indicates the direction of the major principal stress.*

8) Excavate the first 1.75-m-diameter hole to a depth of 6.5 m and install the confining system.

9) Excavate the second 1.75-m-diameter hole to form the pillar.

10) Install additional instrumentation in the open hole and install the heaters.

11) Heat the pillar gradually so that the onset of failure could be easily detected and monitored.

12) At the end of the heating phase, gradually release the confinement pressure.

13) Conduct post-experimental characterization of the pillar to document the extent of damage.

In most of the individual steps the observational design method approach was used to adjust the experiment to the observations made with the objective of optimizing the outcome.

Like all major experiments conducted at the Äspö HRL, the experiment was assigned a project/ technical manager who was responsible for the day-to-day operations. A panel of internationally recognized experts reviewed the project on as-needed basis. The project was successfully completed in December 2006.

## 2.1    Geotechnical setting

The general location of the experiment at the Äspö HRL is shown in Figure 2-1. Because of the need for elevated stresses, the experiment was located at the 450-m level where the stress magnitudes and geology were well known. Mapping of the adjacent tunnels showed that the volume of rock where the APSE would be located could be classed as a typical Äspö diorite.

## 2.2    Geology and rock mass quality

Prior to the excavation of the APSE tunnel a cored borehole was drilled approximately parallel to the planned tunnel axis. That hole confirmed the general quality of the rock mass and indicated that there was a slightly altered zone about 60 m from the borehole collar. It was decided to try to avoid this zone by changing the tunnel alignment from the initial bearing of N040E to N046E. When the tunnel had been excavated it was obvious that the zone was not aligned as anticipated, as it intersected the tunnel. The zone is indicated in Figure 2-2 as the shear zone and is further described in subsequent sections.

The experiment drift was excavated using drill and blast technique. Extraordinary care was taken to minimize the excavation disturbed zone (EDZ) in the floor of the drift as discussed in Chapter 3. Once the APSE tunnel was excavated, detailed mapping of the tunnel walls was performed. The mapping indicated the heterogeneous nature of the dominant rock type, Äspö diorite, and that portions of the rock mass were slightly altered. The alteration was not expected to affect the rock mass properties. Fracture mapping showed that most of the fractures were sealed, but several water-bearing fractures were logged. The water-bearing fractures typically strike NW-SE, parallel to the direction of the major principal stress.

Once the geological mapping was completed, the rock mass quality for the inner part of the tunnel was assessed in eleven 5-m panels using the Q system. The mean Q-values for the rock mass in the segments varied from 16 to 309 with an average value of 96 /Barton 2003/. The pillar was located within a panel with a Q-value of 19.

The location of the pillar was chosen based on the fracture mapping and the rock mass quality. The chosen location contained a healed shear zone with a total width of approximately 20 cm that would intersect the upper part of the pillar, Figure 2-2. The healed mylonitized Äspö diorite in the shear zone was clearly weaker than the fresh Äspö diorite. However, scoping calculations indicated that the zone would remain stable. A displacement (LVDT) sensor was mounted parallel to the shear zone at the centre of the pillar (Chapter 4).
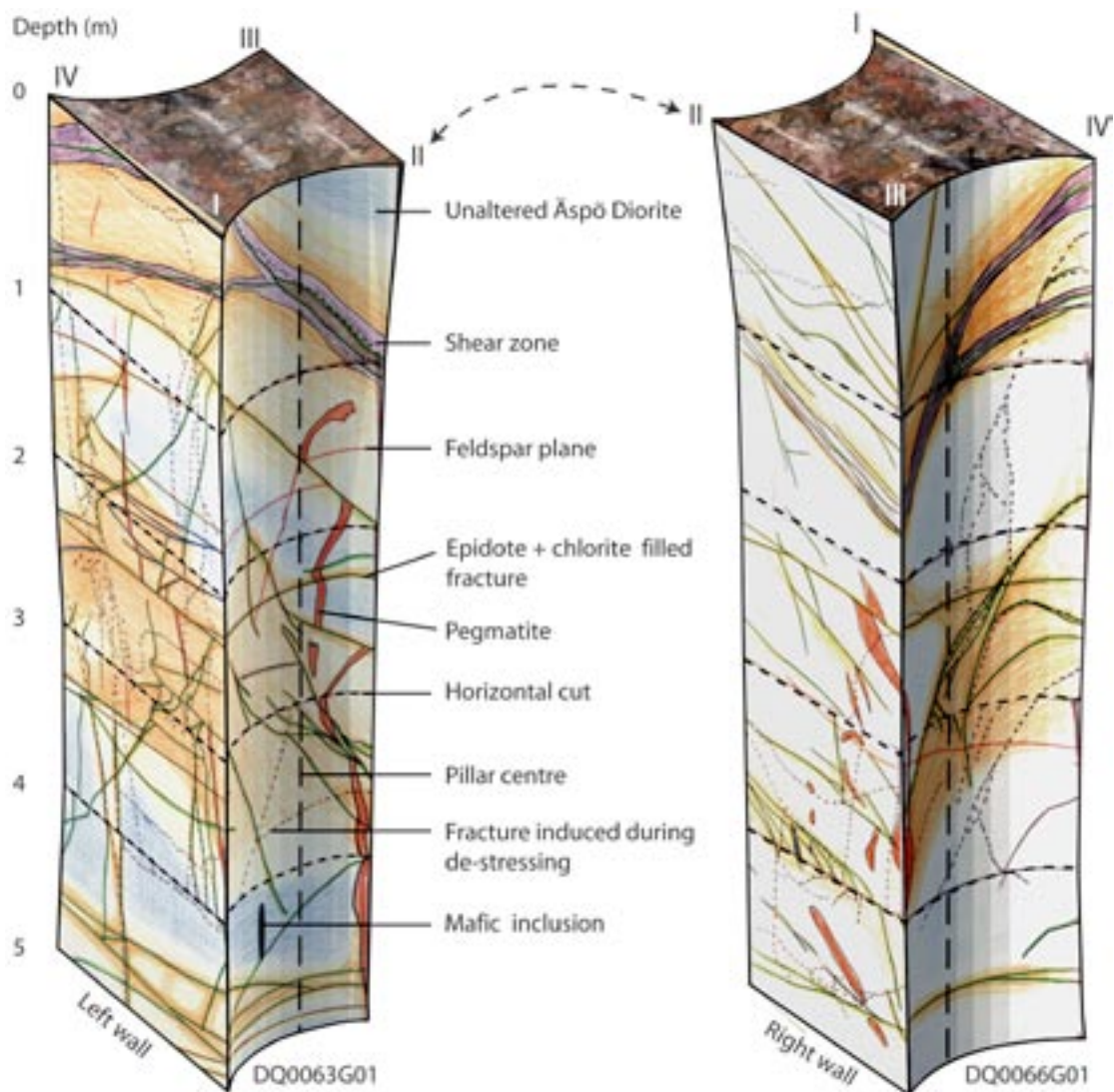
***Figure 2-2.*** *Compilation of the geological mapping of the five pillar blocks.*

The excavation of the 1.75-m-diameter hole which formed the pillar was carried out with a modified TBM /Andersson and Johansson 2002/. The holes intersected water-bearing fractures and the flow in the open (DQ0063G01) and confined (DQ0066G01) holes was approximately 10 and 30 l/min, respectively. Once the experiment was completed, the walls of the large-diameter holes were mapped and photographed in detail. In addition, when the pillar had cooled down after the heating phase it was removed in 1-m-high blocks cut with a diamond wire saw (Chapter 10) to allow detailed inspection of geology and rock mass quality. The blocks were mapped /Lampinen 2005/ and the top surfaces were photographed with a high-resolution camera. The visualization software Surpac was used to compile three-dimensional geological models of the pillar to a depth of 5 m (Figure 2-2). The heterogeneous nature of the rock mass is clearly illustrated in Figure 2-2.

The geological mapping of the tunnel floor, the large-diameter boreholes and the pillar walls is presented in greater detail in Figure 2-3 to Figure 2-7.
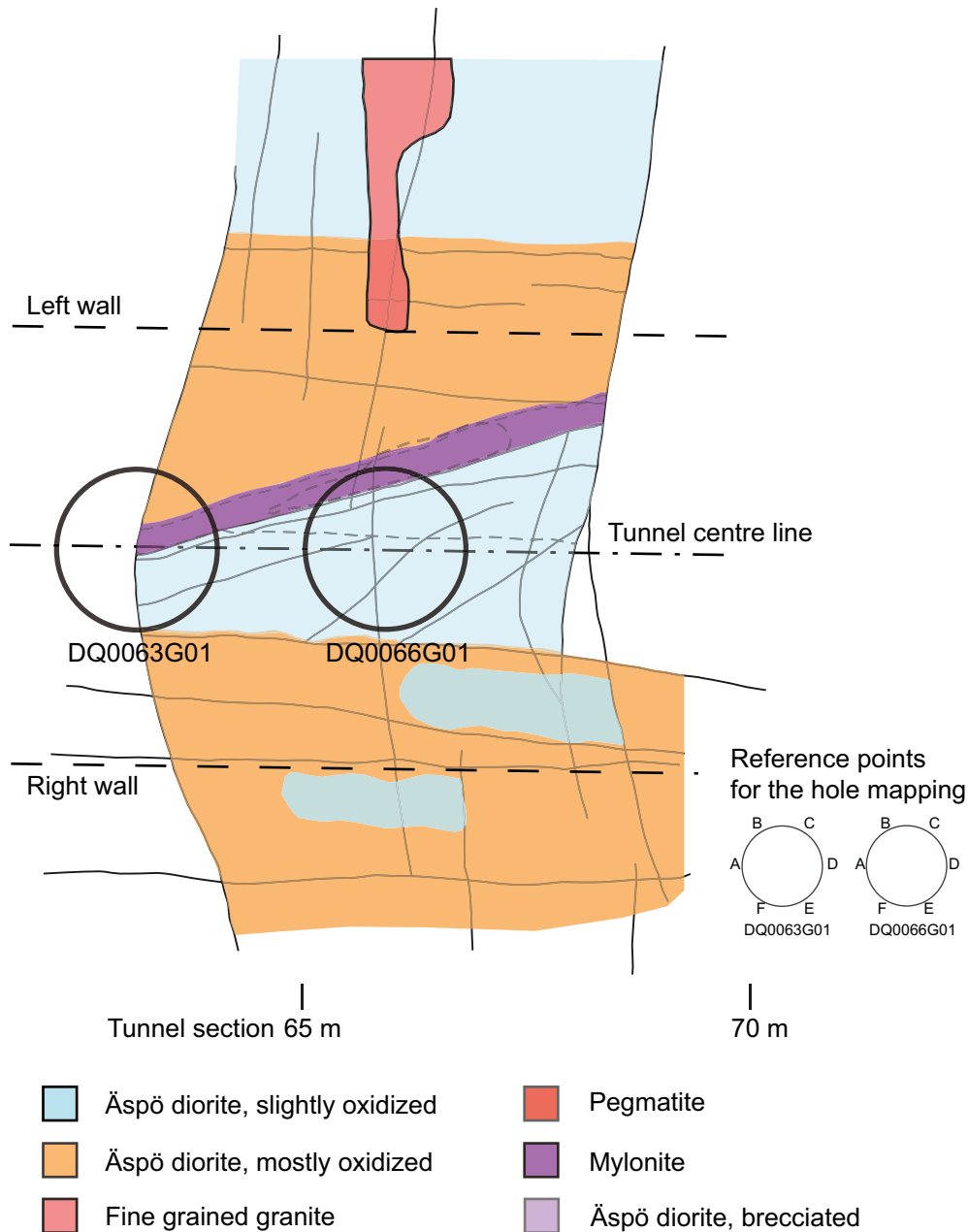
**Figure 2-3.** *Geological mapping of the tunnel floor at the pillar location. The large-diameter holes and the reference points A to F used during the mapping of the hole walls are indicated in the figure.*

The floor mapping in Figure 2-3 and the mapping of the deposition holes in Figure 2-4 and Figure 2-5 have an approximate cut-off that is approximately 0.5 m. Hence, structures shorter than that are not included in the mapping.

The mapping of the pillar walls (Figure 2-6 and Figure 2-7) was done with a cut-off length of approximately 0.1 to 0.5 m. The figures also present the mapped fractures separately. As described in Chapter 10, fracturing was induced in the pillar as the pillar blocks were excavated, and these fractures are highlighted in the figures. Fracture 08 (Figure 2-5) is of particular interest for the outcome of the experiment, since it was one of the few open water-bearing fractures close to the pillar. It was evident that fracture 08 would intersect the pillar. A concern with fracture 08, but also

28
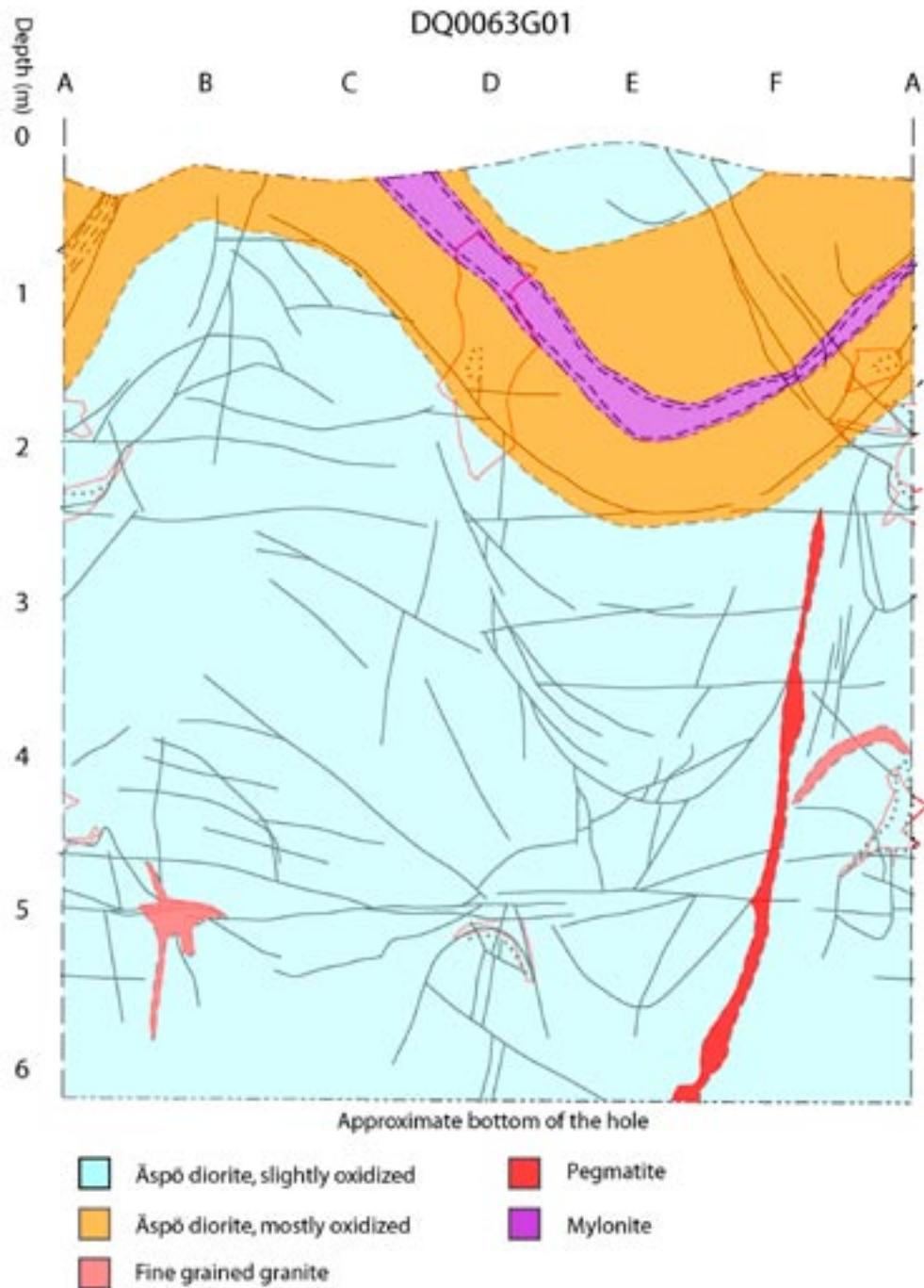
**Figure 2-4.** *Geological mapping of large-diameter hole DQ0063G01. All mapped fractures are included (both sealed and open).*

fracture 14, was that they could displace (shear) during the different phases of the experiment. Displacements could re-distribute the stress field in the pillar. Accurate back calculations of the actual stresses in the pillar during the different phases of the experiment would then become difficult to perform. The AE system was used to keep track of displacements of this kind, and a detailed study of fracture 08 is presented in Appendix 2f.
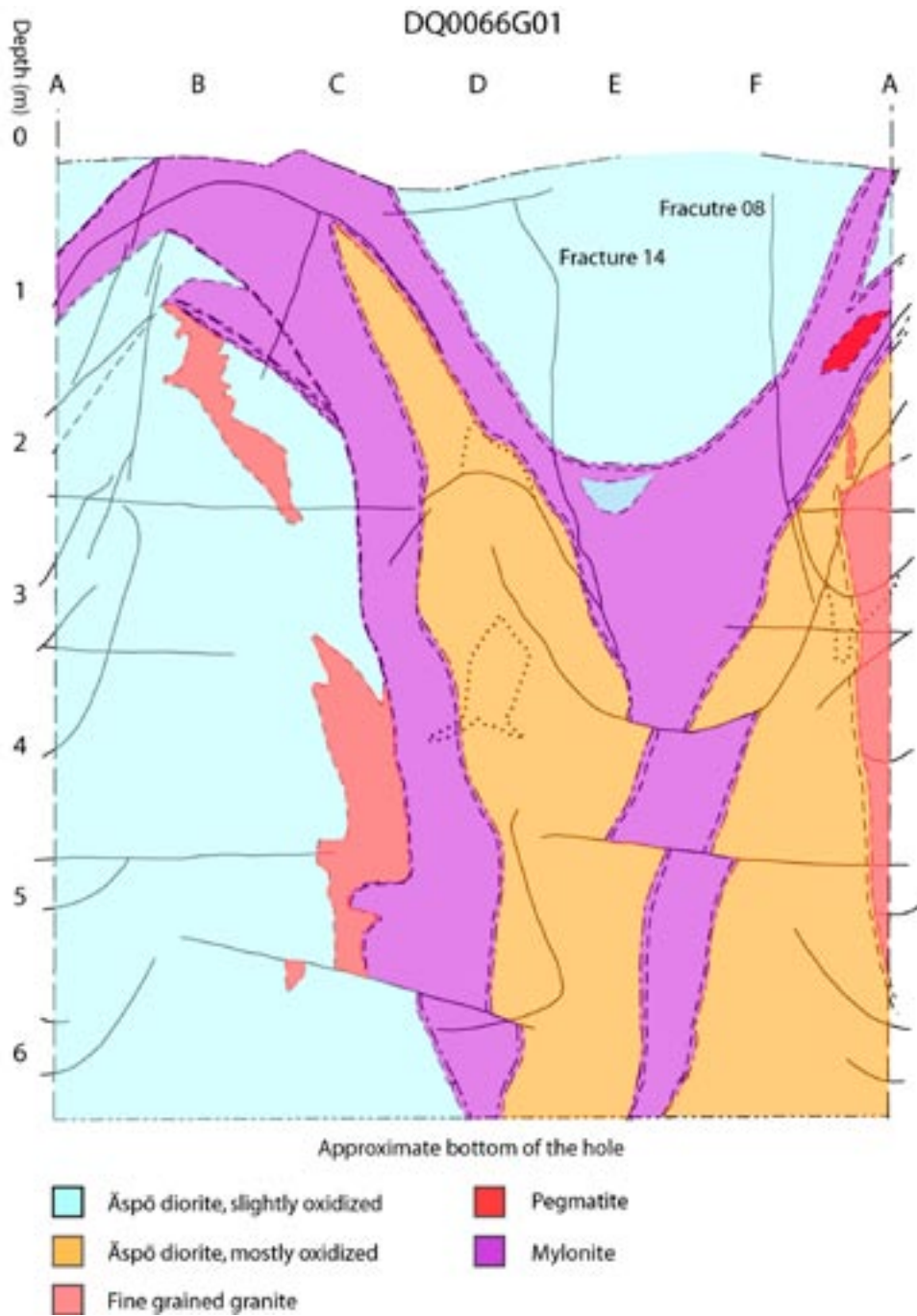
**Figure 2-5.** *Geological mapping of large-diameter hole DQ0066G01. Fractures 08 and 14 are indicated in the figure. All mapped fractures are included (both sealed and open).*
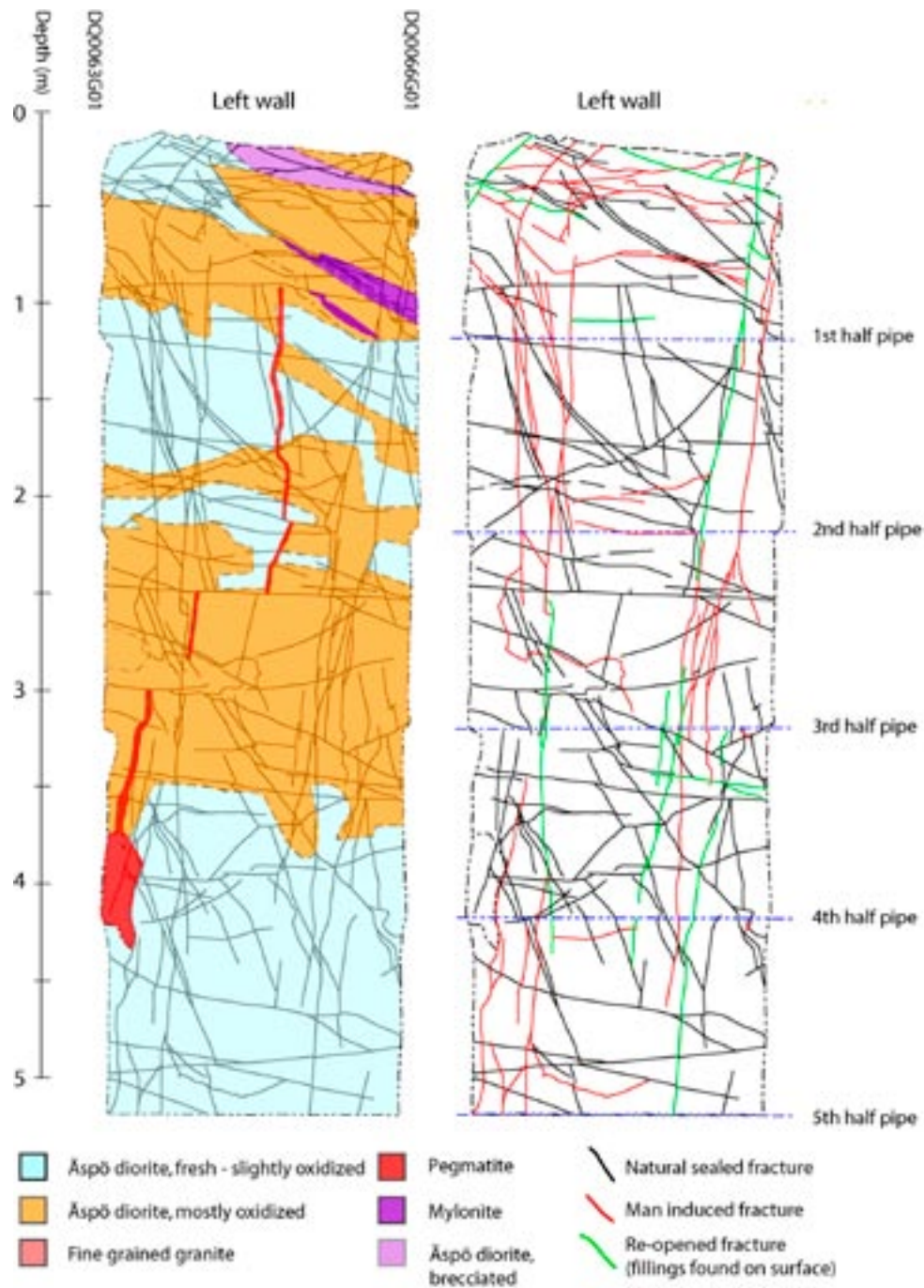
***Figure 2-6.*** *Geological mapping of the left pillar wall (A-wall). The half pipes originate from the boreholes used for the wire sawing (Chapter 10).*
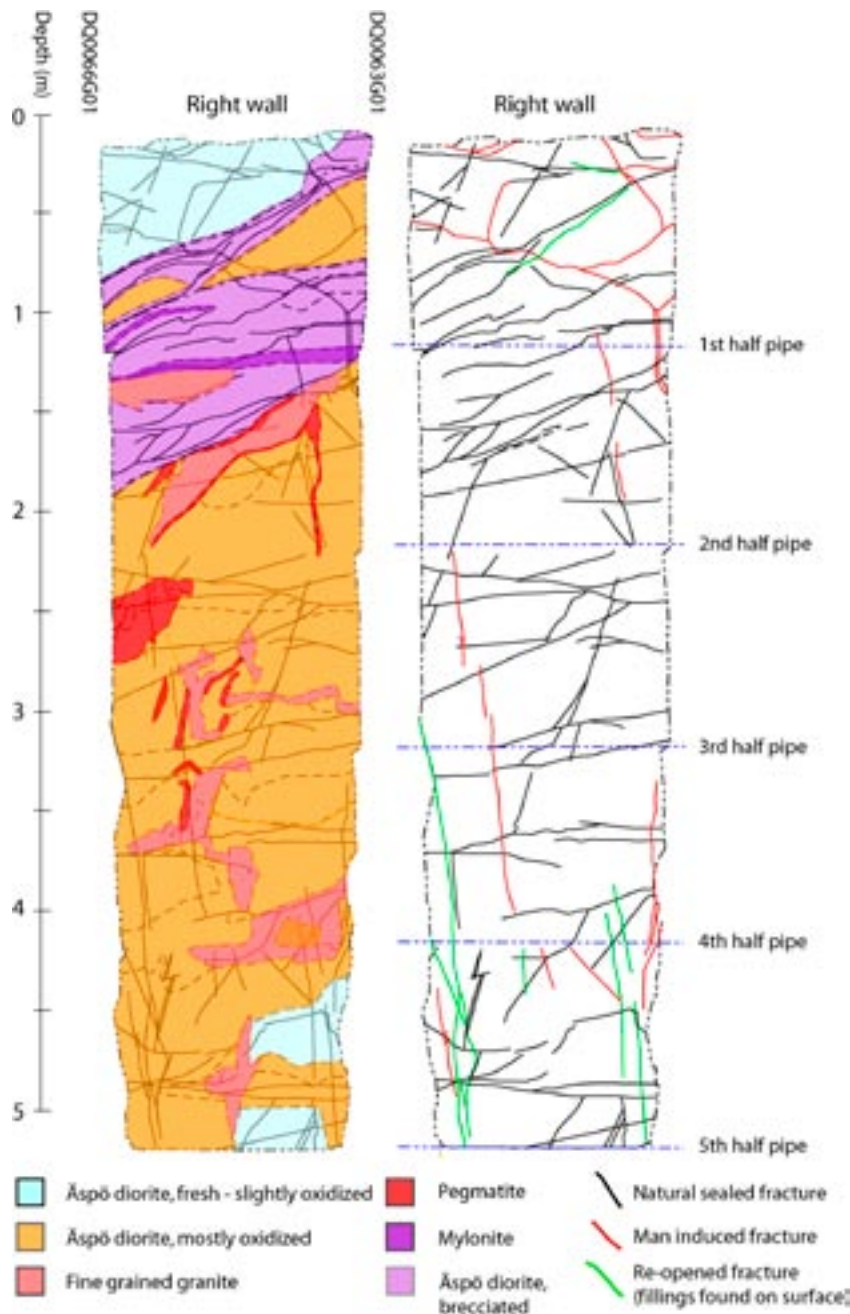
*Figure 2-7.*  *Geological mapping of the right pillar wall (B-wall).*

## 2.3   Intact rock and fracture properties

Thirteen vertical and one inclined 76-mm-diameter cored boreholes were drilled in the vicinity of the planned pillar (Chapter 3). The cored boreholes served as pilot holes for the 1.75-m-diameter boreholes that would form the pillar and as installation holes for the monitoring instruments. Cores from these holes were selected for laboratory testing.

The behaviour of intact rock in laboratory testing is well documented. Eighteen samples were tested using the ISRM-recommended testing procedure /Brown 1981/. As discussed in the introduction, /Martin and Chandler 1994/ noted that in addition to the peak strength, the onset of cracking in laboratory samples was also an important material property that could be linked to rock mass damage. /Stacey 1981/ also used the onset of cracking in intact samples to develop his extensional strain criterion. To determine the onset of cracking for Äspö diorite, axial and lateral strains were recorded for each test. The number of acoustic emission events was also recorded for the uniaxial

compressive tests. In addition to the mechanical properties, a number of tests were carried out to establish the thermal characteristics of Äspö diorite /Staub et al. 2004/. The results from all the successful laboratory tests on intact samples from the experiment area are given in Table 2-1. It should be mentioned that the friction angle and cohesion values taken from the average Äspö HRL data correspond to a slightly lower UCS than the experimental data.

It was anticipated that the damage to the pillar would be dominated by stress-induced fracturing of the intact rock. However, it was not known whether the natural fractures and the heterogeneity of rock mass would play a significant role in the failure process. Testing of fractures induced in the laboratory on intact core samples was carried out to establish their stiffness and strength characteristics. The Mode I (chevron bend method) and Mode II (punch through shear test) fracture toughness for Äspö diorite was also established using the procedures described by /Ouchterlony 1988/ and /Backers et al. 2002/, respectively, to evaluate this potential. Normal stiffness was determined according to /Donath 2002/. All successful results for the fracture characteristics are presented in Table 2-2.

## 2.4    Thin sections

When the blocks are examined with the naked eye, the red colouring on the walls of the blocks gives the impression that the grain size and the quantity of feldspars varies between the oxidized and the unaltered diorite. In the general case, the oxidized diorite appears to have a smaller grain size and more felsic mineralogy but, this type of appearance might be deceiving. Thin sections of different oxidation stages were therefore found necessary in order to verify the reason behind the red colouring.

**Table 2-1. Intact rock mechanics parameters derived from laboratory tests on core samples. Modified from /Staub et al. 2004/.**

| Parameter | Mean value | Range | Unit |
|---|---|---|---|
| Uniaxial compressive strength | 211 | 187–244 | MPa |
| Young's modulus, intact rock | 76 | 69–79 | GPa |
| Young's modulus, rock mass | 55 | – | GPa |
| Poisson's ratio, intact rock | 0.25 | 0.21–0.28 | – |
| Friction angle, intact rock | 49* | – | Degrees |
| Cohesion, intact rock | 31* | – | MPa |
| Tensile strength | 14.9 | 12.9–15.9 | MPa |
| Thermal conductivity | 2.60 | 2.39–2.80 | W/m, K |
| Volume heat capacity | 2.10 | 2.05–2.29 | MJ/m$^3$, K |
| Linear expansion | 7.0 | 6.2–8.3 | (1/K)×E–06 |
| Density | 2.75 | 2.74–2.76 | g/cm$^3$ |
| Initial temperature of the rock mass (measured in situ) | 14.5 | – | °C |
| Crack initiation stress, AE | 121 | 80–160 | MPa |
| Crack initiation stress, strain gauge | 95 | 83–112 | MPa |

* Average data from Äspö HRL. Not tested on the APSE cores.

**Table 2-2. Mechanical parameters of laboratory-induced fractures derived from core samples.**

| Parameter | Mean value | Unit | Standard variation |
|---|---|---|---|
| Mode I toughness, $K_{IC}$ | 3.8 | MPa/m$^{1/2}$ | 0.1 MPa/m$^{1/2}$ |
| Mode II toughness, $K_{IIC}$ | 4.4 to 13.5 | MPa/m$^{1/2}$ | |
| Initial normal fracture stiffness, $K_{NI}$ | 175 | GPa/m | 68 |
| Normal fracture stiffness, $K_{NH}$ | 26,976 | GPa/m | 22,757 |
| Shear stiffness | 15.7/35.5 | GPa/m | |
| Residual angle | 31/30 | Degrees | |

The thin sections were made from samples taken from the slabs formed during yielding and removed before the blocks were sawn. The removal of the slabs is described in Chapter 6. The samples were selected so that Äspö diorite in different alteration stages was studied for mineral composition, grain size and induced microfractures. The descriptions presented here are modified from /Lampinen 2005/. Photographs of the samples used for the thin sections are presented in Figure 2-8

## 2.5 Sampling

The mineral distribution in the thin sections was quantified by a simple point count procedure. In this procedure, the number of identified minerals on a given reference line on the thin section was counted, and from these counts the relative content of each mineral was calculated. Three horizontal lines parallel to the base of the samples and evenly distributed along its height were used for the point count.

Four rock samples with varying degrees of oxidation were selected for making thin sections. The slabs were stored in boxes and organized into ~ 0.5- to 0.6-m sections. In other words, all the slabs removed between 2.7 and 3.3 m are stored together (Appendix 2e). The location of the samples for making the thin sections is therefore only known to within which approximately half-metre section it belongs to. In Table 2-3, the samples and their ID (Figure 2-8) are listed together with the



Unaltered Äspö Diorite, UD

Oxidized Äspö Diorite 1, OD-1

Oxidized Äspö Diorite 2, OD-2

Mylonitic Äspö Diorite, MD

*Figure 2-8.* *Photographs of the rock samples used to make the thin samples.*

34

approximate depth from which they are taken. The rock slab samples OD-1, OD-2 and MD could be oriented due to their shape. In these three thin sections, the section plane is horizontal and hence perpendicular to the orientation of the spalling fractures (Figure 2-9). This made it possible to look for microfractures induced during the yielding process.

The MD sample was selected to represent mylonitized diorite purely on the basis of its textural appearance, not its depth level. The sample has all the qualities of a mylonite: extreme oxidation, dense epidote vein network and massive-like grain size. However, the hole depth level, 4.90 m, from which the sample is presumably taken is not mapped as a mylonitic zone. Nevertheless, the rock at that depth is extremely oxidized diorite and is in many ways similar to "real" mylonite. The location of sample MD is shown in Figure 2-10.

**Table 2-3. Approximate depth of sampling for the thin sections.**

| Type of alteration | ID | Depth of sampling (m) |
|---|---|---|
| Unaltered Äspö Diorite | UD | 2.7 to 3.3 |
| Oxidized Äspö Diorite 1 | OD-1 | 2.7 to 3.3 |
| Oxidized Äspö Diorite 2 | OD-2 | 2.1 to 2.7 |
| Mylonitic Äspö Diorite | MD | 4.3 to 4.9 |
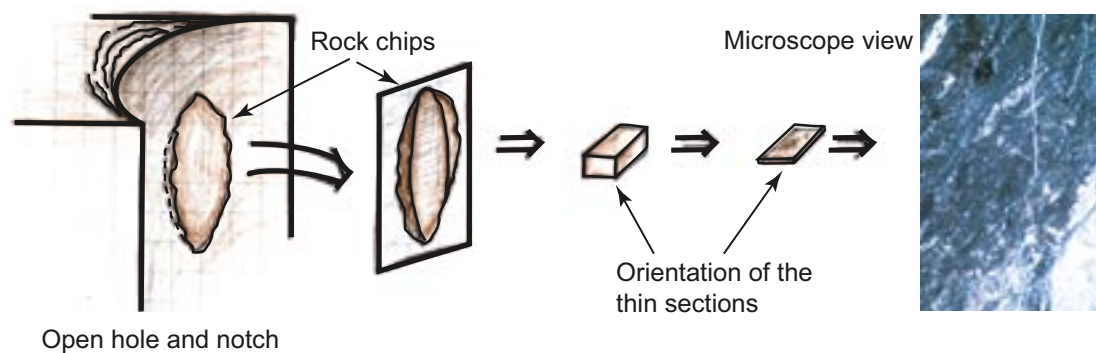


*Figure 2-9.* *Orientation of the thin sections in relation to the boundary of the open hole where the spalling took place and also the anticipated microfracturing. Modified from /Lampinen 2005/.*



*Figure 2-10.* *The approximate location of sample MD at a depth of 4.9 m. Note the strong oxidation.*

## 2.5.1 Microscopy results

Detailed information on the minerals and fracturing in the thin sections is found in /Lampinen 2005/ together with all the photographs taken through the microscope.

### *Alteration*

The general mineralogical distribution of Äspö diorite is presented in Table 2-4. It can be seen in the table that plagioclase constitutes almost half of the mineralogical composition of Äspö diorite. The rest consists mainly of quartz, biotite and K-feldspar. When this statistic is compared with the mineralogical distribution of the thin sections (Figure 2-11), a clear difference can be seen in relation to the mean mineralogical composition in Table 2-4. An effect of the oxidation to the mineral composition is also indicated by increased calcite and reduced plagioclase content.

Alteration (mineral replacement) is as prominent in the thin sections as the red oxidation on the rock surface. The total Si content of the rock appears to remain at same level, although the amount of feldspars, plagioclase and K-feldspar decreases as the amount of quartz and calcite increases (Figure 2-11). These replacement sequences are presented in Table 2-5.

**Table 2-4. Arithmetic mean values of modal analyses of the four most common rock groups in the Äspö area (modified from /Wikman and Kornfält 1995/).**

| Mineral | Fine grained greenstone (%) | Äspö diorite (%) | Småland (Ävrö) granite (%) | Fine grained granite (%) |
|---|---|---|---|---|
| Quartz | 2 | 15 | 25 | 30 |
| K-feldspar | + | 12 | 25 | 39 |
| Plagioclase | 27 | 46 | 37 | 20 |
| Biotite | 18 | 15 | 7 | 2 |
| Chlorite | 2 | 1 | 1 | 2 |
| Muscovite | – | + | + | 3 |
| Fluorite | – | + | + | + |
| Pyroxene | 1 | – | – | – |
| Amphibole | 36 | 2 | + | – |
| Allanite | – | – | + | – |
| Epidote | 9 | 6 | 2 | 2 |
| Monzanite | – | – | – | + |
| Prehnite | + | + | + | + |
| Pumpellyite | + | + | + | + |
| Sphene | 1 | 2 | 1 | + |
| Calcite | + | + | + | + |
| Apatite | 1 | 1 | + | + |
| Zircon | + | + | + | + |
| Opaques | 2 | 1 | 1 | 1 |

**Table 2-5. Mineral replacement sequences in the thin sections.**

| Replacement sequence | Present in thin section |
|---|---|
| Plagioclase → quartz + calcite (partial-total) | UD, OD-1, OD-2, MD |
| K-feldspar → quartz + calcite (partial) | MD |
| Biotite → chlorite (total) | UD, OD-1, OD-2, MD |
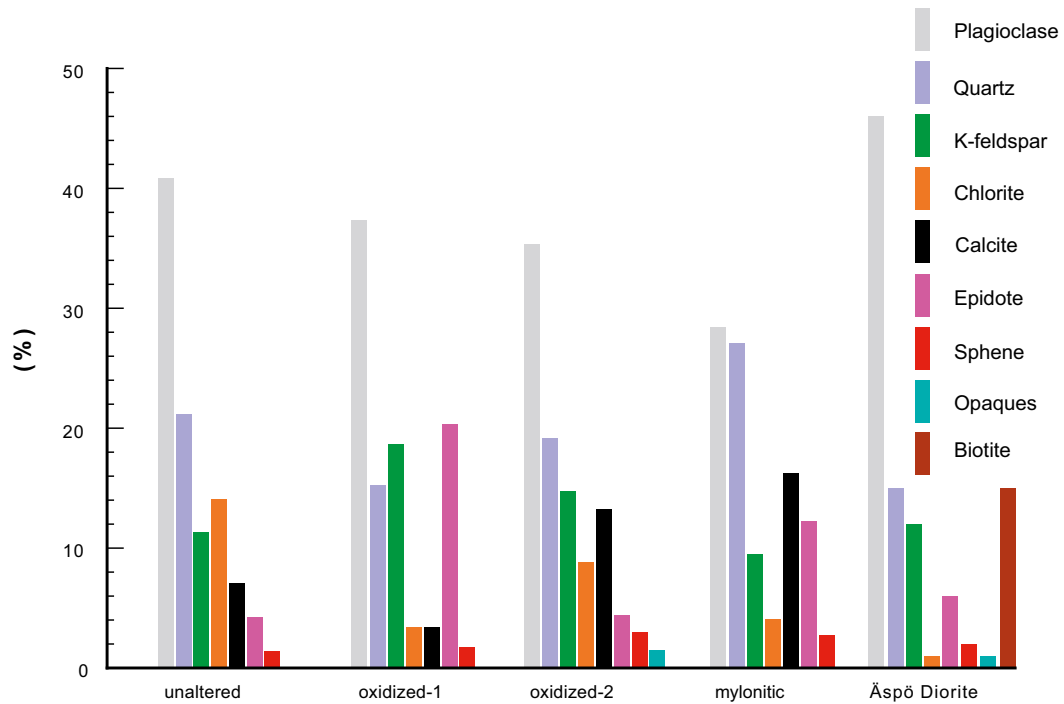
*Figure 2-11.* *Distribution of different minerals in the thin sections.*

It seems that plagioclase has been altered even in the least altered pillar rock sample, OD-2 (Figure 2-12). No biotite, which has presumably all been altered to chlorite, was found in the thin sections. The alteration of the plagioclase and the absence of biotite indicate that the alteration may be greater and more dispersed than is reported in /Magnor 2004/, at least in the pillar rock volume.
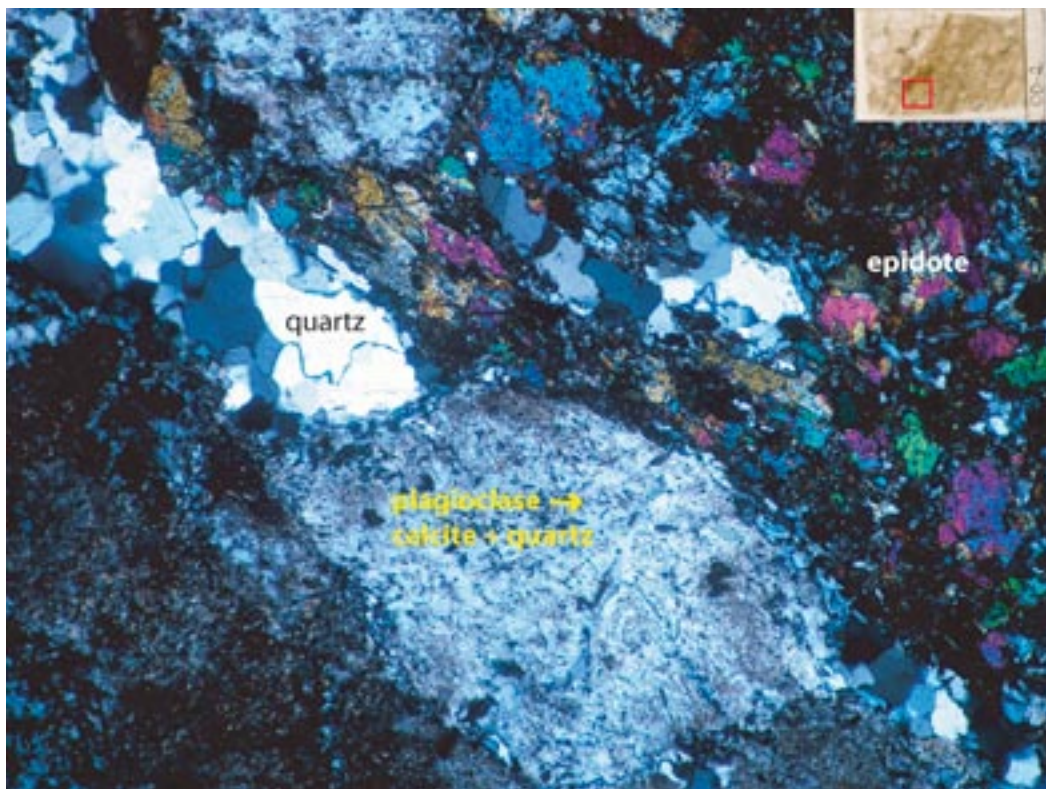


*Figure 2-12.* *Microscope image of sample OD-2 in polarized light. Altered plagioclase crystals and quarts porphyroclasts. The image width is 4 mm.*

The observations show that the plagioclase alteration proceeds along a front that moves inward from grain boundaries and fracture and cleavage surfaces. Albite twinning planes are observed in the microscope image in Figure 2-13 across the grains without interruption and the crystal outlines do not change size or shape during alteration. The preserved twinning structures in the plagioclase indicate that the reaction occurs without altering the silicate frame structure of the plagioclase.

The observed alteration features that were made from the four thin sections are in agreement with a previous study done by /Eliasson 1993/. The alteration features detected in the granitic rocks of Äspö according to Eliasson are summarized in Figure 2-14. When the microscopy observations are compared with that study, the following statements can be made:

1) When the mineralogy part of Figure 2-14 is studied, it can be seen that chlorite exists only in the altered parts of the Äspö granitic rocks. All thin sections in this study contained chlorite and are hence at least slightly altered.

2) The exchange reaction of $K^+$, $Ca^{2+}$ and $Na^+$ proposed in this text is in agreement with information presented in Figure 2-14. The alteration process proposed for the Äspö diorite is therefore probably a correct conclusion.

3) In Figure 2-14, the porosity of the rock increases and its density decreases as alteration proceeds. This implies that the strength of the rock is most likely to decrease as the degree of alteration increases.

It can be concluded that the more the Äspö diorite in the APSE pillar rock volume is oxidized, the more it is altered, and this reduces its strength. Laboratory tests have shown that red staining of the rock does not reduce its strength noticeably. Higher degrees of alteration (such as mylonitization) are needed to significantly influence the UCS results.
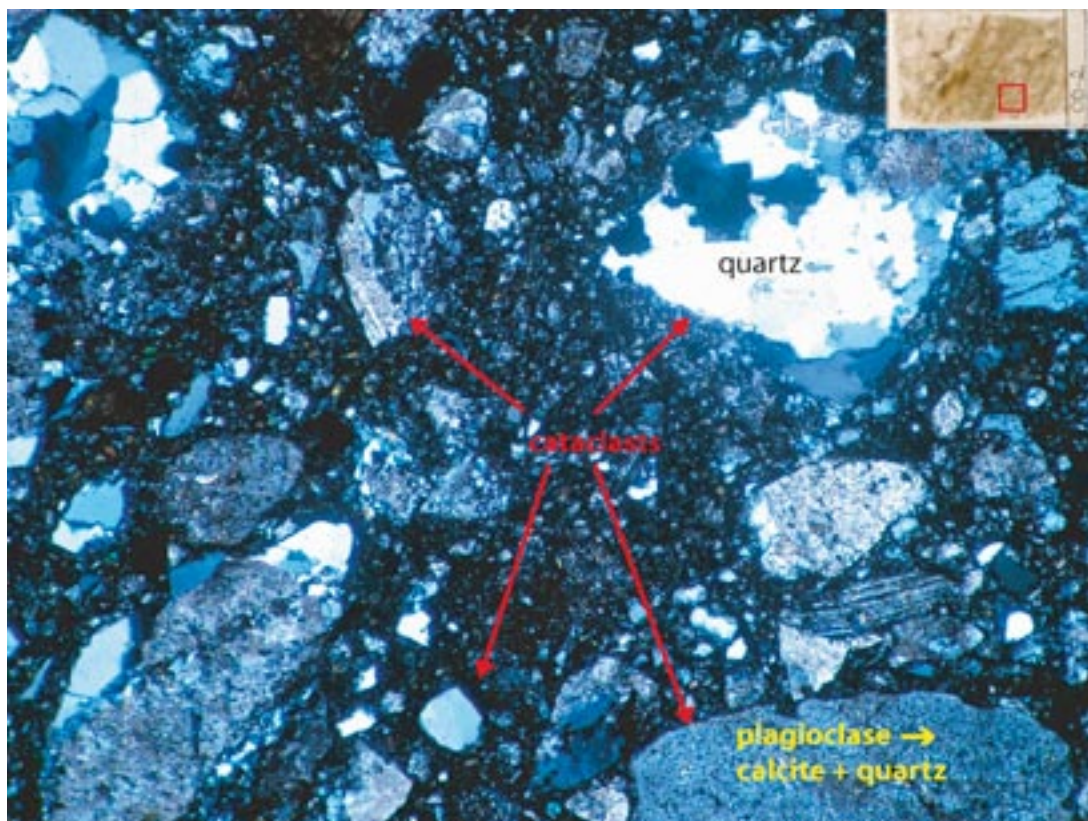


*Figure 2-13. Microscope image of sample OD-2 in polarized light. Cataclastic shear band with brecciated matrix and sharp porphyroclasts. Some twinning in the altered plagioclase grains. The image width is 4 mm.*

38
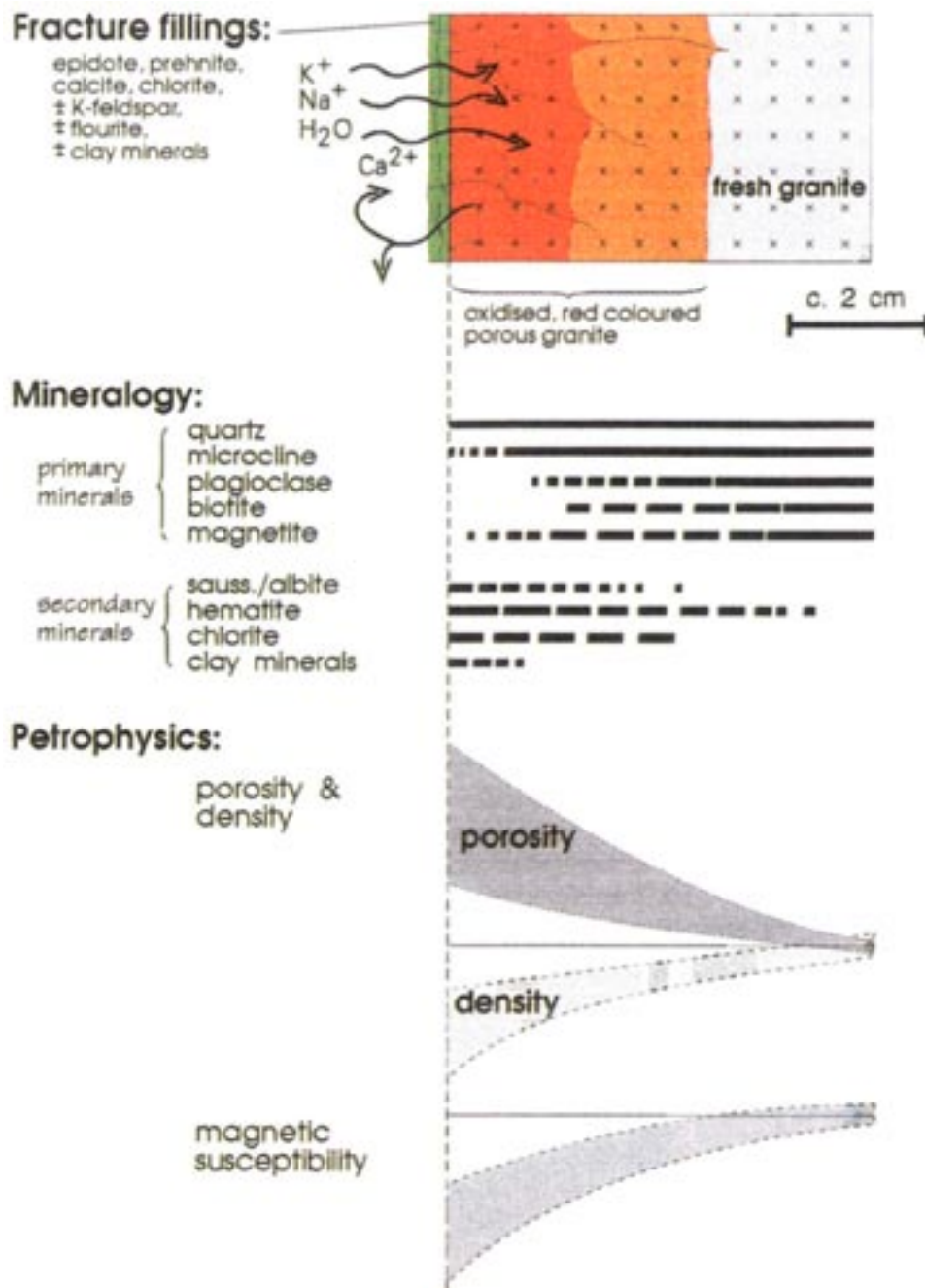
**Figure 2-14.** *Schematic illustration of the most important alteration features in the red colouring along fractures in the Äspö diorite. Modified from /Eliasson 1993/.*

### Grain size

The grain size of the minerals does not seem to be affected by the degree of alteration of the sample. This can be noted from the mineral grain size charts in Figure 2-15. The grain size variation in the unaltered (UD) thin section and in both of the oxidized ones (OD-1 and OD-2) is very similar. The only exception is the mylonite sample (MD), which lacks large K-feldspar porphyroclasts. This change in mineral grain size is probably related only to the brittle shearing that has brecciated the rock. Alteration itself doesn't seem to break minerals and thereby reduce grain size. Changes in mineral size seem in this case to be purely related to shear structures. The brecciated minerals (cataclasts) within the epidote veins can be seen in the microscope images in Figure 2-16.
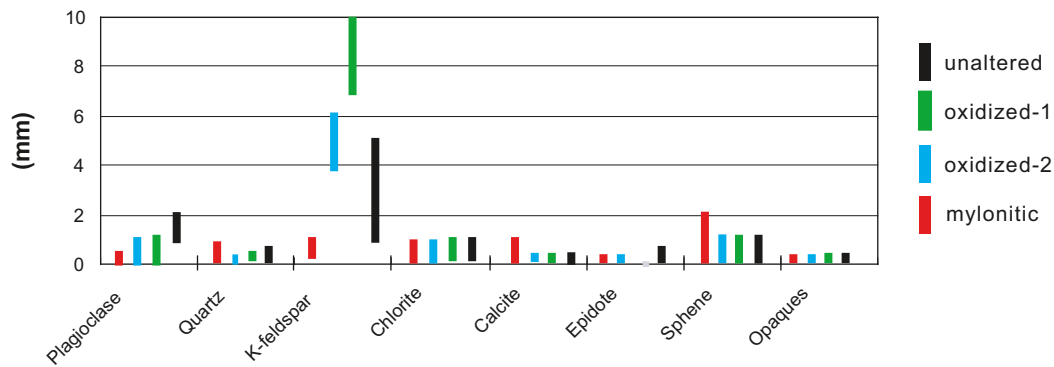
**Figure 2-15.** *Grain size variation of all minerals in thin sections.*



**Figure 2-16.** *Microscope image of sample MD in normal light showing an epidote vein which is actually a microscopic cataclastic shear zone. The image width is 4 mm.*

### Microfracturing

Microfracturing induced during the heating phase is only observed with certainty in one of the thin sections, the microscope image in Figure 2-17. The microfracture observed there is located in the epidote + chlorite band and cuts across the direction of the foliation. The orientation of the microfracture, which is parallel to spalling fractures, and the fact that the fracture in Figure 2-17 has a coarse trace that doesn't follow crystal boundaries and has no mineral filling suggests that it stems from the yielding during the APSE experiment.

40

For instance the brittle fracturing in the MD sample (Figure 2-18) is smoother and more planar compared with the anticipated spalling-related fracturing in Figure 2-17. Pre-existing microfracturing does not seem to follow any previous structures in the rock sample and it cross-cuts for example the foliation in the rock. Further, the brittle fracturing in the MD sample has a smooth trace, which implies that this fracturing is not formed in the spalling process but during, or after, the formation of mylonitic shear structures. Fracturing could be due to a more fragile quality of rock that is caused by intensive alteration. On the other hand, the relationship between alteration and fracturing could be the other way a round, i.e. intensive alteration could be due to fracturing and resultant induced fluid activity.

The fracturing in the UD thin section (Figure 2-19) could also be related to spalling, but since the exact orientation and location of the thin section hand specimen is not known, this cannot be known for certain.
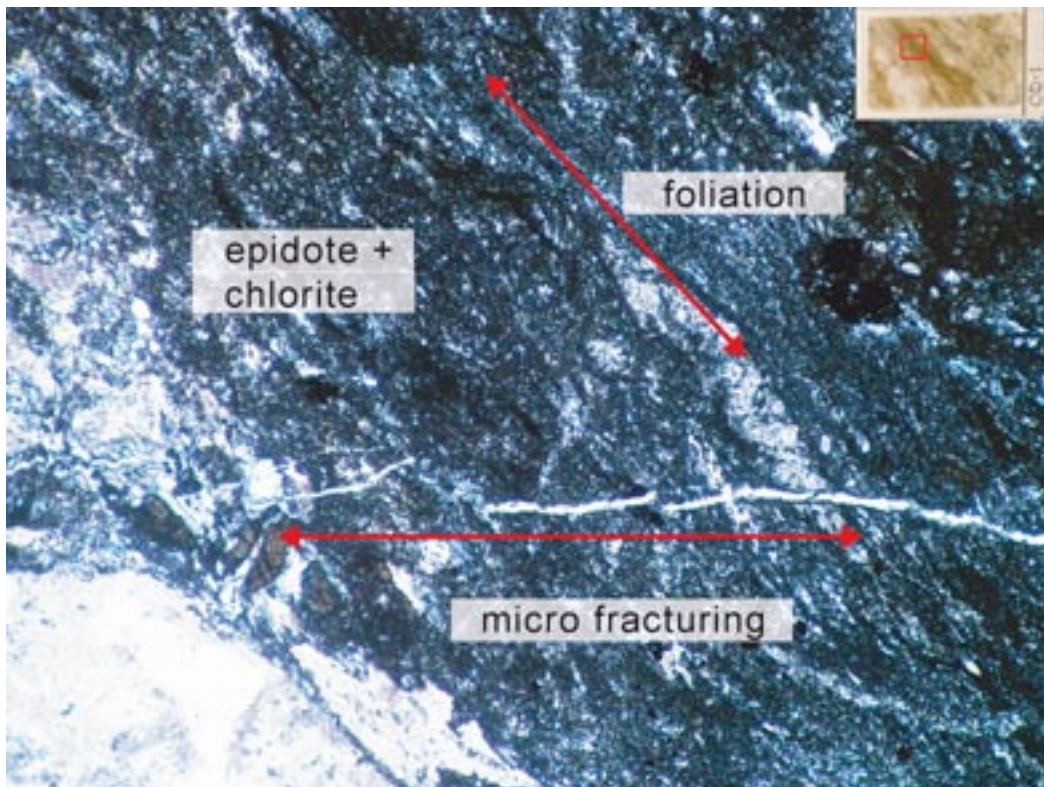


*Figure 2-17.* *Microscope image of sample OD-1 in normal light. Microfracturing in the epidote and chlorite vein with a geometry that can be anticipated for the spalling-related fracturing. The image width is 4 mm.*
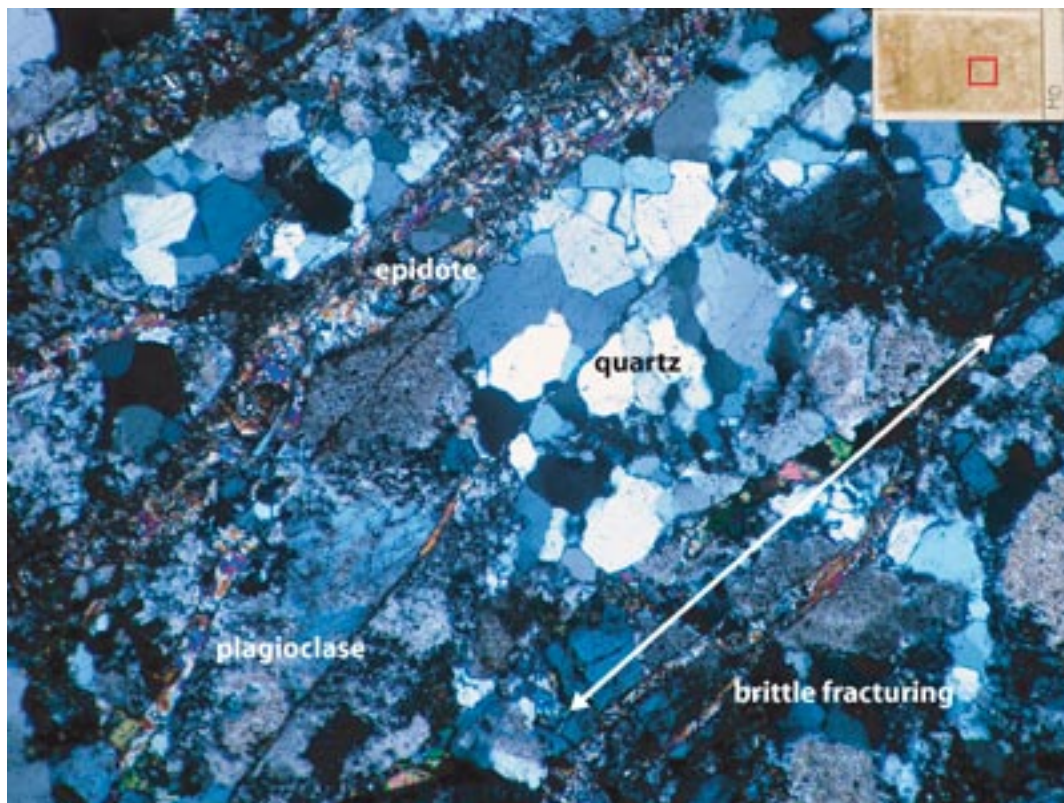
*Figure 2-18.* *Microscope image of sample MD in polarized light. Altered feldspars, quartz and intensive brittle fracturing filled with epidote. The image width is 4 mm.*
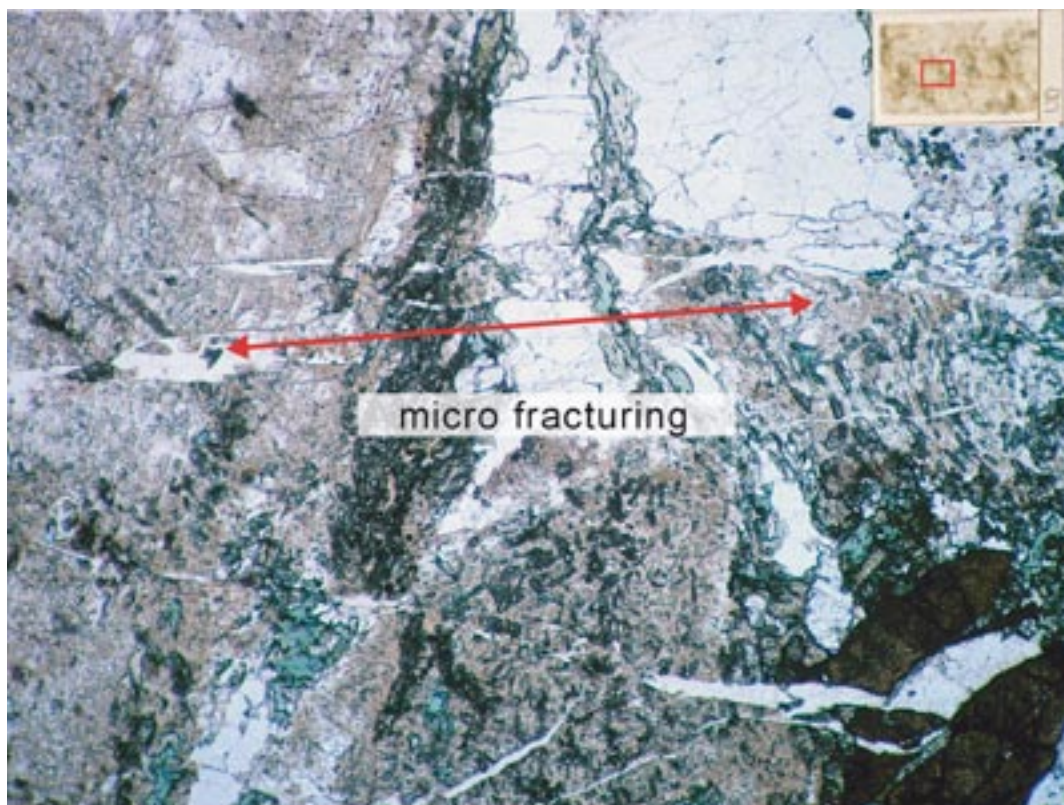


*Figure 2-19.* *Microscope image of sample UD in normal light. Fractures that could be induced during the yielding of the pillar. The orientation of the sample is unknown and the origin of the fractures is not certain.*

## 2.6    Rock stress

The in situ stress magnitudes and orientations were key parameter for the design of the experiment. The state of stress at the Äspö HRL had been characterised using hydraulic fracturing, triaxial overcoring and back analysis /Hakami 2003/. In the vicinity of the APSE /Christiansson and Janson 2002/ reported stress measurements with three different methods in two orthogonal boreholes. The results of those measurements are summarized in Table 2-6. In addition to the stress measurements from the orthogonal holes, a series of CSIRO triaxial overcoring tests were carried out for the ZEDEX experiment located on the 420 m level (Figure 2-1). Those results also supported the findings of /Christiansson and Janson 2002/.

To verify the stress tensor in Table 2-6, back analysis of convergence measurements was performed during the excavation of the experiment drift, /Andersson and Martin 2003, Staub et al. 2004/ using the boundary element code Examine3D /Rocscience/. At a section located 39 m into the drift, seven convergence pins were installed 0.3 to 0.5 m behind the face (Figure 2-20). The pins, which were approximately 700 mm long, were grouted into boreholes and read using a Kern Distometer (Figure 2-21) with an approximate accuracy of ± 0.05–0.1 mm. During the excavation of the pilot drift, the convergence in sections 1-4, 1-7, 3-2, 3-4, 3-7, 5-4, 5-6, 7-4, 4-5, 4-3 and 4-1 was measured five different times: (I) the first reading 0.5 m behind the face, (II) the second after the first 2 m round, (III) the third after the second 2 m round, (IV) the fourth after the third 2 m round, and (V) the fifth after the fourth round, which was 4 m in length.

The results from some of the measurements are presented in Figure 2-22. It is obvious that the mid-wall horizontal displacements are greatest. Compare, for example, the measurements between pins 3-4 and 3-7 or 5-6.

**Table 2-6. Probable stress tensor for the experimental location as assessed before the excavations.**

|                                  | $\sigma_1$ | $\sigma_2$ | $\sigma_3$ |
| -------------------------------- | ---------- | ---------- | ---------- |
| Magnitude [MPa]                  | 25–35      | 15         | 10         |
| Trend (Äspö 96)                  | 310        | 090        | 208        |
| Plunge (degrees from horizontal) | 30         | 53         | 20         |
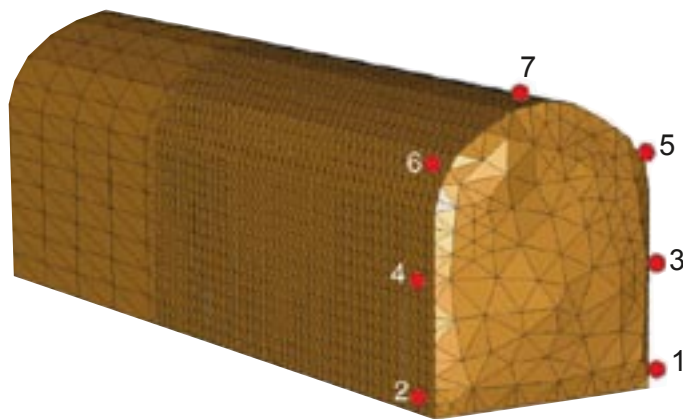


***Figure 2-20.*** *Location of the seven convergence pins 39 m into the drift. The pin locations are plotted on the Examine3D model used for the back calculation.*

**Figure 2-21.** *The convergence was measured with a Kern Distometer. The convergence pins were installed approximately 0.5 m behind the face.*
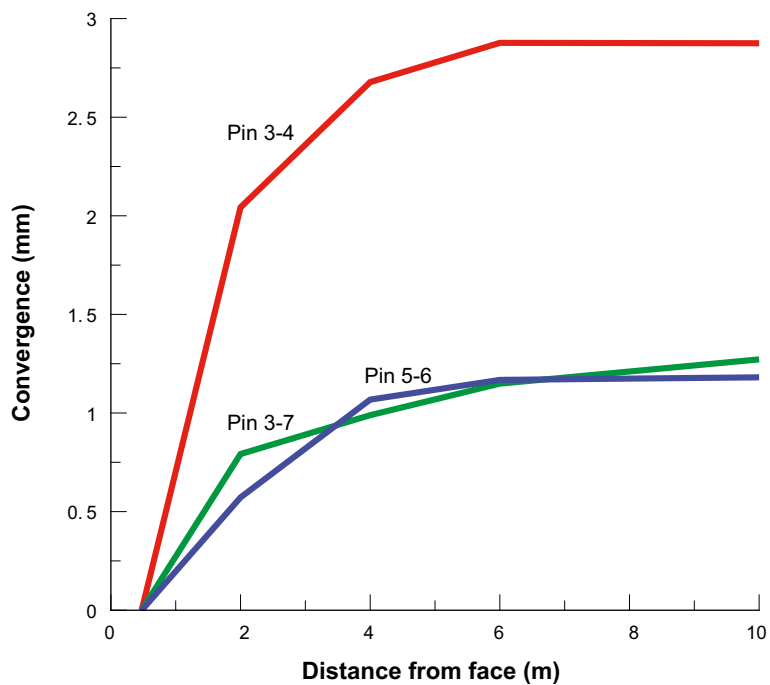


**Figure 2-22.** *Results of the convergence measurements during the excavation of the pilot drift.*

Back calculation of the convergence measurements was carried out using Examine3D, a three-dimensional linear elastic boundary element program. Detailed face profiles and perimeter geometry were used to construct the Examine3D model. Altogether, 36 different realizations were carried out with varying input parameters until a good fit was found between the modelled values and the measured ones. The magnitude of the major principal stress varied between 23 and 35 MPa and the plunge between 0 and 30 degrees from horizontal. The second principal stress varied between 10 and 17 MPa. Young's modulus of the rock mass varied between 35 and 60 GPa. The minor principal stress and Poisson's ratio had small effects on the outcome and were not varied. A comparison of the predicted Examine3D results and the measured convergence displacements is presented in Figure 2-23. Note the good agreement in shape between the two data sets. Because convergence measurements only record a portion of the total displacements, the measured curves must be adjusted for the portion not recorded. From /Chang 1994/ it can be estimated that under elastic conditions, convergence measurements made close to the face record approximately 40 to 50% of the displacements. For these measurements, and the tunnel profile, it is assumed that 50% of the total displacements were recorded. The higher value is chosen because of the damaged zone induced in the face by the blasting. The measurements verify this assumption quite well. The resulting best fit stress tensor was obtained with a rock mass Young's modulus of 55 GPa and a Poisson's ratio of 0.26 (Table 2-7). The major difference between the stress tensor in Table 2-6 and the tensor in Table 2-7 is related to the plunge and the trend.

**Table 2-7. Back-calculated and best-estimate stress tensor for the APSE site.**
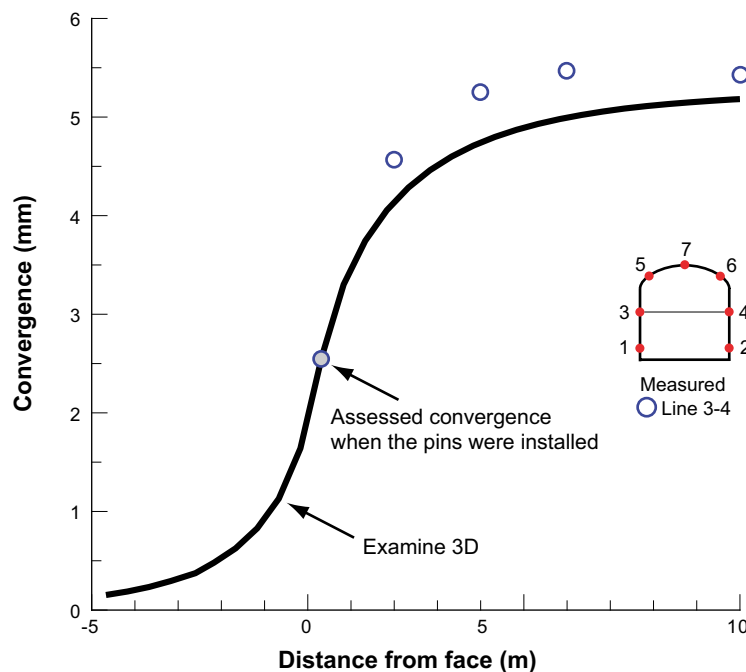
|  | $\sigma_1$ | $\sigma_2$ | $\sigma_3$ |
|---|---|---|---|
| Magnitude [MPa] | 30 | 15 | 10 |
| Trend (Äspö 96) | 310 | 090 | 220 |
| Plunge (degrees from horizontal) | 0 | 90 | 0 |



*Figure 2-23.* *A comparison of the measured convergence with the computed convergence from Examine3D. When plotting the figure it is assumed that 50% of the total displacements took place before the pins were installed.*

After the field work the geometry of the breakout zone in the open hole was studied to determine whether the direction of the horizontal stresses might be slightly off. This was not found to be the case. As an extra check, two new realizations were therefore made for comparison with the convergence data. In the first, the trend of $\sigma_1$ and $\sigma_3$ was rotated 10 degrees clockwise (to 320 and 230 degrees, respectively). In the second realization, the rotation was kept unchanged and the plunge of $\sigma_1$ was changed to 10 degrees. The results from the two realizations were close to the best fit stress tensor obtained previously, but not better in either of the cases.

## 2.7    Scoping calculations and predictive modelling

Scoping calculations comprised an essential and fundamental element in the experiment design. Predictive modelling was used later for detailed modelling of the rock mass response.

## 2.8    Scoping calculations

The design of the experiment involved estimating the stress magnitude required to induce damage in the pillar and designing the experiment to achieve these target stress magnitudes. Scoping calculations were therefore necessary to:

1. Establish the shape and orientation of the APSE access tunnel.

2. Establish the width of the pillar that would result in stress magnitudes at the boundary of the pillar in the target range.

3. Establish the thermal energy required to increase the stress magnitudes at the boundary of the pillar above the target range.

The onset of damage measured in the laboratory tests on intact rock was used to establish the target stresses for when damage to the pillar could be expected (80 to 160 MPa). This range of values was in keeping with the findings reported by /Martin et al. 1997/ for the massive Lac du Bonnet granite. The selection of this design value was very important because if damage to the pillar occurred at lower stress magnitudes because of heterogeneity and fractures, failure of the pillar could occur in an uncontrolled violent manner. On the other hand, if the strength of the pillar was underestimated the stress magnitudes required to cause failure would not be achieved. In addition, if the thermal stresses required to cause damage were underestimated and higher temperatures were required, the reliability of the monitoring system could be compromised.

The boreholes used to form the pillar from the floor of the APSE access tunnel were excavated using a converted TBM (Chapter 3) that gave a finished hole diameter of 1.75 m. This is also the diameter of the emplacement holes in the KBS-3 concept. The distance between the two 1.75-m-diameter holes greatly influences the stress concentration in the pillar separating them. If a thin pillar is chosen high stresses will be induced, but a thin pillar is more sensitive to rock mass heterogeneity, geological anisotropy and fractures. Fracture trace lengths from mapping of excavations in the vicinity of the APSE show that a pillar with a width of 1 m should reduce the risk that a fracture would cut through the pillar. The risk of geological uncertainty can be reduced further if the pillar width is greater than 1 m. However, the stresses in a wider pillar are lower and higher temperatures are required to achieve the target stresses.

The geometry of the APSE access tunnel was determined after the diameter of the holes and the distance between them had been initially set. The tunnel was oriented perpendicular to the trend of the maximum horizontal stress to maximize the excavation-induced stresses. Estimating the excavation-induced stresses required three-dimensional stress analysis software due to the complex geometry. However, because it was anticipated that the pillar response would be essentially elastic until the application of the thermal stresses, three-dimensional elastic analyses were considered suitable for conducting the scoping analyses to establish the stresses in the pillar.

The location of the APSE experiment in the Äspö HRL was chosen to minimize the disturbance to other ongoing experiments. However, as shown in Figure 2-1 there are several other excavations in the vicinity of the APSE experiment. These excavations distort the stress field, and yet it was important that the pillar was placed in an as uniform stress field as possible. Three-dimensional elastic analyses showed that a tunnel length of 70 m would reduce the effect of the adjacent tunnels to less than 2%. By locating the pillar at least 15 m from the tunnel face the perturbations due the tunnel end effects were also eliminated.

The shape of the APSE access tunnel was optimized using the finite element program Phase2 (Rocscience).

Three dimensional elastic analyses were used to establish the stresses in the pillar. Figure 2-24 presents the principal tangential stress on the boundary of the excavation. The stresses on the pillar boundary at a depth of 1 m were within the 90 to 160 MPa target range. It was expected that these excavation-induced stresses would be sufficient to induce at least some damage in the first metre of the pillar below the tunnel floor. The stress situation in the pillar is further discussed in Chapter 8.

## 2.9    Predictive modelling

When the scoping calculations to establish the geometry had been completed with Examine3D, predictive modelling was carried out with the codes JobFem, FLAC3D and FRACOD. The modelling is summarized in /Andersson 2003/.

JobFem /Stille et al. 1982/ is a 2D finite element code. Its primary use was to determine the layout of the heaters and the heater output. Coupled thermo-mechanical modelling was used to predict the stresses in horizontal planes as the temperature and hence the thermal-induced stress increased. To be able to include the stress effect from the drift, the excavation-induced 3D stress tensor was calculated at the nodes of the 2D finite element mesh. This was done with Examine3D by placing field points in the 3D space at the exact relative location to the large holes as the nodes in the 2D model had. These 3D stresses were projected on a 2D plane which was imported to JobFem.

FLAC3D /Itasca 2002/ is a 3D finite element code. A complete 3D model of the experiment was constructed. The model predicted the temperature development and coupled modelling gave the totally induced stresses. Adiabatic boundaries for the openings were used.

FRACOD /Shen 2005/ is a fracture modelling code based on the boundary element method. The code replicated the 2D stress field calculated with JobFem and predicted fracture growth in the pillar at two horizontal planes at depths of 0.5 m and 1.5 m.
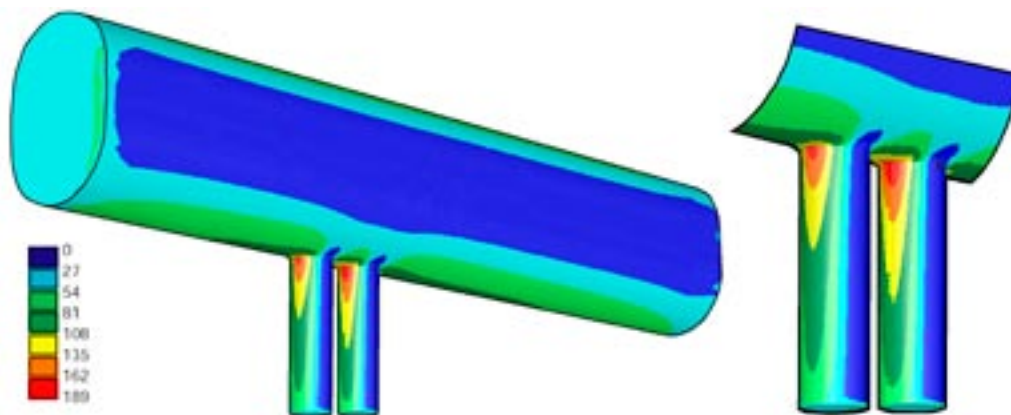


*Figure 2-24. Maximum stress on the excavation surface (MPa). The right part of the figure is an enlargement of the pillar area.*

# 3    Excavations

The design chosen for the tunnel should ensure high stresses beneath the centre of the tunnel floor. The two large-diameter holes bored close to each other further increased the stress in the pillar created between them. After boring of the large-diameter holes the stresses should be elevated to a level where spalling just about occurs. The closer to the spalling limit the stress level caused by the geometry gets, the less thermal power needs to be applied to the rock to propagate the spalling. To maximize the geometry-induced stresses, the tunnel was oriented perpendicular to the major principal stress direction. The floor was arched to get the maximum stress concentration in the centre of the floor where the pillar should be located. The choice of pillar width was not trivial. A thin pillar would be more stressed but also more sensitive to small-scale variations in geology. The width finally chosen represented a compromise between these two variables.

## 3.1    Tunnel excavation

The tunnel trends N046E in the Äspö96 coordinate system as indicated in Figure 3-1. The direction of the major principal stress and the Äspö96 system in relation to magnetic north is also shown in the figure. The top portion of tunnel had straight walls and an arched roof, while the invert had a rounded tunnel floor with a ~ 2-m radius. The tunnel provided uniform concentration of excavation-induced stresses in the tunnel floor.
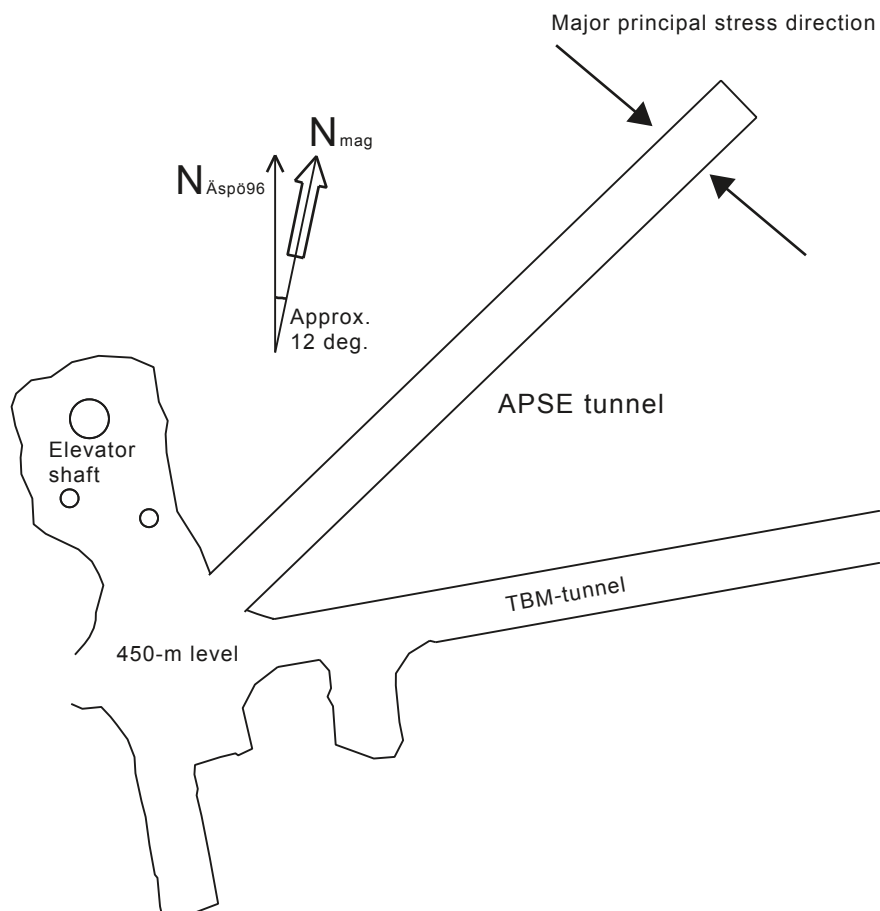


**Figure 3-1.** *The orientation of the experiment tunnel in relation to the direction of the major principal stress and the relationship between the Äspö-96 coordinate system and magnetic north.*
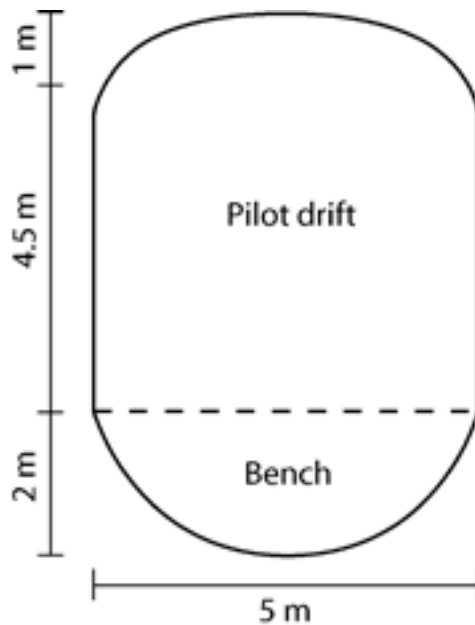
***Figure 3-2.*** *Section of the tunnel. The tunnel was blasted as a pilot drift and a separate bench to reduce the EDZ as much as possible.*

A theoretical section of the experiment tunnel is shown in Figure 3-2. The total height of the tunnel is approximately 7.5 m and the width 5 m. Because of the different geometry of the top and bottom of the tunnel, the tunnel was excavated in two stages (Figure 3-2). Once the top heading was completely excavated the floor was removed. The major advantage of this strategy was to minimize the damaged zone in the floor. Because there was no overburden on the floor the blasting charges could be significantly reduced, minimizing the damaged zone. It was important to ensure that the rock mass response near tunnel and pillar boundaries was essentially elastic and not damaged by the blasting. The blasting and resulting EDZ are studied in /Olsson et al. 2004/.

## 3.2　Large-diameter boreholes

The large 1.75-m-diameter boreholes were excavated with a TBM machine converted for vertical drilling. Figure 3-3 shows the cutter head being fitted into the frame on the surface. The large-diameter boreholes do not have exactly the same depth. The inner hole, DQ0066G01, which was confined, was bored to a depth of 6.5 m. The outer open, instrumented hole, DQ0063G01, was bored to 6.2 m. The reason for this was that the boring machine did not work very well towards the end of the boring due to technical problems and the penetration rate was very low. An elastic 3D model of the stress distribution between the two holes indicated that the effect of a 0.3 m difference in hole length was small and only evident at the bottom of the pillar. To save time it was therefore decided to stop the boring at 6.2 m. The mean diameter of the large-diameter holes is approximately 1.75 m. The centre-to-centre distance between the two holes at 0.5 m below the tunnel floor is 2.78 m, which gives an actual pillar width of 1.03 m. The pillar width was surveyed at certain depths, and the results are presented in Table 3-1.

Based on visual observation and tapping on the borehole wall, no evidence was found of a thin TBM cutter-induced damaged zone on the perimeter of the hole that would affect the stresses close to the boundary of the holes, i.e. the rock mass response outside the obvious zones of yielding appeared elastic.

**Figure 3-3.** *Fitting of the cutter head into the frame. The converted TBM machine used for the excavation of the 1.75-m-diameter holes.*

**Table 3-1. Measured pillar width. Figures are missing between the depths –0.62 and –2.22 m where spalling occurred during boring.**

| Depth (m) | Hole depth (m) | Pillar width (m) |
|-----------|----------------|------------------|
| –446.29   | 0.22           | 1.011            |
| –446.69   | 0.62           | 1.047            |
| –448.29   | 2.22           | 1.054            |
| –448.69   | 2.62           | 1.061            |
| –449.09   | 3.02           | 1.054            |
| –449.49   | 3.42           | 1.06             |
| –449.89   | 3.82           | 1.061            |
| –450.29   | 4.22           | 1.063            |
| –450.69   | 4.62           | 1.079            |
| –451.09   | 5.02           | 1.063            |
| –451.49   | 5.42           | 1.068            |
| –451.89   | 5.82           | 1.055            |

## 3.3    Cored boreholes

Fourteen cored boreholes were drilled close to the pillar for heating and instrumentation purposes. All holes except KQ0064G08 were drilled vertically. KQ0064G08 was drilled with a plunge of 60 degrees to the northwest. The locations of the boreholes, including the large-diameter confined hole, are shown in Table 3-2 in relation to the centre point of the large-diameter hole DQ0063G01, the open instrumented hole. A plan view of the boreholes is shown in Figure 3-4.

The cored boreholes drilled for installation of heaters and instruments were positioned to get the best possible coverage with the acoustic system. The acoustic holes were therefore placed closest to the pillar to ensure that the waveforms originating from the pillar would not be distorted by other boreholes and that those boreholes would not generate noise that would disturb the monitoring of AE events in the pillar (Figure 3-4).
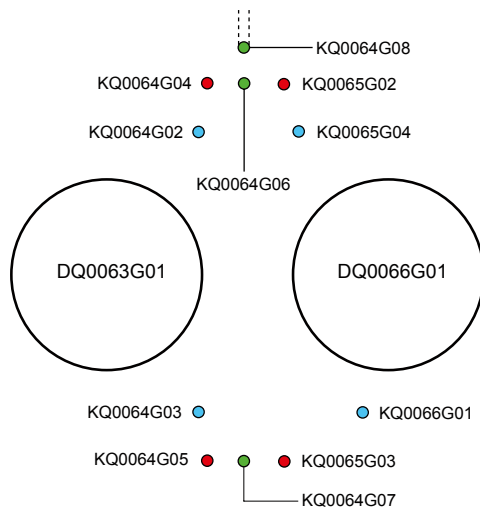
**Figure 3-4.** *Plan view of the cored boreholes drilled for heating and instrumentation purposes close to the large-diameter boreholes. The boreholes were drilled for temperature monitoring (green), heaters (red) and AE system (blue).*

**Table 3-2. The location of the cored boreholes and the confined large-diameter hole in relation to the centre of DQ0063G01. The distance along the tunnel axis is measured towards the face.**

| Borehole ID code | Distance along tunnel axis (m) | Distance perpendicular to tunnel axis (m). Negative value on left side of tunnel centre. | Purpose of hole |
|---|---|---|---|
| DQ0066G01 | 2.783 | 0.030 | Displacement and temperature monitoring |
| KQ0064G02 | 0.917 | −1.377 | AE |
| KQ0064G03 | 0.924 | 1.460 | AE |
| KQ0064G04 | 1.024 | −1.859 | Heater |
| KQ0064G05 | 1.024 | 1.903 | Heater |
| KQ0064G06 | 1.413 | −1.849 | Temperature monitoring |
| KQ0064G07 | 1.415 | 1.929 | Temperature monitoring |
| KQ0064G08 | 1.401 | −2.090 | Temperature monitoring |
| KQ0065G02 | 1.801 | −1.857 | Heater |
| KQ0065G03 | 1.823 | 1.929 | Heater |
| KQ0065G04 | 1.928 | −1.373 | AE |
| KQ0065G05 | 1.915 | 1.426 | Not used |
| KQ0066G01 | 2.624 | 1.447 | AE |

## 3.4    Water inflows

There was water inflow in three of the cored boreholes, all located on the right side of the pillar. There were also inflows in both of the deposition holes. The inflows are listed in Table 3-3. The boreholes were left open throughout the experiment.

Before the experimental tunnel was excavated, an exploratory cored borehole was drilled roughly parallel to the north wall. Water flow and temperature measurements were conducted in that borehole. The water temperature at the approximate section of the pillar was between 14 and 14.5°C.

**Table 3-3. Measured water inflow in large-diameter and cored boreholes in the experimental volume.**

| Hole ID | KQ0065G03 | KQ0065G05 | KQ0066G01 | DQ0063G01 | DQ0066G01 |
|---|---|---|---|---|---|
| Inflow (l/min) | 5.36 | 6.21 | 2.00 | Estimated 10–13 | 30.5 |

52

# 4    Monitoring system and installations

Three types of monitoring systems were used to monitor the experiment: I) temperature, II) displacement and III) acoustic emission. The selection and location of these monitoring sensors was based on the scoping calculations and the predictive modelling. As stated in Chapter 2, one of the objectives of the experiment was to establish the effect of confinement on the brittle fracturing process. Also included in this section is a description of the confining system and the heaters used to increase the temperature in the pillar. The temperature and displacement monitoring systems, as well as data handling, are presented in detail in /Eng and Andersson 2004/.

## 4.1    Temperature monitoring

Monitoring of the temperature during the heating phase of the experiment was essential for calibration of the thermal model. This calibrated model could then be used to back-calculate the stress distribution in the pillar. In addition, the air temperature in the open 1.75-m-diameter borehole where the displacement monitoring sensors were installed was monitored so that temperature corrections of the transducers could also be performed if found necessary.

The thermocouples were spatially distributed around the pillar to permit monitoring of anisotropies in the evolving temperature distribution. Temperature monitoring points were located in: 1) vertical cored boreholes between the heater holes, 2) one inclined cored borehole, and 3) on the pillar walls. A plan view of the instrument set-up and a section showing the depths of the thermocouples are presented in Figure 4-1. The boreholes in which thermocouples were installed were back-filled with sand to provide good thermal coupling to the rock and to prevent air convection within the holes. When positioned at the pillar wall, the thermocouples were inserted in small-diameter boreholes to ensure good coupling to the rock.

The temperature sensors used were corrosion-resistant type K thermocouples, manufactured by Pentronic (www.pentronic.se). The accuracy of these sensors for measuring absolute temperature was about 1°C, but the error was a fraction of that between consecutive samples. The thermocouples were calibrated at both 0°C and 100°C. The harsh experimental environment with elevated temperatures and salt water made it necessary to waterproof the sensors using a shielding material of cupronickel, which is extremely corrosion-resistant.
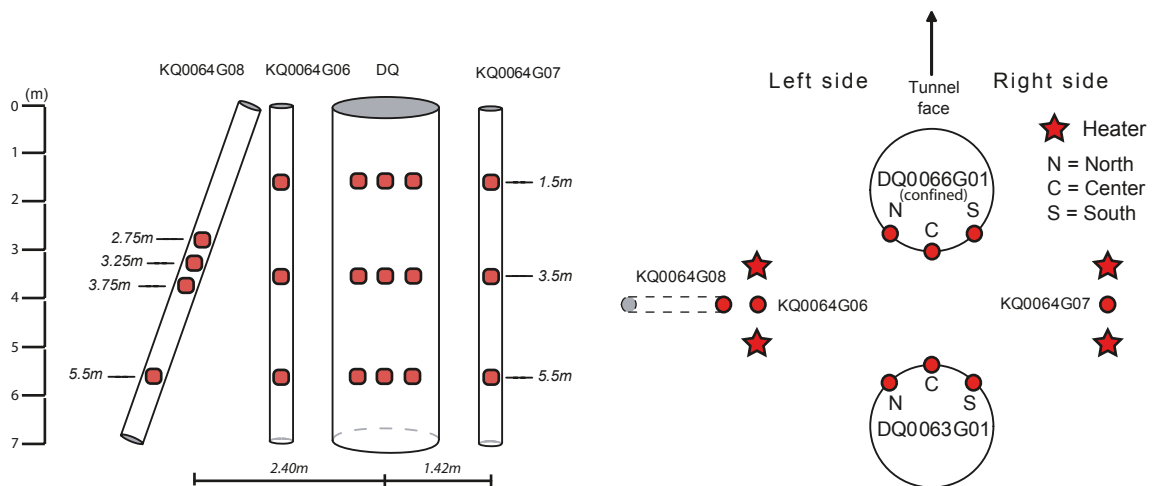


***Figure 4-1.*** *Plan view of the instrumentation of the experimental volume and a vertical section perpendicular to the tunnel axis showing the symmetrical depth distribution of the thermocouples and the borehole ID codes.*

## 4.2 Displacement monitoring

The experiment was designed to allow displacements associated with the pillar yielding process to be monitored at various stages of pillar loading. LVDT (Linear Variable Differential Transformer) type instruments were chosen to monitor these displacements because they are robust, reliable, have high resolution and can be placed in waterproof casings. The deformation of the pillar due to thermal stresses was expected to be less than 1 mm. However, once yielding started, the displacements could approach 10 mm or more because of the large dilation associated with the yielding process. Hence it was necessary to use two types of LVDT sensors to capture I) the thermally induced elastic displacements and II) the stress-induced displacements associated with the yielding process. The major difference between the two types is the measuring range. The short-range LVDTs had a shorter measuring span but higher accuracy, while the opposite was true of the wide-range LVDTs.

The short-range LVDT sensors used were Schaevitz GCD-121-250. The sensor tip is spring-loaded, has a measuring range of 12.7 mm and delivers an output of ± 10V. The actual resolution of the sensor is 0.00635 mm. Each sensor was individually temperature-calibrated before and after the experiment. The results from the two calibrations were very similar, and only the first calibration was used to assess the total temperature drift. The temperature increase of the sensors was less than 10°C during the experiment, which was the approximate temperature increase in DQ0063G01 (Chapter 6). The sensor with the largest temperature-induced variation in the output signal gave a displacement error of 0.0022 mm per °C.

The wide range LVDT sensors used were the Geometrik Miniextensometer (www.geometrik.se). The spring loaded sensor tip had a measuring range of 40 mm. The output signal, 4–20 mA, gives an accuracy of 0.025 mm. These sensors were also calibrated before and after the experiment with very similar results. The temperature drift for these sensors was between 0.001 to 0.01 mm per °C.

The set-up of the LVDTs was changed during the experiment as the notch propagated down the hole wall. This is illustrated in Figure 4-2. The horizontal distance between adjacent LVDTs at the same instrument level is approximately 20 cm. The exact depth of the instruments is given in Table 4-1.

**Table 4-1. Sensor row depths. Here a distinction is also made between the two sensor types.**

| Level | Position no. (from left) | Sensor type | Depth [m] (below –446.07 m) |
|---|---|---|---|
| 1 | 1–6 | Long-range | 2.46 |
| 1 | 1–6 | Short-range | 2.52 |
| 2 | 2–12 | Short-range | 2.99 |
| 2 | 2–12 | Long-range | 3.07 |
| 3 | 13–18 | Long-range | 3.50 |
| 3 | 14–17 | Short-range | 3.58 |
| 4 | 20–23 | Short-range | 4.10 |
| 4 | – | Long-range | Not installed |
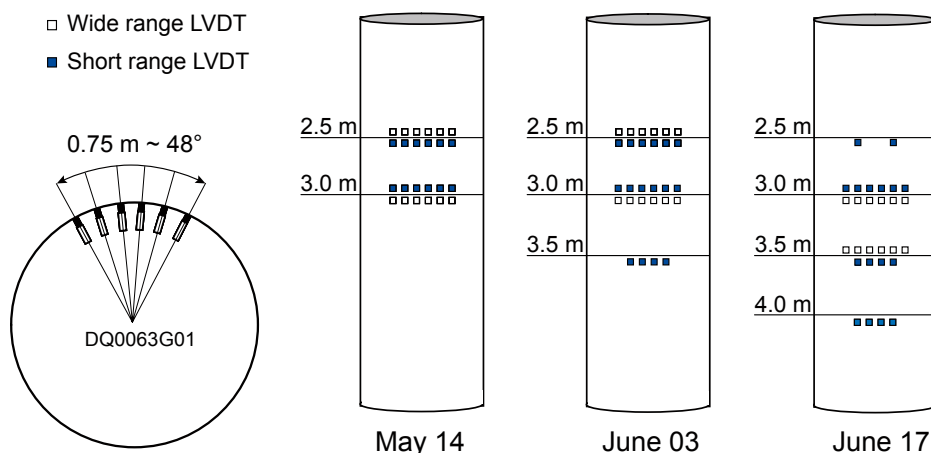


*Figure 4-2. Complete measuring layout for both the short- and wide-range sensors.*

The LVDTs were mounted on steel pipes as illustrated in Figure 4-3 and Figure 4-4. One additional short-range LVDT was mounted directly on the rock wall parallel to the shear zone (Figure 4-5).



*Figure 4-3.* *LVDTs mounted on a steel pipe in the open hole. The upper LVDT is of the short-range type and the lower of the wide-range type.*



*Figure 4-4.* *Function check of the radially mounted LVDTs after installation. A laptop connected to the Äspö LAN was brought down into the hole for immediate access to the LVDT response during the check.*
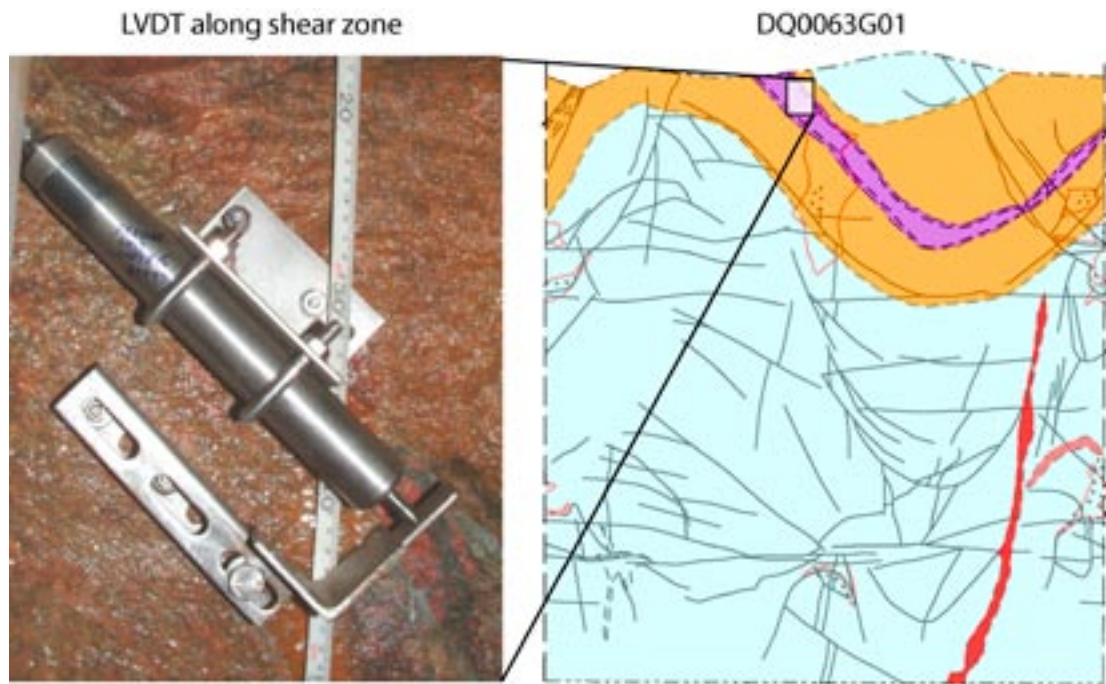
***Figure 4-5.*** *Short-range LVDT placed along the shear zone.*
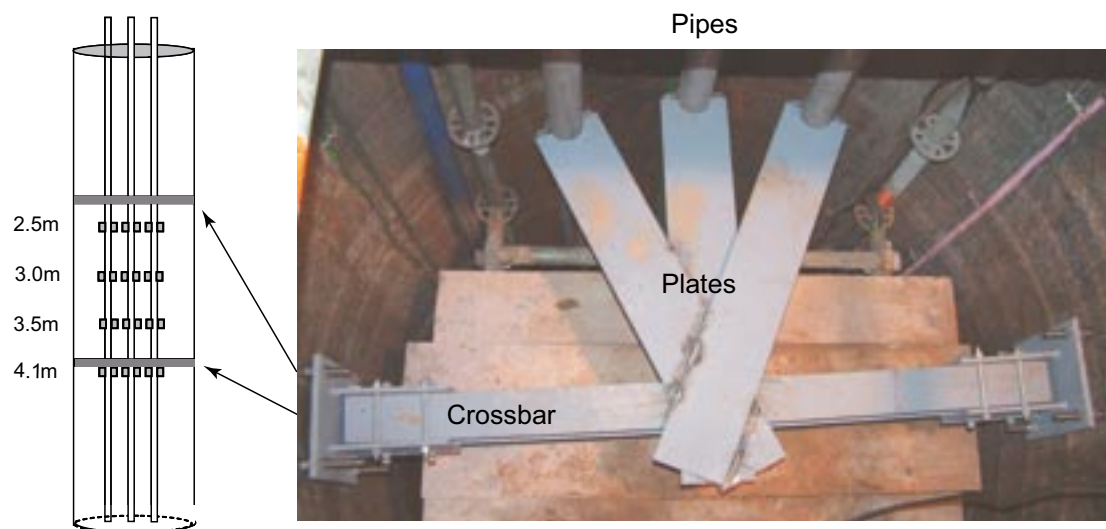


***Figure 4-6.*** *The stabilizing crossbars and the plates connecting them with the pipes inside the large hole. The left-hand image shows the vertical positions of the crossbars together with the instrument levels.*

Predictive modeling had indicated that the temperature in the open hole could increase by up to 60°C during the heating phase. It was therefore important that the sensor's supporting system was designed to accommodate thermal expansion. The steel pipes were bolted to the borehole bottom but were free to expand vertically. The steel pipes could not be allowed to deflect horizontally since it would immediately bias the results from the LVDTs. Crossbars were therefore mounted at approximately 2 and 4 m depth in the open hole perpendicular to the tunnel axis (Figure 4-6). The crossbars were designed so that they would not interfere with the rock deformations while providing stiff lateral support to the LVDTs.

Scoping calculations indicated that the total error of the complete displacement monitoring measurement system due to thermal expansion was less than 0.01 mm per °C temperature increase or approximately 0.1 mm for the total actual temperature increase of ~ 10°C in the hole. The direction of the thermally-induced error is compression of the LVDTs (i.e. hole wall moving towards the centre of the hole).

### 4.2.1 Calibrations

All sensors used were calibrated for accuracy prior to installation. The short-range sensors were calibrated by the instrument owner Ontario Power Generation and the long-range sensors by the manufacturer. The complete calibration sheets can be found in /Eng and Andersson 2004/.

### 4.2.2 Sources of error

The sources of error in the displacement readings are mainly temperature-dependent. When the temperature increases, the supporting structure is affected and the pipes, plates and crossbars are subject to thermal expansion. The sensors themselves are subject to temperature-dependent drift. These factors have been addressed in the post-experimental analysis of errors in Appendix 2c. The total error in the displacement monitoring has been found to be too small in relation to the displacements to be of any significance.

### 4.2.3 Data logging

The output signal from the instruments was monitored by DataScan modules located on the tunnel wall a few metres from the pillar. The instrument output signal was relayed to the monitoring computer using the ScadaPro software. The monitoring computer was connected to the Äspö LAN which made it possible to log on from any internet connection and check readings or modify the logging schedule. The monitoring of crucial components of the experiment such as the pressure in the confined hole and the heater output was supplemented with alarm levels so that, if triggered, a test message with details of the event was sent to the engineer's mobile phone. Almost immediate action could therefore be taken in case anomalies occurred.

The data from each sensor was continuously logged during the experiment. Sensor outputs were saved to the hard drive of the on site computer every minute, which was therefore the time resolution of the logging.

### 4.2.4 Logging of work at the experimental site

The acoustic emission system and the displacement monitoring instruments are very sensitive and hence easily disturbed. To help ensure the quality of the sampled data, procedures were established for access and work at the experimental site. The experimental drift is 70 m long. A locked gate was set up ten metres from the entrance to prevent unauthorized access. Anyone passing the gate had to fill in a log list. The list contains particulars on time of entry, kind of work performed and when the individual left the site again. When visits were made for various reasons in the open hole, the AE system was switched off to keep the data set as free from noise as possible. These times were noted separately.

All the visits in the open hole affected the displacement monitoring. To make it easier to follow the actual displacements over time, a copy of the measured data was filtered. In this case filtering means that man-made disturbances were removed from the data set making the graphs much easier to read. For this purpose the data sampled during the disturbed periods were removed. To make the data curves readable, the data after the disturbed period were adjusted, raised or lowered, to the level prior the disturbance. An example of this is shown in Figure 4-7. This makes the data set continuous and it only shows the total displacements from the start of the experiment. It is important to note that this kind of filtering was only done at times when the log lists stated that some kind of activity had taken place in the open hole. The filtered periods are shown in Appendix 4a. The filtering process is described in greater detail in /Eng and Andersson 2004/.

*Figure 4-7.* *Example of the data filtering process. The white area is considered to be disturbed. The black line represents the measurement data from one sensor during the disturbed period. The red line represents the resulting data after filtering. As the figure shows, the filtering application removes the data from the disturbed time interval and the following data are adjusted to make a seamless continuous curve. The result is a data set that shows only the effective displacements during the experiment.*

## 4.3 Acoustic Emission monitoring

It is well known that acoustic emission (AE) monitoring is suitable for tracking brittle damage in rock. The AE monitoring system consisted of twenty-four ultrasonic transducers mounted on four portable borehole frames (Figure 4-8). The transducers responded to the frequency range 35–350 kHz and were connected to 60 dB pre-amplifiers contained in junction boxes at the side of the tunnel. Each AE frame contained 6 sensors: two transmitters and four receivers. The sensors were spring-loaded against the borehole wall ensuring good coupling to the rock. The AE sensors were distributed to effectively monitor the pillar between the two deposition holes as failure progressed from the top of the pillar towards the bottom.

The AE system worked in two operating modes. The first mode passively monitored the AE activity. The sensitivity and accuracy of the AE system was calibrated using pencil lead breaks of 0.7 mm HB leads and by tapping with the operational end of a screwdriver to create AE events on the wall of the open hole. The source location error of these AE events was within a radius of 4 cm. The second operating mode actively acquired waveforms by pulsing the ultrasonic transducers and scanning across the pillar volume. By repeating these ultrasonic surveys at increments in time, the variation in P- and S-wave velocities and signal amplitudes was obtained along 128 different ray paths. A detailed description of the AE monitoring system is presented in /Haycox et al. 2005/.

## 4.4 Confining system

In the KBS-3 concept the bentonite in the emplacement borehole will generate a swelling pressure of approximately 5–7 MPa. One of the objectives of the experiment was therefore to establish the effect of confining stress on brittle fracturing. This objective required the design and construction of a confining system that could be placed in one of the 1.75-m-diameter boreholes. The confining
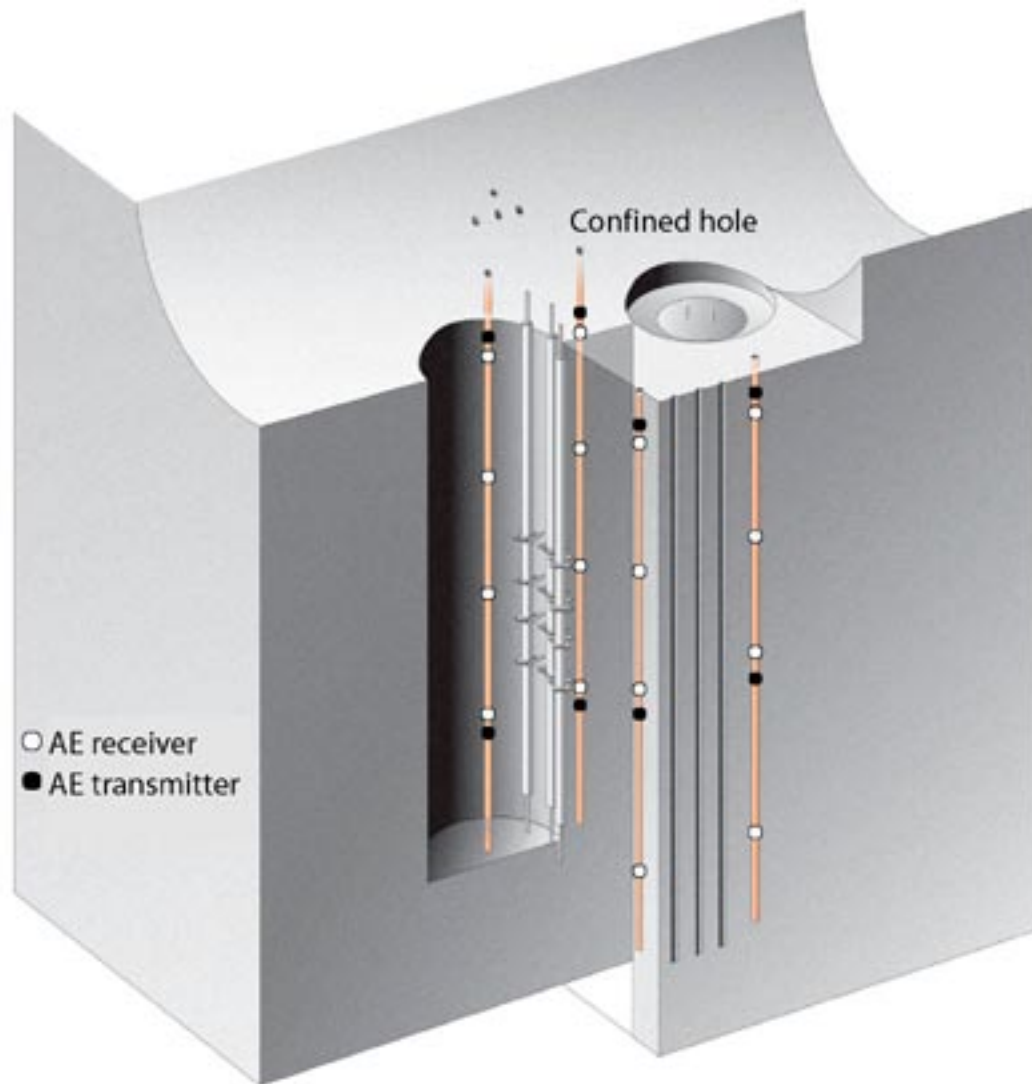
*Figure 4-8.* *A schematic of the AE acquisition system and sensor configuration. There are two ultrasonic transducers and four receivers in each instrumented borehole.*

system was constructed of a rubber bladder approximately 1.75 m in diameter and 6 m long installed in a system consisting of steel plates connected by strong textile straps (Figure 4-9 and Figure 4-10). The textile straps had to fit tightly against each other to ensure that the bladder would not protrude through a small gap and burst. When the bladder was filled with water and pressurized it was self-supporting in the hole.

To maintain a constant pressure in the bladder, even if small leakages occurred through the steel lid, it was connected to a pressure vessel containing water that was pressurized with nitrogen gas in order to maintain the design pressure of 0.7 MPa above atmospheric pressure.

The pressure in the bladder was monitored by a pressure transducer located at the top steel lid and connected to the monitoring system. As the temperature in the surrounding rock increased, the temperature in the bladder also increased, resulting in thermal expansion of the water. To maintain the design pressure during heating, water had to be removed from the bladder periodically. This was done manually, but as an extra safety precaution a pressure release valve was also mounted on top of the steel lid.

*Figure 4-9.* *The specially constructed rubber bladder and the confining equipment. The vertical textile straps connected to the horizontal steel plates kept the bladder in place as it was expanded by a water pressure.*
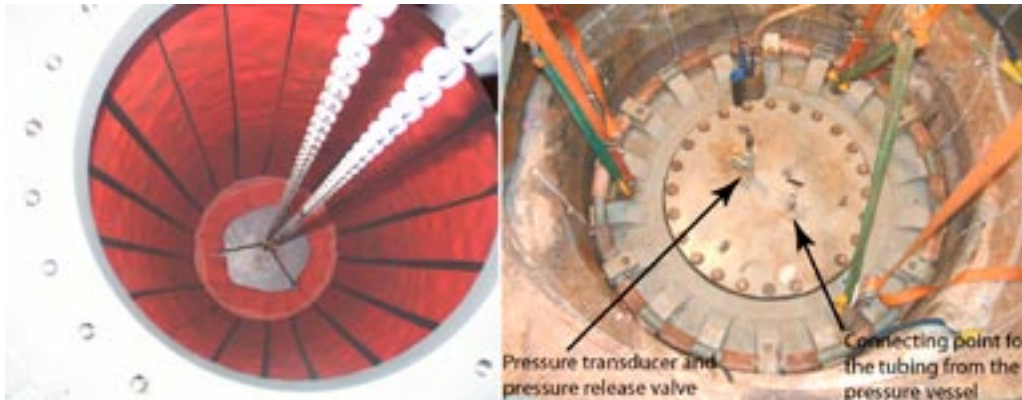


*Figure 4-10.* *Photographs of the textile straps and the top steel lid.*

## 4.5 Heating system

The pillar was heated with 4 electrical heaters with a heated length of 6.5 m, which were installed in four vertical boreholes (Figure 4-11). The heaters, which had a casing made of stainless steel, were inserted into sealed cupper tubes that prevented the heaters from coming in contact with the saline water. The space between the 25-mm-diameter copper tubes and the 76-mm-diameter boreholes was filled with sand to provide good thermal coupling to the rock. Only one heater per heated borehole was needed to meet the estimated heating requirements for the experiment. But in order to ensure redundancy and so that the heater output could be increased if necessary, one extra independent heater was placed in each of the four boreholes.

The power input to the heaters was controlled by individual thyristors. The thyristors were hooked up to the monitoring system and logged. Further details about the heating system are found in /Eng and Andersson 2004/.

The predictive numerical modelling assumed adiabatic boundary conditions for the tunnel floor. To simulate these boundary conditions, the tunnel floor around the pillar was insulated with rock wool. In addition, an insulated hut with a manhole was constructed over the open borehole in order to provide access for visual inspections and maintenance while maintaining the thermal boundary conditions (Figure 4-12).
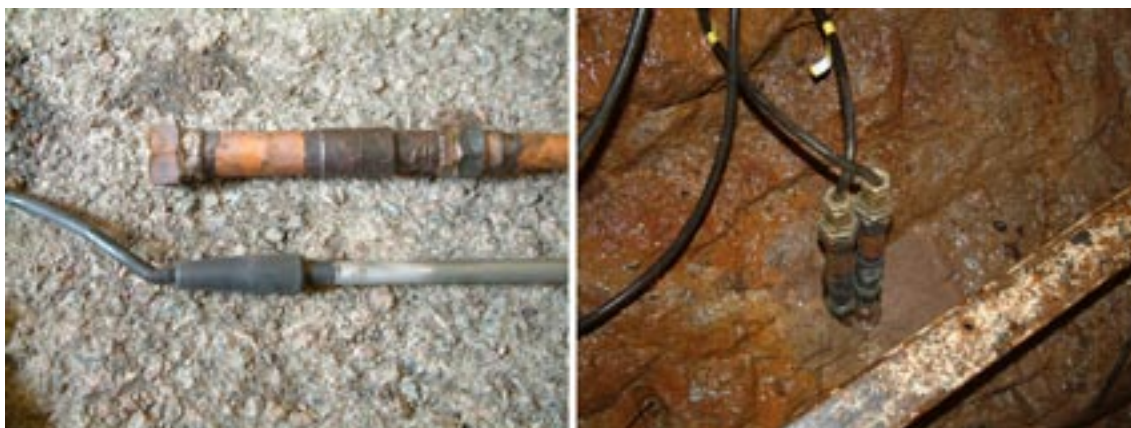
*Figure 4-11.* *Left: the heater below the cupper tube before installation. Right: heater and redundant heater placed in one of the heater holes. All four heater holes were back-filled with sand to ensure good thermal coupling to the rock.*
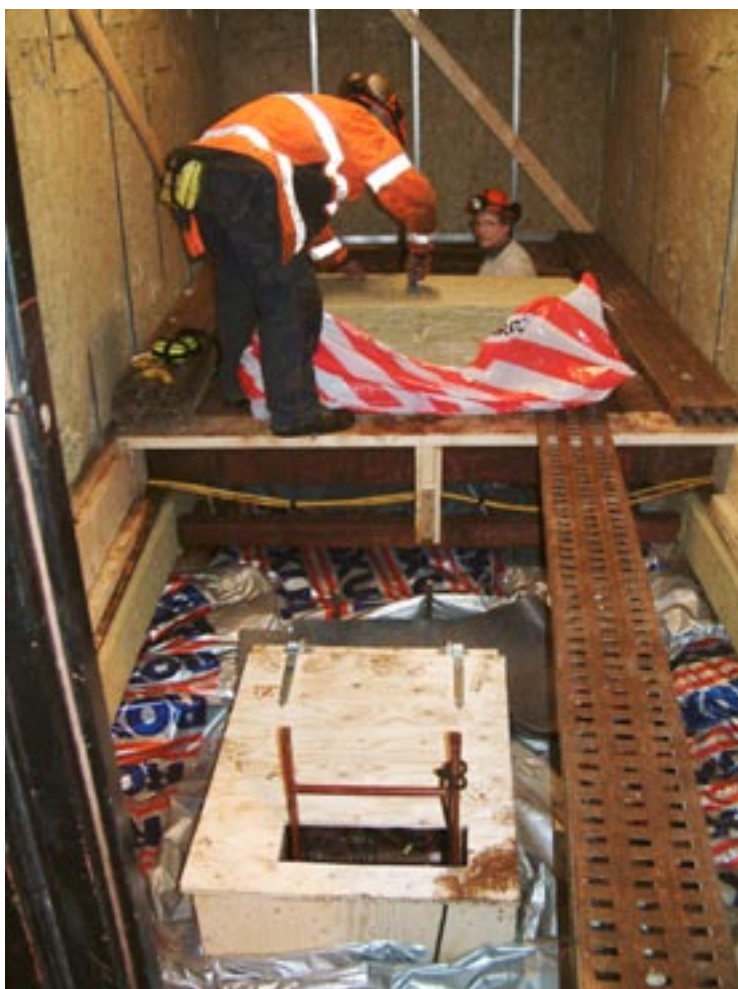


*Figure 4-12.* *Photograph of rock floor insulation and the insulated plywood construction placed on top of the open hole (DQ0063G01) to prevent air convection.*

Water was seeping into the heater hole KQ0065G03 (the others were dry). The water inflow rate in KQ0065G03 was 5.36 l/min. The water came from the steeply dipping water-bearing fracture (Chapter 2) intersecting the borehole at a depth of approximately 6.1 m. The water seepage had to be managed. If it were allowed to flow up the hole along the heaters, the cooling effect would have been too great. It was first discussed whether the borehole should be grouted and then re-drilled. If that had been done, it is possible that the water would have taken a different path and turned up in another of the heater or instrument boreholes. Injecting grout under high pressure in the hole might also affect the pillar if grout penetrated through interconnected fractures. Another solution was therefore chosen. A packer was placed above the fracture and the water was led through the packer pipe out of the hole. Approximately 0.5 m of grout was placed on top of the packer to insulate the packer rubber from some of the heat from the heaters. The heaters were then placed in the borehole. A drawing of the arrangement is shown in Figure 4-13. The end depths of the electrical heaters in the different boreholes are given in Table 5-4.

**Table 4-2. End depth of the electrical heaters. The reference depth is –446.07 m (top of pillar).**

| Borehole ID | KQ0064G04 | KQ0065G02 | KQ0064G05 | KQ0065G03 |
|---|---|---|---|---|
| Heater end depth [m] | –452.40 | –452.46 | –452.35 | –450.85 |
| Effective heater length [m] | 6.5 | 6.5 | 6.5 | 5.0 |
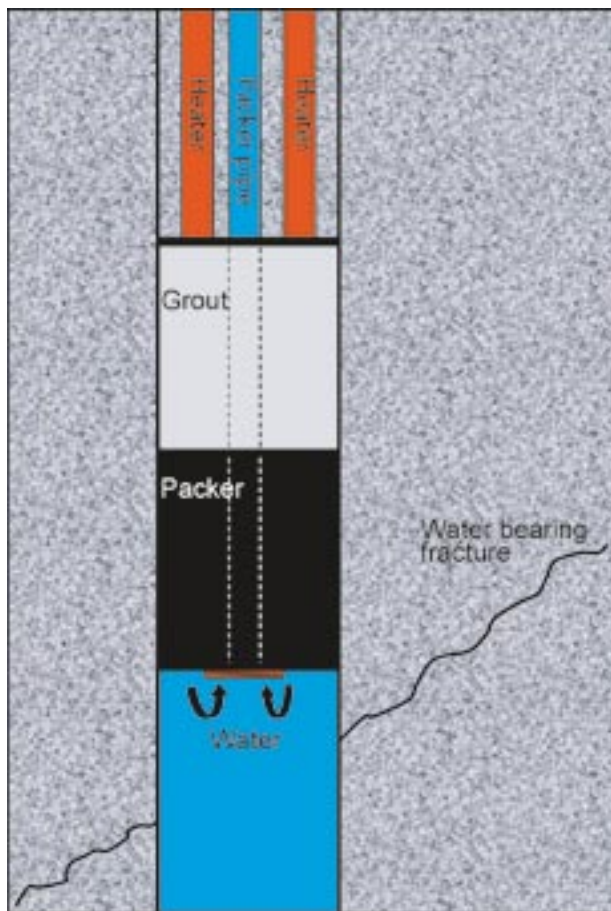


**Figure 4-13.** *Drawing of the arrangement to evacuate water from KQ0065G03.*

# 5    Heating

After two days of initial tests, the heaters were turned on at around noon on May 14, 2004. This day is experiment day 0. During the first couple of days two things became obvious: I) the rate of heat increase in the rock was much slower than had been predicted by the models, and II) the temperature between the heaters in KQ0064G07 (on the right side) increased much slower than in KQ0064G06 (on the left side), Figure 5-1. The reason is probably the water-bearing fracture in heater hole KQ0065G03 and the measures that were taken to reduce cooling of the heaters. This involved positioning the end of that heater at a depth of approximately 4.8 m instead of at ~ 6.5 m as described in Chapter 4.

When the temperature on one side of the pillar is higher than on the other side, the thermally induced stress will not be uniform. To make evaluation of the thermally induced stresses as easy as possible, the power input to the heaters could be adjusted to make the temperature on both sides as even as possible. Since yielding started only a few days after the start of the heating, we knew that high enough temperatures would be reached to ensure propagation of the spalling down the hole. It was therefore decided to reduce the power input on the warmer left side (without increasing the power input on the right side) to compensate for the temperature differences. An initial compensatory power reduction was done on day 18 (June 1st), after which the temperature on the left side between the heaters decreased by about 5°C.

During the second and third weeks in June the temperature was almost constant (Figure 5-1). Acoustic activity during the third week was relatively low, indicating that a steady state had been reached. Equilibrium between thermal input and output resulted in a constant temperature. At this point in time the spalling had propagated from a depth of 2 m to 3 m in the hole (spalling during drilling stopped at ~ 2 m), see Chapter 8. To collect more data it was desirable to propagate the spalling another 2 m down to a depth of approximately 5 m. To achieve this, the power input to the heaters was almost doubled on June 21st (day 38).
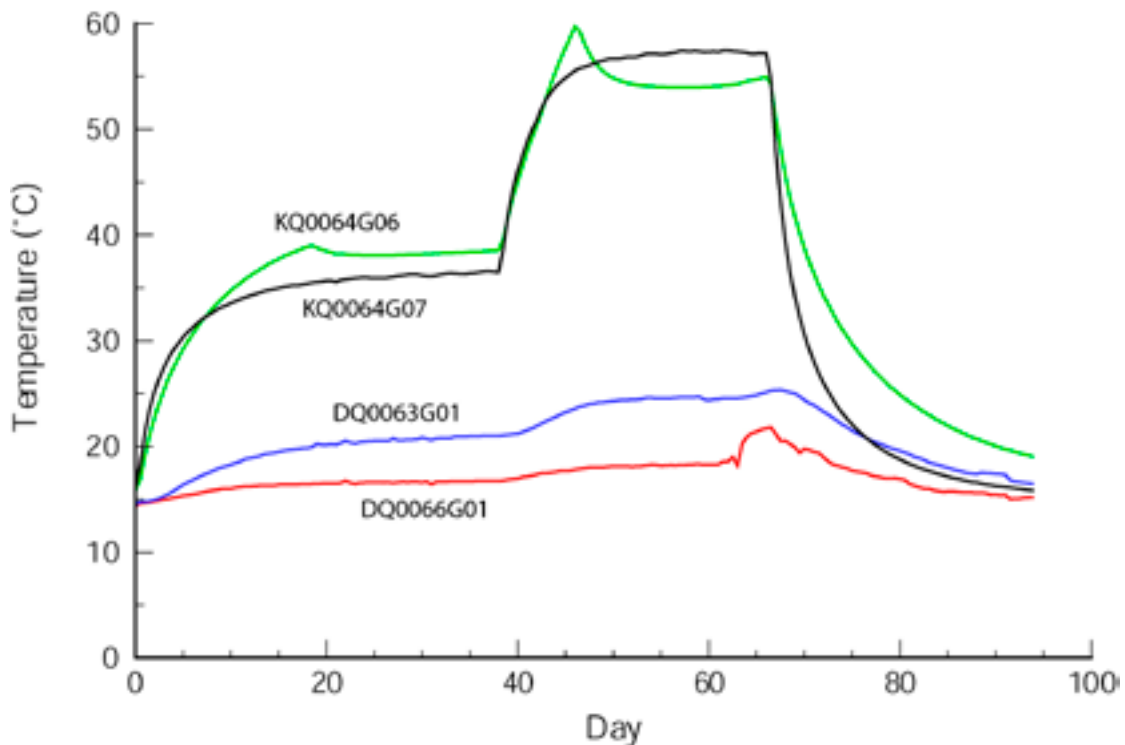


**Figure 5-1.** *Temperature at a depth of 3.5 m depth below the tunnel floor on different dates. The response to the reduction of the power input to the left-side heaters is clearly evident. Hole wall temperature from large-diameter hole DQ0063G01.*

After the power increase the temperature again rose faster on the left side of the pillar. Another adjustment of the power input was therefore necessary, and the input to the left-side heaters was reduced one last time. The power input to the heaters during the experiment is shown in Table 5-1. A graph depicts the temperature at a depth of 3.5 m between the heaters on either side of the pillar and at the centre position of the open hole wall, DQ0063G01, in Figure 5-1. The power reduction to the left side heaters is clearly evident in the temperature graph.

The power to the heaters was turned off on July 19 (day 66).

The temperature of the water evacuated through the packer pipe next to the heater in KQ0065G03 was measured at 16.2°C on July 6th. The temperature increase was approximately 2°C compared with in situ conditions and the flow rate was 5.36 l/min. This gives a cooling capacity of approximately 747 W. The temperature on the heater surface above the rock was at that time measured to be 250°C.

The temperature between the rock surface and the insulation between the heaters on the left side was measured on 9 occasions between June 23rd and July 6th. The average temperature was 36.5°C. The highest and lowest measured temperatures were 38.8 and 35.5°C, respectively.

**Table 5-1. The power per metre of the heaters during the experiment. The heated length of each heater is 6.5 m.**

| Date (day) | Output [W/m] | | | |
| | Left side heaters | | Right side heaters | |
| | KQ0064G04 | KQ0065G02 | KQ0064G05 | KQ0065G03 |
| --- | --- | --- | --- | --- |
| 2004-05-14 (0) | 200 | 200 | 200 | 200 |
| 2004-06-01 (18) | 170 | 170 | 200 | 200 |
| 2004-06-21 (38) | 354 | 354 | 400 | 400 |
| 2004-06-29 (46) | 263 | 263 | 400 | 400 |
| 2004-07-19 (66) | 0 | 0 | 0 | 0 |

# 6 Monitoring and observations

## 6.1 Temperature

The results of temperature monitoring are presented in this chapter. All depths given in the result graphs are in relation to the centre of the drift floor. A plan view of the temperature monitoring positions is shown in Chapter 4 as reference.

### 6.1.1 DQ0066G01

The temperatures in DQ0066G01, which was the confined hole, were approximately seven degrees lower than in the open hole DQ0063G01. This is probably due to the water that leaked between the rock wall and the confinement equipment. Most of the water leaking into the hole originated from its lower parts. The water was evacuated along the permeable textile straps. A constant-flowing water curtain was then created along the borehole wall, which cooled it off. The total inflow to the hole was approximately 30 l/min.

From day 61 (July 14), anomalies can be seen in the temperature readings from the large-diameter holes. This is due to the release of the confinement (Chapter 9) followed by the evacuation of the water from the confined hole. When the water was pumped out of the hole, the temperatures on the hole wall approached the temperatures measured in the open hole. The pumping of the water was stopped when the AE monitoring of the pressure release was finished. The hole then quickly became flooded, resulting in cooling of the hole wall.

The temperature at position "S" is a few degrees lower than the opposite point at position "N". Position "S" includes the measuring points that are closest to the heater in KQ0065G03, which was not completely inserted into the hole due to the water-bearing fracture (Chapter 4) that intersected that hole at a depth of approximately 5 m. The "S" position is also close to a sub-vertical fracture from which approximately 2.4 l/min leaks into hole KQ0065G05 and cools down the rock. The measured temperatures at the centre positions of DQ0066G01 are presented in Figure 6-1. The temperatures at the "N" and "S" positions are given in Appendix 2a.
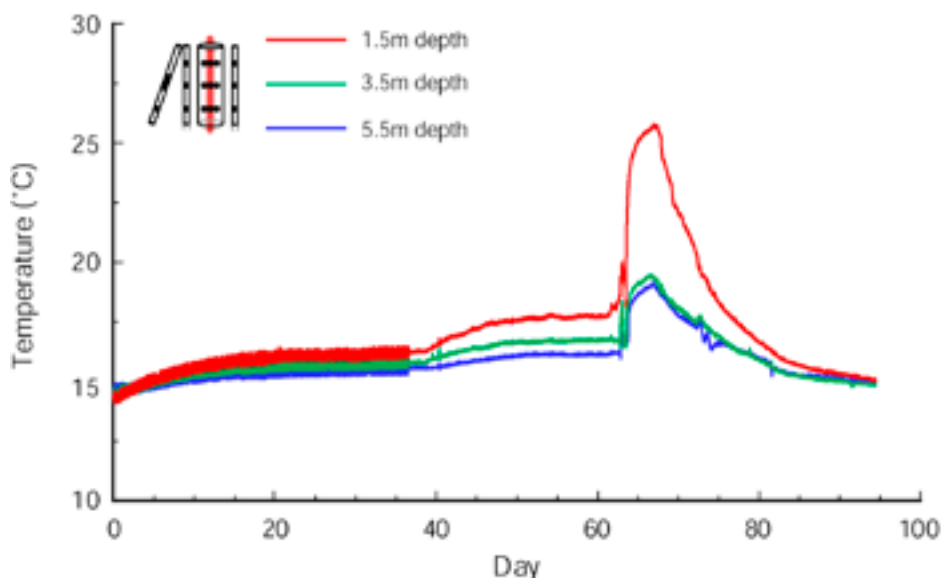


*Figure 6-1.* *Measured temperatures in DQ0066G01 at position "C".*

## 6.1.2  DQ0063G01

The temperature readings in DQ0063G01 are very uniform. The temperature at a depth of 5.5 m at position "S" is a bit lower than at position "N", most likely due to the not fully inserted heater in KQ0065G03, Chapter 4. The measured temperatures at the centre positions of DQ0063G01 are shown in Figure 6-2. Figure 6-3 shows the air temperature measured close to the LVDTs at a depth of 4 m. The air temperature was also monitored at a depth of 2 m, but it was almost identical at the two measuring levels. The 2-m transducer was therefore disconnected and the data channel used for an additional LVDT in late June. The temperatures at the "N" and "S" positions are given in Appendix 2a.
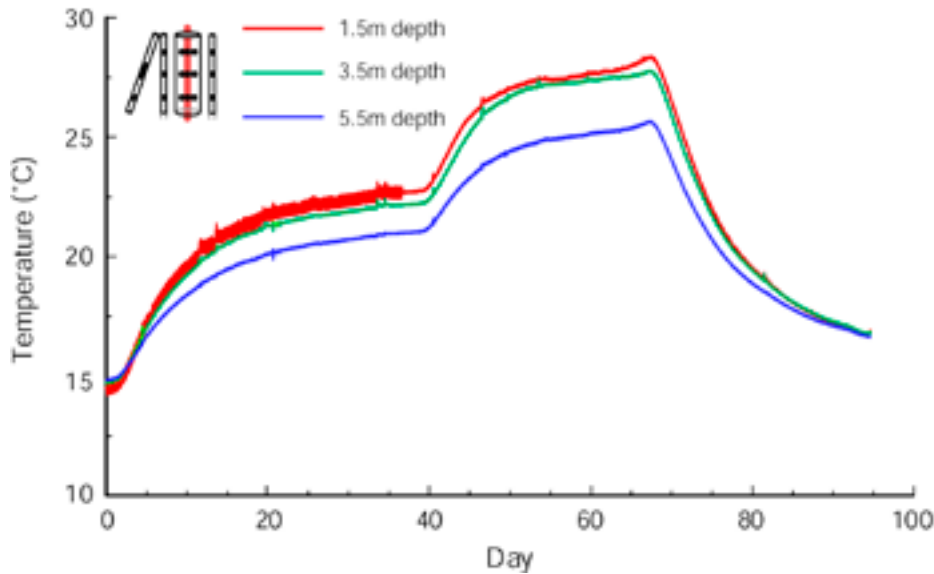


***Figure 6-2.*** *Measured temperatures in DQ0063G01 at position "C".*
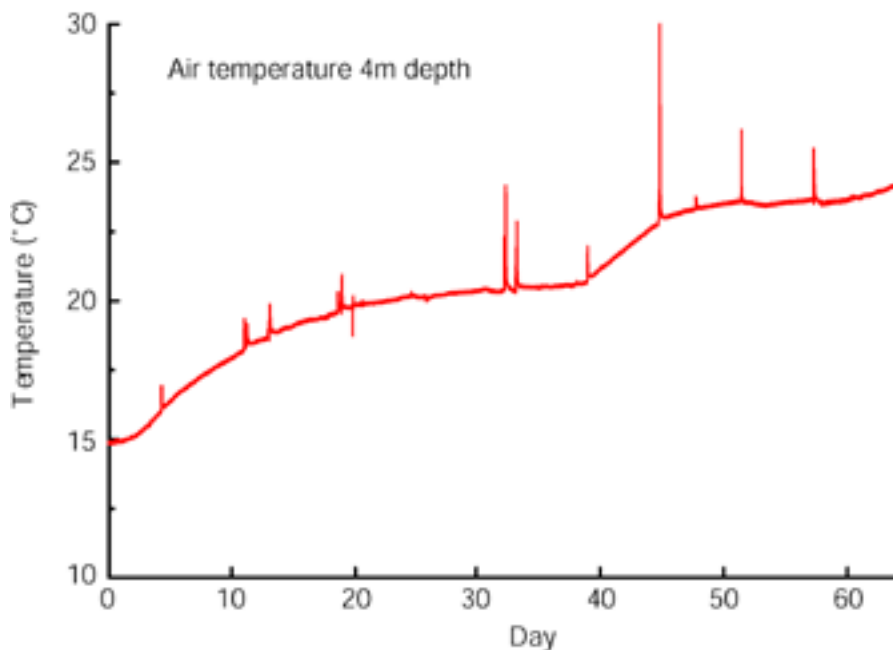


***Figure 6-3.*** *Air temperature in DQ0063G01. The temperature fluctuations due to the inspections conducted in the hole are clearly evident.*

66

### 6.1.3    KQ0064G06, between the heaters on the left side

This borehole is located midway between the two heater holes on the left side of the tunnel when looking at the face (Chapter 4). The c/c distance between this hole and the heater holes is ~ 0.40 m.

The measured temperatures are shown in Figure 6-4. On studying the results it can be seen that the temperature at a depth of 5.5 m is higher than at a depth of 3.5 m. This is should not be the case since the thermocouple at 3.5 m is in the centre of the heated volume. No geological explanations have been found. The installation of the thermocouples was double-checked before heating began, but the anomaly was noted after all the installations had been removed and a specific check could therefore not be done. However, photographs of the installations do not indicate that the thermocouples were coupled to the wrong data taker. The temperatures at a depth of 3.5 m are compared in Chapter 5, and the figure indicates that the temperatures at 3.5 m are very similar on both sides on the pillar.

### 6.1.4    KQ0064G08, the inclined hole on the left side

KQ0064G08 was drilled to monitor temperatures a bit further away from the pillar (Chapter 5) and was intended to be used for the calibration of the temperature back-calculation that was scheduled to be performed at a later stage (Chapter 7). The measured temperatures in KQ0064G08 are shown in Figure 6-5.

### 6.1.5    KQ0064G07, between the heaters on the right side

This borehole is located midway between the two heater holes on the right side of the tunnel when looking at the face (Chapter 5). The c/c distance between this hole and the heater holes is 0.40 m. The temperature differences between the three different depths are greater here than on the left side, most likely due to the not fully inserted heater and the water-bearing fracture (Chapter 4).

The temperature at a depth of 1.5 m decreased for a few days starting on day 43 (June 26). During this time, steam was rising from the heater holes. The reduced temperature is probably due to the fact that the water in the holes started to boil. When all the water had evaporated, the temperature started to increase again and that is what can be seen on day 45 (July 28). The measured temperatures in KQ0064G07 are shown in Figure 6-6.
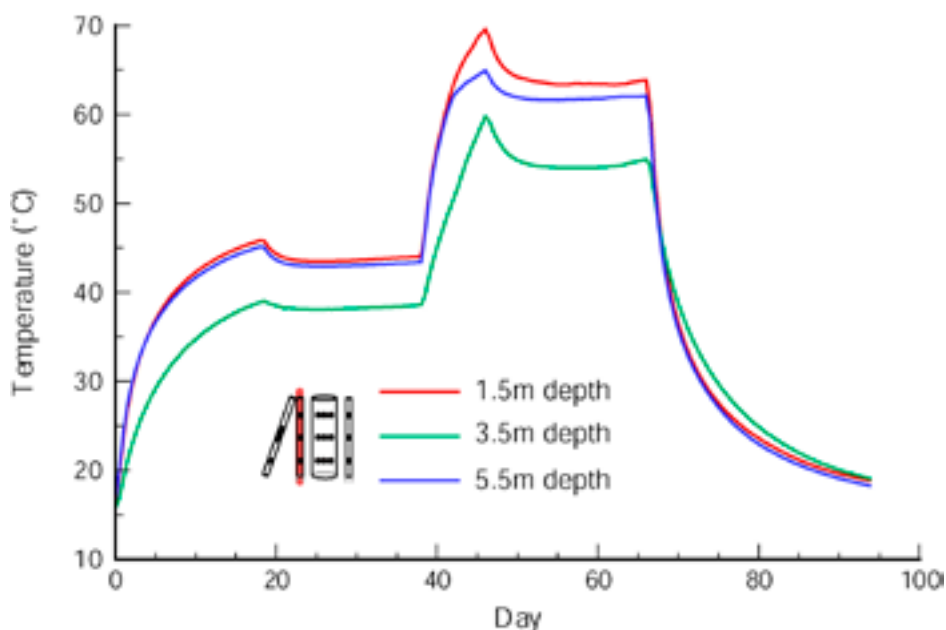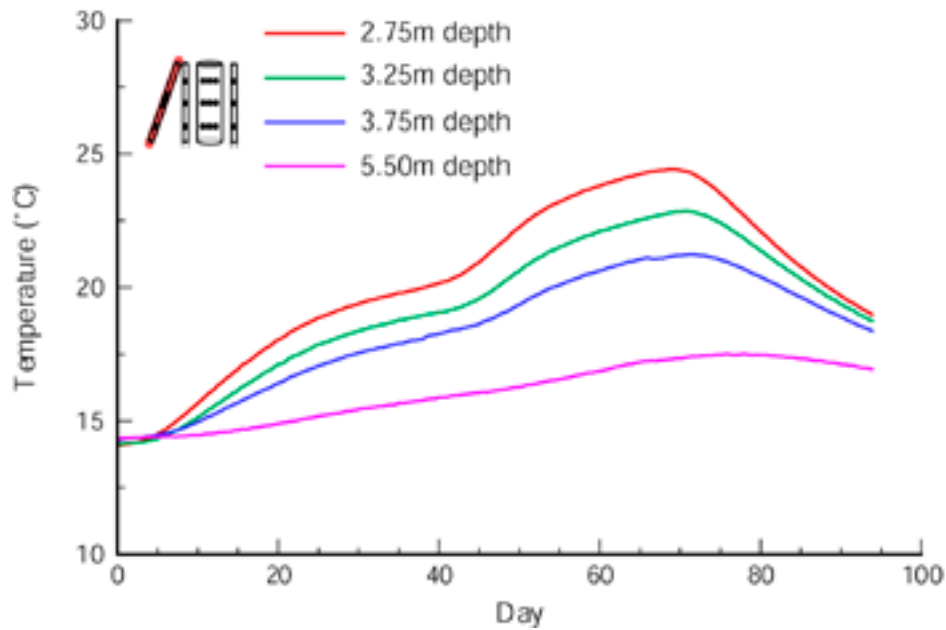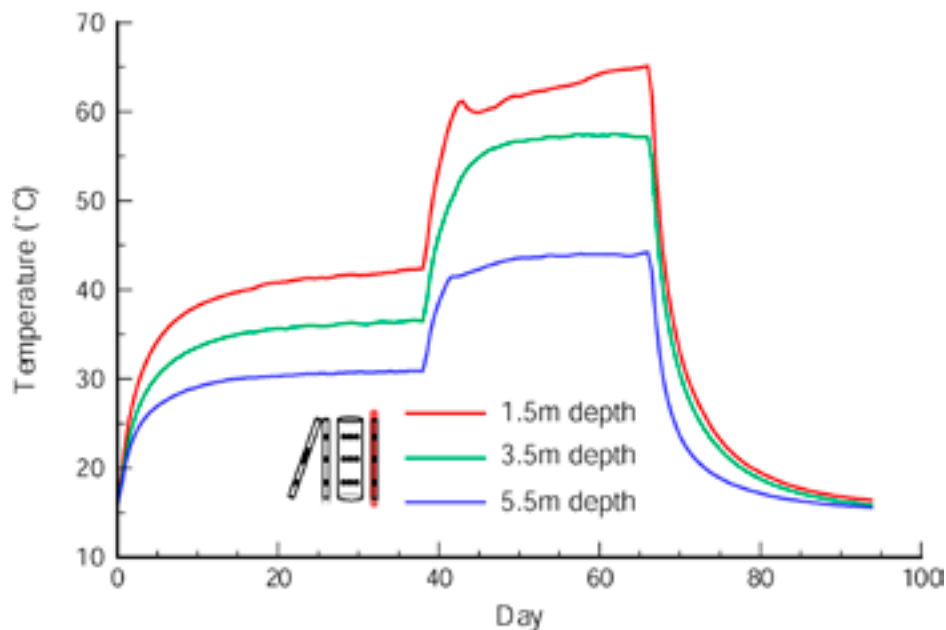


***Figure 6-4.*** *Measured temperatures in KQ0064G06.*

**Figure 6-5.** *Measured temperatures in KQ0064G08.*



**Figure 6-6.** *Measured temperatures in KQ0064G07.*

## 6.2   Displacements

The readings from the different LVDTs and the other transducers were stored in the data acquisition system once every minute. The time the displacements occurred is therefore known to the minute. The clock for this monitoring system and the one for the acoustic emission system differed by less than 1 minute, depending on when in the experiment cycle the comparison is made. This enabled the possibility to correlate AE and displacements.

In this chapter the displacements for the short-range sensors are plotted against time for each instrument level. If the times of the displacements at the different levels are compared, the "speed" of the propagating notch is indicated. All displacement readings are individually plotted in Appendix 2b.

68

When the graphs are studied the displacements are in some cases larger than the monitoring range that has been specified for the LVDTs. When the displacements were close to the limit of a given LVDT, it was moved radially a few mm backwards. This enabled the complete deformation curve to be measured with each transducer. The data were then filtered as described in Chapter 4 to produce a seamless result graph.

The displacement graphs indicate how the deformations occur stepwise. This coincides well with the acoustic records, which show clusters of AE events with quiet periods in between. What is probably happening is that when the strain energy induced in the system by the increasing temperature reaches the rock strength, the elasticity in the system propagates the fractures further than would be the case if the system had been perfectly stiff (a stiff testing machine is of importance when performing axial tests on cores). The slow temperature/stress increase therefore creates a quiet window in the pillar until enough strain energy to propagate the fracturing has been stored up.
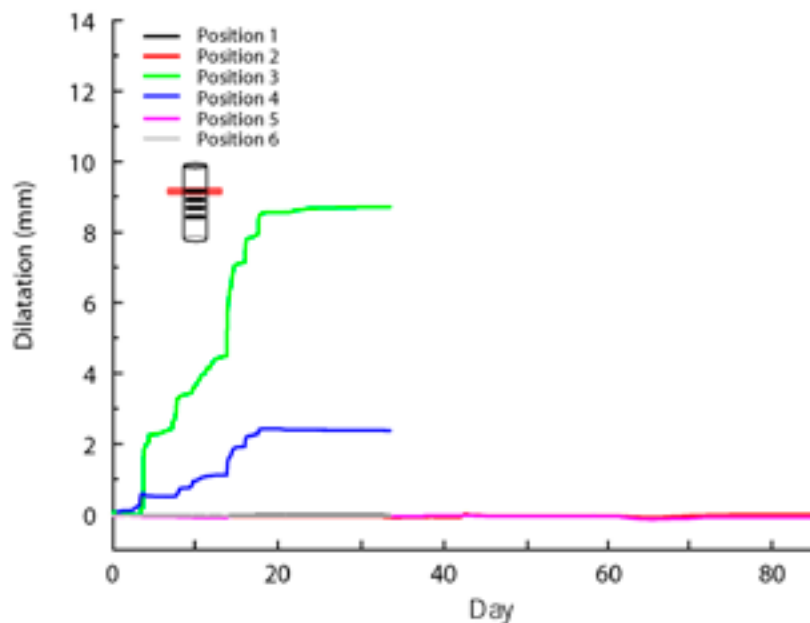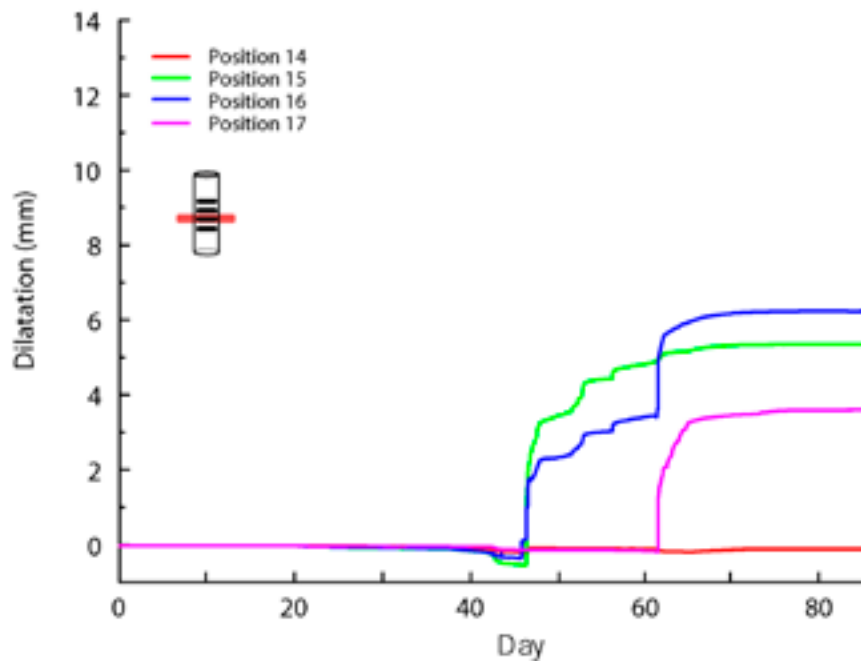


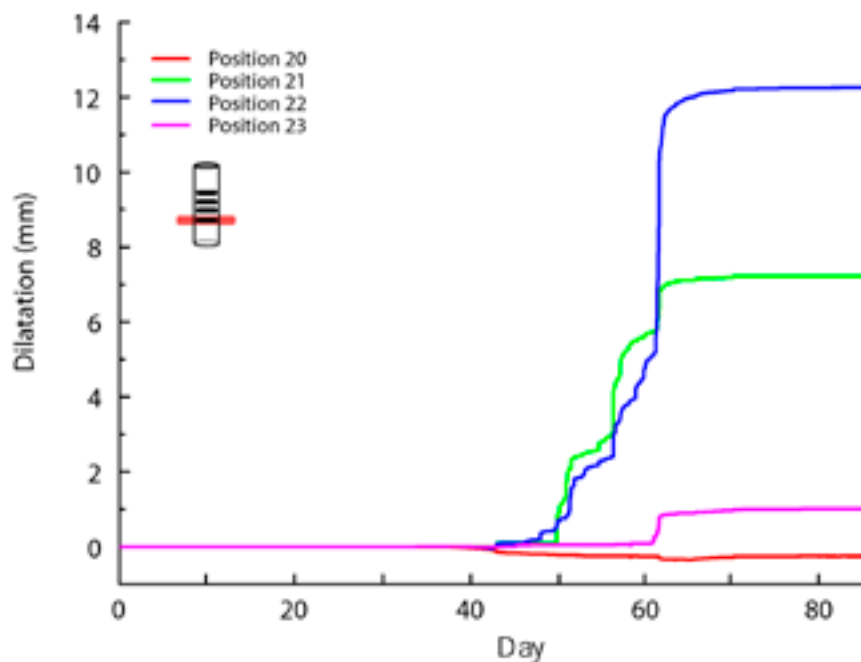*Figure 6-7.* *Deformations of the short-range sensors at the 2.5 m instrument level.*
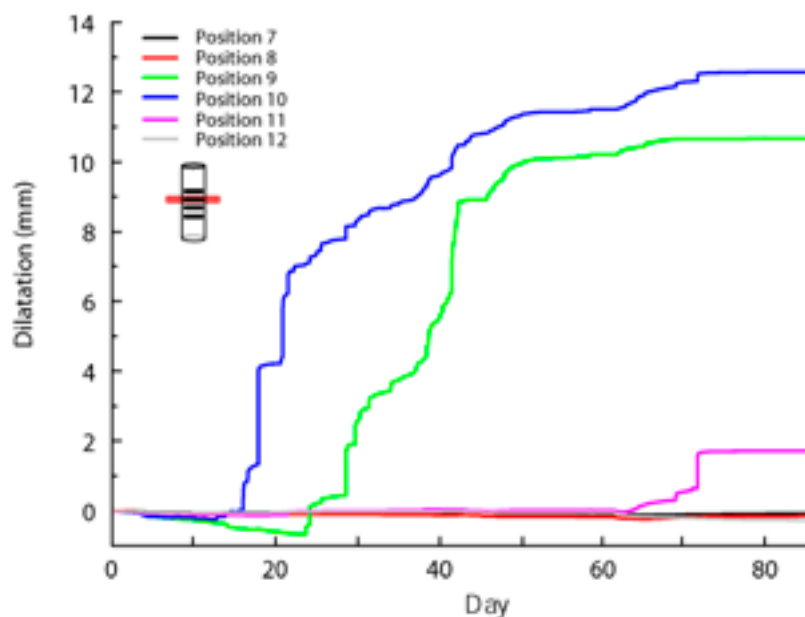


*Figure 6-8.* *Deformations of the short-range sensors at the 3.0 m instrument level*

An effort has been made to correlate the acoustic events with displacements, but without success. It was found that AEs were in many cases located too far from where the displacement was measured to be related to this deformation. It was also found that large displacements (on an mm scale) took place without events occurring closer than 10 cm from the transducer at the time of displacement.

The energy released during the fracturing was in some cases too low for the AE system to pick it up. It is likely that the slow loading rate enabled the fractures to propagate with a minimum of energy release in some cases. This would mean that the fracture in this case propagates continuously, like in a stiff testing system.



**Figure 6-9.** *Deformations of the short-range sensors at the 3.5 m instrument level.*



**Figure 6-10.** *Deformations of the short-range sensors at the 4.1 m instrument level*

The LVDT placed along the ductile shear zone located in the upper part of the pillar (Chapter 4) indicated some movement along the plane of the shear zone. The deformation was quite small, approximately 0.5 mm. The plot is shown in Figure 6-11. The LVDT is extended, which means that the right part of the shear zone has moved to the left.

The rock at the centre instrument positions at depths of 3 and 3.5 m (position 9, 10 and 15, 16, respectively) exhibits a radial expansion before the dilatation is initiated. The reason for this is probably a 3-dimensional stress re-distribution. When the rock above the LVDT yielded, the stresses were forced deeper into the pillar, which relaxed the rock close to the LVDT and caused the observed effect of a contraction. The propagation of the notch can also be seen in the plots, since the upper instrument position reacts before the lower one at the same level. The reason why the instruments at a depth of 2.5 m do not indicate the contraction in the graphs is probably because they were installed so close to the pre-existing notch that the contraction may have taken place before the instruments were installed. The absence of contraction at the 4.1 m level is more difficult to explain, but the spalling pattern is also quite different there. A weaker part of the rock started to yield from the 5 m level and propagated upwards (Appendix 2e). The two spalling fronts have created a complex geometry where the stresses are probably distorted. The contraction (radial expansion) of the spalling front is plotted in detail in Figure 6-12 and Figure 6-13.

To exclude the possibility that the monitored radial expansion was an effect of the monitoring system itself, the sources of error in the system were identified and quantified (Appendix 2c). After studying the monitored displacements and comparing sources of error associated with increasing temperature and pipe deflection, it can be concluded that the radial expansion measured is not due to a systematic temperature-induced error in the monitoring system. Nor has evidence been found that the observations can be explained by deflection of the pipes on which the LVDTs were mounted. It can be concluded that the radial expansion is an actual phenomenon.

Efforts were made to back-calculate the radial expansion measured (Appendix 2d). The 2D and 3D modelling of the very pillar centre (when the notch approaches) indicates deformations in the same direction as the radial expansion. However, the deformations are only 10% of those measured in situ, so it cannot be argued that the models predicted the radial expansion – especially since the notch had to be introduced in the 2D model in order for the deformations to turn up. In the field the LVDTs picked up the incoming notch before spalling was initiated at their location. This is a true 3-D problem.

In addition to numerical modelling, an analytical approach was also adopted (Appendix 2d) using Hooke's generalized law. A cubic rock block was imagined to have one side free after the compression on the top side was released. A radial expansion of the same magnitude as in the case of the numerical modelling was indicated.
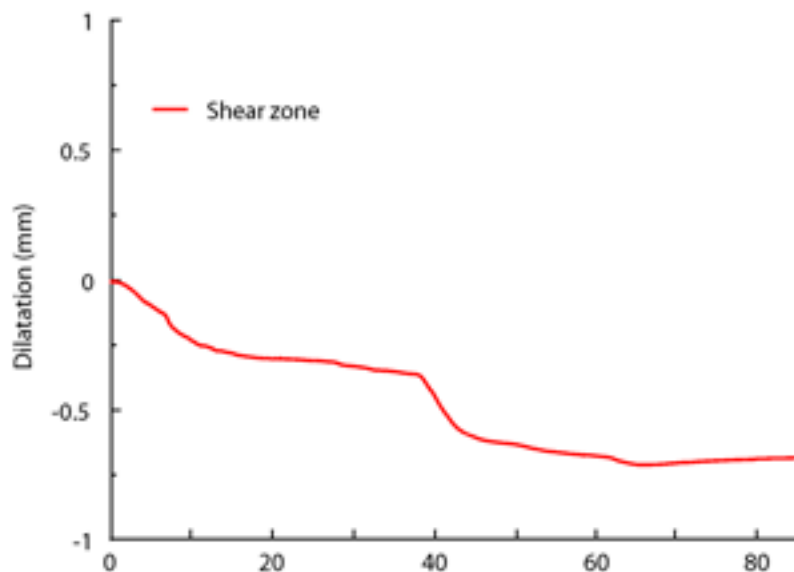


**Figure 6-11.** *Deformations along the shear zone at the top of the pillar.*

71
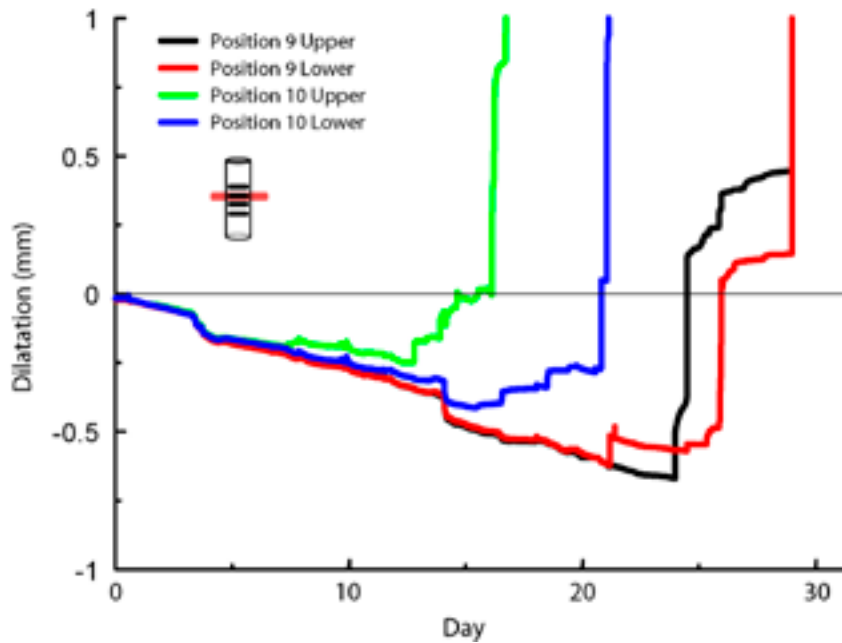
***Figure 6-12.*** *Contraction of rock before dilatation is initiated at 3 m level.*
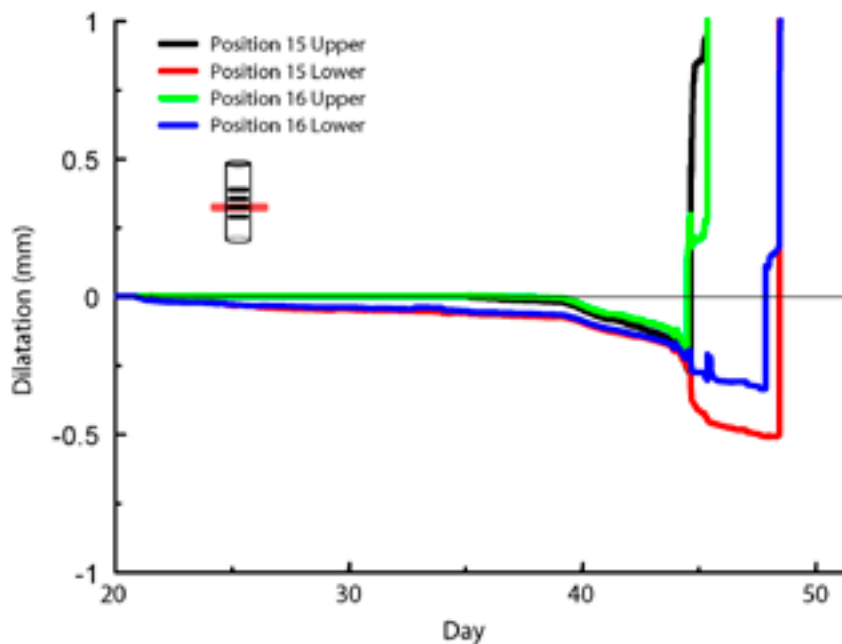


***Figure 6-13.*** *Contraction of rock before dilatation is initiated at 3.5 m level.*

When the deformations from the transducers located outside the spalled area were compared with modelled results, the measured displacements were found to be of the same magnitude as those modelled close to the pillar centre. This can be seen as an indication of the fact that the elastic modelling probably is quite close to what is actually happening, but the complex geometry and stress situation inside the notch makes it impossible to model this exactly.

The 2D modelling clearly showed that the effect of a 3 cm thick EDZ is negligible when studying radial expansion.

The scoping calculations performed indicate the complexity of modelling the problem. Different notch geometries have been found to give results that are comparable for some observations but not for others. The tools used were not adequate to simulate the problem, but it is uncertain whether more complex 3D codes could do a better job. Their major contribution would be their plastic analysis capabilities combined with the possibility of modifying the material in the notch as it yields. That is probably not enough. The formation of the slabs with extensional fracturing probably controls the behaviour of the rock. The slabs deeper inside the pillar can probably carry some load perpendicular to the tunnel axis, thereby making the stress distribution in the notch very complex.

## 6.3    Yielding observations

Drawings of the propagation of fracturing and yielding were made on 15 different occasions during the experiment. The rock wall was photographed on most of these occasions as well as at certain other times.

Two types of sketches were made. One type was on a more detailed scale and includes the fracturing around the LVDT positions. The other type was on larger scale and shows the depth and width of the spalled zone. Both types of drawings include observations made during the visit in the hole.

When the heaters had been turned off and the rock mass had cooled down, the slabs created by the spalling was carefully removed. The slabs were collected in approximately 0.5 m depth sections. All the slabs from one section were collected in a separate basket. Approximately 0.1 m$^3$ of slabs was removed.

Laser scanning of the pillar wall in the open hole was performed before and after the slabs from the spalling had been removed. The result of the latter scanning is presented in section 6.3.2. The scanning result gives the final size of the spalled zone and the volume of spalled rock in 0.05 m increments, Figure 6-18.

The general observations and conclusions are summarized in this chapter. The observations, drawings and photographs are presented in chronological order in Appendix 2e.

### 6.3.1    General yielding observations

As the v-shaped notch was formed and migrated down the borehole, the behaviour of the rock can be summarized in four different observations, which also have been illustrated in Figure 6-14.

1.  As the notch tip approached an instrumented level, the radial expansion was measured.

2.  Below the notch tip, small rock slabs (chips) started to form tangentially to the borehole wall, the first indication of dilation. These chips were roughly a quarter of a fingernail in size and very thin. After a while, larger thin chips of coin size were observed.

3.  Discrete fractures started to form. The fractures became the boundaries of the slabs and ranged in length from a few centimetres to approximately 10 cm.

4.  More fractures formed, creating larger slabs beneath the ones already formed. As the fractures grew deeper into the pillar, their angle increased from being tangential to the hole wall for the first superficial chips. The strike and dip of the notch's sides were mapped and are presented in Figure 6-15. The total opening angle of the notch is approximately 130 degrees. In the end, many slabs were located on top of each other. The dilatation of the rock wall increased as the slabs formed. The total deformation was the sum of the distances between each slab.
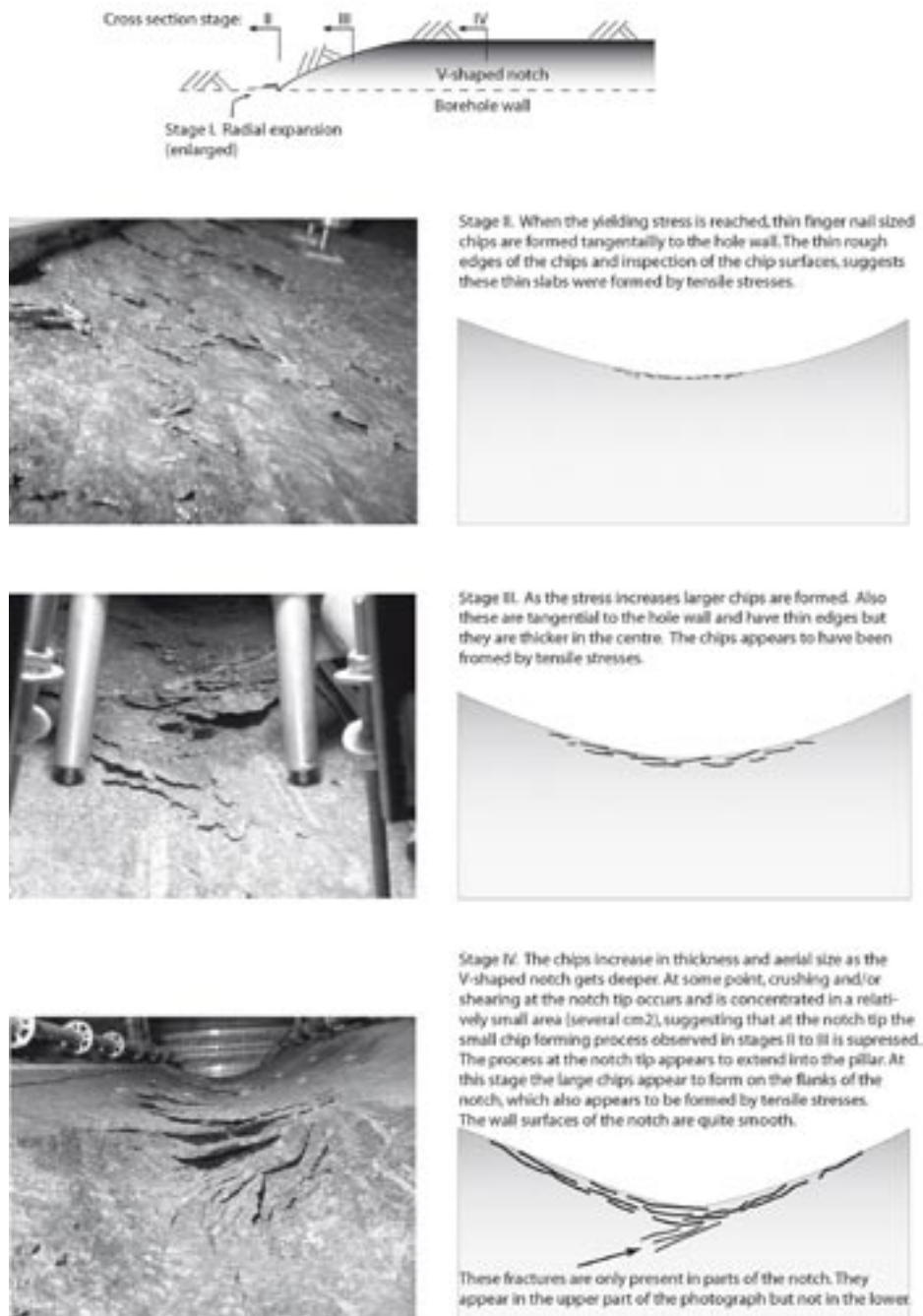
**Figure 6-14.** *Illustration of the yielding process in an overstressed granitic rock.*

The notch was located at a certain hole depth until the rock approximately 20 cm above it had reached a spalled width at the hole surface of 40–50 cm. The notch now migrated a bit further down and remained there until the spalled width above it reached 40–50 cm and the process was repeated.

All observations indicate that the initiation of brittle failure is purely tensile. Only in the deepest part of the notch was there evidence that shearing had also occurred.
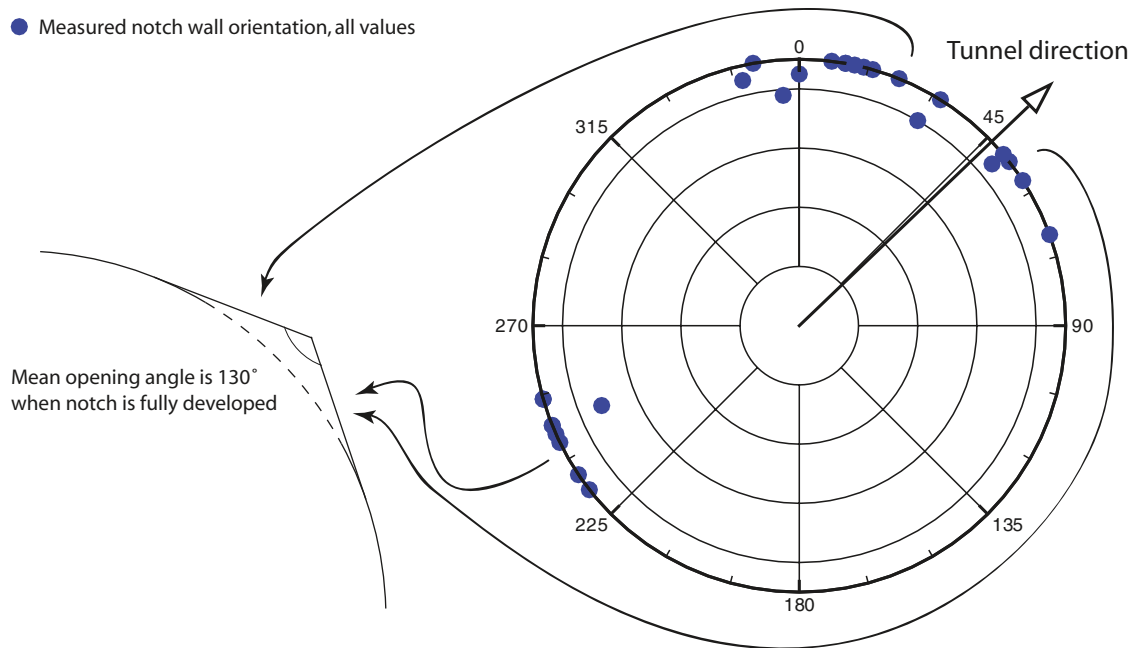
***Figure 6-15.*** *Lower hemisphere projection of the notch walls. The total opening angle of the notch was approximately 130 degrees.*

## 6.3.2    Geometry of the yielded zone

Before the start of heating and after the removal of the chips/slabs, the parts of the pillar wall that were spalled and drummy were mapped. Every 10 cm down the hole, the extent and depth of the yielded area was measured to the left and right of the centre line of the pillar. Moreover, the drummy area was mapped by tapping a screwdriver against the rock wall. Yielding/spalling was defined as occurring in parts of the rock wall where chips/slabs had fallen off or been removed. The results of the mapping, including the location of the notch after heating, are presented in Figure 6-16. The notch is located very close to the left boundary of the drummy area after heating (Appendix 2e). This is an effect of the induced fractures coming in from the left described in the sections about the removal of the slabs. Only the very superficial slabs created on the right side could be removed. The fractures from the left therefore continue beneath the rock surface, making it drummy.

To establish the full three dimensional geometry of the overstressed region, i.e. the failed zone, the pillar wall was scanned using laser technology. The distance between the laser points was 3 mm and the radial accuracy of the measurement was slightly less than 3 mm. The wet surface of the pillar wall disturbed the scanner, causing the somewhat poor radial accuracy. The data set was used to assess the width and the depth of the failed area as well as the location of the maximum depth. The data set was further used to determine the volume and area of the spalled zone. A visualization of the survey is presented in Figure 6-17 where the width and depth of the spalled zone is indicated.

To obtain the information from the data set, horizontal sections were taken at depth increments of 50 mm along the pillar wall. The sections were compared with the theoretical contour of the borehole, which was used as a baseline to determine the width, depth and area of the spalled volume. The volume was automatically calculated by the software and was given as a mean value between each 50 mm section. The volume of yielded and removed rock over the depth of the notch is presented in Figure 6-18. If all 50 mm increments are summarized, the total volume of rock removed was approximately 0.1 m³.
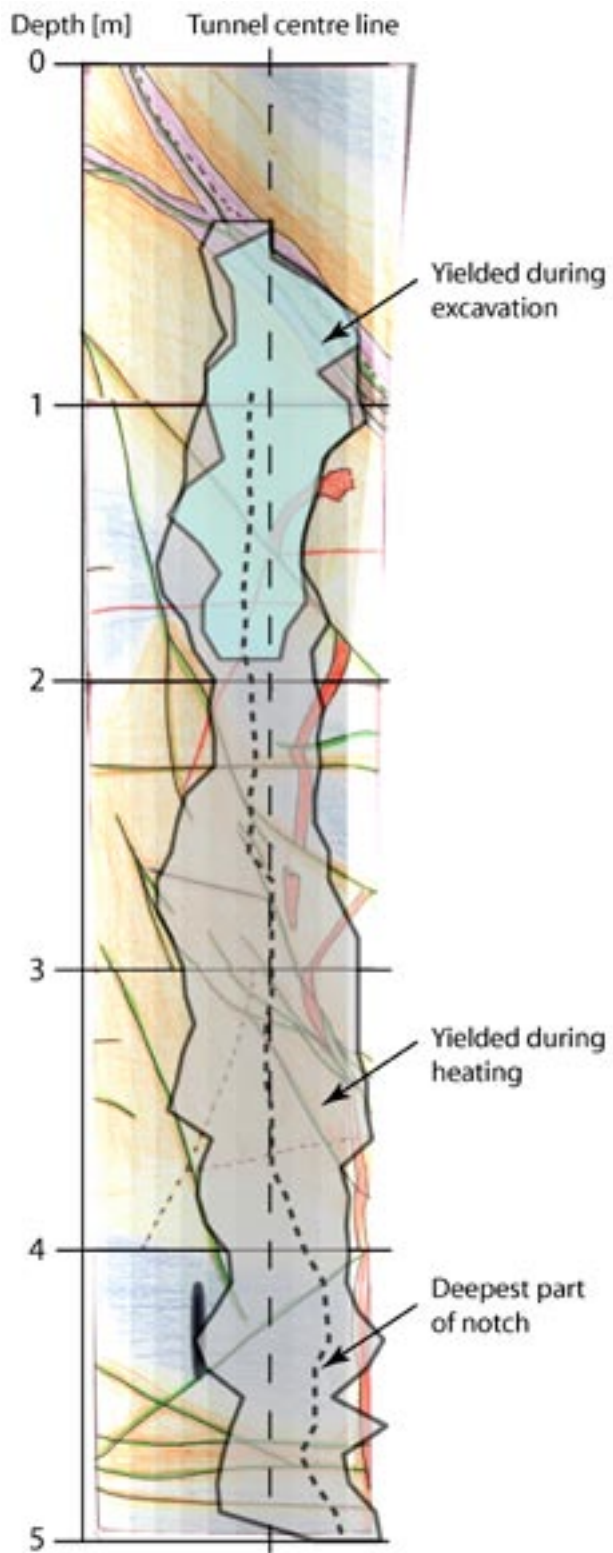
***Figure 6-16.*** *Yielded areas before and after heating.*
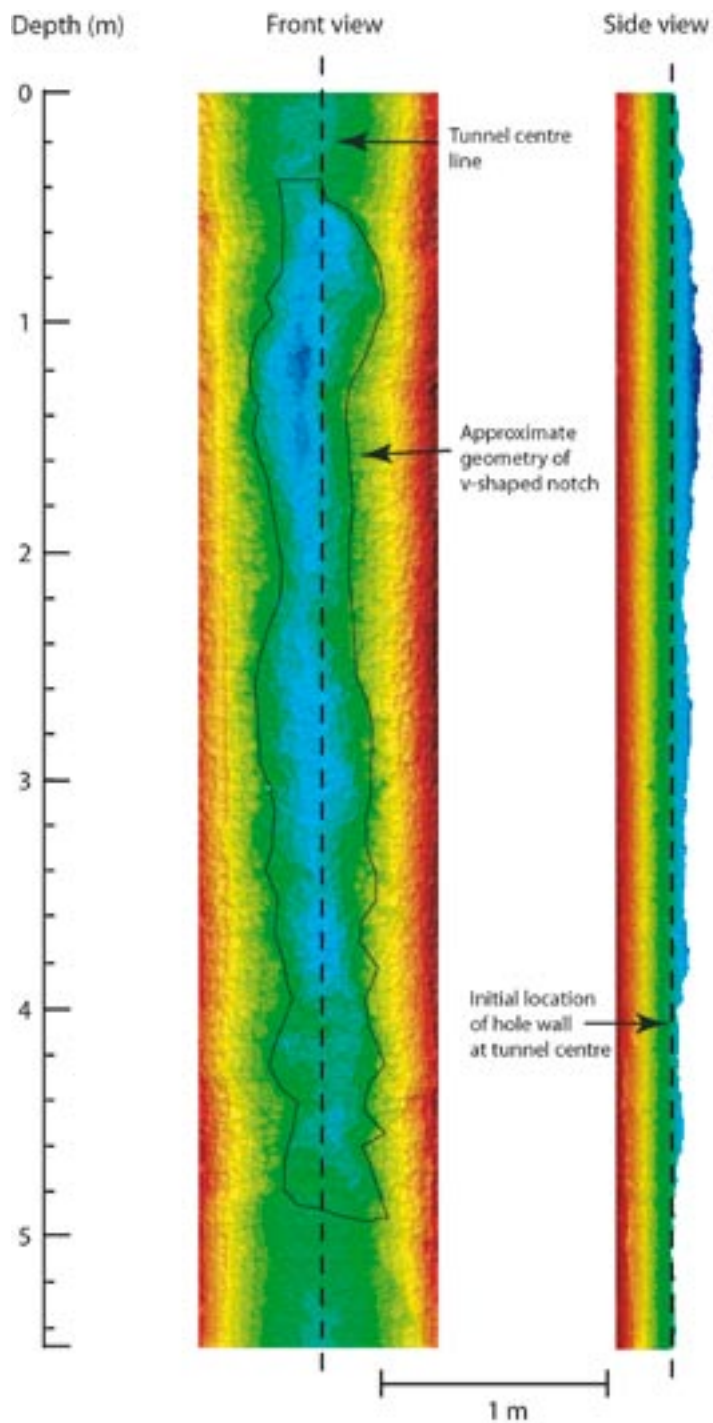
***Figure 6-17.*** *Result of the laser scan. The left-hand figure shows the approximate geometry of the notch. The right-hand figure shows the depth of the notch and the dashed line indicates the location of the borehole wall before yielding was initiated.*
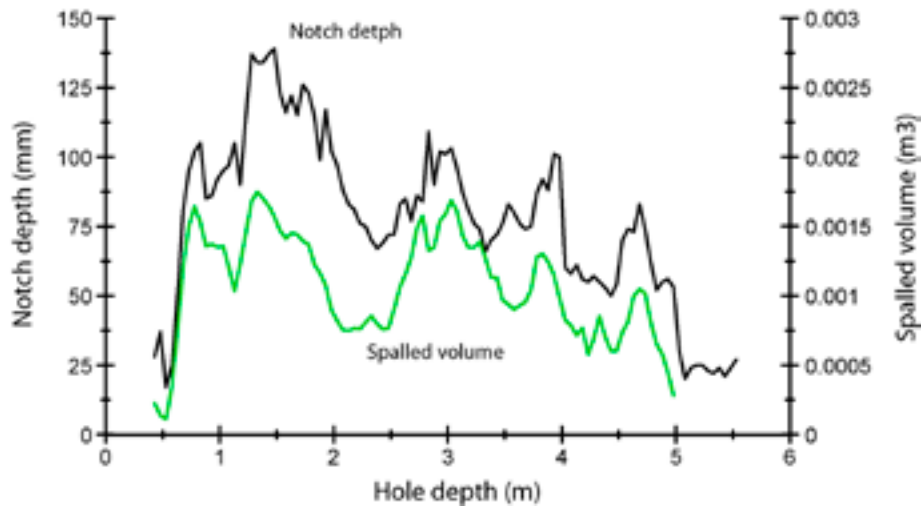
***Figure 6-18.*** *The volume of spalled and removed rock and the depth of the notch, both shown in 50 mm increments.*

The width of the spalled volume presented as the total breakout angle is plotted together with the notch depth in Figure 6-19. The radius of the borehole can be approximated at 875 mm (1.75 m diameter). The mean breakout angle for all the 50 mm sections is 32 degrees. /Martin et al. 1997/ measured yielded profiles at four locations in a 3.5-m-diameter circular test tunnel. Those profiles gave total breakout angles of 56, 55, 58 and 73 degrees. In an adjacent 1.24 m diameter vertical borehole a total breakout angle of between 34 and 50 degrees was reported. The results from the pillar stability experiment are hence close to what has been reported.
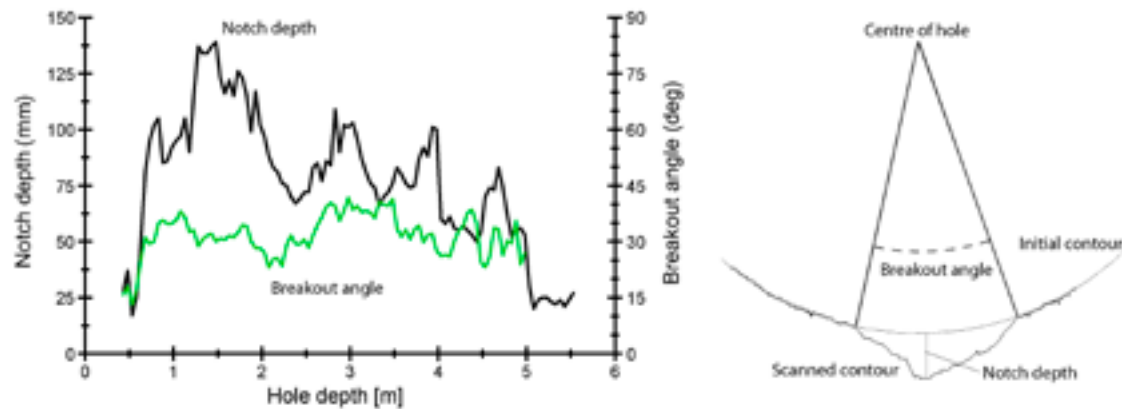


***Figure 6-19.*** *Left: notch depth and breakout angle for hole depths in 50 mm increments. Right: Breakout angle is defined as the angle for a sector with the centre point at the hole's centre point which intersects the scanned contour as it coincides with the original contour. Notch depth is the longest distance perpendicular to the original contour of the spalled contour, i.e. depth of yielding.*

78

## 6.4    Acoustic Emission

An overview of the results of the acoustic monitoring during the excavation of the holes and the heating phase of the experiment is presented in this section. The acoustics associated with the release of the confinement pressure are described in Chapter 9. The results and the monitoring equipment used are reported in /Haycox et al. 2005/.

As is described in Chapter 4, the sensitivity of the acoustic sensors for the APSE was such that they would record a pencil-lead break on the boundary of the hole. Hence, simply recording acoustic events does not necessarily indicate significant rock mass damage or yielding. This is important to remember when studying the AE record files. Spatially distributed AEs or AE clusters are not evidence that failure has occurred within a small volume of rock. Rather, what is recorded is usually the formation of small fractures or crushing of asperities.
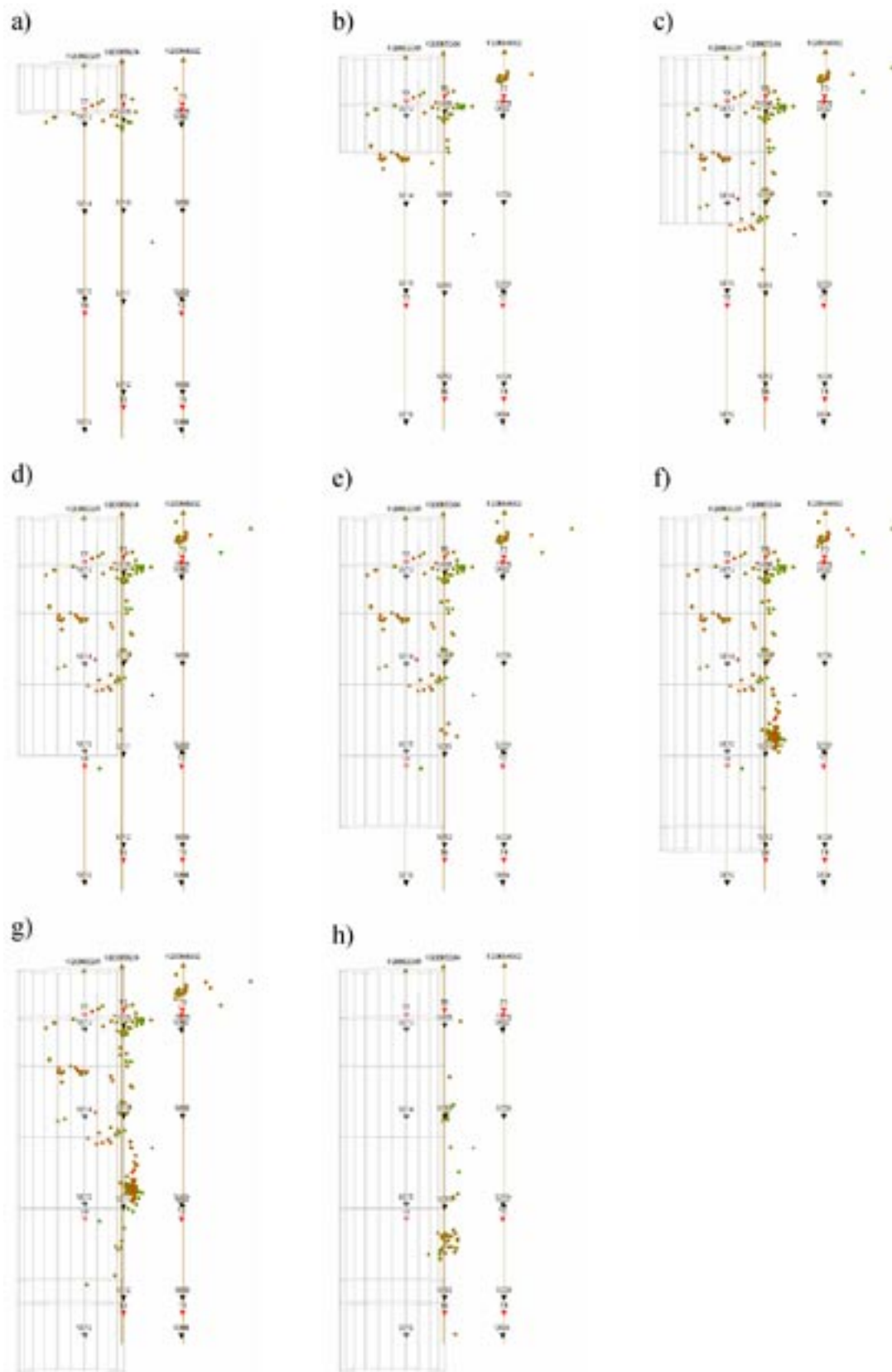
### 6.4.1    Excavation of the first hole

The rock mass response to the excavation of the first hole was essentially elastic. This conclusion is drawn based on the fact that relatively few events were recorded at the open boundary of the borehole. This conclusion is supported by the fact that thorough sounding of the hole walls did not reveal yielding of the rock except at certain discrete locations. Figure 6-20 shows the locations of the AEs, which are mainly located in the upper half of the hole.

### 6.4.2    Excavation of the second hole

During the excavation of the second hole there was an increase of acoustic events, and as can be seen in Figure 6-21 the vast majority were located in the open hole, providing an initial indication of the effect of the confining pressure. There are a number of events in the shear zone located in the upper part of the pillar, but no general yielding was observed. At the end of the excavation, yielding suddenly occurred between the approximate depths 0.5 and 1.95 m, and the notch described in Chapter 8 was formed. The records do not indicate that yielding occurred within the pillar volume. This second hole was also thoroughly sounded and inspected, and aside from the obvious yielded zones, no additional damage was found. It was concluded that the rock mass response was still elastic.

### 6.4.3    Heating of pillar

Figure 6-22 shows the acoustic emission events recorded as the temperature in the rock mass increases. AE data after day 60, which include the release of the confining pressure and the cooling of the experimental volume, are not discussed in this section but are presented in Chapter 9. All accumulated AEs during the excavation and heating of the pillar are shown in Figure 6-23. The relationship between AE and tangential stress is discussed in Chapter 8. Except in the yielded zones, the rock mass response is considered to be elastic throughout the heating phase as well. A concern regarding the sub-vertical fracture 08 is raised in Chapter 2. The AE records do not indicate that this fracture has displaced and distorted the stress field. The discussion behind this conclusion is presented in Appendix 2f.

**Figure 6-20.** *Location of acoustic emissions during the excavation of the first 1.75-m-diameter deposition hole DQ0066G01. Views (a) to (g) show accumulated events recorded during each stage of drilling with the last view, (h), one week after excavation. Data modified from /Haycox et al. 2005/.*
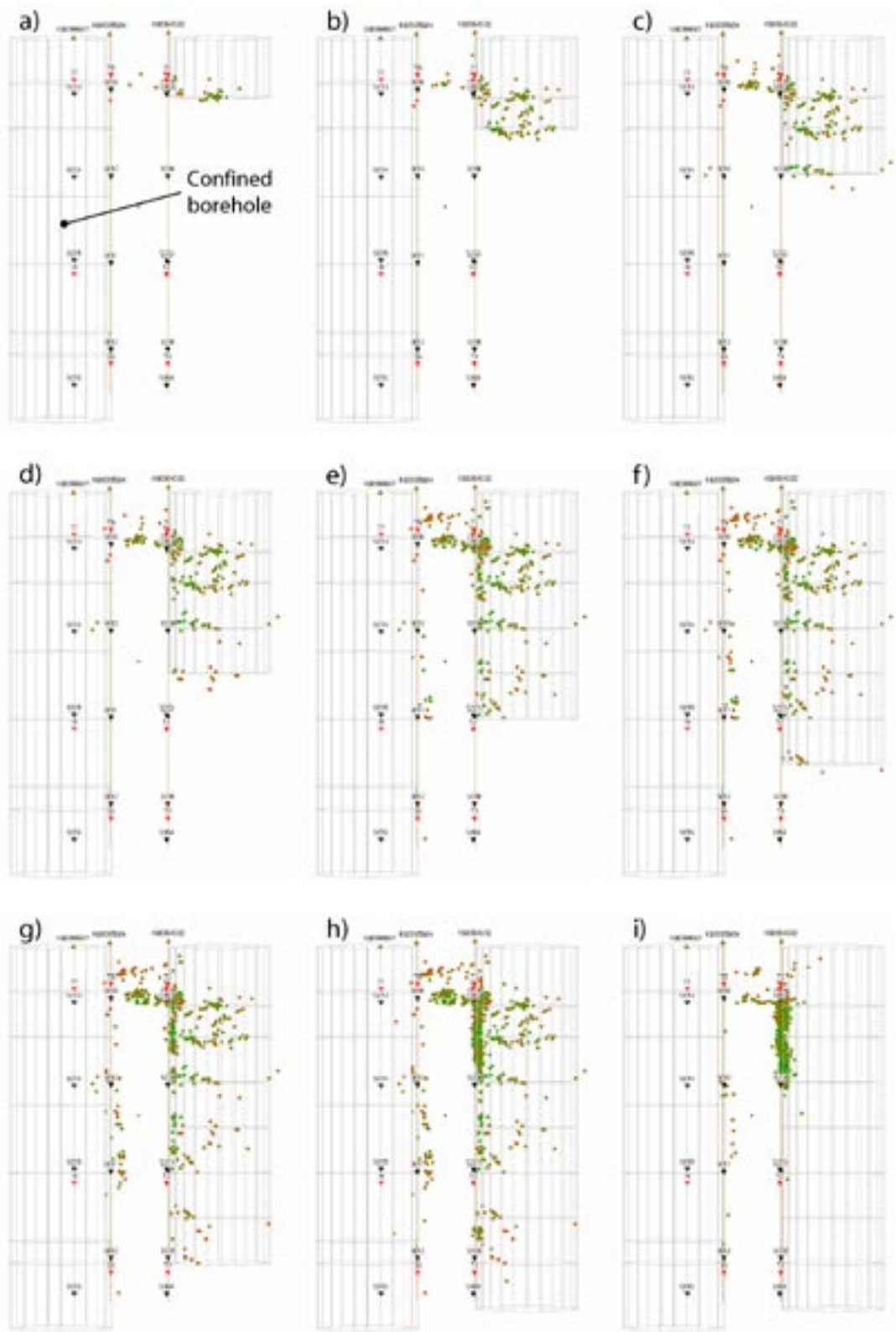
**Figure 6-21.** *Location of acoustic emission events during excavation of the 2nd 1.75-m-diameter deposition hole DQ0063G01. Views (a) to (h) show accumulated events recorded during each stage of drilling with the last view, (i), one week after excavation. Data modified from /Haycox et al. 2005/.*

81
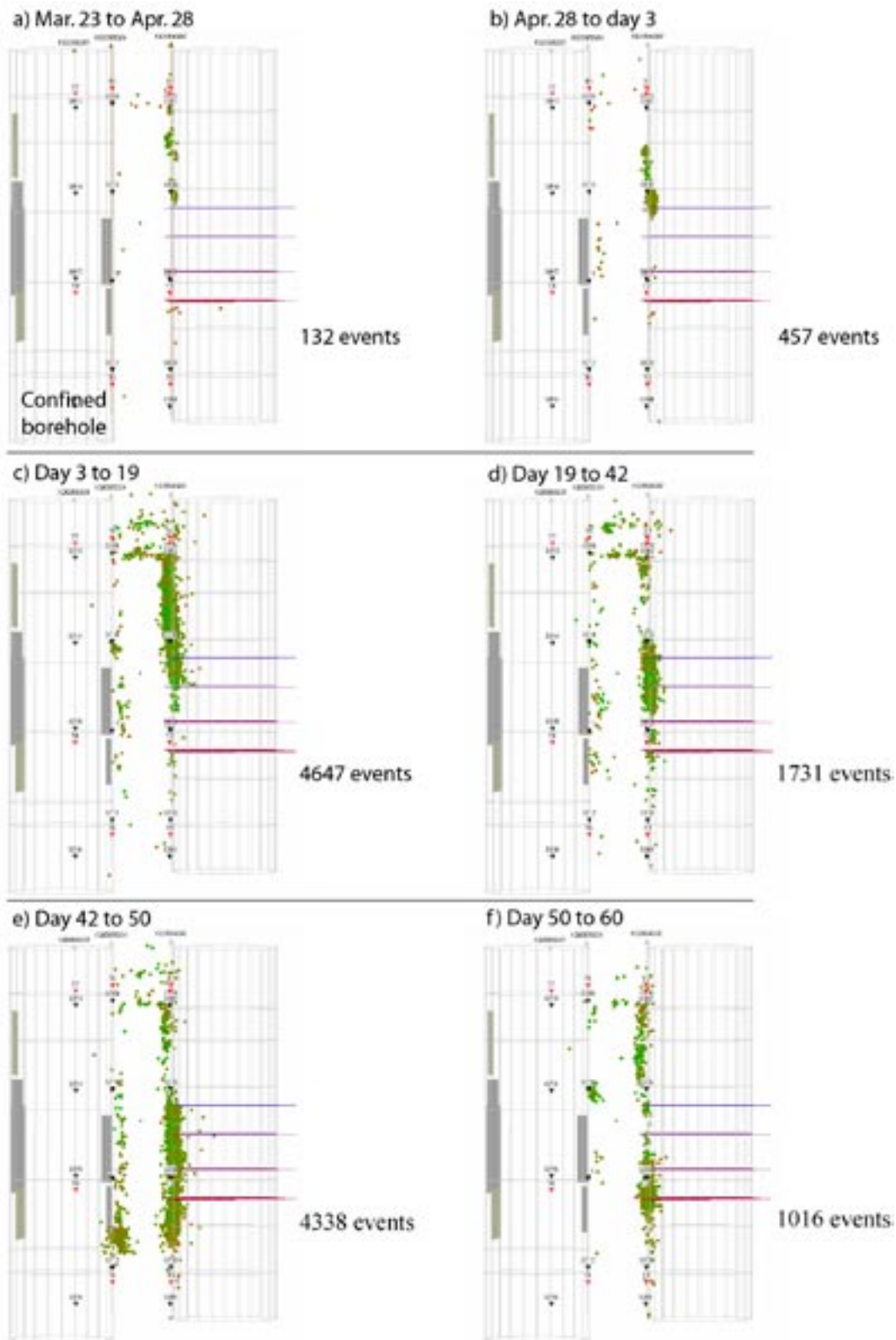
**Figure 6-22.** *Location of acoustic emission events during the heating phase of the experiment. Grey shaded areas are steel plates used to cover the irregular zones created during the drilling of the first hole and provide good contact between the water-filled bladder that provided the confining stress and the rock wall. Data modified from /Haycox et al. 2005/.*

AE record during drilling and heating
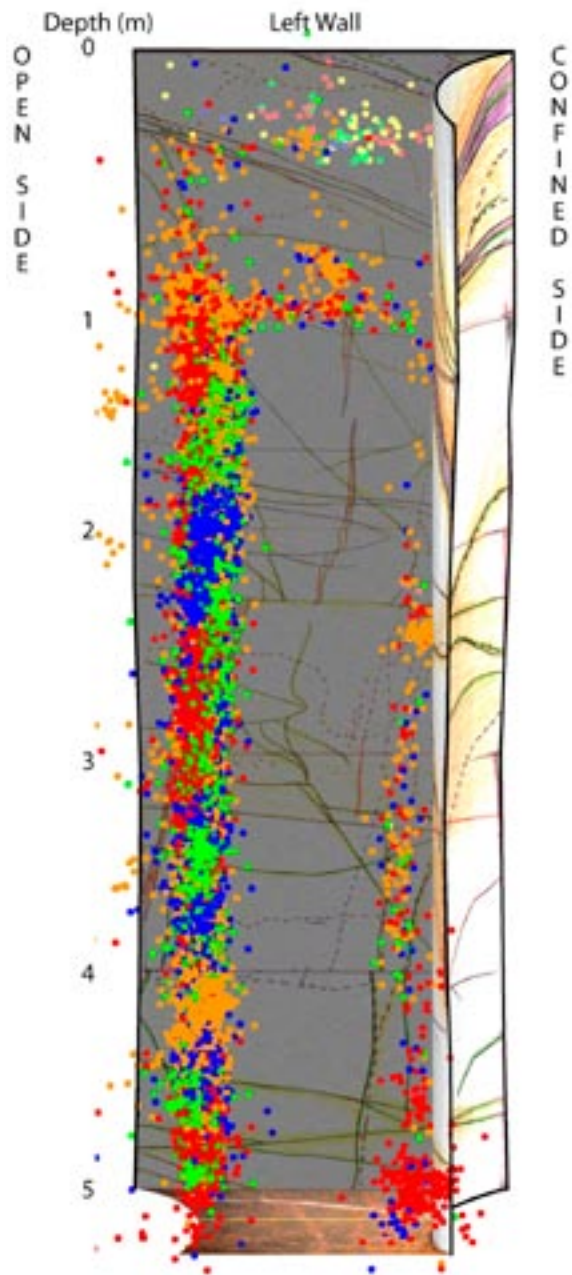


*Figure 6-23.* *All source-located AE events during excavation and heating of the pillar. Acoustics from the release of the confining pressure are not included.*

### 6.4.4    Equilibrium of the excavation-induced notch

The acoustic records illustrate the delicacy of the equilibrium of the notch. After the excavation of the second hole, the AE intensity quickly decreased and was low until late April (Figure 6-24). The events then migrated approximately 0.3 m further down the hole. The locations of these events are shown in Figure 6-25, were the events recorded from April 26 until the day the heaters were turned on are presented. The week before April 26 was the week when the LVDTs were installed, and a great deal of time was spent in the hole by two persons. The small changes in temperature caused by the individuals working in the confined space probably changed the stresses slightly and then triggered additional yielding in the notch. This was the first indication of the close relationship between stress thresholds and yielding.
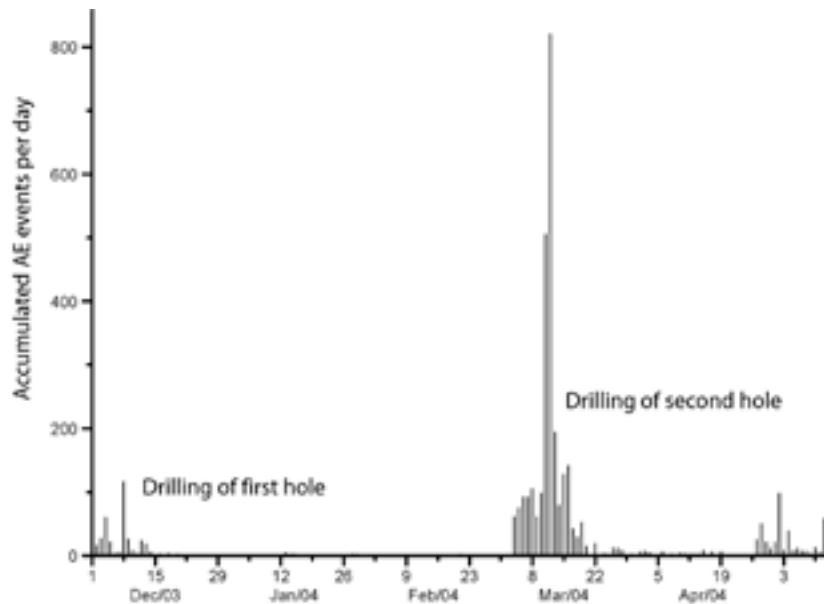


**Figure 6-24.** *Histogram of the acoustic events in the pillar from the start of the drilling of the first hole until the start-up of the electrical heaters. Note that during this stage of the experiment the AE system was disabled between 07:00 and 17:00 hours when installation work was carried out in the experimental tunnel.*
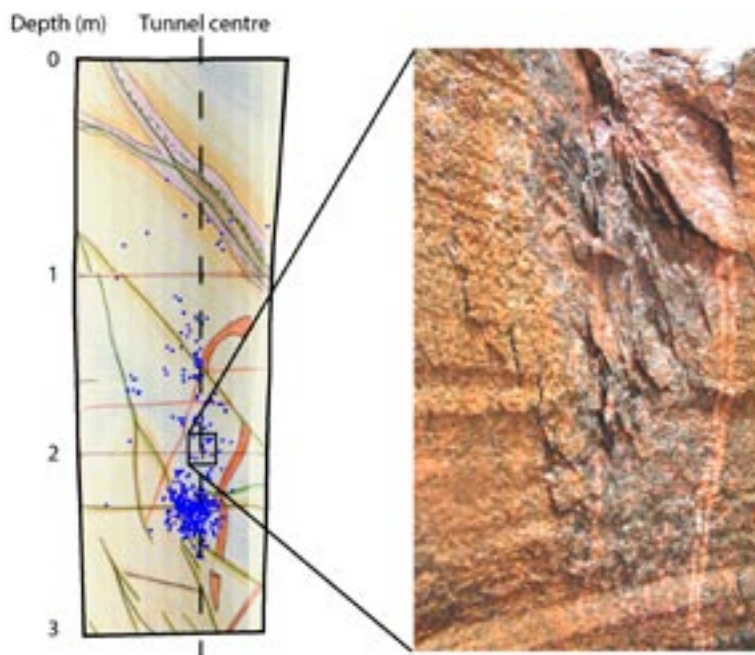


**Figure 6-25.** *Acoustic events initiated by small temperature changes in the hole. The photograph of the notch was taken shortly after the excavation of the hole.*
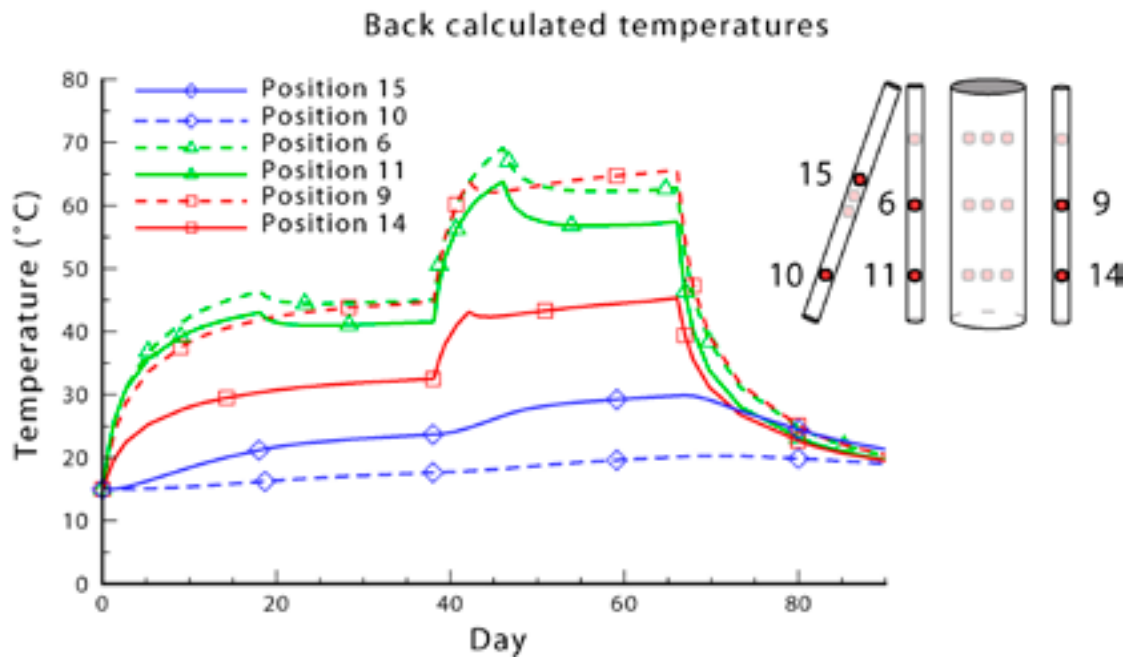
# 7 Back calculation of thermal stress

The thermal induced stresses were back-calculated using the finite element program Code_Bright /CIMNE 2000/. The modelling is described in detail in /Andersson et al. 2006/ and /Fälth et al. 2005/. The model consisted of the experimental pillar volume surrounded by a large section of the APSE drift (Figure 7-1). The temperature monitoring results from the centre of the pillar wall were used as thermal boundary conditions. The thermal properties of the rock, and to a lesser extent the output from the heaters, were adjusted to keep the temperatures between the heaters as close to the monitored temperatures as possible. Once the calibrated thermal modelling was completed, the thermally induced stresses were determined at specific data points using a linear elastic material model.

During the calibration of the model to the boundary conditions it became evident that the thermal conductivity determined in the laboratory on core samples from the experimental volume was underestimated. It was found that a thermal conductivity of 3.2 W/(m,K) was a better representation of the site conditions. This value is 23% higher than the conductivity determined in the laboratory (Table 2-1).

The model produced good results within the experiment volume (Figure 7-2). The difference between the back-calculated temperatures and the monitored ones was only a few degrees there. The back-calculated difference between the initial ambient temperature and the maximum temperature after heating was overestimated by a factor of 1.6 in the embedment. In absolute measures this corresponds to an over prediction at day 60 of 5.5°C at position 10 (Figure 7-2). This had to be compensated for; otherwise the stress contribution from the embedment would be overestimated.
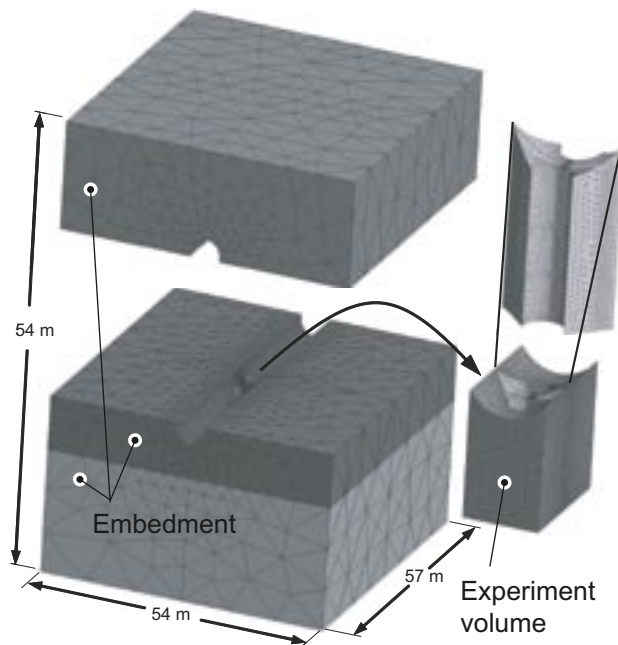


*Figure 7-1.* *Dimensions of the thermal model, consisting of the experiment volume located within the embedment.*

***Figure 7-2.*** *Graph of the results of back calculation of the temperatures. Since the temperatures in the large holes were used as boundary conditions they are not included.*

The thermally induced stress is directly proportional to the temperature and the coefficient of thermal expansion. A reduction of this coefficient by a factor of 1.6 in the embedment would therefore give correct stresses. The thermally induced stresses are also a function of Young's Modulus. The pillar only contained one open fracture located in the lower part of the pillar, fracture 08. The Young's modulus derived from laboratory samples was therefore used for the pillar volume. However, the embedment part of the model included the typical large-scale (tunnel scale) fractures of the Äspö diorite rock mass. A different Young's modulus was therefore used in the embedment. This modulus was determined by back calculation of convergence measurements made during the excavation of the tunnel to be 55 GPa (Chapter 2).

The thermally induced stress was calculated using both the laboratory-determined values of Yong's modulus and the coefficient of thermal expansion and the back-calculated values of the same two parameters. The temperature-increased stresses obtained using the back-calculated values are 5 to 7 MPa lower at maximum temperature than when laboratory values are used. It was assessed that the back-calculated parameters gave the best estimate of the actual thermally induced stress in the pillar, and these results have been used in the evaluation of the experiment. The thermal and elastic properties used for the pillar are summarized in Table 7-1

**Table 7-1. Thermal and elastic properties used in the model.**

| Property | Value | Unit |
|---|---|---|
| Young's modulus in pillar | 76 | GPa |
| Young's modulus in embedment | 55 | GPa |
| Coefficient of thermal expansion in pillar | $7.0 \cdot 10^{-6}$ | m/K |
| Coefficien of thermal expansion in embedment | $4.4 \cdot 10^{-6}$ | |
| Density | 2,730 | kg/m³ |
| Thermal conductivity | 3.2 | W/(m,K) |
| Thermal capaciticity | 2.10 | MJ/(m³,K) |

## 7.1 Modelling results

The results of the back calculation at depths of 3.5 m and 5.5 m are shown in Figure 7-2. The results can be compared with Figure 7-3, which shows the monitored data at the same locations.

The greatest difference between the back-calculated and measured temperatures is at positions 10 and 15 located in the inclined hole. A plot made of the back-calculated data from horizontal sections at depths of 1.5 m, 3.5 m and 5.5 m illustrates the temperature distribution in the experimental volume, Figure 7-4. The plot was made for day 52, which is when the maximum temperature reached a steady state.
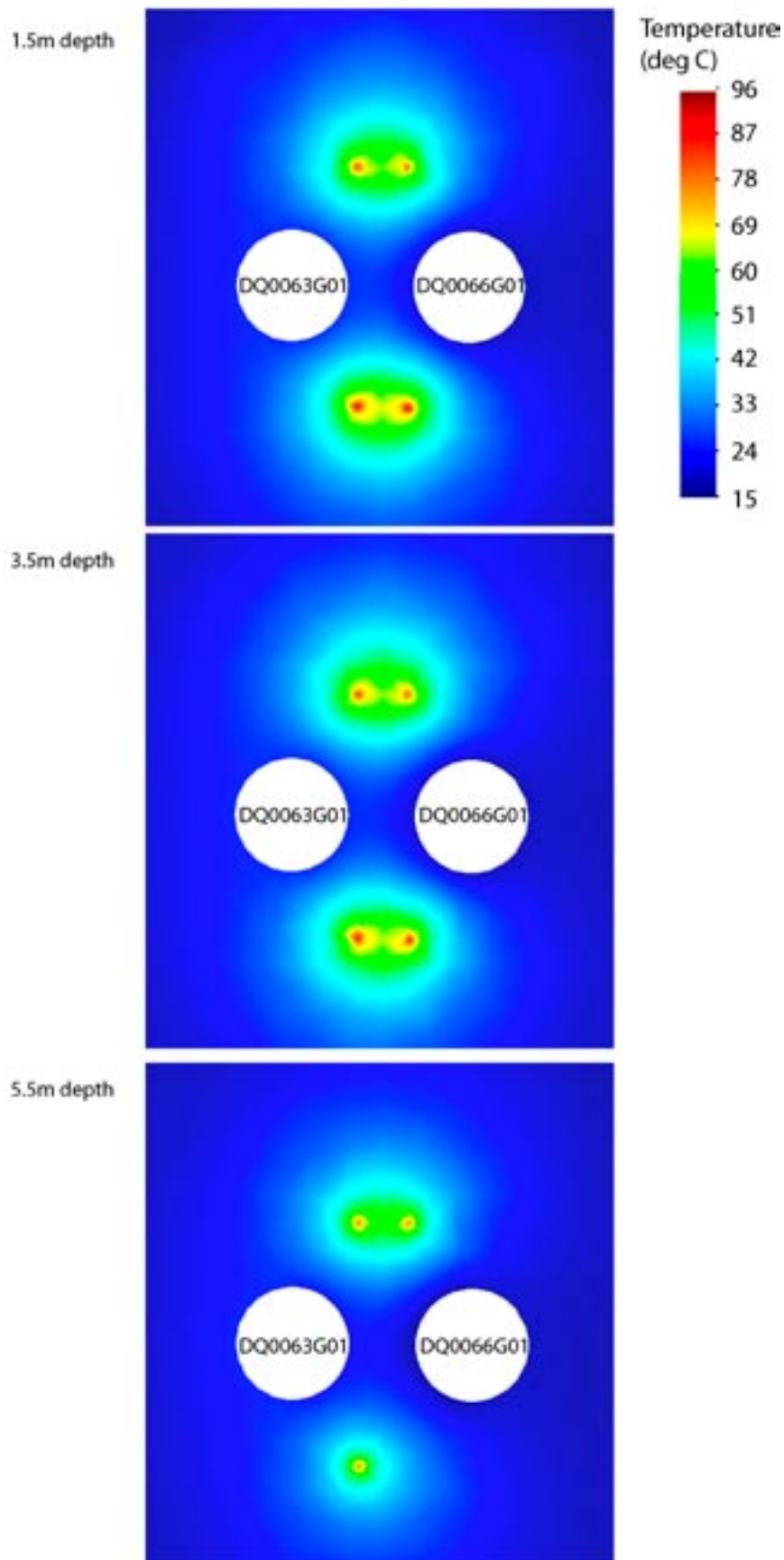
In Figure 7-5, the thermally induced tangential stress and the total induced stress at day 50 are plotted as a function of the hole depth. The total tangential stress is calculated by adding the excavation-induced tangential stress to the thermally induced stress (Chapter 8). The jagged curve for the thermally induced stress is caused by the model discretization. The variability between two adjacent elements resulted in a difference of approximately 2 MPa. The difference is relatively small in comparison with the total tangential stress. In the next section, these tangential stresses are used to establish the stress magnitudes required to cause yielding of the pillar. It should be noted that these calculated stresses are for a linear elastic isotropic model and no attempt is made to estimate the amount of stress redistribution that may occur as a result of yielding.

## 7.2 Thermal stresses and Acoustic Emission Events

Examples of the calculated thermally induced tangential stress 3 mm into the pillar at four different depths are given in Figure 7-5 together with the accumulated number of acoustic events recorded for each day. Figure 7-6 clearly shows that the daily number of acoustic emission events increases when the stress increases. The steady state for thermal stresses was reached around day 45. This steady state was maintained until day 67, when the heaters were turned off. As can be seen in the figure, a steady state was also reached around day 20. The notch had at this time only propagated about halfway down the hole. The thermal output was therefore increased to propagate the notch further down the hole so that more observations and monitoring could be done.
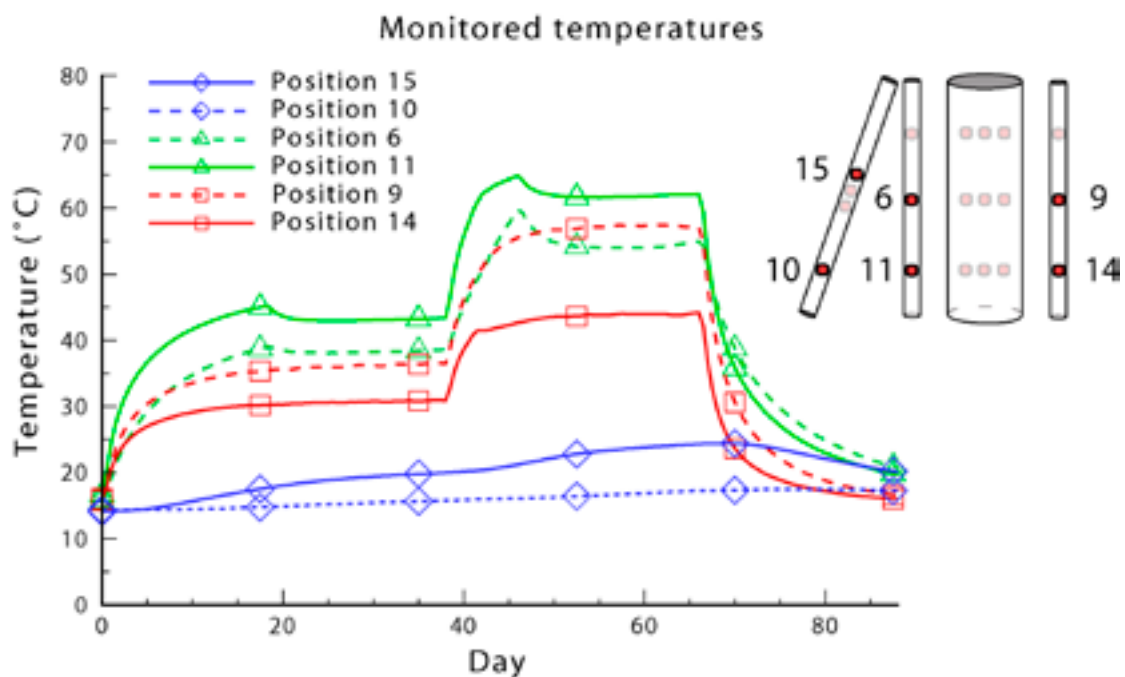


*Figure 7-3.* *Graph of monitored temperature data.*

**Figure 7-4.** *Back-calculated temperatures (degree C) at day 52 in a planar view at depths of 1.5 m, 3.5 m and 5.5 m.*
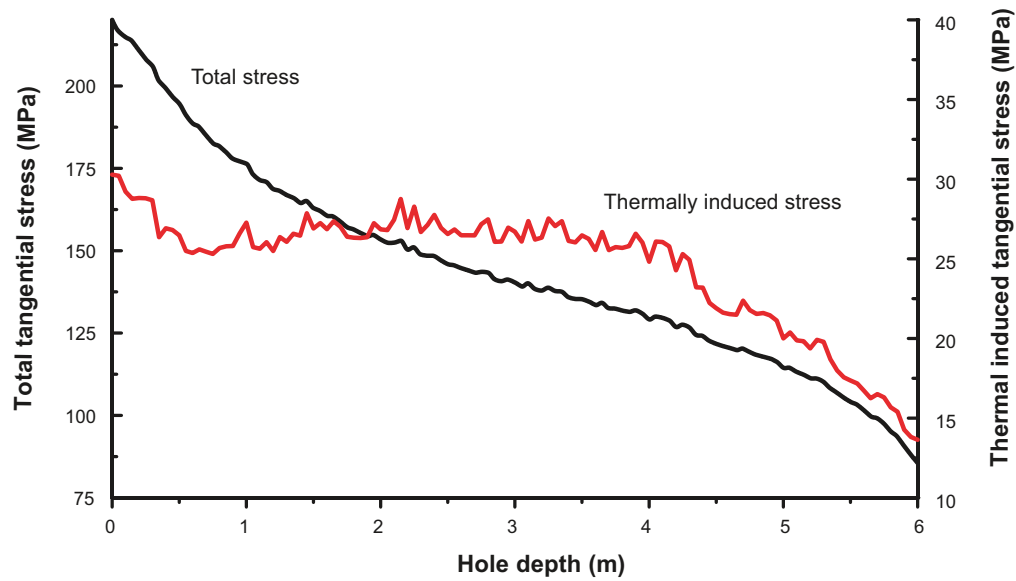
***Figure 7-5.*** *Thermally induced and total induced tangential stress along the hole wall at day 50.*

The decrease of the confining pressure began at day 61, and the AEs after that day are not included here but presented in Chapter 9. The relationship between the increasing tangential stress and the AE events are clear. Many AEs were recorded during the release of the confinement, but they faded away within two days of the final pressure drop. There was no elevation of the acoustic emissions count during the cooling period beginning at day 67. The mean value between day 67 and day 83, when the AE system was disabled, was only 10 events per day. During the last week of measurements the average was slightly above 1.
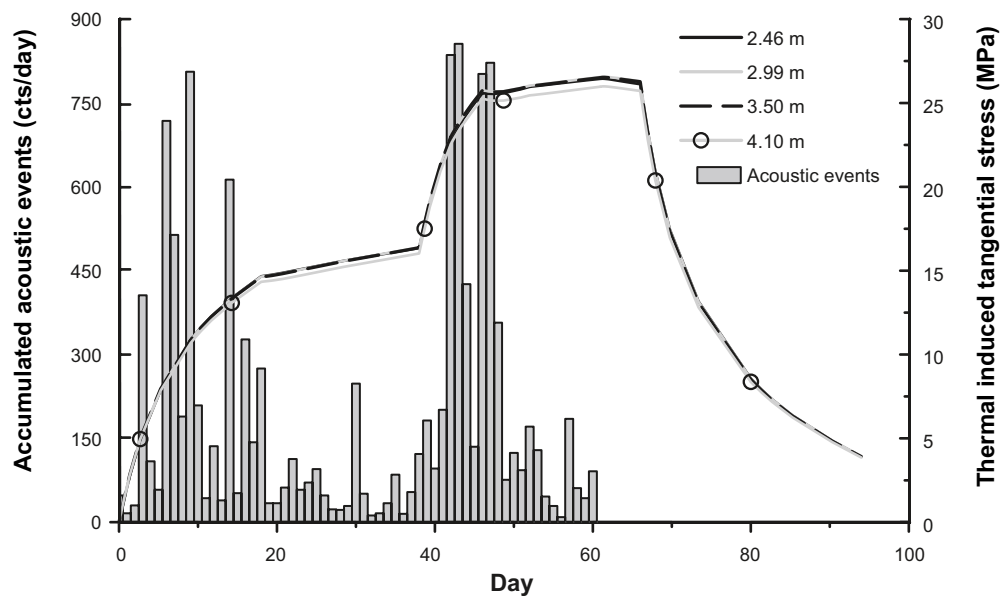


***Figure 7-6.*** *Thermally induced tangential stress close the four instrument levels and the associated daily acoustic events. The induced thermal stress is very similar between 2.46 m and 4.10 m. Note that the number of daily acoustic events increases when the stress increases. The reduction of the confining pressure began at day 61 and that part of the data set is not included.*

# 8    Yield strength

## 8.1    Stresses during excavation and heating

The main objective of the experiment was to establish the stress magnitude that triggered the onset of rock mass yielding, i.e. measurable damage. The excavation-induced stresses were determined using the three-dimensional boundary element program Examine3D (Rocscience). Figure 8-1 presents the excavation-induced modelled maximum tangential stress on the open surfaces of the experiment volume.

### 8.1.1    Excavation-induced stress

For this experiment it was important to devise a consistent method for estimating the stresses at specific locations. A general description of the stress calculations is given in Chapter 2. In numerical programs, such as Examine3D, the stress calculated at any point is related to the size of the element used in the stress calculation. It is well known that extreme stress gradients occur next to excavation boundaries, so it was important that the stresses determined at any location should not be significantly influenced by these stress gradients and the size of the element. Using the Kirsch solution for stresses around a circular opening under plane strain conditions, it was determined that if the excavation-induced stress was calculated at locations 3 mm from the boundary of the opening using an element size of 100 mm, the error was reduced to less than ~ 2.5%. This means that if the stress magnitude was calculated to be 100 MPa, the actual stress magnitude could be $100 \pm 2.5$ MPa.

The maximum tangential stress acting 3 mm into the pillar wall down to a depth of 6 m is shown in Figure 8-2. The stresses shown in Figure 8-2 were calculated 0.1 m to the left of the pillar centre. In designing the experiment, the tunnel axis was aligned approximately 6 degrees from the trend of $\sigma_2$, i.e. the tunnel axis was not perpendicular to the trend of $\sigma_1$. This resulted in the maximum tangential stress not being located in the centre of the pillar, but slightly to the left of the pillar centre when looking towards the end (face) of the tunnel (Figure 8-3). In the upper part of the pillar, the centre/deepest part of the v-shaped notch is located approximately 0.1 m to the left of the pillar centre, which is in agreement with the stress concentration at that location (Figure 8-3). At a depth of 3.5 m the v-shaped notch is not aligned exactly with the maximum stress concentration, and at 4.5 m depth the v-shaped notch is clearly not aligned with the stress concentration. These results would suggest that the orientation of the in situ stress tensor used in designing the experiment is probably not correct. An Examine3D
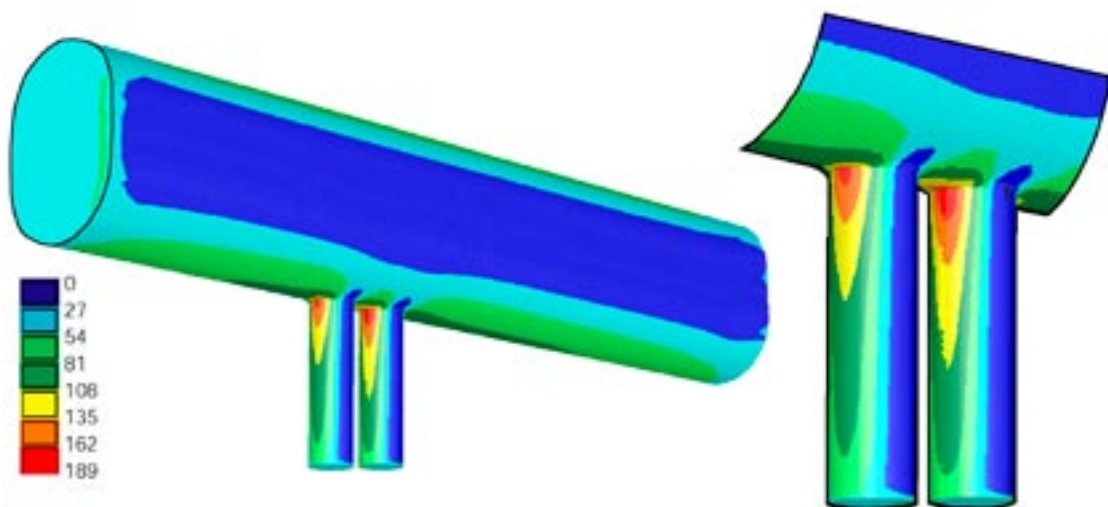


*Figure 8-1.* *The inner part of the APSE drift with the induced maximum tangential stress (MPa) on the surface.*

analysis was carried out with the stress tensor rotated so that the horizontal principal stresses has been rotated 10 degrees clockwise. Figure 8-3 also shows those results, and while there is better agreement between the location of the maximum stress concentration and the location of the v-shaped notch at depths of 3.5 and 4.5 m, the agreement is less at a depth of 2.0 m. It is clear from these data that if the v-shaped notch is solely stress–induced, the orientation of the stress tensor could be modified to produce the minimum error. But it is more likely that the inhomogeneity in the rock also affects the alignment with the notch. The stress tensor should therefore not only be adjusted to minimize the error with the actual breakout geometry. It was determined that the orientation error, which is probably less than ± 5 degrees in trend and plunge, does not significantly affect the stress magnitudes. There is therefore little reason for further back analysis of the stress tensor.

Figure 8-3 also shows the location of all the acoustic events recorded within ± 0.1 m of each presented depth. The acoustic emission events do not perfectly align with the v-shaped notch, except at a depth of 4.5 m. This was also reported by /Martin 1997/ and highlights the difficulty of associating individual seismic events with physical damage.

### 8.1.2    Stress path

The excavation of the boreholes bounding the pillar caused the stresses to redistribute. Because of this stress redistribution, stresses near the boundary of the excavation can change significantly depending on its geometry in relation to the orientation and magnitude of the far-field stress tensor. Examine3D was used to track the stress path for point A located 0.1 m to the left of the centre of the hole at a depth of 2 m and 20 mm into the pillar wall during the excavation phases. The stress path, which is plotted in Figure 8-4 in the $\sigma_1$, $\sigma_3$ space, was determined by excavating the first hole in three stages and then continuing with the second hole in five stages. The excavation of the first hole increased the minimum stress (Sigma 3), the intermediate stress (Sigma 2) as well as the maximum stress (Sigma 1). Hence, because the mean stress was increasing, the excavation-induced stresses associated with the first hole would not have caused any damage to the rock mass at the location of point A.

With the excavation of the second hole Sigma 3 decreases, and Sigma 2 and Sigma 1 increase. Hence, the deviator stresses are increasing while the mean stress is decreasing. From Figure 8-4 it is clear that there is significant unloading (sigma 3) and loading (Sigma 1) as the second hole is excavated.
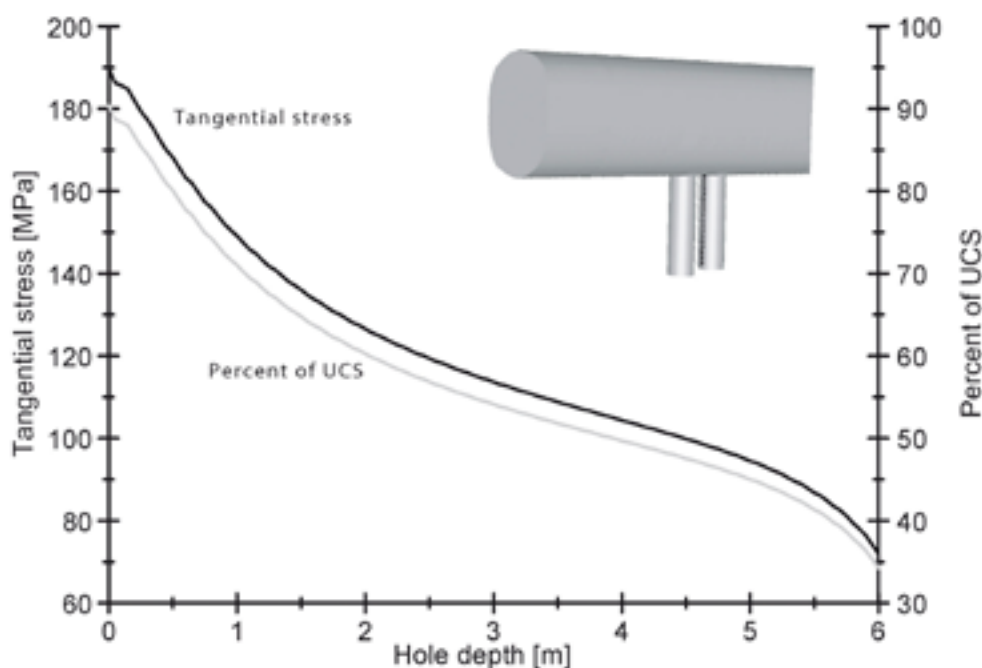


*Figure 8-2.* *Excavation induced tangential stress along the most stressed part of the pillar. The dashed line indicates where the stress is modelled slightly to the left of the pillar centre in the second hole, DQ0063G01.*
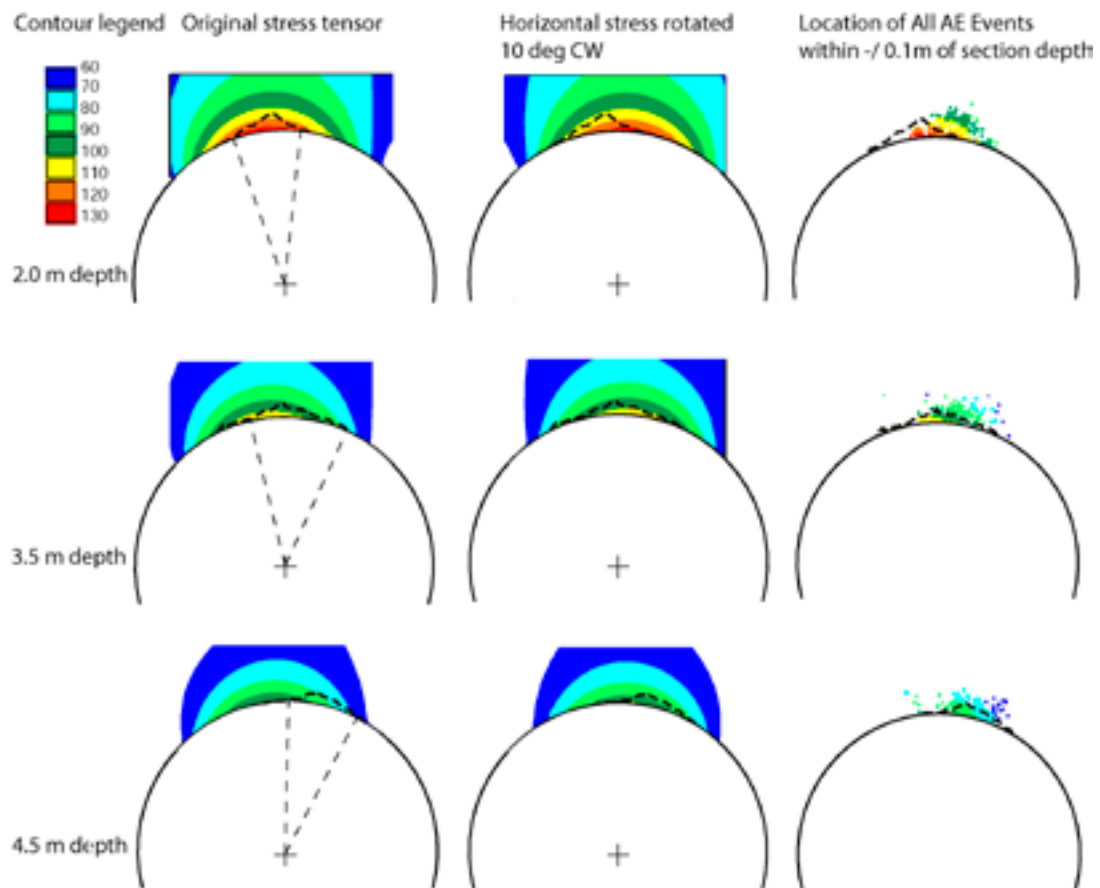
***Figure 8-3.*** *Maximum principal stresses on the boundary of the excavation determined using Examine3D for the stress tensor back-calculated in Chapter 2 and with the orientation of the stress tensor rotated 10 degree so that the major principal stress is trending 320 degrees. Also shown is the geometry of the v-shaped notch and the location of all the acoustic emission events located within ± 0.1 m of the presented depths.*



| | | |
|---|---|---|
| 1) In situ | S2, 15 MPa |
| 2) First hole 2.0 m | S2, 19 MPa |
| 3) First hole 4.0 m | S2, 19 MPa |
| 4) First hole complete | S2, 19 MPa |
| 5) Second hole 1.0 m | S2, 21 MPa |
| 6) Second hole 1.95 m | S2, 41 MPa |
| 7) Second hole 2.5 m | S2, 34 MPa |
| 8) Second hole 5.1 m | S2, 34 MPa |
| 9) Second hole completed | S2, 35 MPa |
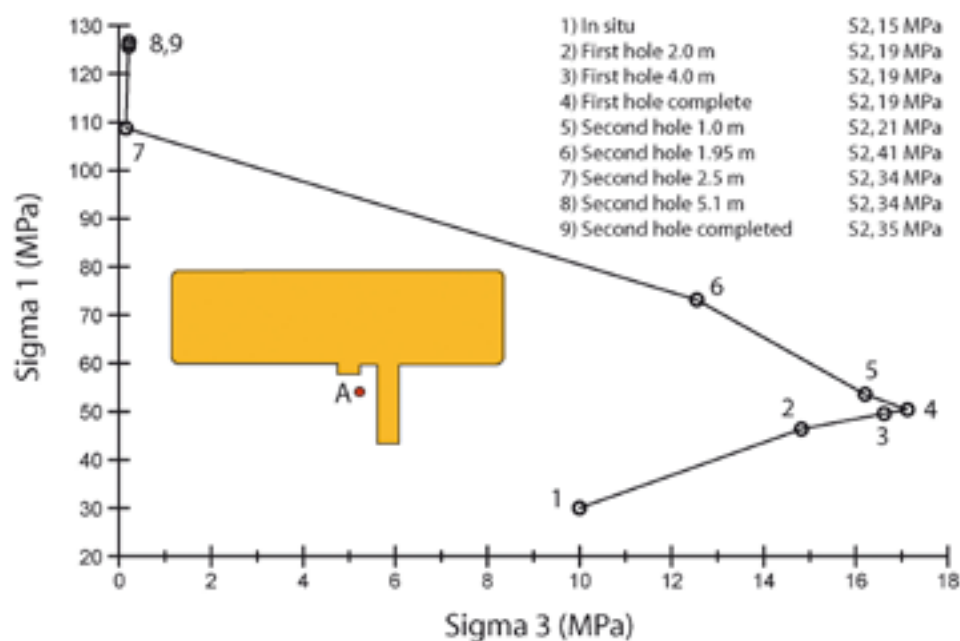
***Figure 8-4.*** *Stress path for point A located at a depth of 2 m close to the boundary of the second hole. Circles indicate the stress at the modelled excavation stages. Sigma 2 (S2 in figure) stresses are also provided for each excavation stage.*

### 8.1.3 Rock mass strength

The stress path experienced by the pillar as the boreholes were excavated indicated both loading and unloading processes. These processes may lead to the formation of an excavation-induced damaged zone. In hard rocks such as granite, the excavation damaged zone caused by excavation-induced stresses is typically referred to as brittle failure or "spalling". /Ortlepp 1997/ gave a detailed description of large-scale brittle failure observed in deep South African mines. For the pillar stability experiment, brittle failure is defined as the onset of small rock "chips" forming on the boundary of the excavation in the region of maximum tangential stress and is used here as the first visible indication of rock mass yielding. The "chips" range in size from smaller than a fingernail to approximately 0.1 m².

To be able to determine the onset of the excavation induced damage, i.e. the rock mass yield strength for the APSE, it was essential to determine the yielding location accurately and establish boundary conditions at the time the yielding occurred. The following sections describe how the onset of yielding (spalling) was determined.

### 8.1.4 Observations while excavaating the two large-diameter boreholes

As shown in Figure 8-2, the tangential stress on the wall of the large-diameter boreholes reaches a maximum at the collar of the borehole and gradually decreases with borehole depth. Hence, the excavation of the second hole will cause a gradual increase in the tangential stresses on the first hole as the second hole advances as shown in Figure 8-4. Once the 1.75-m-diameter holes were excavated they exposed a minor mylonitized shear zone cutting through the uppermost part of the pillar (Chapter 2). This healed shear zone was visible in the tunnel floor on the left side of the experimental volume and was located at a depth of approximately 1 m at the right part of the pillar. During the excavation of the second hole a localized area of overstressing initiated in the vicinity of the shear zone approximately 0.5 m below the borehole collar and propagated down to a depth of ~ 2 m (Figure 8-5).

The time and location of this overstressed area was clearly recorded by the AE monitoring system. The AE record shows that the part closest to a depth of 0.5 m was activated when the depth of the second hole was approximately 4 m (see Figure 8-4). The response at this stage was limited, however, and relatively few events were recorded (424 events in 96 h of monitoring). The night after the boring depth had reached 5.1 m, 60 AE events were recorded during the following 7 hours (no boring occurred during this period). When the hole was advanced to a depth of 6.1 m on the
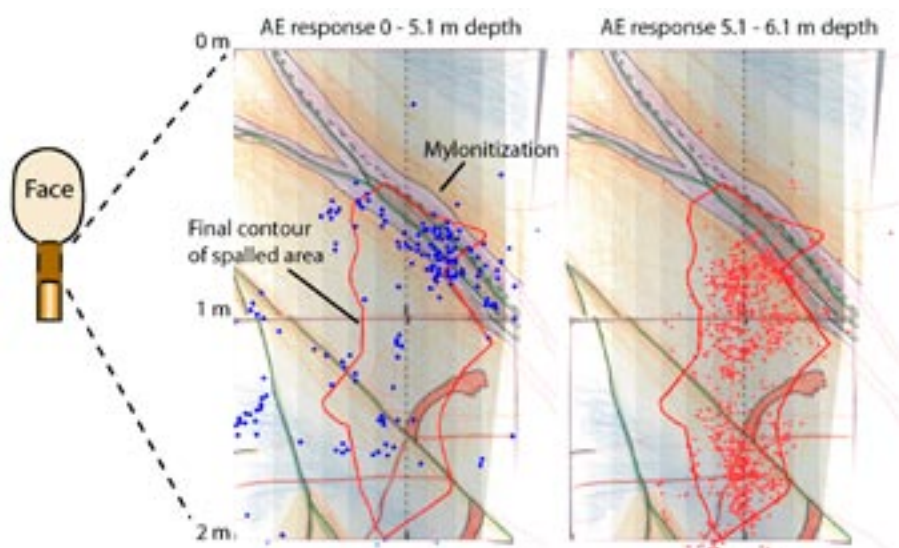


***Figure 8-5.*** *Acoustic Emissions on top of the geological mapping for the upper two metres of the second hole during excavation. Left: All AE events up until a hole depth of 5.1 m. Right: AEs after the hole depth had reached 6.1 m. The mylonitized shear zone is indicated in the upper part of the figures and the dashed line is the centre line of the pillar.*

following day, the AE activity suddenly increased throughout its entire 1.5-m length (~ 0.5-m to ~ 2-m depth). During a 7-hour monitoring period following drilling, the AE system recorded 310 events (Figure 8-5). The AE activity in this zone was then quite intense for a few days as the rock was overstressed. The tangential stress increase that caused the overstressing was approximately 1 to 2 MPa (Figure 8-4) as the hole was excavated from 5.1 m depth to its full depth of 6.2 m. Hence, a distinct stress level threshold needs to be reached before the rock yields.

During the boring of the large-diameter boreholes, AE events were only recorded ahead of the borehole bottom once. This occurred when the second hole was bored to a depth of approximately 0.8 m. Seventeen events were then source-located up to 0.1 m ahead of the bottom of the hole. These AE events were source-located in the vicinity of the weaker mylonitized shear zone intersecting the hole at that approximate depth (Figure 8-5). During all other monitoring periods, the AE events were located along the walls of the holes. During the excavation phase of the second hole, AE events never occurred below a depth 5.3 m, even though the final borehole depth was 6.2 m.

Three-dimensional stress modelling was used to determine the tangential stress at a depth of 5.3 m, which was the depth limit for the acoustic emissions in the open hole during the boring. At this depth there was no visible evidence of yielding, i.e. no chips had formed. The tangential stress 3 mm into the hole wall was calculated to be 91 MPa, corresponding to $0.43\sigma_c$. This would represent the lower bound for stress-induced damage. Three-dimensional stress modelling of different stages of the excavation indicates that the maximum stress magnitude immediately beneath the hole bottom is less than the $0.43\sigma_c$ that is required to cause the AE events in the hole walls. This explains why AEs were not recorded ahead of the borehole face (except for the few events in the mylonitic rock).

## 8.1.5    Observations during heating

Two methods were used to determine the time and location of spalling during heating: I) displacement monitoring using the LVDTs and II) visual observations of the pillar wall in the open hole. While the acoustic monitoring system was used to locate the seismic activity, there is no correlation of this seismic activity to the first signs of rock mass yielding. In addition, the first visible sign of damage was the formation of very thin rock flakes (about 10 mm in diameter), and because there is little energy released when these are formed it is possible that they were not detected. Greater reliance was therefore placed on the LVDT measurements and the visual observations then the AE system.

## 8.1.6    Yielding indicated by LVTDs

The LVDTs were installed to record radial deformations as yielding induced by the thermal stresses migrated down the pillar wall. All of the LVDTs placed near the centre of the pillar showed a radial expansion (i.e. pillar contraction) varying between 0.2 and 0.5 mm (Figure 8-6). As shown in Figure 8-6, the transition from contraction to dilation of the pillar, i.e. expansion of the rock mass, was rather abrupt and rapid. The onset of dilation indicated by the LVDTs is defined as the time the transducer is compressed more than its initial setting, the "0" value. The procedure for picking the first yielding occasion is also shown in Figure 8-6. In most cases the yielding time was quite obvious.

The return to the "0" value for determination of the onset of dilation was chosen because of its correlation to physical damage. When the hole was inspected during the expansion of the LVDTs, no damage was visible. It was not until compression of the LVDTs started that physical damage close to them was noted. The rock surface then looked similar to the points were visual observations of spalling were made. This means that basically the same type of damage is compared in the two different observation methods.

Attempts to back-calculate the compression of the transducers are described in Appendix 2d. The calculations could only reproduce ~ 10% of the radial expansion measured.
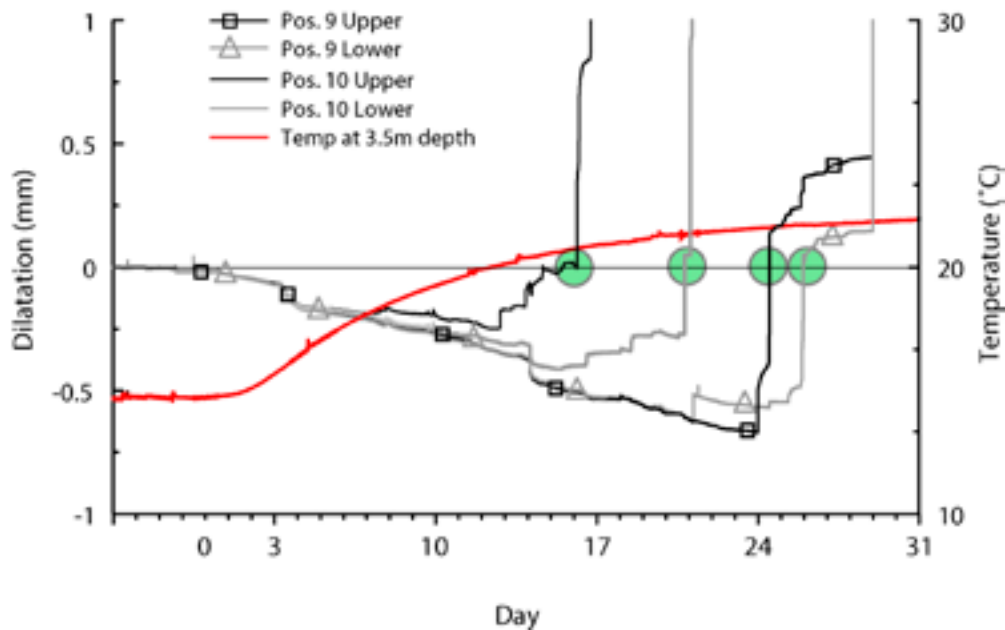
**Figure 8-6.** *Displacement records at 3 m depth. Circles indicates when the transducers were compressed more than their initial setting. The negative displacements are an elastic radial expansion of the hole preceding the brittle failure. The measured temperature at the hole wall approximately 0.5 m below the LVDTs is also given.*

### 8.1.7 Visually observed yielding

Yielding was defined to have occurred when small (fingernail-sized) rock chips formed on the surface of the hole. These locations together with the fracturing were mapped during the inspections in the hole. Locations of yielding could be determined by visual observations of the rock wall, but could not be used to determine the exact time of the occurrence of yielding since the yielding could have taken place at almost any time between two hole visits. The precise temperature-induced stress when the spalling occurred is therefore not known. However, the rate of temperature increase was quite low. The stress change due to temperature changes between two inspections is estimated to be only 2 MPa. Hence the uncertainty in the stress magnitudes associated with visually observed yielding is quite small, less than 2% of the maximum tangential stress.

The locations of yielding determined by the LVDTs and the visual inspections are numbered sequentially in Figure 8-7 on top of the geological mapping. The numbers were assigned in the order spalling took place. For example, number 10 in Figure 8-7 shows the location of the tenth observed spalling area. As can be seen, most of the points occur in chronological order with respect to depth, reflecting the yielding of the rock mass as the temperature increased and the migration of the yield surface down the borehole. The only real outliers are numbers 13, 14 and 15, and these are described later. These three points have not been used to estimate the mean stress magnitude associated with spalling.

### 8.1.8 Time dependency

Yielding was observed during the excavation of the 1.75-m-diameter holes and during the heating phase of the experiment. After the excavation of the first 1.75-m-diameter hole, spalling was observed at two isolated locations. It appeared that these locations were related to localized weak zones in the rock mass. The spalling in the second hole occurred in one area. The spalling in that area was initiated at the end of the boring of that hole and occurred at a calculated stress increase of only 1 MPa, Figure 8-4.

During the heating phase the yielding occurred as the tangential stresses increased. Often the yielding would occur by a start/stop manner. For example, nothing would happen for a while until and then suddenly spalling would occur and last for a few minutes. The intermittent spalling resembled the build-up and release of stress. Very few acoustic emission events were recorded in between the spalling occasions. The acoustic emission frequency was clearly lower for those periods when the thermally induced stress increase was nearly constant, Chapter 7.

96
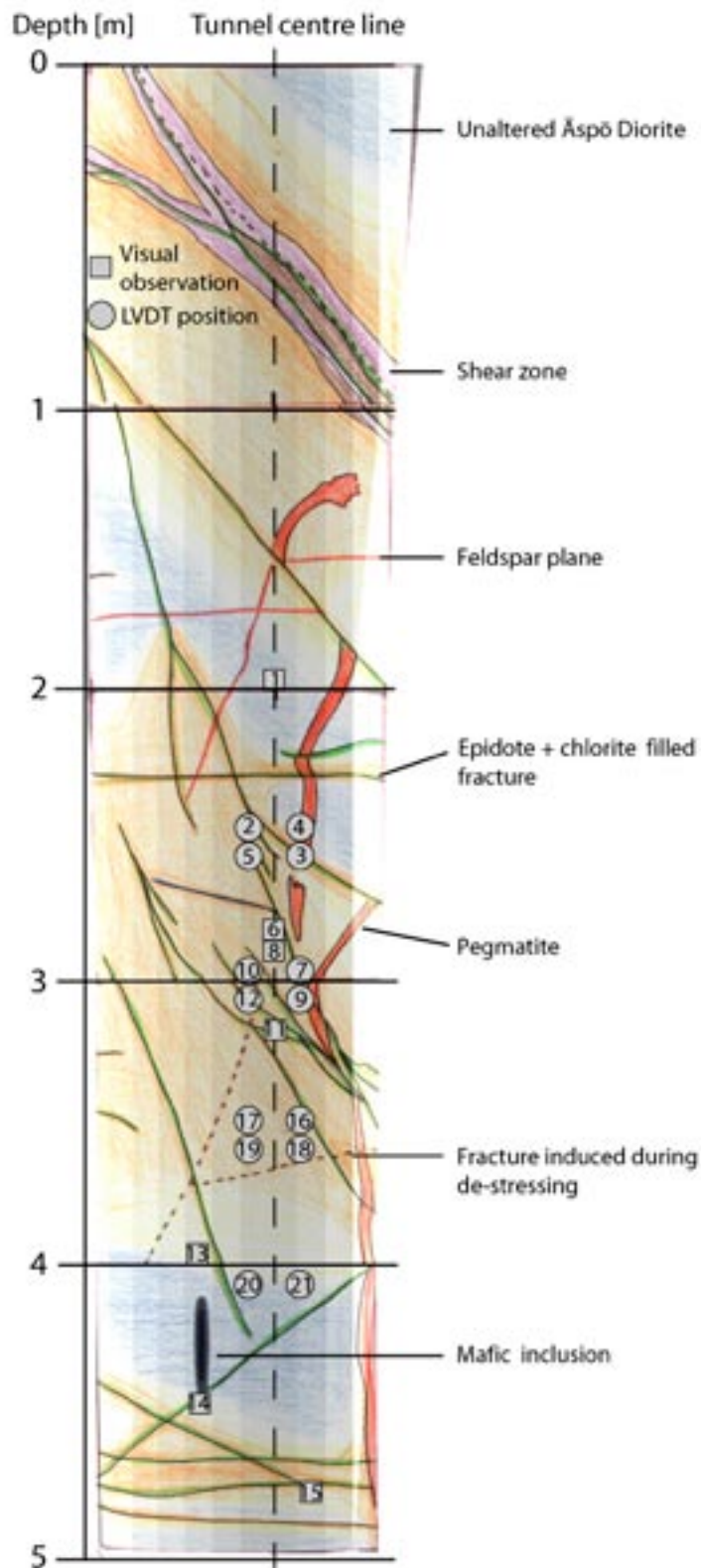
**Figure 8-7.** *Illustration of the yielding locations numbered in the order they occurred placed on top of the geological mapping. Circles indicate LVDT positions and squares visual observations.*

The observations made during the excavations and the heating of the pillar clearly indicate that there is no significant time dependency involved in the spalling process. It is not enough that the stress is close to the spalling strength for a long period of time. The spalling strength has to be exceeded before something happens. This is illustrated in Figure 8-6 where the deformations suddenly increase even though the temperature increase is very small.

## 8.2    Rock mass yield strength

The rock mass yield strength is defined in this paper as the tangential stress 3 mm into the pillar at a point where yielding of the rock mass was clearly identified. As described earlier, yielding is defined as the onset of dilation as recorded by the LVDTs, or the visual observation of small rock chips on the rock wall. The total stress acting at these locations when yielding commences can be estimated by adding the excavation-induced stress to the thermally induced stress. The total tangential stresses in the pillar for points 2, 10, 17 and 20 (Figure 8-7) are shown in Figure 8-8.

The rock mass yield strength for all the points monitored is shown in Table 8-1 as both total tangential stress magnitude and a ratio to the laboratory uniaxial compressive strength (UCS). The mean stress associated with yielding is 125 MPa with a standard deviation of 6 MPa. When expressed as a ratio to the UCS, the mean yield stress is $0.59\sigma_c$, with a standard deviation of $0.03\sigma_c$.

The pillar consists of Äspö diorite with varying degrees of oxidation. Based on laboratory tests, the oxidation does not appear to have any affect on the compressive strength of the rock. The oxidation is most noticeable in the vicinity of the mylonite zone. The rock type for most of the spalling points is Äspö diorite, with the exception of points 14 and 15. Point 14 is located in a greenstone inclusion and point 15 is located in a weakened part of the rock.

The majority of the spalling points, 12 points, are located in fresh diorite. Five of the points ( 3, 4, 8, 11 and 21) are located at or close to pegmatite veins. The other four locations are adjacent to mylonitizations (7, 13 and 15) or in one case a greenstone inclusion (14).

There is fresh diorite at point 13, but the point is adjacent to a small expansion bolt mounted in the rock wall. It is likely that the 10-mm-diameter holes drilled for these bolts concentrate stresses in this small area. No attempt was made to account for this additional stress concentration.

The spalling depth for the greenstone inclusion in point 14 was deeper than for the surrounding rock. At the time of the spalling observation for point 14, only the greenstone had failed with the surrounding diorite remaining intact. Laboratory testing of the greenstone indicates that it is slightly stiffer, ~ 7% more so /Rhén et al. 1997/ than the diorite. An embedded stiffer material attracts stress, and this stiffness contrast may have been sufficient to initiate yielding in the greenstone. The rock mass spalling strengths for points 13 and 14 are, however, within the standard deviation of the mean rock mass spalling strength.
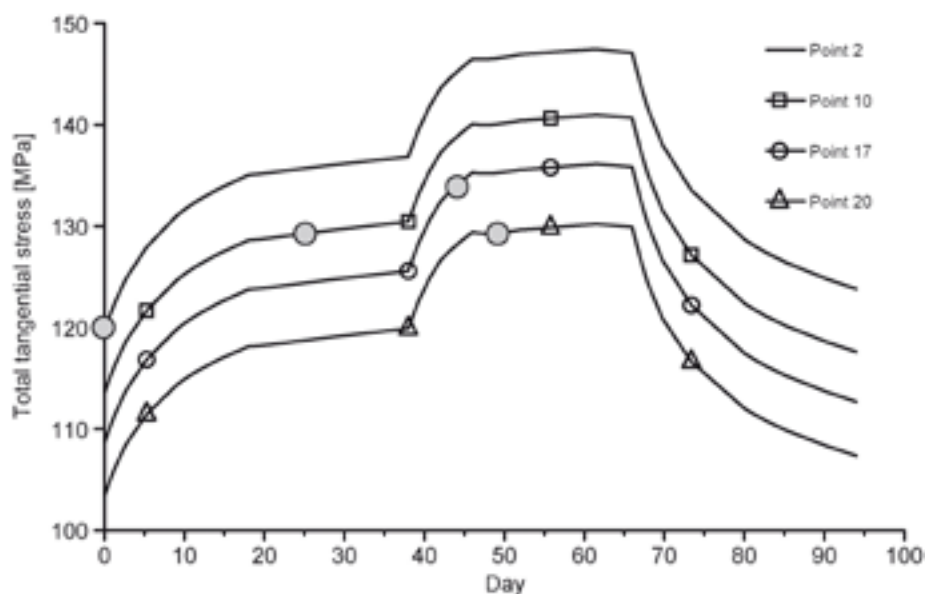


***Figure 8-8.*** *Total tangential stress for four instrument locations in the pillar. Filled grey circles indicate the time of yielding and hence the yield strength for that point.*

**Table 8-1. Yield stress and geology for each of the spalling points.**

| Point # | Depth (m) | Yielding stress (MPa) | Yielding stress in % of $\sigma_c$ | Geology |
|---------|-----------|------------------------|--------------------------------|---------|
| 1 | 1.96 | 127 | 60 | Fresh |
| 2 | 2.46 | 120 | 57 | Fresh |
| 3 | 2.52 | 114 | 54 | Fresh, end pegmatite vein |
| 4 | 2.46 | 116 | 55 | Fresh, pegmatite vein |
| 5 | 2.52 | 124 | 59 | Fresh |
| 6 | 2.9 | 128 | 61 | Fresh |
| 7 | 2.99 | 119 | 56 | Fresh, touches mylonite |
| 8 | 2.95 | 129 | 61 | Fresh, little pegmatite |
| 9 | 3.07 | 119 | 57 | Fresh |
| 10 | 2.99 | 129 | 61 | Fresh |
| 11 | 3.20 | 128 | 61 | Fresh, little pegmatite |
| 12 | 3.07 | 128 | 61 | Fresh |
| 13* | 3.95 | 117 | 56 | Fresh, close to thin mylonite. Close to bolt |
| 14* | 4.50 | 111 | 53 | Greenstone inclusion, |
| 15* | 4.80 | 93 | 44 | Oxidized, mylonitic, close to pre-existing fracture |
| 16 | 3.50 | 124 | 59 | Fresh |
| 17 | 3.50 | 133 | 63 | Fresh |
| 18 | 3.58 | 125 | 59 | Fresh |
| 19 | 3.58 | 133 | 63 | Fresh |
| 20 | 4.10 | 129 | 61 | Fresh |
| 21 | 4.10 | 119 | 57 | Fresh, close to vertical pegmatite vein |
| **Mean values ± Std** | | **125 ± 6** | **59 ± 3** | |

\* Point is not used when the mean value of the spalling strength is calculated.

## 8.3 Correlation to laboratory strength

Seven uniaxial compressive strength tests and eight triaxial compressive strength tests were carried out on samples taken form the experiment volume using the procedures recommended by the ISRM, /Brown 1981/ and /Hakala and Heikkilä 1996/. During testing, the unconfined and confined samples were monitored using lateral and axial strain gauges, and the unconfined samples were also monitored using an acoustic emission detection system. The stress magnitudes associated with crack initiation and volumetric strain reversal plus the peak strength were determined for each sample using the methodology first proposed by /Brace et al. 1966/. The crack initiation stress was determined using both strain gauges and counting of acoustic emission events. Five of the UCS samples were taken within 1 to 2 m of the pillar location. Axial stress for these samples is plotted against axial and radial strain in Figure 8-9, and a summary of the laboratory results is given in Table 8-2.

**Table 8-2. Results from uniaxial compressive strength tests on cores from the experiment. Grey rows indicate unstable tests that were not used in the evaluation.**

| Sample | AE $\sigma_{ci}$ (MPa) | $\sigma_{ci}$ (MPa) | $\sigma_{cd}$ (MPa) | $\sigma_c$ (MPa) | E GPa | v – | AE $\sigma_{ci}/\sigma_p$ | Strain Gauges $\sigma_{ci}/\sigma_p$ | $\sigma_{cd}/\sigma_p$ |
|--------|------------------------|---------------------|---------------------|------------------|-------|-----|---------------------------|--------------------------------------|------------------------|
| KQ0064G01 – 6.26 | 135 | 89 | 189 | 222 | 73.6 | | 0.61 | 0.40 | 0.85 |
| KQ0065G01 – 7.37 | 80 | 92 | 187 | 187 | 76.3 | 0.25 | 0.43 | 0.49 | 1.00 |
| KQ0065G01 – 5.29 | 130 | 112 | 213 | 244 | 78.1 | 0.26 | 0.53 | 0.46 | 0.87 |
| KQ0065G01 – 5.43 | 100 | 101 | 215 | 237 | 76.8 | 0.28 | 0.42 | 0.42 | 0.91 |
| KQ0064G07 – 4.99 | 160 | 89 | 190 | 190 | 74.1 | 0.28 | 0.84 | 0.47 | 1.00 |
| KA3376B01 – 33.32 | – | 87 | 172 | 195 | 67.4 | 0.27 | – | 0.45 | 0.88 |
| KA3376B01 – 61.58 | 100 | 87 | 186 | 203 | 68.8 | 0.28 | 0.49 | 0.43 | 0.92 |
| KQ0064G07 – 5.38 | 50 | – | 56 | 132 | 72.8 | 0.27 | 0.38 | – | 0.43 |
| KA3376B01 – 61.72 | 70 | 50 | 85 | 85 | 74.0 | 0.21 | 0.83 | 0.59 | 1.00 |
| **Average** | **118** | **94** | **193** | **211** | **73.6** | **0.27** | **0.56** | **0.45** | **0.92** |
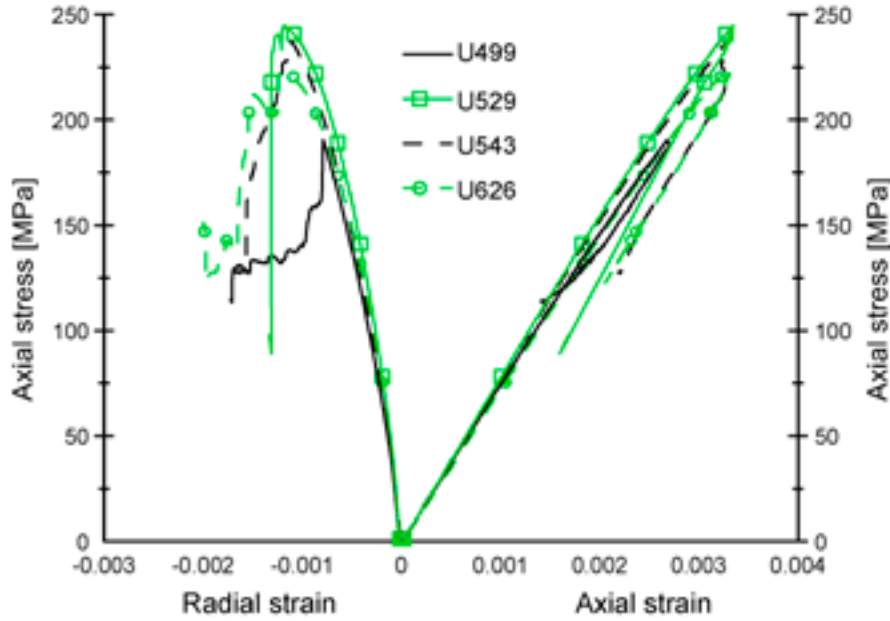
**Figure 8-9.** *Radial and axial strain plotted against axial stress for five uniaxial compressive test samples taken close to the pillar. The samples responded uniformly, indicating a very homogenous rock mass.*

Using the methodology suggested by /Martin and Chandler 1994/, crack volumetric strain reversal was used as an indicator of the crack initiation stress. To calculate the crack volumetric strain, the elastic volumetric strains, $\varepsilon_{v,e}$ (Equation 2) are subtracted from the total measured volumetric strains $\varepsilon_v$ (Equation 1). $\nu$ corresponds to Poisson's ration, E to Young's modulus and $\sigma_1$ to the axial stress. Since only uniaxial compressive tests are compared the $\sigma_3$ term is 0.

$$\varepsilon_v = \frac{\Delta V}{V} \approx \varepsilon_{axial} + 2\varepsilon_{lateral} \qquad \text{(Equation 1)}$$

$$\varepsilon_{v,e} = \frac{\Delta V}{V_{elastic}} = \frac{1-2\nu}{E}(\sigma_1 - \sigma_3) \qquad \text{(Equation 2)}$$

Figure 8-10 indicates the crack volumetric strain and suggests that crack initiation ranges from 89 to 112 MPa, with a mean value of 94 MPa.
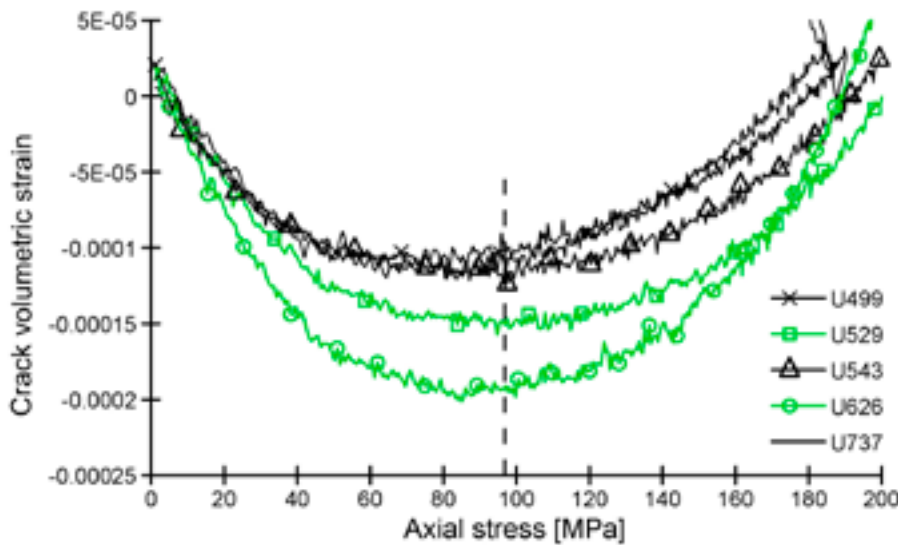


**Figure 8-10.** *Axial stress versus volumetric strain for five uniaxial compressive tests performed on cores from the experiment volume. The vertical dashed line indicates the mean stress for the crack volumetric strain reversal.*

100

As can be seen in Table 8-2, the strain gauges gave a mean crack initiation stress value of $0.45\sigma_c$ while the acoustic method gave a mean crack initiation stress value of $0.56\sigma_c$. Figure 8-11 shows the number of AE events versus axial stress for the uniaxial tests. As noted by /Eberhardt et al. 1998/, it is sometimes difficult to simply use the number of acoustic emission events as an indicator of crack initiation due to the fact that the large number of events associated with spalling masks the subtle change that occurs with crack initiation. Nonetheless, the AE events clearly indicate damage to the uniaxial samples in the pre-peak region between stress magnitudes of 80 and 160 MPa.

Figure 8-12 shows the failure envelope for Äspö diorite and the linear best-fit crack initiation stress based on the strain gauge data. The crack initiation stress has also been determined for triaxial tests, and the slope of this best-fit crack initiation stress locus has been determined by a least-squares approximation to be:

$$\sigma_1 = 0.44\sigma_c + 2.17\sigma_3 \qquad \text{(Equation 3)}$$
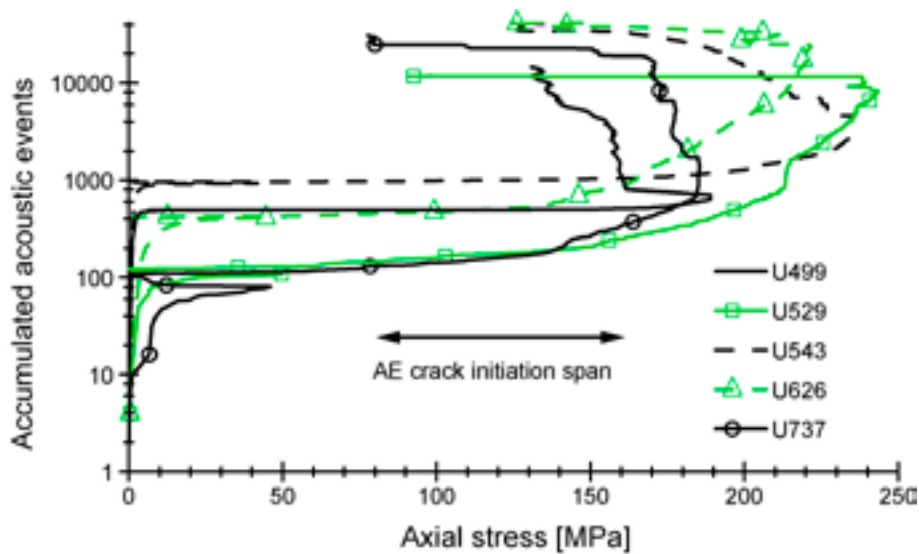


**Figure 8-11.** *Accumulated acoustic events plotted against axial stress during uniaxial compressive testing of the five samples. The crack initiation span for the samples is between 80 and 160 MPa with a mean value of 120 MPa. Acoustic emissions occurring below axial stresses of 50 MPa stem from settling of the testing equipment and are not used in the evaluation.*
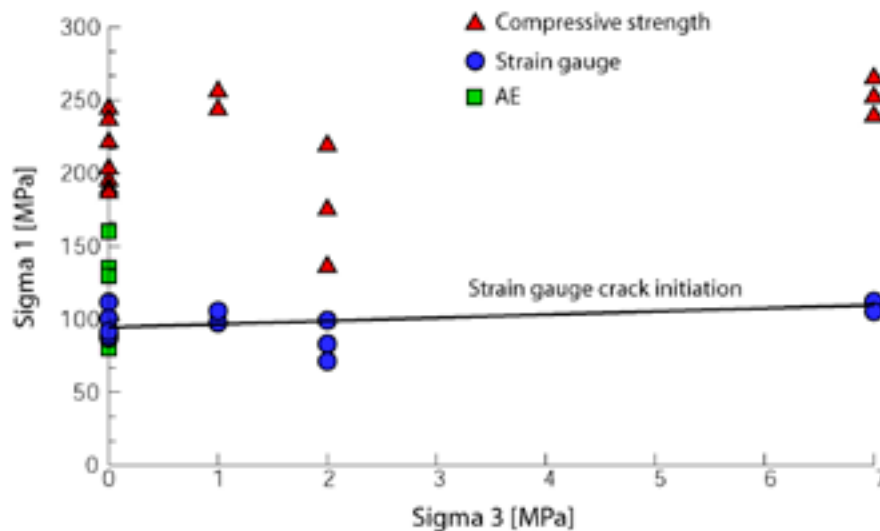


**Figure 8-12.** *Failure envelope for the test specimens taken in the experiment volume. The crack initiation stress determined using the AE and volumetric strain reversal methods is also included.*

Equation 3 is in keeping with the findings of other researchers. For example, /Scholz 1968, Holcomb and Martin 1985, Pestman and Van Munster 1996/ studied crack initiation in granite, sandstone, and marble using acoustic emission techniques. Their results indicate that, for confined conditions, the damage-initiation surface, in σ1– σ3 space, can be approximated by:

$\sigma_1 = 0.4\sigma_c + (1.5 \text{ to } 2)\sigma_3$

As previously described, numerical modelling of the excavation of the large-diameter holes in combination with the in situ AE records indicated that AE events were initiated in the rock mass when the tangential stress exceeded $0.43\sigma_c$. This threshold value is approximately the same as the mean crack initiation stress determined using the strain gauges on the laboratory samples. It is also similar to the findings reported by /Martin 1997/ and may represent a conservative stress magnitude for the onset of stress-induced damage in the Äspö diorite rock mass.

## 8.4    Extension strain

/Stacey 1981/ noted that the onset of fracturing in brittle rock could be determined using the critical extension strain. Stacey defined the critical extension strain as: Fracture of brittle rock is initiated when the total extension strain in the rock exceeds a critical value which is characteristic for that rock type.

Stacey suggested that the critical extension strain could be determined from laboratory tests by plotting axial versus radial strains. Stacey suggested that a small change in the curve's slope could be interpreted as axial macro scale fracturing in the samples.

Laboratory results from the APSE are plotted in Figure 8-13 as axial stress versus radial strain. It can be seen from the curves in Figure 8-13 that the slope changes slightly when the radial strain is 0.0001 and the axial strain is 0.0005. This is the point on the stress-strain curve that corresponds to the critical extension strain defined by Stacey. These values correspond to an axial stress of 40 MPa or $0.2\sigma_c$. This value is close to Stacey's findings for quartzite and approximately half of the reported critical extension strain value for diabase.

The stresses determined at the spalling locations were also used to calculate the extension strain at those points. These strains were compared to the results from the UCS tests shown in Figure 8-9. The objective was to correlate the strains at rock mass yielding to the strains and associated stresses in the laboratory tests.
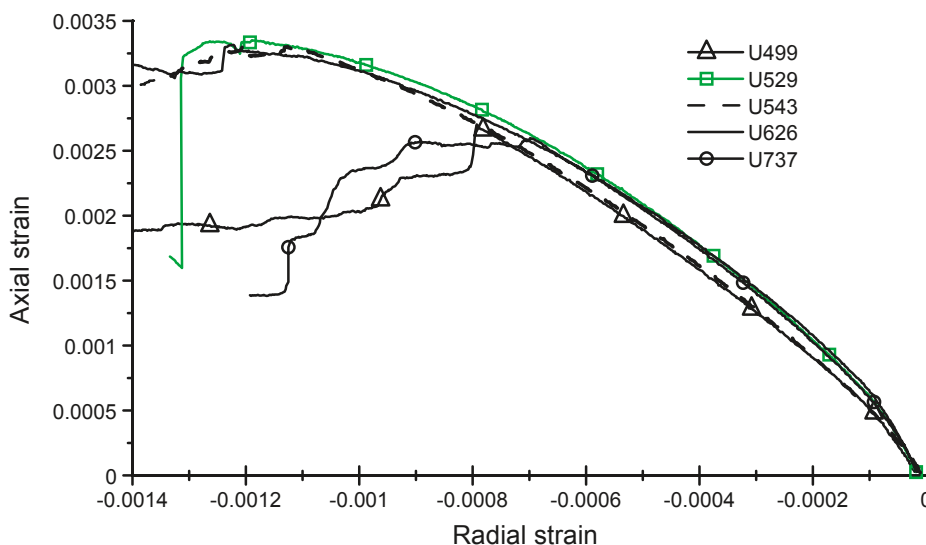


***Figure 8-13.*** *Axial versus radial strain for five uniaxial compressive tests performed on cores from the experiment volume.*

Hook's generalized law (Equation 4) was used for the strain calculations. Young's modulus (E) and Poisson's ratio (ν) determined on intact core samples were used in the equation:

$$\varepsilon_3 = \frac{1}{E}\left[-\Delta\sigma_3 + \nu\left(\Delta\sigma_1 + \Delta\sigma_2\right)\right]$$
(Equation 4)

where $\varepsilon_3$ is the strain in the direction of the least principal stress and $\Delta\sigma_1$, $\Delta\sigma_2$ and $\Delta\sigma_3$ are the changes in principal stress from the in situ condition (in situ stress subtracted from total stress). The conceptual model is a rock block strained by the in situ stresses. The stresses are then changed to the state calculated at the time of yielding and the corresponding strains determined. The difference in strain between these two stress states is presented in Table 8-3. The direction of $\varepsilon_3$ is into the open hole since $\sigma_3$ is zero on the border of the hole. According to Table 8-3, the mean value of the back-calculated strains where the in situ spalling occurred is 0.00049. This strain is almost five times greater than the strain defined as the critical radial strain in Figure 8-13. In fact, the curve is nearly a straight line at this strain.

**Table 8-3. Radial strain at the spalling points calculated from the spalling strength stresses.**

| Point | mStrain | Point | mStrain |
|-------|---------|-------|---------|
| 1 | 0.52 | 12 | 0.52 |
| 2 | 0.49 | 13* | 0.47 |
| 3 | 0.46 | 14* | 0.45 |
| 4 | 0.47 | 15* | 0.38 |
| 5 | 0.51 | 16 | 0.49 |
| 6 | 0.52 | 17 | 0.53 |
| 7 | 0.48 | 18 | 0.50 |
| 8 | 0.52 | 19 | 0.53 |
| 9 | 0.48 | 20 | 0.52 |
| 10 | 0.52 | 21 | 0.47 |
| 11 | 0.52 | | |
| | **mean 0.49** | | |

* Point not included in calculation of mean value.

## 8.5    Discussion

By combining the acoustic records with three-dimensional stress modelling at various stages of the excavation, a relationship between stress and AE initiation was established. Acoustic events were initiated when the tangential stress exceeded 43% of the uniaxial compressive strength. Back calculations of the observations of spalling during the heating phase indicated that the tangential stress required to initiate spalling had to exceed $0.59\sigma_c$. These results are in close agreement with findings from the Mine-by Experiment reported by /Martin and Read 1996/. The fact that the findings from the Mine-by test tunnel in massive unfractured Lac du Bonnet granite are similar to findings from the Äspö Pillar Stability Experiment suggests that local moderate fracturing and heterogeneity does not significantly affect the spalling strength.

It has been shown that the crack initiation stress in laboratory samples provides a reasonable, lower-bound approximation for the rock mass spalling strength in the absence of in situ data. However, determining the crack initiation stress is not simple. A great deal of care must be exercised in using either strain gauges or acoustic emission technology. For the APSE, the strain gauges provided more consistent data and appeared to correlate with the stress level associated with the onset of AE events in situ.

It was not possible to establish a reliable critical extension strain from laboratory axial versus lateral strain curves. The methodology suggested by Stacey gave a spalling strength of 40 MPa. The methodology appears to be too conservative for the Äspö diorite.

The spalled volume and the notch depth compiled for the 50 mm sections obtained from scanning are shown in Figure 8-14. When normalised to the hole radius, the notch depth ranges between 1.07a to 1.15a, where $a$ is the initial hole radius. The mean value between 1 to 4 m depth is 1.1a. A correlation between notch depth and the ratio of the maximum tangential stress and the uniaxial compressive strength for granitic rock is given in /Martin et al. 1997/. APSE data are plotted together with these results in Figure 8-15, and the APSE data fit the relationship derived by Martin quite well.
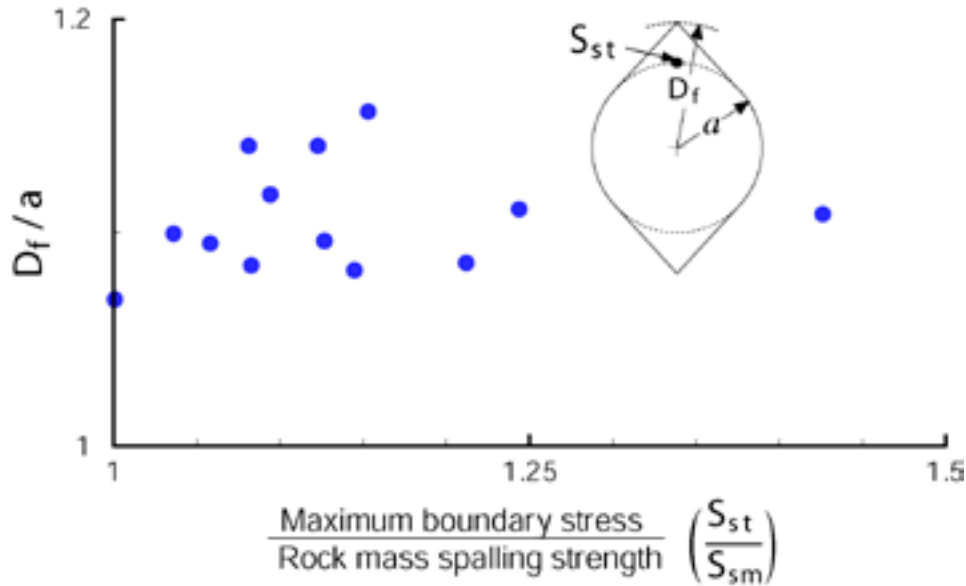


**Figure 8-14.** *Relationship between depth of yielding and maximum tangential stress for the APSE pillar.*
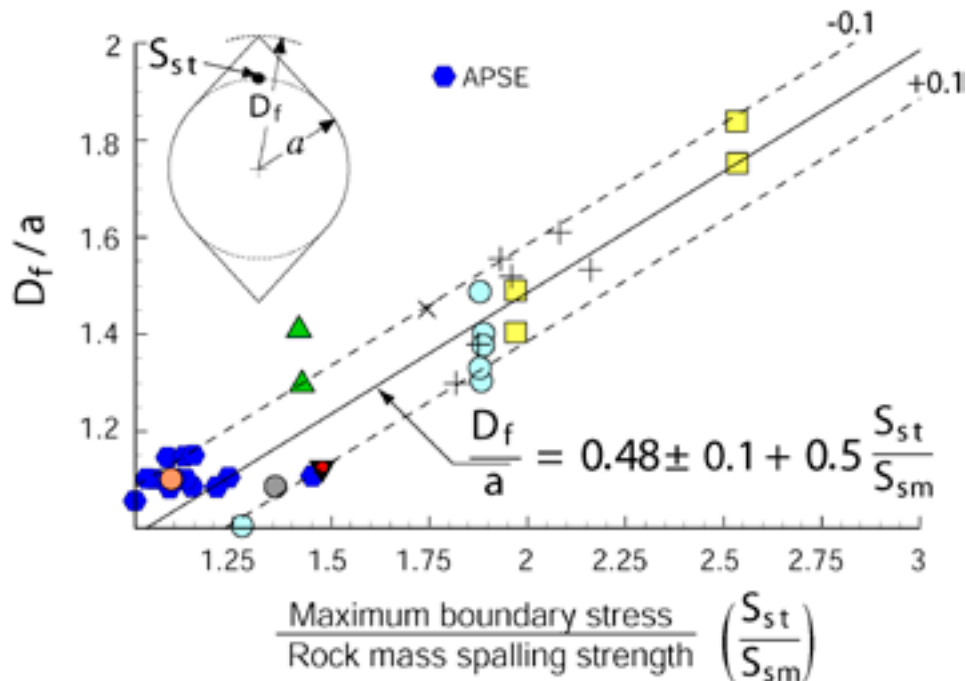


**Figure 8-15.** *Relationship between depth of yielding and maximal tangential stress at the boundary of the opening. Modified from /Martin et al. 1997/.*

# 9 Effect of confinement

During the drilling of the first hole (DQ0066G01) that was later confined, yielding occurred in weak, altered, parts of the hole wall located relatively close to the most stressed zone of the hole. The confinement equipment required a smooth hole wall to work against. Cavities in the hole wall would cause the rubber bladder to deform and be punctured. To avoid this, the cavities caused by yielding were filled. In the upper part of the pillar where water leakage was low, a cement mixture was used. A thin steel mesh had to be put up in those cavities as reinforcement to hold the cement during curing. The mesh was fastened with short bolts drilled a few centimetres into the rock wall. In the lower part of the hole, where the water inflow was more intense, another technique was used. Steel plates, Figure 9-1, were bolted against the rock wall with approximately 5 cm long bolts drilled into the rock wall. The volume behind the plates was filled with sand.

The patching of the hole wall has of course affected the rock. However, the cement is much weaker than the rock and the steel plates are deformable. The patching techniques used should therefore have a very limited effect on the rock response immediately adjacent to the patching locations.

## 9.1 Monitoring and observations

The confinement pressure was monitored during the entire experiment and should always exceed 700 kPa but never 800 kPa above atmospheric pressure. The 800 kPa restriction was the pressure the equipment had been tested and approved for. The temperature increase of the water in the bladder resulted in a volumetric expansion of the water. Since the bladder's volume is fixed, the volumetric change will increase the confinement pressure as the temperature rises. Water was therefore manually tapped from the bladder to keep the pressure below 800 kPa. The confinement pressure and the temperature at a depth of 3.5 m in the confined hole is shown din Figure 9-2.



*Figure 9-1. Photograph of steel plates bolted to the hole wall.*

At the planning stage of the experiment it was decided that when the spalling had propagated far enough down the hole and the temperature and AE frequency had reached a steady state the confinement pressure should be released in 50 kPa decrements. In early July the temperature at the hole wall had started to level out, as had the temperature between the heaters, Figure 9-3. The figure also indicates that the AE frequency had stabilized at a relatively low level at the same time. It was decided that a steady state had been reached and that the confinement pressure could be reduced. This work was commenced on July 14 (day 61).
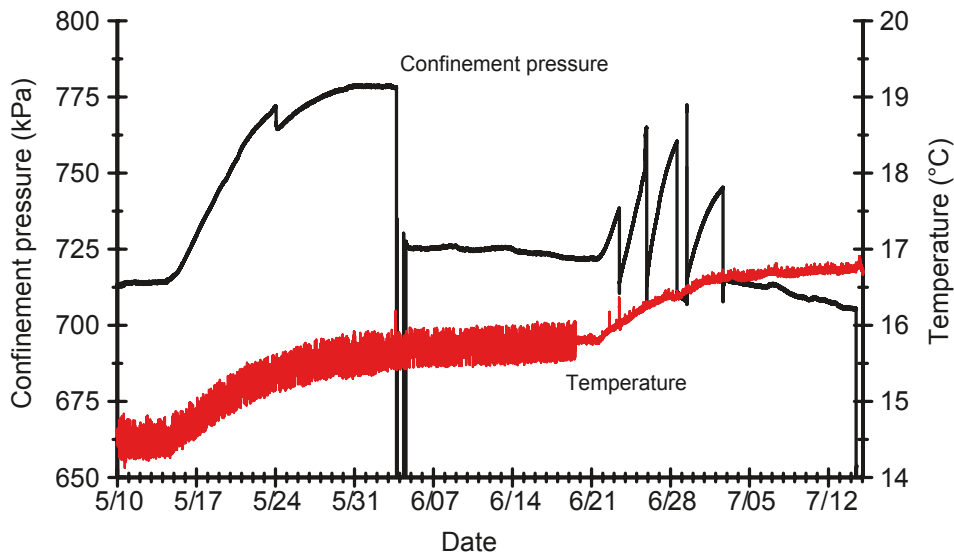


*Figure 9-2.* *Confinement pressure and temperature. The pressure drop on day 21 is not real. The pressure transducer was removed to seal a small leak in a valve. The pressure was maintained at approximately 725 kPa during the entire experiment.*
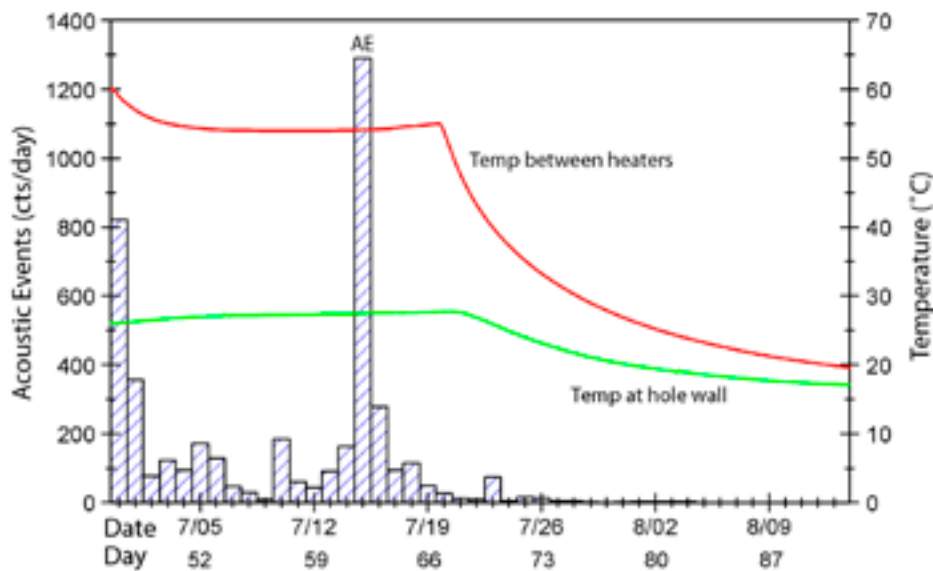


*Figure 9-3.* *Acoustic frequency in counts per day in relation to the temperature between the left heaters and at the pillar wall at a depth of 3.5 m. The confinement pressure was released on July 14 and 15.*

## 9.2    Release of confinement

The first 50 kPa decrement of the confinement pressure was done at around noon at July 14. There was no response in the rock that was detected by the acoustic system and there were no displacements. Another six decrements were done that day, leaving the pressure at approximately 350 kPa above the atmospheric pressure overnight. The pressure reduction times are listed in Table 9-1. Note that only the main pressure drops are listed in the table. Figure 9-4 shows the complete record for pressure release and acoustic emission. The elasticity in the system made it necessary to release small additional volumes of water to prevent the pressure from increasing too much in between the 50 kPa pressure drops.

After a night with very little acoustic activity the next 50 kPa drop was done on the morning July 15, and not much happened. The next pressure drop down to 250 kPa triggered both AE and displacements of the transducer at position 22. A more detailed presentation of AE and the confinement pressure is shown in Figure 9-5. Figure 9-6 shows the monitoring results from the transducers that indicated displacement during the pressure drop.

**Table 9-1.  Date and time of the pressure drops. The times for minor adjustments within the pressure intervals are not included.**

| Pressure [kPa] From – To | Date and time |
|---|---|
| 700–650 | July 14, 10.35 |
| 650–600 | July 14, 11.40 |
| 600–550 | July 14, 13.10 |
| 550–500 | July 14, 14.14 |
| 500–450 | July 14, 15.19 |
| 450–400 | July 14, 16.18 |
| 400–350 | July 14, 17.17 |
| 350–300 | July 15, 08.26 |
| 300–250 | July 15, 10.29 |
| 250–200 | July 15, 12.53 |
| 200–150 | July 15, 16.20 |
| 150–0 | July 15, 21.06 |
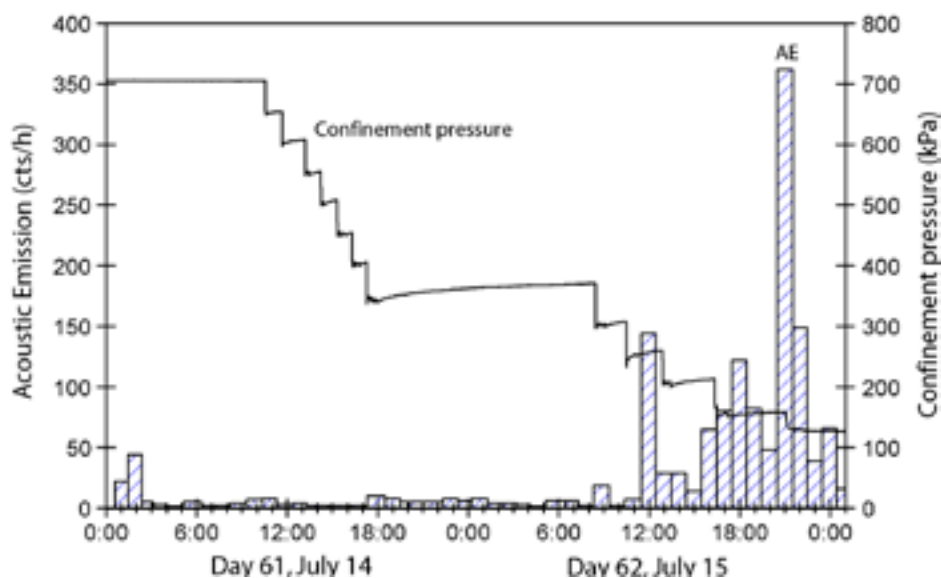


**Figure 9-4.** *Confinement pressure and acoustic frequency in counts per hour during the release of the confinement.*

107
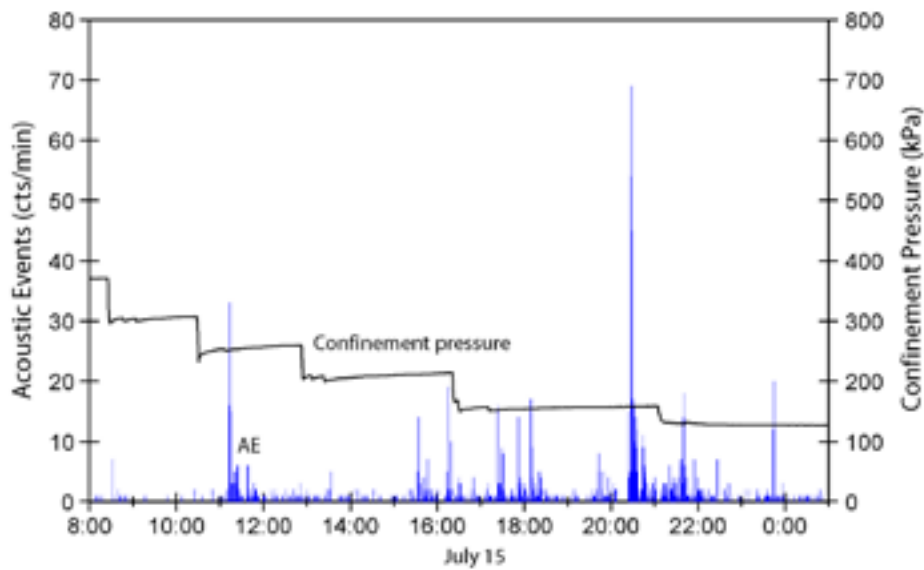
**Figure 9-5.** *Confinement pressure and AE counts per minute during the pressure drop on July 15 (day 62). Note that the AE response occurs some time after the actual pressure drop.*
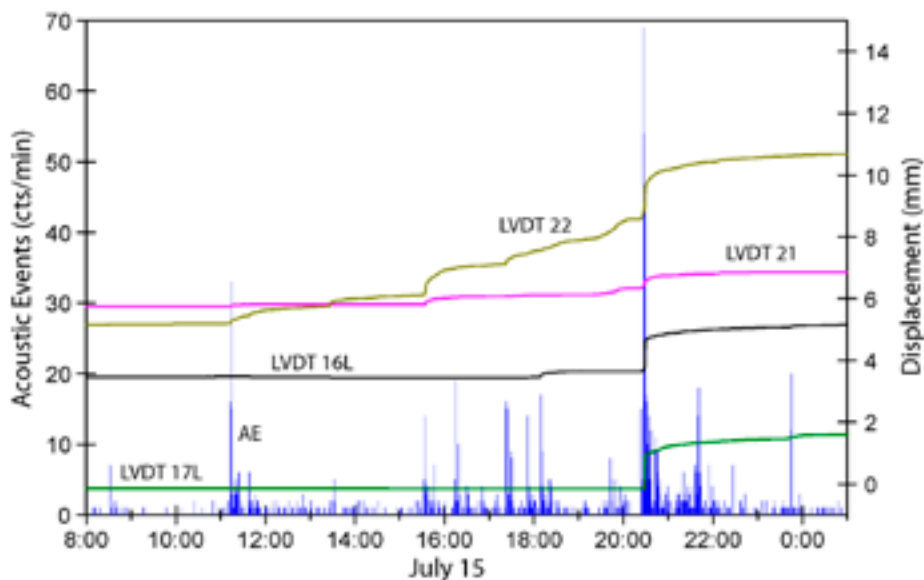


**Figure 9-6.** *Displacement and AE counts per minute during the pressure drop on July 15 (day 62).*

The drop down to 200 kPa induced some more AE and the displacements at transducer 22 continued. As stated previously in the report, the AE was located in the general area of the displacements but could not be correlated with actual monitored displacements.

The majority of all AE events and displacements during the release of the confinement occurred when the pressure was reduced to 150 kPa. During a 4-hour period after that pressure drop, displacements and AEs occurred at an increased level, Figure 9-5. However, the background level of AEs after the 150 kPa pressure period was much higher than that measured from the beginning of July.

The last pressure drop for the day should reduce the pressure to 100 kPa. Unfortunately, the pressure transducer malfunctioned during that drop and transmitted a constant value. This was not noticed until it was too late and all the pressure had been released. The actual pressure in the graph should therefore be zero after 21.30 h. Note that the hole was still filled with water. The transducer was
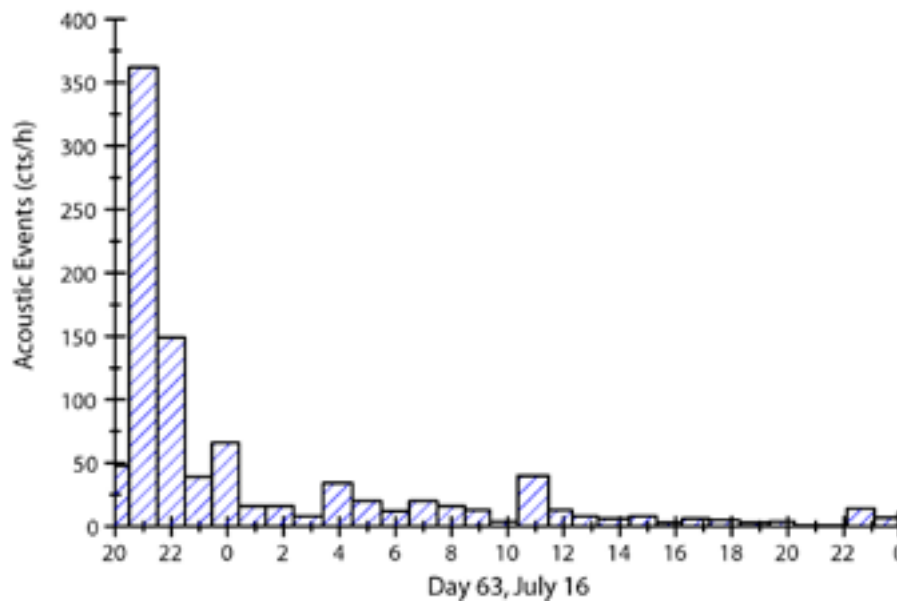
**Figure 9-7.** *Decay of acoustic emissions on July 16 (day 63). The hole was totally evacuated of water in the afternoon, but that did cause an increase in AE frequency.*

removed the next day and tested. Nothing was wrong with it then. It was therefore concluded that the measured pressure is accurate until shortly after the pressure release from 150 kPa started and that the transducer jammed when the pressure started to go down.

It is interesting to note that after 21.30 h, when the pressure was reduced from 150 kPa to 0, the acoustic response was rather limited with small accompanying deformations. One might expect that such a large pressure drop would induce a great deal of acoustic activity, which was obviously not the case.

The acoustic activity quickly died off after the total release of the confinement. In the afternoon of July 16 the hole was totally evacuated of water, but that did not cause any additional AE. The acoustic count per hour for July 16 is given in Figure 9-7.

### 9.2.1 Location of AEs

The acoustic emissions caused by the release of the confinement pressure were monitored and source-located. The results were imported into the Surpac model used to visualise the geology. Plots of the AE locations during different stages of the release of the confinement pressure are shown in Figure 9-8 to Figure 9-10.

When the acoustic emissions started to pick up due to the decreasing confining pressure, the vast majority of the events were located in the open hole. During the release of the confining pressure down to 150 kPa the acoustics are concentrated at depths of between 3.5 and 4.5 m slightly to the right of the pillar centre. When the pressure was completely released (150 to 0 kPa on July 15), approximately one-third of the events were located on the pillar wall of the confined hole (Figure 9-8). The figure shows that the events on the confined side occur at three different locations. I) a few events can be associated with the shear zone in the upper part of the hole; II) at a depth just below 2 m, events occur where a few healed fractures intersect; III) in the lower part, between depths of 4 and 5 m, the events are associated with the open water-bearing fracture 08 that intersects the pillar at a depth of approximately 4 m on the right side (Figure 9-9 and Figure 9-10).

The pillar was quickly stabilized after July 16 and a few events took place in the shear zone and the intersection of fractures on the confined side (Figure 9-10). At the open hole side, the events also took place in an area with healed fractures at a depth of 3.5 m.

109
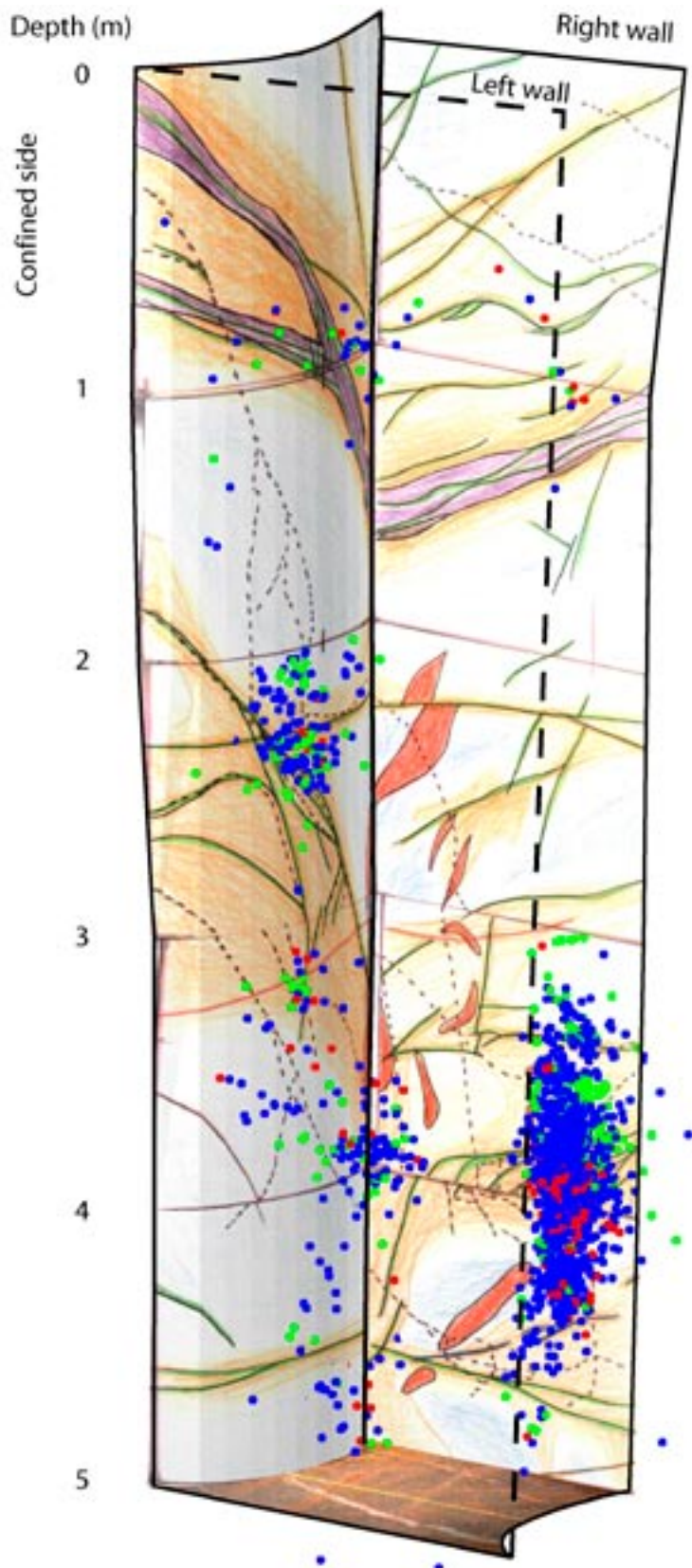
***Figure 9-8.*** *Location of AEs at the confined side viewed from the open side. The figure contains all data from day 61 to day 63.*
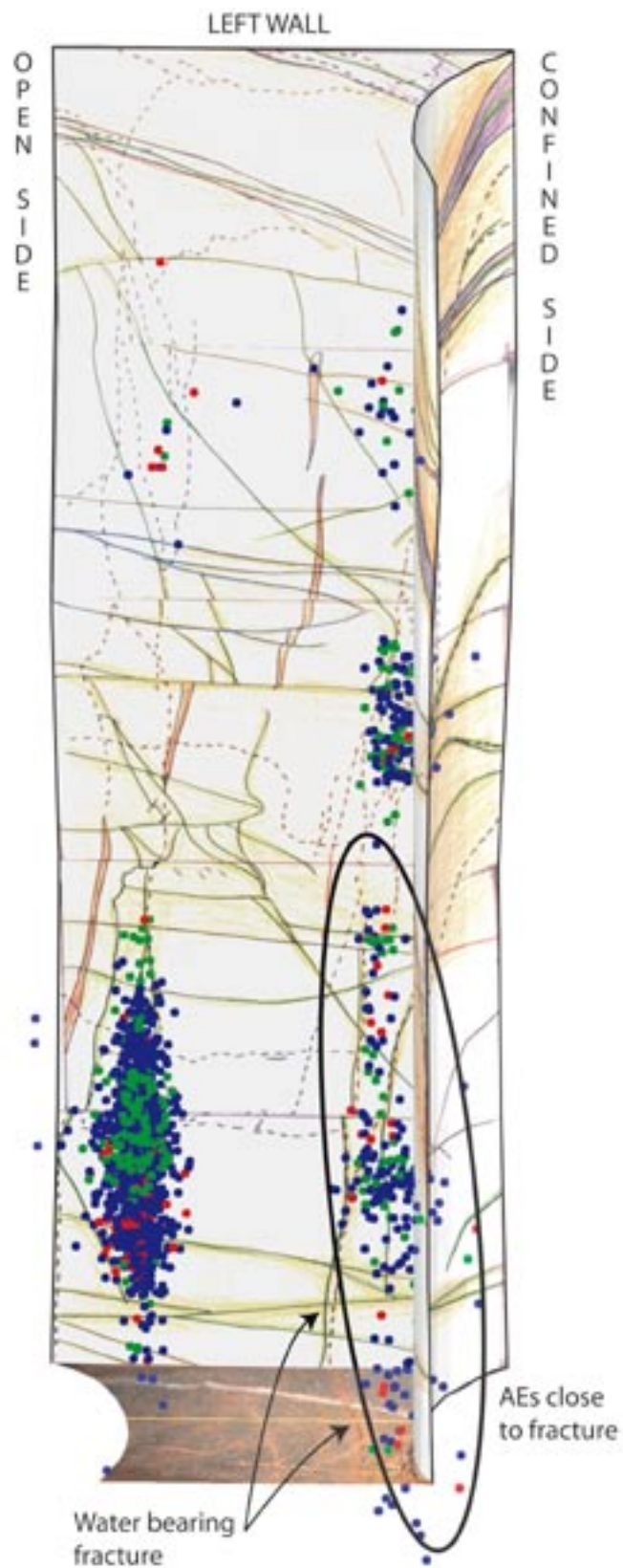
**Figure 9-9.** *Location of the AEs in relation to the water-bearing fracture. The figure contains all data from day 61 to day 63.*
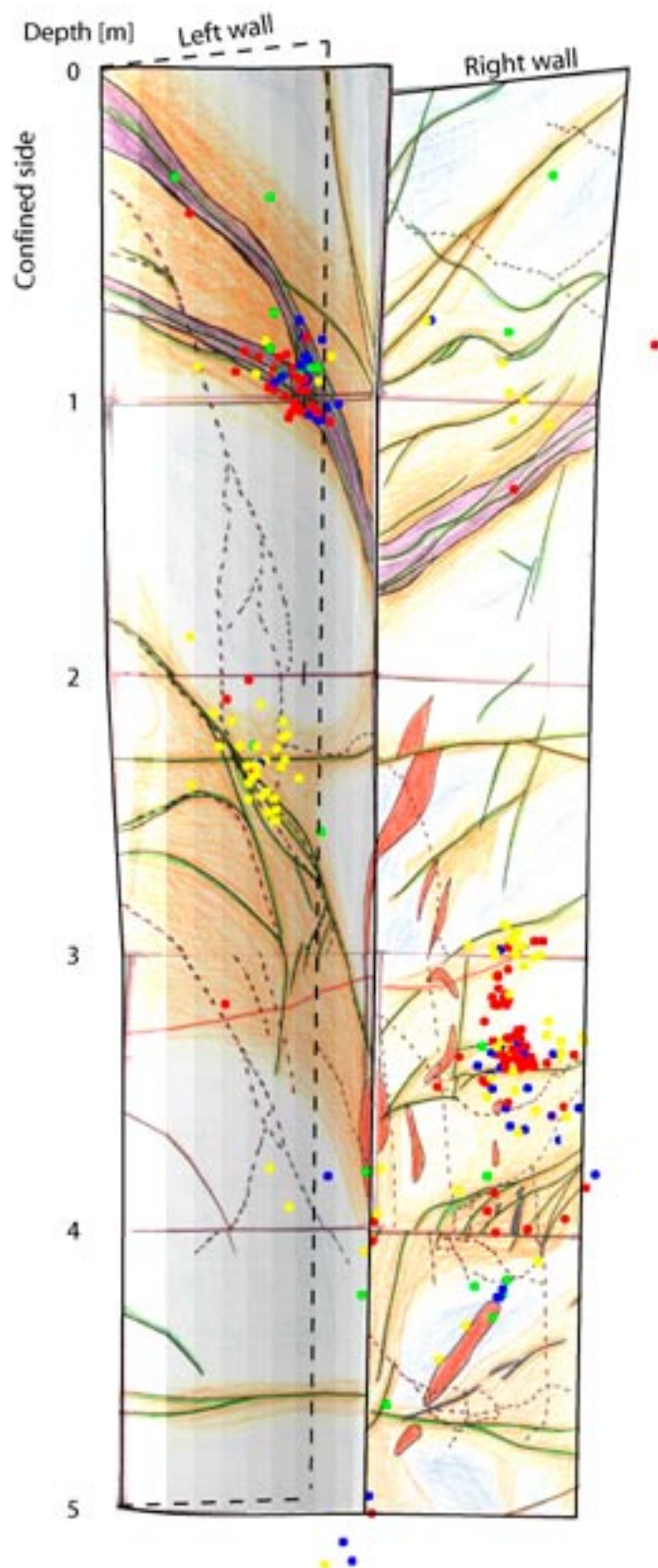
**Figure 9-10.** *Location of AEs from day 64 to day 66.*

## 9.3    Pressure and water volumes

The pressure was released by opening a valve and letting water out of the bladder. The volume of water was measured each time. When the pressure fell to 550 kPa and the valve was closed the pressure increased quite rapidly. Pressure increase after closure of the valve was observed after the previous pressure drops as well, but the rate of pressure increase then was very small. When 550 kPa was reached, however, the valve had to be opened a second time to keep the pressure at the targeted level. This had to be done after all the subsequent pressure reductions. The reason is probably that the textile straps act like springs.

The volume of water released for the compensational pressure drops was also measured and normalized to the resulting pressure change. The normalized volumes are presented in Figure 9-11. Consider an example: To release the pressure from the initial value of 450 kPa to 400 kPa, the valve had to be opened three times (twice to compensate for the pressure increase). The volume that needed to be removed to lower the pressure to the target level corresponded to 0.035, 0.032 and 0.031 ml per kPa of pressure. As can be seen in the figure, there is a clear correlation between the values plotted. As the total pressure in the system decreases, the ratio of volume to pressure decreases.

## 9.4    Summary and conclusions

The effect of the confining pressure was clearly demonstrated. During the heating phase of the experiment, very few AEs originated from the confined side of the pillar. AE frequency and yielding damage during release of the confinement pressure were also very low at that side. Instead the vast majority of the AEs and the dilatation were concentrated at the notch tip location in the open hole. The fact that yielding initiated here is perfectly consistent with the observations made of spalling in general and in this experiment in particular. The part of the notch located deepest into the pillar, and particularly the notch tip, is in a highly instable equilibrium. Extremely small stress changes trigger the yielding process. The distinct stress threshold that has to be exceeded before spalling is initiated has been discussed in Chapter 8. The reduction of the confinement is a good example of this. A pressure reduction of 450 kPa in the confined hole was enough to initiate the spalling process again in the open hole. The change of stress in the open hole due to the release of the confinement pressure was intuitively perceived to be very small but has not been quantified. The rock then responded to each of the remaining 50 kPa reductions.
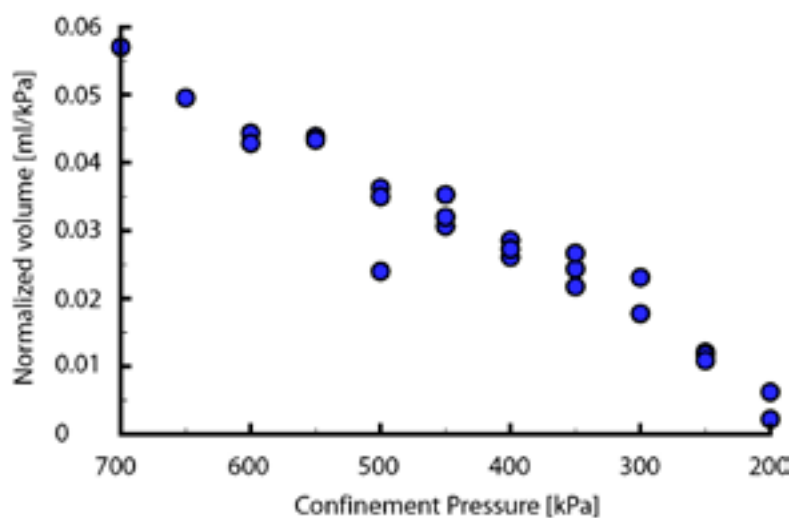


**Figure 9-11.**  *Confinement pressure versus the volume of water removed for a relative pressure change. The point above 700 kPa corresponds to a pressure drop from 700 to 650 kPa and so on.*

The absence of yielding at the pillar wall of the confined hole is interesting. A combination of micro-fracturing and geometry has been posited as a possible explanation that could explain the absence of yielding in the open hole.

**Microfracturing** During the experiment it was observed that displacements occurred without the AE system picking up energy enough to trigger the system. Hence, fracturing could occur without being detected by the AE system. Fractures in the confined hole wall may therefore have formed during the experiment. The fracturing did not form rock chips or other evidence of yielding of the hole wall but softened the rock enough to prevent yielding at the surface.

**Geometry** The intact circular geometry of the hole in combination with the softened zone kept the hole wall stable and suppressed brittle failure. As described in Chapter 10 the hole walls were damaged during the de-stressing that was performed before the pillar blocks were removed. Representative samples could therefore not be taken from the confined pillar sides and studied for microfracturing. Samples were not taken before de-stressing since the high tangential stress acting on the hole wall would cause sample disturbance and the origin of microcracks found in the model could not have been determined.

The AE activity in the pillar ceased almost completely shortly after the release of the confinement pressure and almost nothing was recorded as the temperature dropped to the background level (Figure 9-3). This again indicates that the time-dependent effect of the yielding process is very small, in this case restricted to a few hours. As soon as the threshold is exceeded, yielding is initiated and the overstressed parts of the rock yield quite quickly. Afterwards the rock is stable again and the yielding stops.

The confinement construction seems to have had an almost linear relationship between the released volumes of water per kPa of released pressure. This is probably because the textile straps take up the load from the two steel lids.

# 10 Excavation of pillar blocks

To be able to make as good a geological characterization of the pillar as possible and to study the fracture pattern located inside the pillar caused by the yielding, it was decided to completely remove the pillar from the site. This was done by sawing it into five blocks, each with a height of approximately 1 m.

## 10.1 Excavation methodology

Wire sawing was chosen as the method for excavating the blocks. The technique uses a wire to which industrial diamonds is attached. The grinding action of the diamonds combined with a normal force on the wire makes a clean cut.

It was necessary to drill holes in the pillar at the corners of the blocks. The wire was then inserted in the holes and in the machine which pulled the wire. A typical set-up of the machine is illustrated in Figure 10-1 as one of the walls of the fourth block is sawn. The boreholes that constitute the corners of blocks one, two and three at that wall are also visible. All boreholes were drilled during the same campaign. The excavation sequence for each of the blocks was as follows (Figure 10-2):

1) A horizontal saw cut was made.

2) The block was now hanging from its sides. A steel plate and textile straps were inserted into the horizontal slot. Arched vertical steel plates were then placed on the parts of the horizontal steel plate sticking out into each large hole. The arched plates were intended to keep the rock at the hole surface of the pillar in place.

3) The two vertical cuts were made. The block was now standing on the horizontal steel plate inserted in the first slot.

4) Steel plates were placed around the corners of the block and textile straps were used to press the vertical steel plates against the block to hold it stabile during lifting.

5) The textile straps left underneath the horizontal steel plate were attached to a specially designed lifting device mounted on a mobile crane. The device distributed the forces from the straps evenly on the bottom steel plate.

6) The block was lifted onto a truck. The block was transported to a cavern were it would be mapped later.

## 10.2 De-stressing

The wire saw cannot be used if the normal stresses are too high. If they are, deformations of the rock will jam the wire, making sawing impossible. The compressive stresses on the pillar were too high for wire sawing and therefore had to be reduced before sawing could commence. It was decided to relieve the stresses in the pillar by using the Swedish slot drilling technique.

Slot drilling was performed by drilling of 64-mm-diameter holes with a c/c spacing of ~ 110 mm. The ridge between the two boreholes was then excavated by a 76-mm-diameter drill bit that was guided by a 64-mm pilot hole, Figure 10-3 illustrates the technique and the planned geometry of the de-stressing slot. Drilling each hole took 5 to 10 minutes.
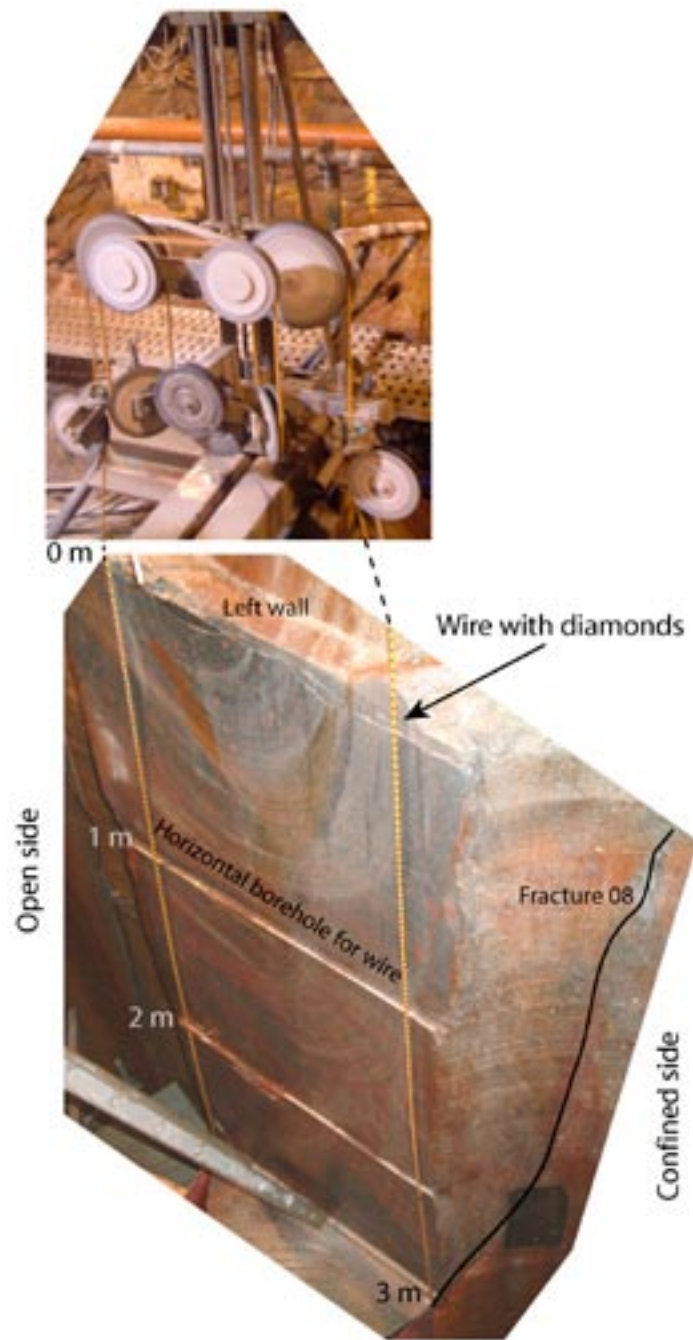
**Figure 10-1.** *The wire sawing machine as one of the vertical walls of block four is sawn.*

Yielding of the rock was more extensive on the left side of the pillar. The blocks were therefore not cut symmetrically around the centre line of the tunnel but optimized so that the entire yielded part of the pillar was retrieved with the blocks (Figure 10-6). The size of the blocks differed somewhat since they were made conical to reduce the risk of jamming as they were lifted.
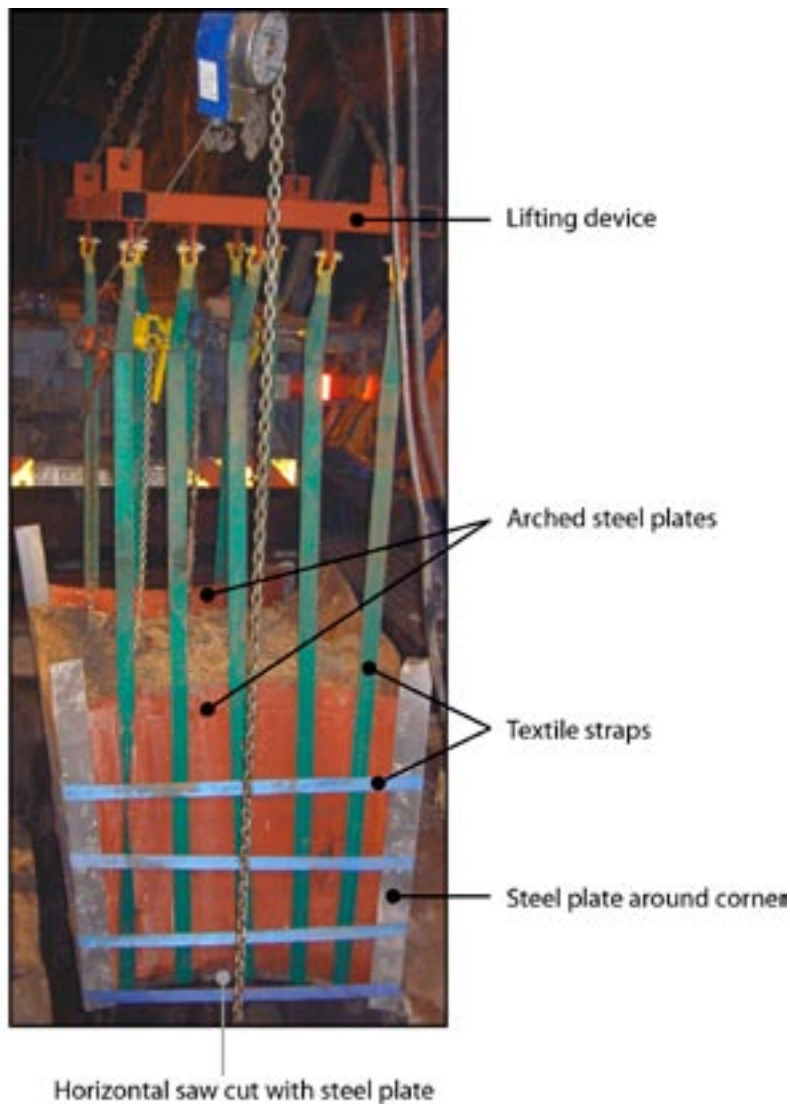
***Figure 10-2.*** *Lifting of block number 1 (the top block). Some of the work steps described in the numbered list above are indicated in the figure.*

Predictive numerical modelling with Phase2 indicated that the rock was likely to fail during de-stress drilling. The geometry of the slot was optimized to minimize the damage indicated by the numerical model. It was clear that the slot should be excavated as far away from the pillar as possible, so the slot was made close to the tunnel wall. It was also found from the modelling that the slot should be arched and that the end points should be located close to the boundaries of the borehole to reduce the damage, as illustrated in Figure 10-3. The drilling sequence greatly influenced the amount of damage in the model. It was therefore decided that drilling should begin in the centre of the slot and every second hole should be drilled to the left and right of this centre hole.
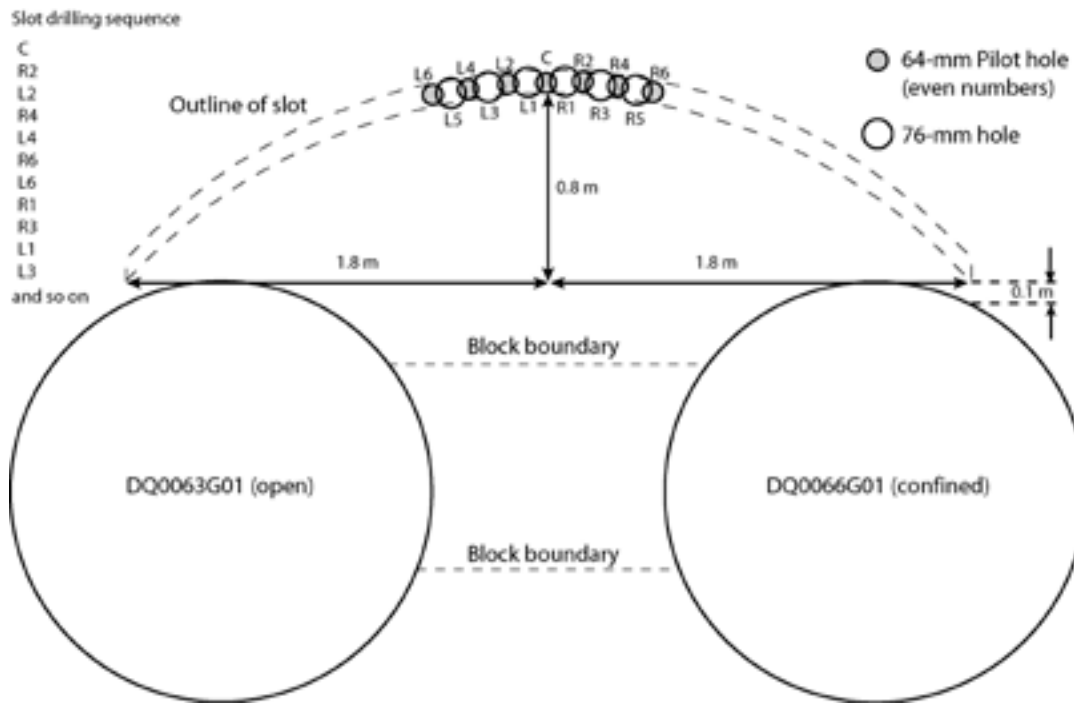
***Figure 10-3.*** *Illustration of the Swedish slot drilling technique and the geometry of the APSE de-stressing slot.*

### 10.2.1  Observations during drilling

All slot boreholes were percussion-drilled with a Tamrock Dino 560 machine, Figure 10-4. When approximately 0.2 m had been drilled on each side of the centre, it was noticed that chipping occurred on both sides of the slot. On the left side the chipping began at a depth of ~ 0.4 m and on the right side right at the surface, Figure 10-4. The chipping stopped when the drilling had reached a horizontal distance of ~ 0.8 m on either side of the centre of the slot. Initial inspection of hole DQ0063G01 was undertaken when the chipping had just stopped. Extensive yielding had taken place as is indicated in Figure 10-5. Before de-stress drilling was initiated, the notch wall was smooth and no slabs were loose, Figure 10-6. In Figure 10-6 there is also photograph of the hole wall after the slabs formed during de-stressing had been removed. As can be seen, there is quite a big difference between the two photos.

In the upper part of the pillar a horizontal fracture at a depth of ~ 0.2 m dilated, Figure 10-7. The fracture is not included in the geological mapping but might still have been a thin closed blast-induced fracture. The fracture could have been dilated by displacement of the shear zone, but no evidence was found of fracture surfaces along the shear zone. It is more likely that bulging of the rock between the slot and the centre of the hole is the reason for the dilation.

In the side of DQ0063G01 facing the tunnel entrance (opposite side to the pillar), yielding was observed at only one location. The yielding included some chipping and the ejection of one small rock piece, as illustrated in Figure 10-8, and occurred at a depth of approximately 5 m.

118

***Figure 10-4.*** *Left: chipping initiated from the top of the right part of the notch. Right: photograph of the drilling of the slot.*



***Figure 10-5.*** *Photograph of the extensive yielding that took place as the slot was drilled.*

*Figure 10-6. Photograph of the pillar taken in DQ0063G01 from a depth of approximately 3 m and up. The photograph on the left was taken before de-stressing began and the one on the right after removal of the slabs created during de-stressing.*



*Figure 10-7. Photograph of the horizontal fracture that dilated during de-stress drilling. Note how it ends/begins close to the shear zone.*

DQ0066G01 was also inspected. No chipping was observed, but many fracture traces. The fractures had not created any slabs that could be removed but were probably caused by dilation of pre-existing fractures and fractures formed during de-stressing. LVDTs were installed in DQ0066G01 to measure the dilatation of fractures 08 and 14 /Ivars 2005/. At fracture the maximum normal displacement was ~ 0.6 mm and the maximum horizontal shear displacement ~ 0.8 mm. The major part of the displacements in fracture 08 took place within a short period of time when the slot was excavated

***Figure 10-8.*** *Yielding at the back side of DQ0063G01. Dilation of rock slabs and the previous location of the ejected rock piece are visible.*

0.2 m to the left and 0.4 m to the right (approximately at stage 14 in the Mohr – Coulomb model, Section 10.4.1). Additional shear displacements took place when the slot length was 0.9 m on both sides (approximately at stage 20). At fracture 14 the maximum normal displacement was measured to ~ 0.06 mm and the maximum shear displacement to ~ 0.3 mm. These displacements occurred at approximately the same time as the shear displacements took place in fracture 08.

When the shape of the slabs is studied and they are compared with the ones created during heating, two major differences are found. The de-stressing slabs have a larger area and are thicker in the centres. No small chips on a cm scale were found on the surfaces of the big slabs. They seem to have been formed instantly. There are also similarities between slabs created during the different types of loading. The edges are thin and they are still shaped like fish scales with the upper end attached to the pillar and the lower dilated, Figure 10-5. It appears as if the yielding of the slabs during de-stressing, as during heating, is due to pure tension. The loading rate therefore does not seem to affect the failure process in any other way than the size of the initially formed slabs.

## 10.3   De-stress fractures in the blocks and host rock

When the first block was removed it became evident that a certain amount of failure had taken place. The failure was limited to the left part of the pillar, which is closest to the slot, and was visible as sub-vertical failed zones close to the edges of the blocks. It appears as if the stresses punched the pillar against the slot and that failure then occurred. A photograph of the left pillar wall is shown in Figure 10-9, where the failed zones and fracture 08 have been marked. Photographs taken of the left sides of blocks 2, 3 and 4 have been assembled and are mirrored in Figure 10-10 to permit direct comparison of the fractures with those in Figure 10-9.

In the left part of block 2 (depth of 1 to 2 m) the failed zone is less distinct and split into several different fractures, probably due to pre-existing healed fractures that have yielded and distributed the failed zone over a larger area. In the lower part of block 4 (close to a depth of 5 m), sub-horizontal fractures are visible. They were caused by the sawing of block 5. Before the excavation of the last block, only a thin weakness plane was visible at that location in the rock wall. The upper part of the last vertical saw cuts were a bit difficult for both of the last two blocks. Horizontal stress may have been created there by cuttings remaining in the slot. During drilling not all cuttings could be removed and they accumulated to approximately half the height of the slot. They may have formed a stress bridge between the host rock and the block.

On the right side the slot re-opened an old fracture that intersects fracture 08 just below the fourth block (depth ~ 4.1 m). The intersection is photographed in Figure 10-11, where fracture 08 is the right fracture indicated by the oxidized band running alongside it.
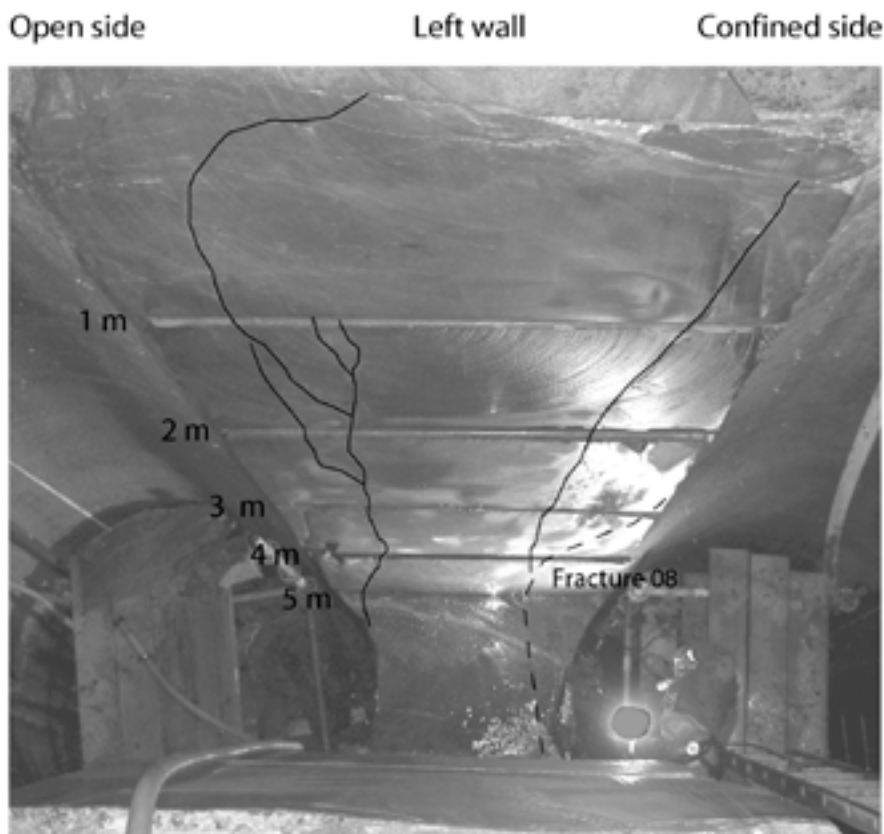


*Figure 10-9. Photograph down the left wall of the host rock after removal of the pillar blocks. The failed zones and fracture 08 (dashed line) are indicated.*
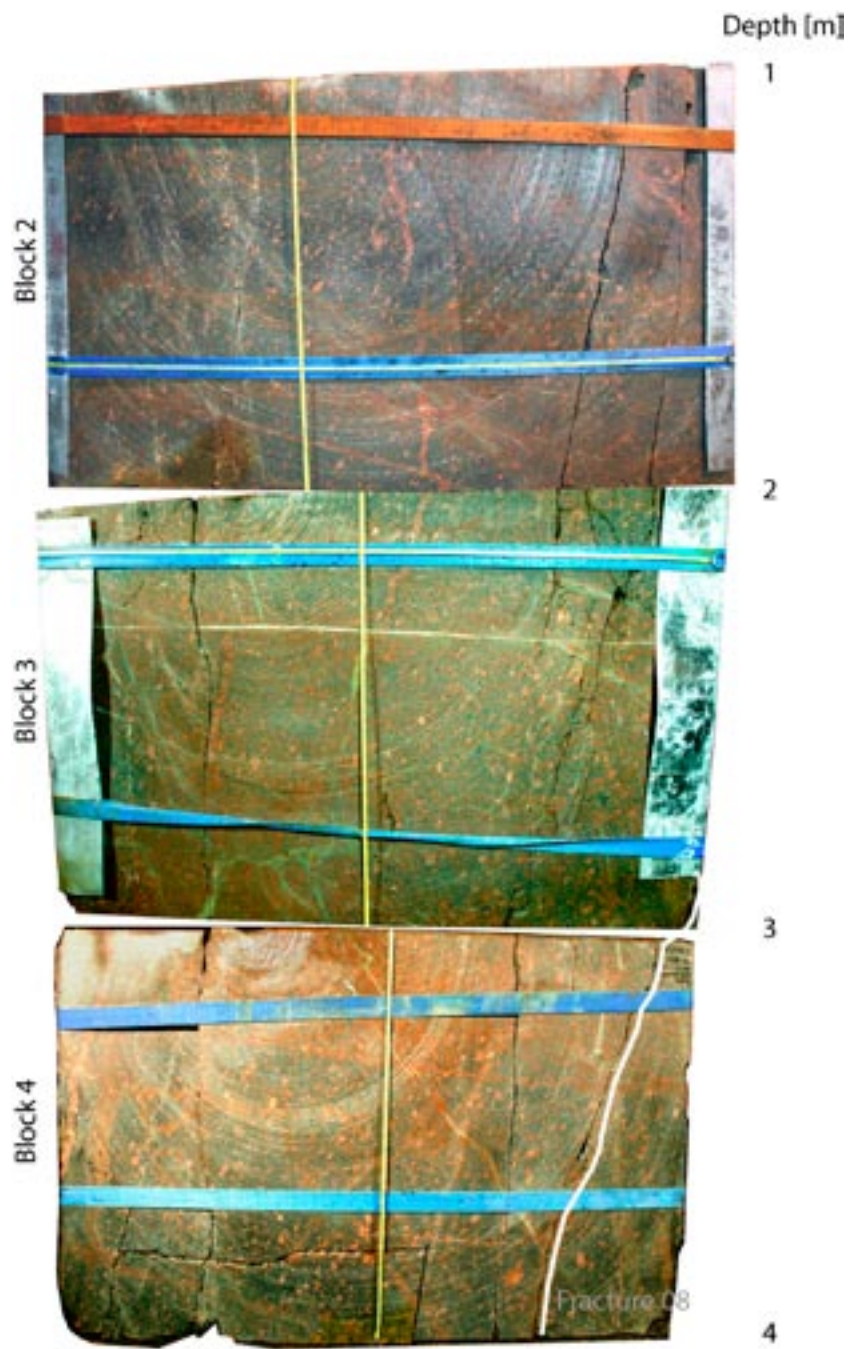
**Figure 10-10.** *Assembly of photographs of the left side of blocks 2, 3 and 4. The photographs have been mirrored to permit direct comparison with the photograph of the remaining wall.*

***Figure 10-11.*** *Photograph taken of fracture 08 in the remaining left wall. The drill pipe is at a depth of 4 m. The intersection between the failed zone and the pre-existing fracture indicated by the oxidized band is clearly visible.*

The failed zones are clearly visible at the horizontal tops of the blocks. When they are studied, the fracturing can be seen to end at the approximate centre of the blocks. Tensile fractures have developed in a horsetail like pattern on the right-hand side of the blocks. The pattern is visible on blocks 2 and 3, but when the arched pillar side of the blocks is studied the fracturing is seen to begin at a depth of approximately 0.5 m and continues down to a depth of ~ 3.5 m. Photographs of the top of blocks 2, 3 and 4 are shown in Figure 10-12.

Close up photographs of the fracturing close to the centre of blocks 2 and 3 are shown in Figure 10-13 and Figure 10-14. The fracturing can be seen to end in what has become the centre of the notch, creating tensile stresses that have fractured the rock in a horsetail like pattern.
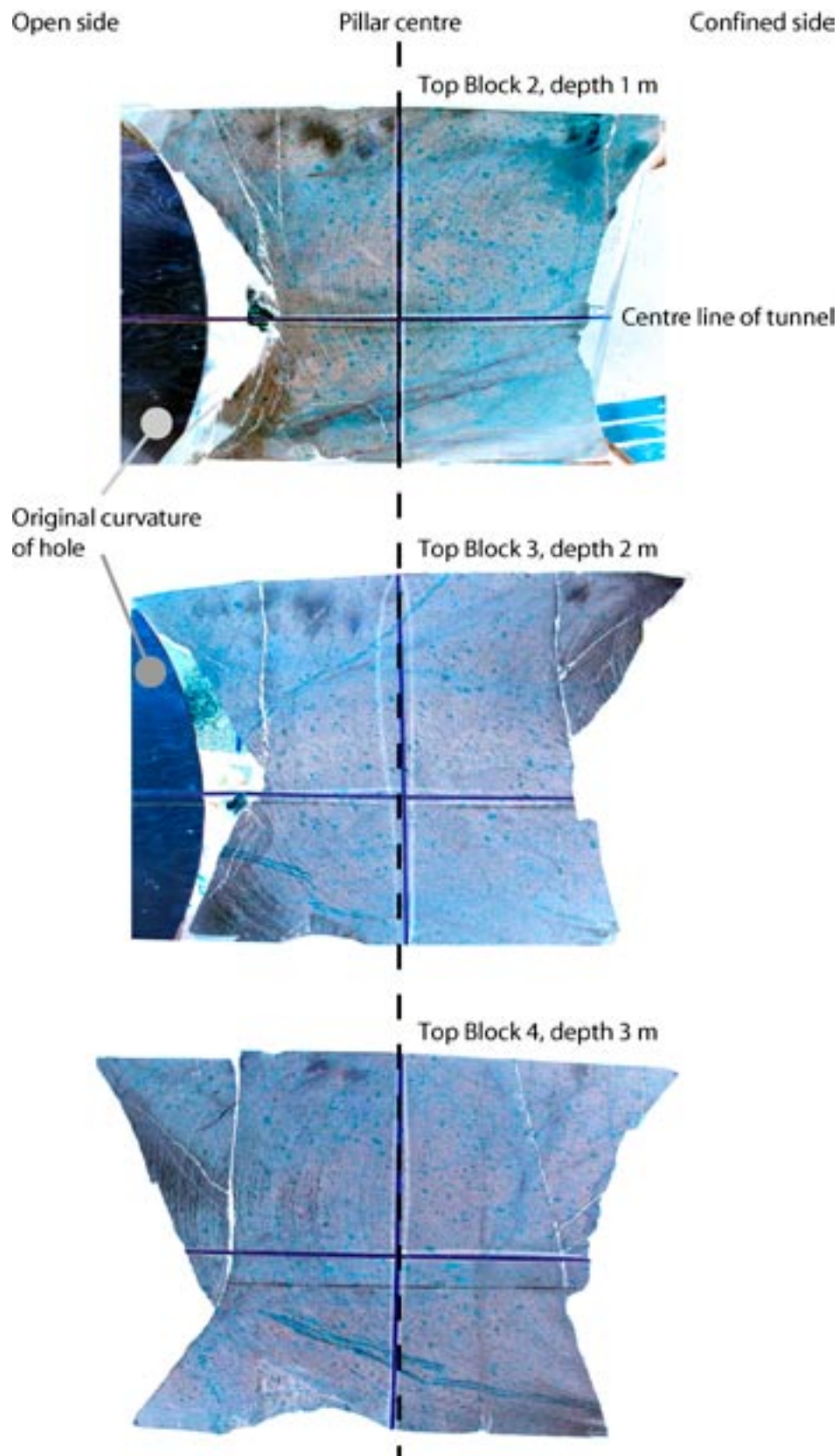
*Figure 10-12.* *Photographs of the tops of block 2, 3 and 4 with the general fracture pattern. The colours have been inverted to better illustrate the fracturing. The white traces of the failed zones are clearly visible above the centre line of the tunnel.*
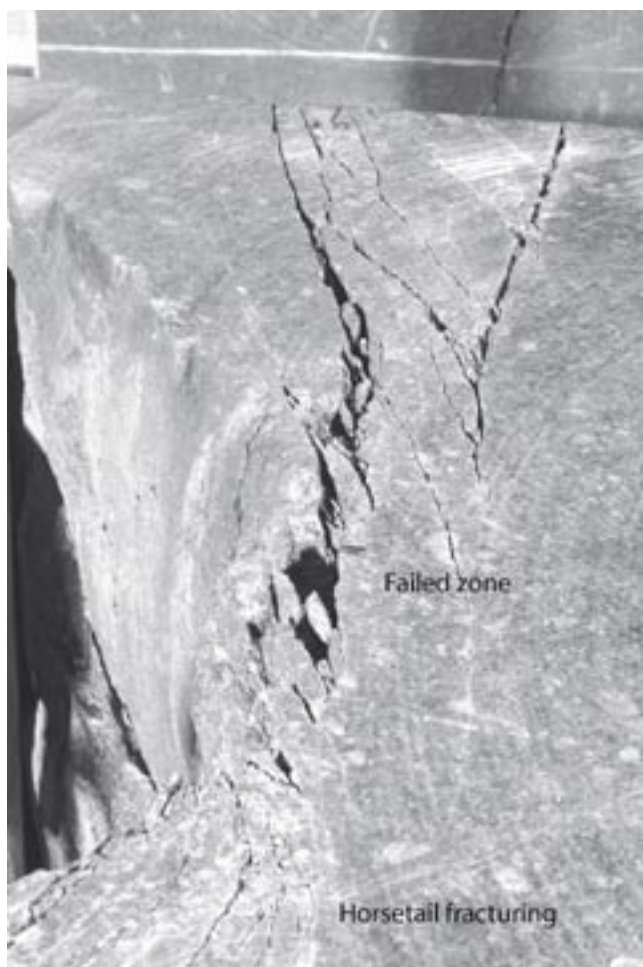
**Figure 10-13.** *Detail of the fracturing on the top of block 2.*
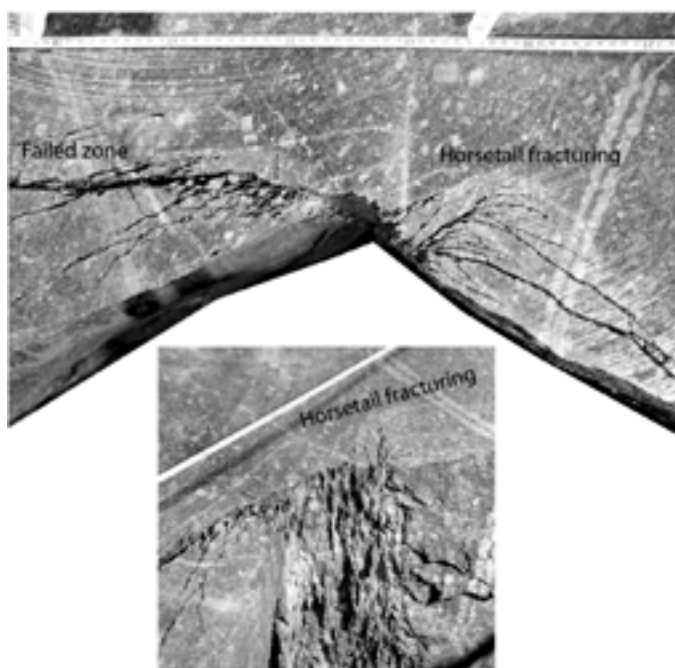


**Figure 10-14.** *Detail of the fracturing on the top of block 3. (Not the resemblance to a galloping horse in the top photo)*

## 10.4 Modelling of de-stress drilling

Back calculations of the de-stress drilling have been carried out with the 2D finite element program Phase2. Both the Mohr-Coulomb and the Hoek – Brown failure criteria has been used. A section located at a depth of 1 m corresponding to the top of block 2 was modelled. The in situ stresses were increased so that the stresses in the 2D plane corresponded to those calculated in the same plane by Examine3D. The models were run in 36 stages which are summarized in Table 10-1. Rock properties used in the model are presented in Table 10-2.

32,452 triangular elements were used in the model, and the element size at the boundaries of the holes is ~ 0.02 m. The hole geometry in the model conforms to the actual survey of each hole.

Young's modulus was set to 55 GPa and Poisson's ratio to 0.25.

### 10.4.1 Mohr – Coulomb modelling results

The 2D model results agree quite well with the actual fracture pattern observed. Result plots from the modelling are presented in Figure 10-15 to Figure 10-24. The locations of the yielded elements are indicated on top of the stress contour.

The result at modelling stage 6 is presented in Figure 10-15 and Figure 10-16. The actual geometry of the notch as mapped on site is included in Figure 10-15. The open hole exhibits very good resemblance to the modelling results. However, the model does not manage to predict the effect of the confining pressure as is indicated by the yielded elements in the confined hole. Except for some minor areas close to the borehole boundaries the modelled area is confined ($\sigma_3 > 0$).

**Table 10-1. Summary of the Phase2 modelling of the de-stress drilling.**

| Stage no | Model specifics |
|---|---|
| 1 | Excavate DQ0066G01 |
| 2 | Apply confining pressure in DQ0066G01 |
| 3 | Excavate DQ0063G01 |
| 4 | Add maximum thermal stress increase |
| 5 | Remove the confining pressure in DQ0066G01 |
| 6 | Remove the thermal stress increase |
| 7–36 | Excavate the slot holes. The holes were essentially excavated in the correct order. In most cases ~ 4 of the smaller (64-mm-diameter) holes was excavated in the same stage. The effect of this in the model was minimal and is not believed to have affected the final result. |

**Table 10-2. Rock properties used in the Phase2 models.**

|  | Peak | Residual |
|---|---|---|
| Tensile strength (MPa) | 14.3 | – |
| Friction angle (deg) | 49 | 41* |
| Cohesion (MPa) | 31 | 16 |
| m (–) | 19.591 | 10 |
| s (–) | 0.3292 | 0.05 |

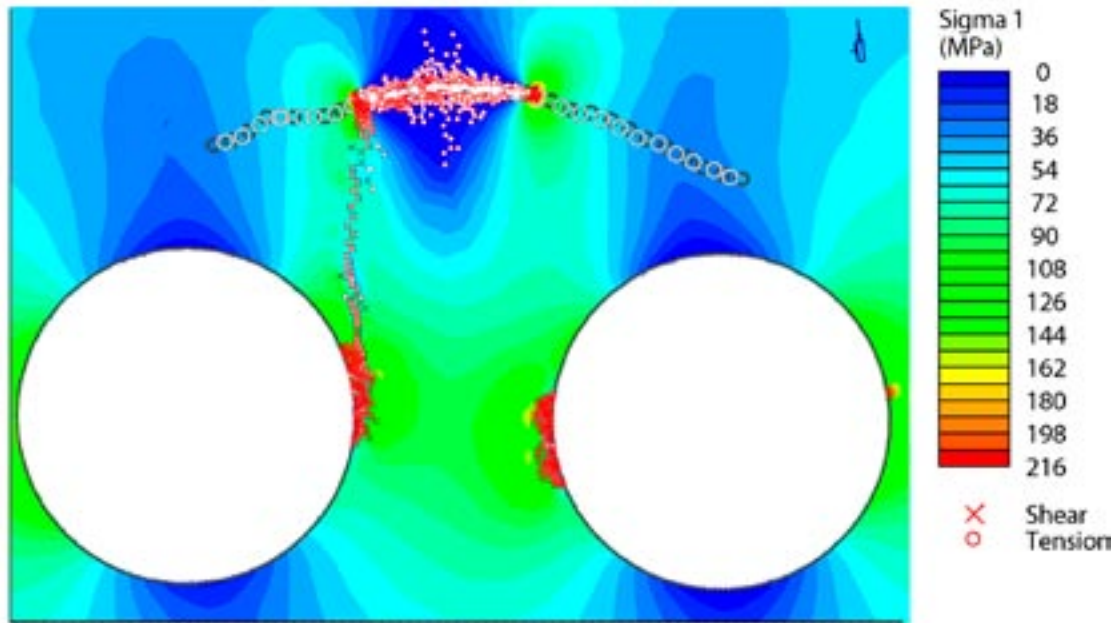*Dilatation angle set to zero since no data exists.
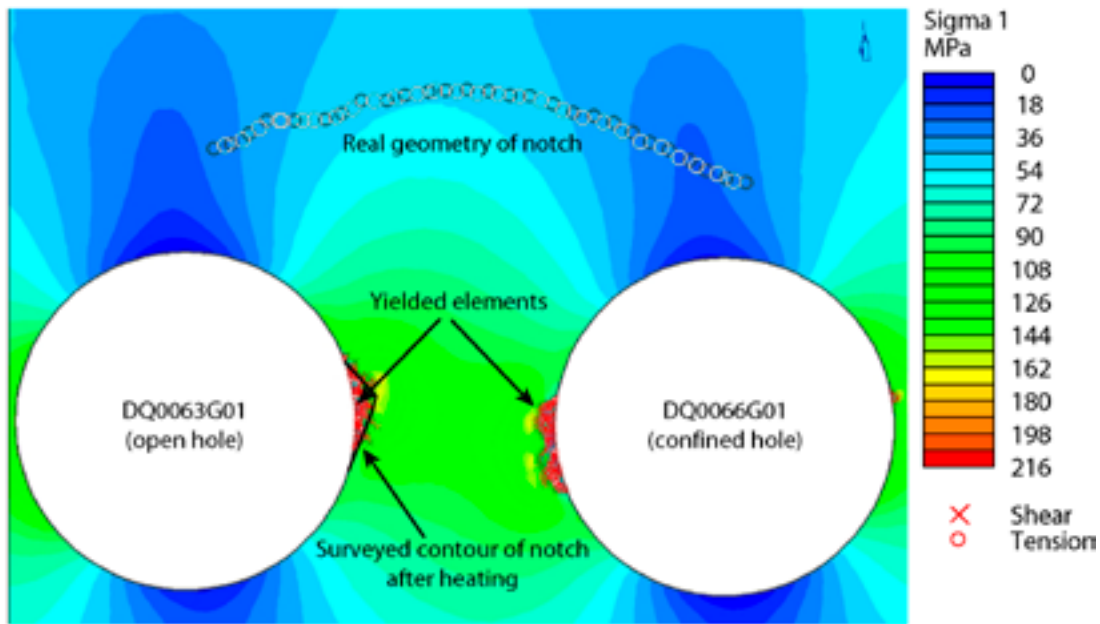
**Figure 10-15.** *Yielded elements and major principal stress at modelling stage 6.*
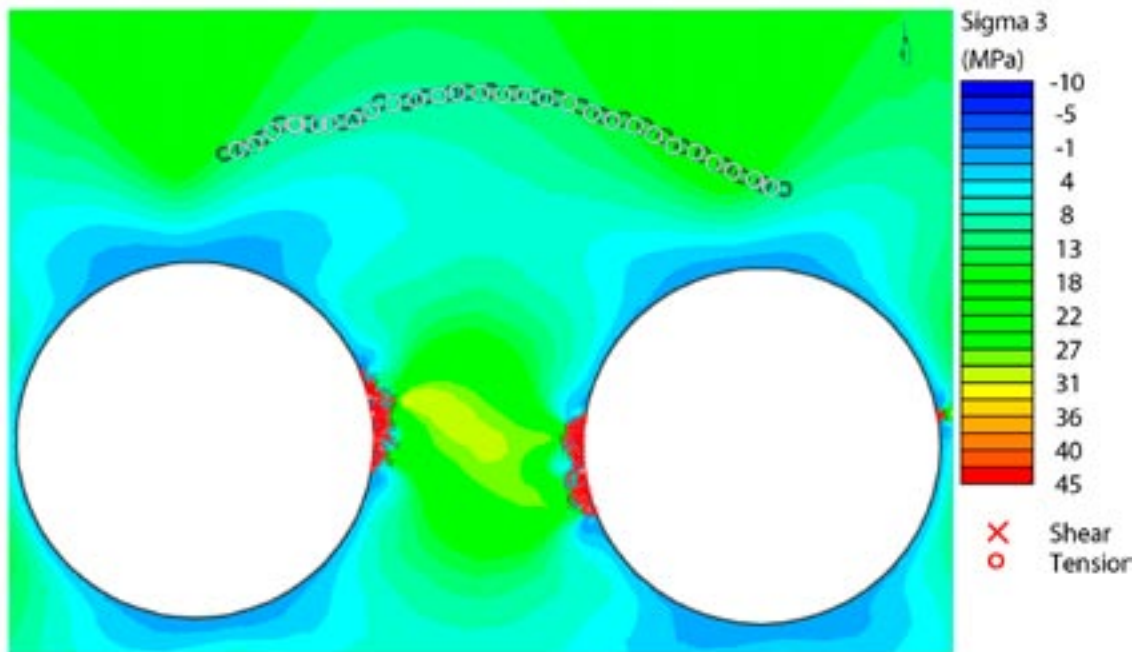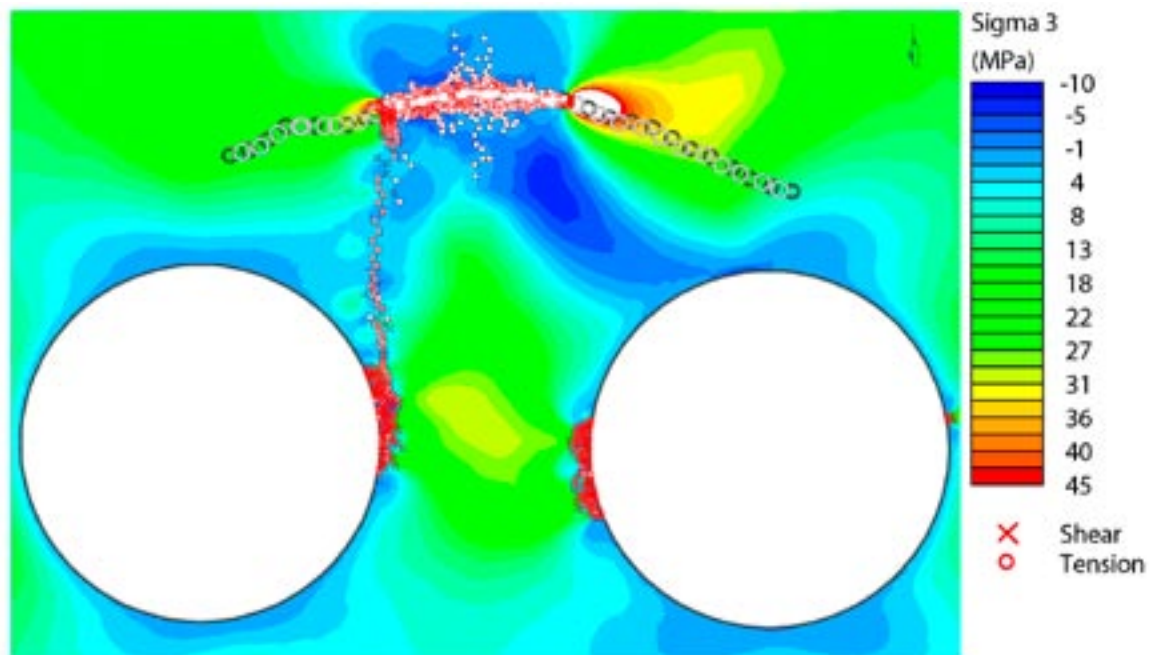


**Figure 10-16.** *Yielded elements and minor principal stress at modelling stage 6.*

The result at modelling stage 14 is shown in Figure 10-17 and Figure 10-18. At stage 14 the slot was excavated 0.45 m to the left and 0.50 m to the right. No failure in the area between the large holes and the slot had formed before stage 14. A thin failed zone now developed in the model between the notch and DQ0063G01. During drilling, chipping was observed in the slot when it extended 0.2 m on either side of the centre (Figure 10-4). Increased failure in DQ0066G01 is indicated, but as previously mentioned virtually no larger slabs formed in that hole. Figure 10-18 indicates that the confinement is close to zero along the failed zone and that a band with tensile stresses has formed between DQ0066G01 and the slot. A similar band was formed between DQ0063G01 and the slot at modelling stage 13.

128

***Figure 10-17.*** *Yielded elements and major principal stress at modelling stage 14. The extent of the notch is indicated. A failed zone has formed between the slot and DQ0063G01.*



***Figure 10-18.*** *Yielded elements and minor principal stress at modelling stage 14. The confinement is around zero along the failed zone and a band with tensile stresses has formed between the slot and DQ0066G01.*

At stage 18 the slot was excavated 0.75 m to the left and 0.65 m to the right (Figure 10-19 and Figure 10-20). Another failed zone was formed between the slot and DQ0063G01, this zone was not present in modelling stage 17 or observed in situ. The magnitude of the tensile stresses between DQ0066G01 and the slot has increased.
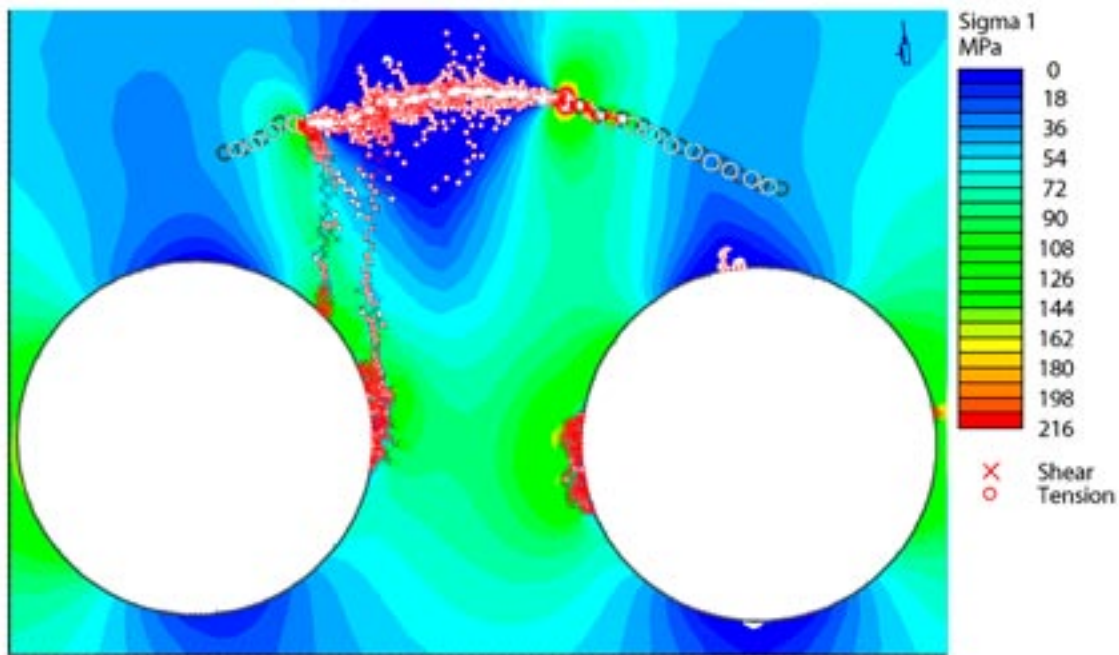
***Figure 10-19.*** *Yielded elements and major principal stress at modelling stage 18. Another failed zone has formed.*
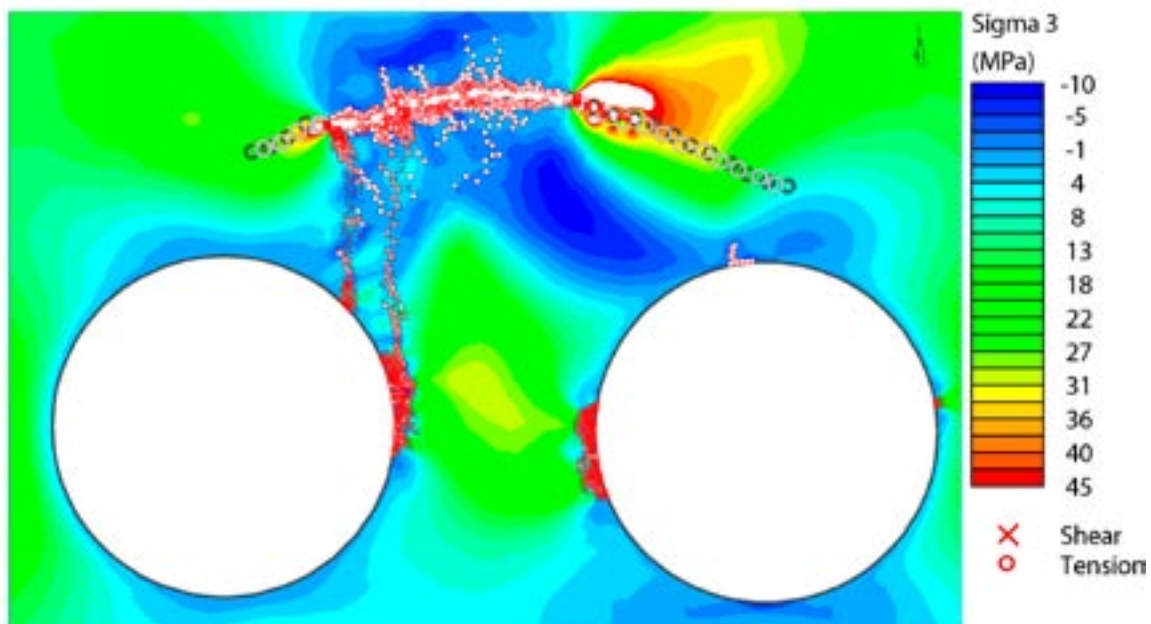


***Figure 10-20.*** *Yielded elements and minor principal stress at modelling stage 18. The magnitude of the tensile stresses between DQ0066G01 and the slot has increased.*

At stage 20 the slot was excavated 0.80 m to the left and 0.70 m to the right (Figure 10-21 and Figure 10-22). A failed zone had now been formed between DQ0066G01 and the slot, at stage 19 the there were no yielding in the model between those locations. At this stage of the slot drilling the observed chipping in the slot had ceased. This may have been due to the formation of the failed zones on both sides of the pillar and the release of stresses.
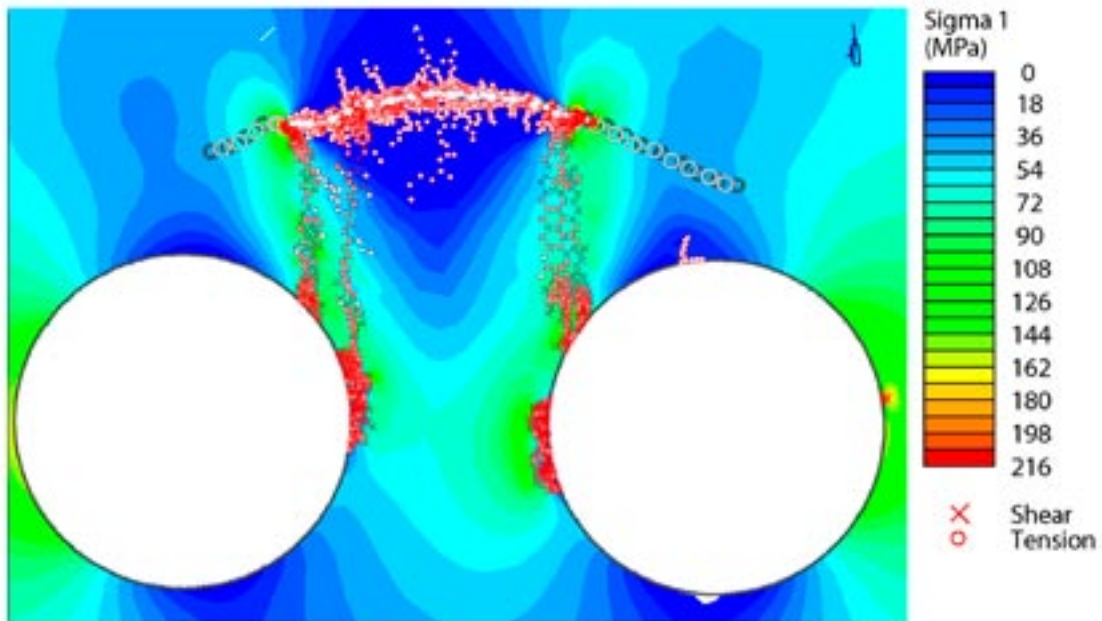
***Figure 10-21.*** *Yielded elements and major principal stress at modelling stage 20. A failed zone has formed between the slot and DQ0066G01.*
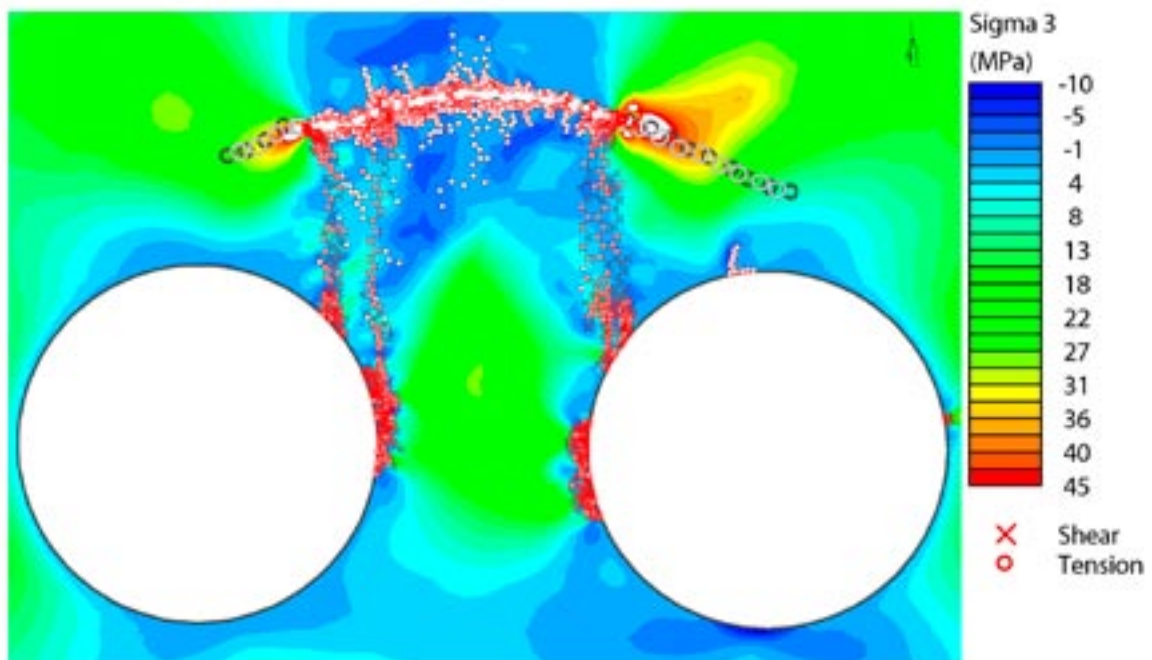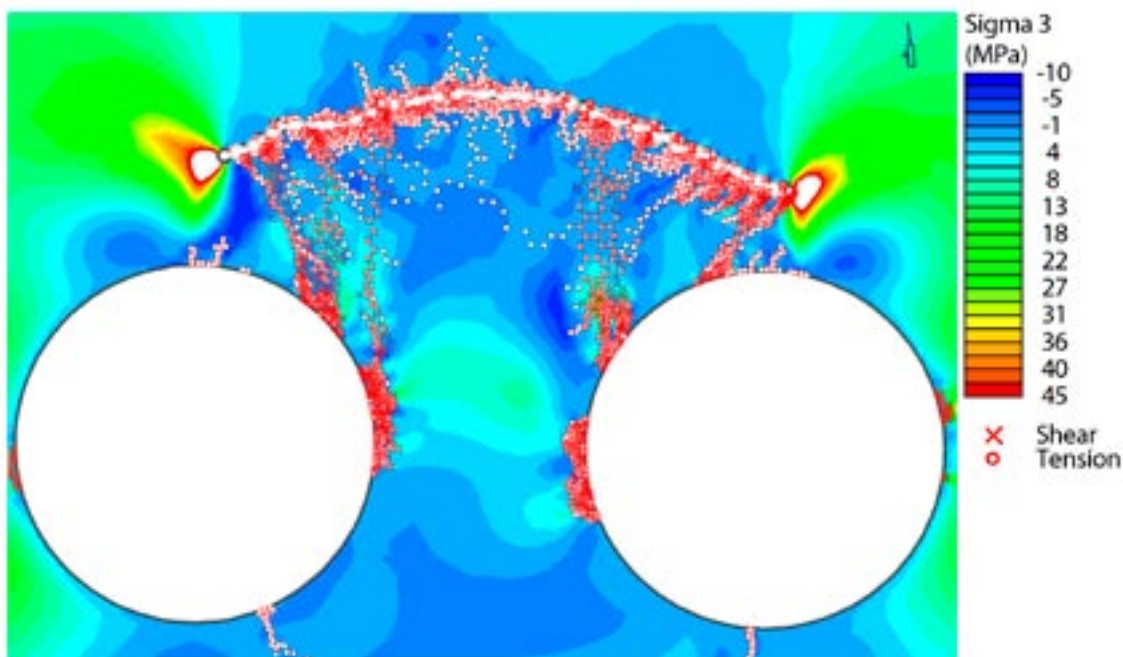


***Figure 10-22.*** *Yielded elements and minor principal stress at modelling stage 20. The forming of the new shear band has reduced the tensile stresses and the confinement along the failed zones is around zero.*

The last stage in the model (36) is presented in Figure 10-23 and Figure 10-24. The actual induced notch was larger than the one indicated by the numerical modelling as indicated in Figure 10-23. The general failure pattern was unchanged but with more yielded elements. A failed zone between the right end of the slot and DQ0066G01 had formed. This failed zone had not been observed in the field but a fracture was re-opened close to that location. The indications of yielding at the hole sides opposite to the pillar were not observed in field either.
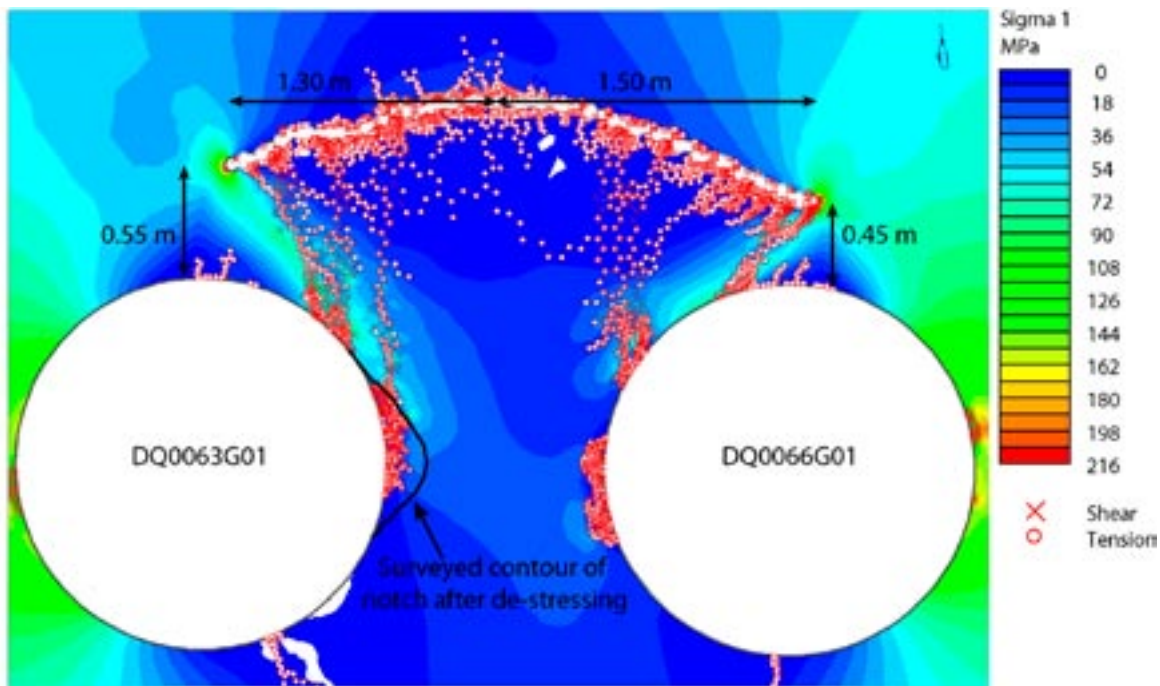
**Figure 10-23.** *Yielded elements and major principal stress The final geometry of the notch is indicated. The general yielding pattern is the same but expanded. A failed zone between the end of the slot and DQ0066G01 is indicated. The failed zone was not observed in field.*



**Figure 10-24.** *Yielded elements and minor principal stress at modelling stage 36, the final stage. Large areas of small tensile stresses have formed. Only the centre part of the pillar is confined.*

Superposition of the photograph of the top of block 2 with inverted colours on the result plot from the model after stage 20 enabled the possibility to compare the modelling results with the actual outcome. The result is presented in Figure 10-25 and agrees reasonably well with the actual fracturing. The modelled failed zones closest to the pillar centre and the real failed zones fit well. The splice of the failed zone on the left side of the block is not captured by the model. Instead the model produced a failed zone to the left of the one initiated in stage 14.

132
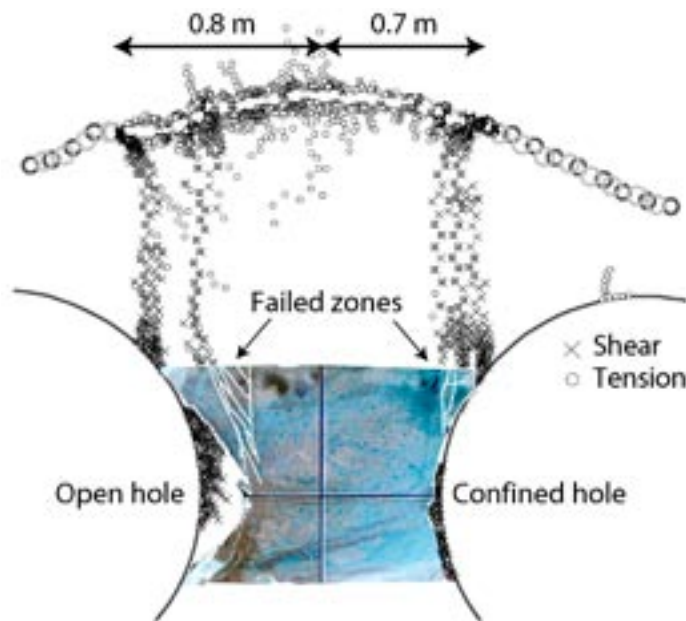
**Figure 10-25.** *Photograph of the top surface of block 2 (with inverted colours) superimposed on the Phase2 result plot at stage 20. The initiated fractures in the failed zones have been enhanced with white lines.*

### 10.4.2 Hoek – Brown modelling results

When studying the results from the model using the Hoek – Brown failure criterion it was soon obvious that the strength of the rock was clearly underestimated. The behaviour of the model is illustrated in Figure 10-26 and Figure 10-27. Because of the bad resemblance with the field observations and the fact that the Hoek – Brown model underestimate the rock mass strength in low confinement environments it was not studied in more detail except for the comparison in the stress path plots.
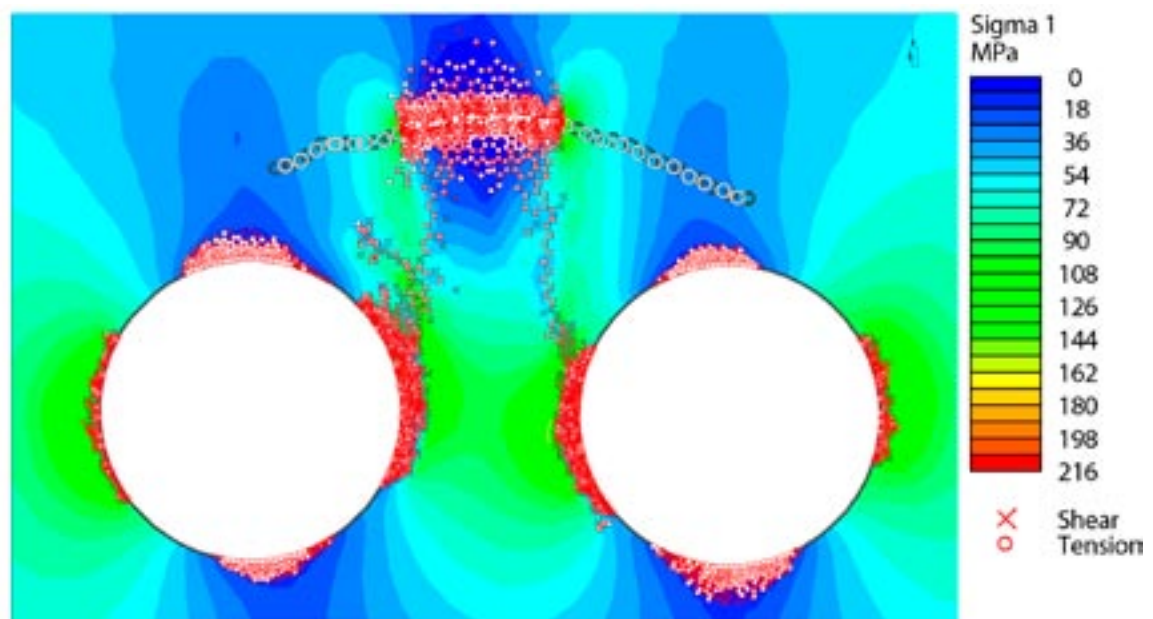


**Figure 10-26.** *Results from the Hoek – Brown model at stage 14. The yielding is much more extensive compared with the Mohr – Coulomb model. Field observations do not support the Hoek – Brown modelling results.*

133
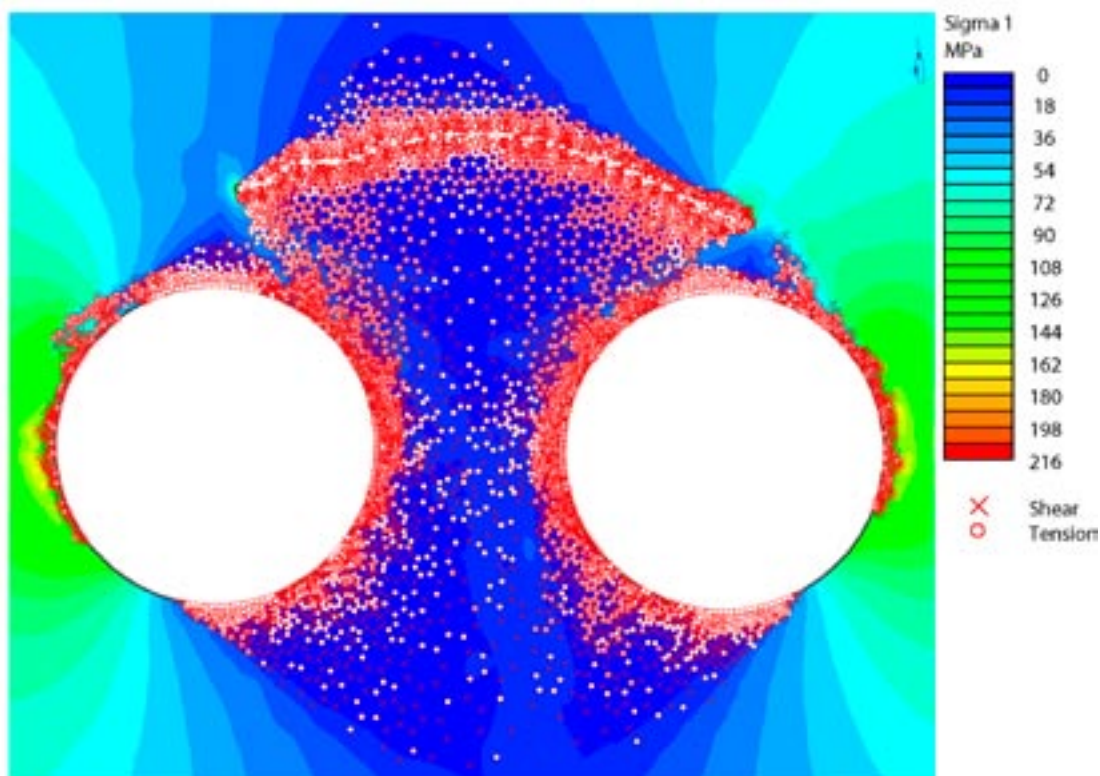
***Figure 10-27.*** *Results from the Hoek – Brown model at stage 36. The model indicates yielding in the entire pillar volume which is totally contradictory to the field observations.*

### 10.4.3  Stress paths

To further study the difference between the Mohr – Coulomb and the Hoek – Brown model the stress paths for four different points have been plotted and studied in more detail. The failed zones seem to be initiated at the slot and then propagate towards the pillar. The stress points have therefore been located close to the slot and approximately half the distance between the slot and the pillar (Figure 10-28). It was necessary to have a certain distance between the slot and the first point to avoid placing the point in the yielded zone surrounding the slot.

In addition to the Mohr – Coulomb and the Hoek – Brown model one additional analyses was performed. The Mohr – Coulomb model presented above used the tensile strength cut off option. This means that when the tensile stress exceeds the tensile strength in an element the residual strength of the rock is automatically applied. In the additional analyses this option was not used. The tensile and shear failure modes are then independent of each other.

The difference between the two types of Mohr – Coulomb models is quite small when looking at the geometry of the failed zones and the number of yielded elements. The failed zones in the two models occur at practically the same locations but in the model without the tensile strength cut off the total number of yielded elements is less. The major difference when studying the yielded elements is that the failed zone passing through R1 and R2 is formed at stage 19 instead of stage 20.

The stress paths are presented in Figure 10-29 to Figure 10-32. The figures also include the Mohr – Coulomb and the Hoek – Brown failure envelopes for both peak and residual strength.

The model includes the actual drilling sequence of the slot. The stress changes in the model can therefore be rather abrupt because one or a few holes was first drilled on one side of the slot where after holes were drilled on the other side of the slot. Another effect of this is that one can not see how the stress path first reaches the peak strength envelope and then the residual strength envelope. All this happens within one modelling stage and is therefore not captures in the stress path plots. The elastic model is of assistance when studying point L1 and R1. At point L1 the rock is still undamaged and hence elastic when the first failed band forms which also is the case at point R1.
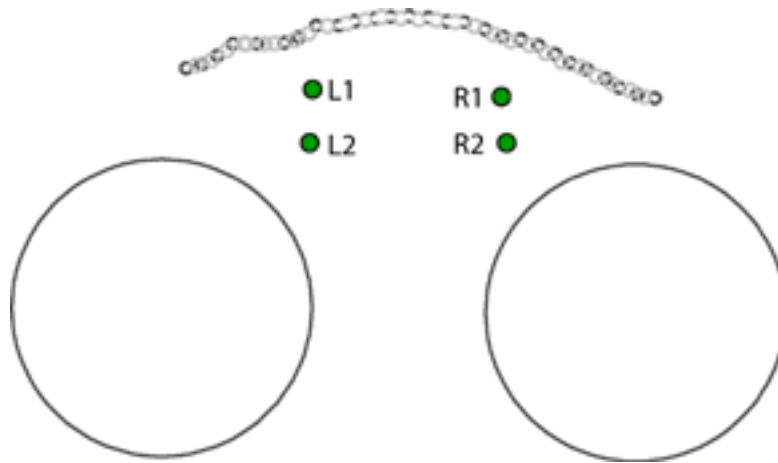
*Figure 10-28. Location of the stress points in relation to the large holes and the slot.*

In the Mohr – Coulomb model the elastic minor principal stresses at point L1, Figure 10-29, is approximately zero at modelling stage 13 (before the failed zone develop) and –11 MPa at the stage the failed zone develop (stage 14, Figure 10-18). At point R1, Figure 10-30, the elastic minor principal stress is approximately –12 MPa at stage 19 (before the failed zone develop) and –19 MPa when the failed zone develops (stage 20, Figure 10-22).

The Mohr – Coulomb model without the tensile strength cut off indicates more tensile stresses after failure. This depends on that the model generally first yields elements in shear. A group of elements yielded in tension then acts like islands in which tensile stresses act. This occurrence is more unusual in the other type of Mohr – Coulomb model since elements there often fail in both shear and tension at the same stage.

In the Hoek – Brown model the minor principal stress is 5 to 6 MPa at the stage before the yield-ing occurs and 2 to 3 MPa after it yielded. The yielding in this model does not initiate at the same locations as the Mohr – Coulomb model but in the early stages of the model two failed zones are indicated (Figure 10-26). These are initiated at stage 10 and 11 for point L1 and R1 respectively.
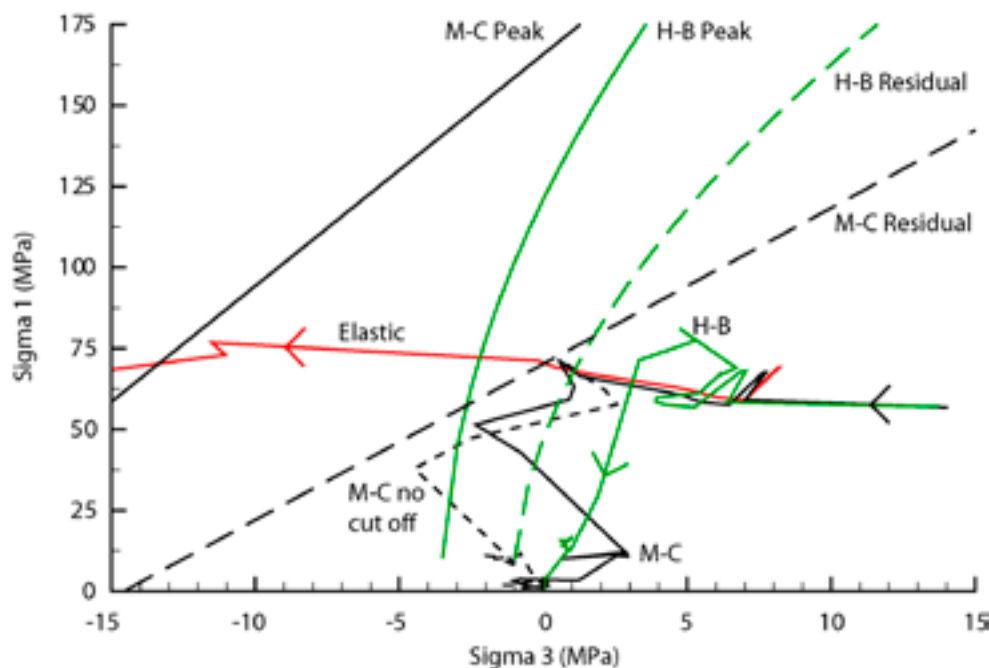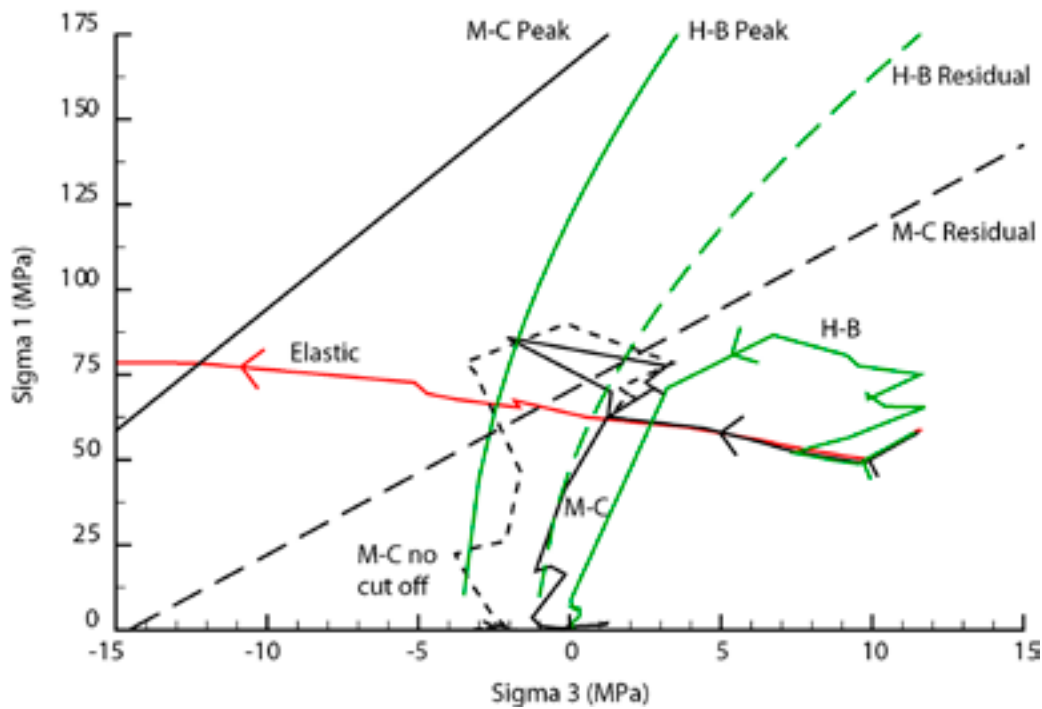


*Figure 10-29. Stress path for point L1.*

**Figure 10-30.** *Stress path for point R1.*

In both Mohr – Coulomb models the tensile stress at point L2 (Figure 10-31) is about –1 MPa at stage 13 (before the failure occurs). At R2 (Figure 10-32) the stress is approximately –7.5 MPa (with tensile cut off) and –9.5 MPa (without cut off) the stage before the failure occurs (stage 19 with tensile cut off and stage 18 without).

The confining stress in the Hoek – Brown model is approximately 4 and 3 MPa for L2 and R2 respectively.
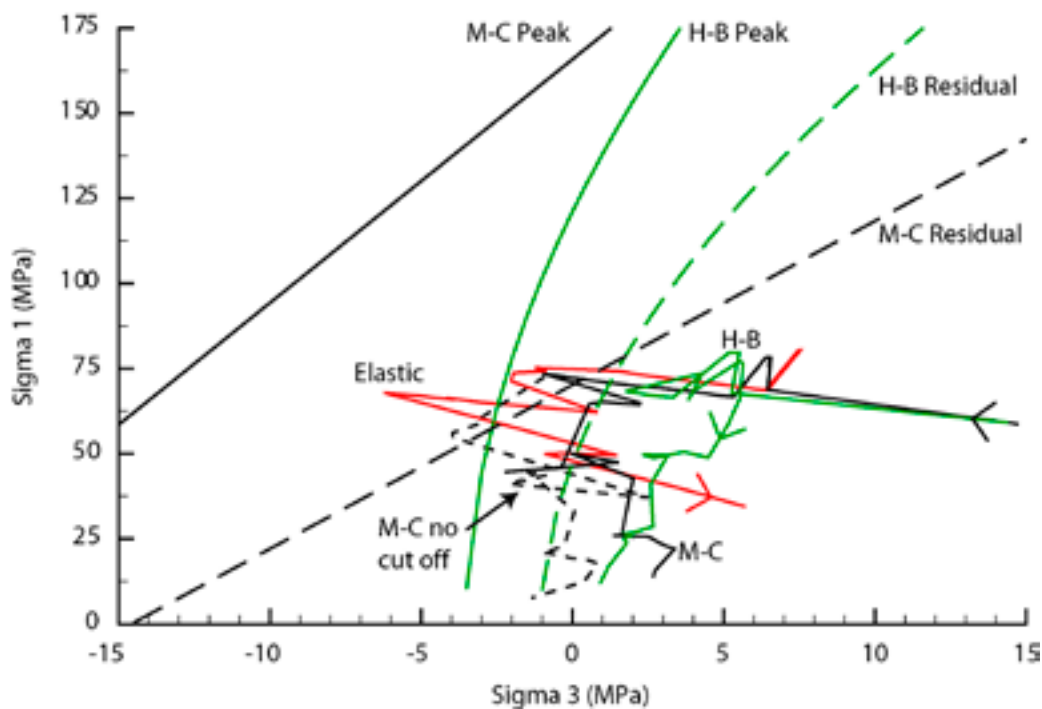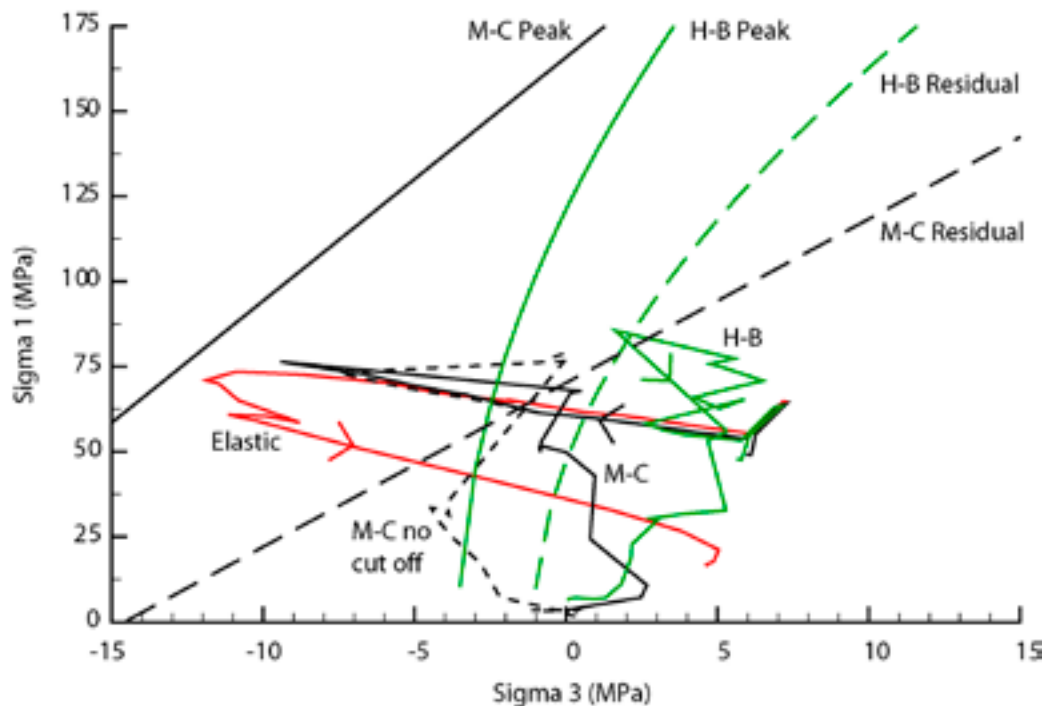


**Figure 10-31.** *Stress path for point L2.*

**Figure 10-32.** *Stress path for point R2.*
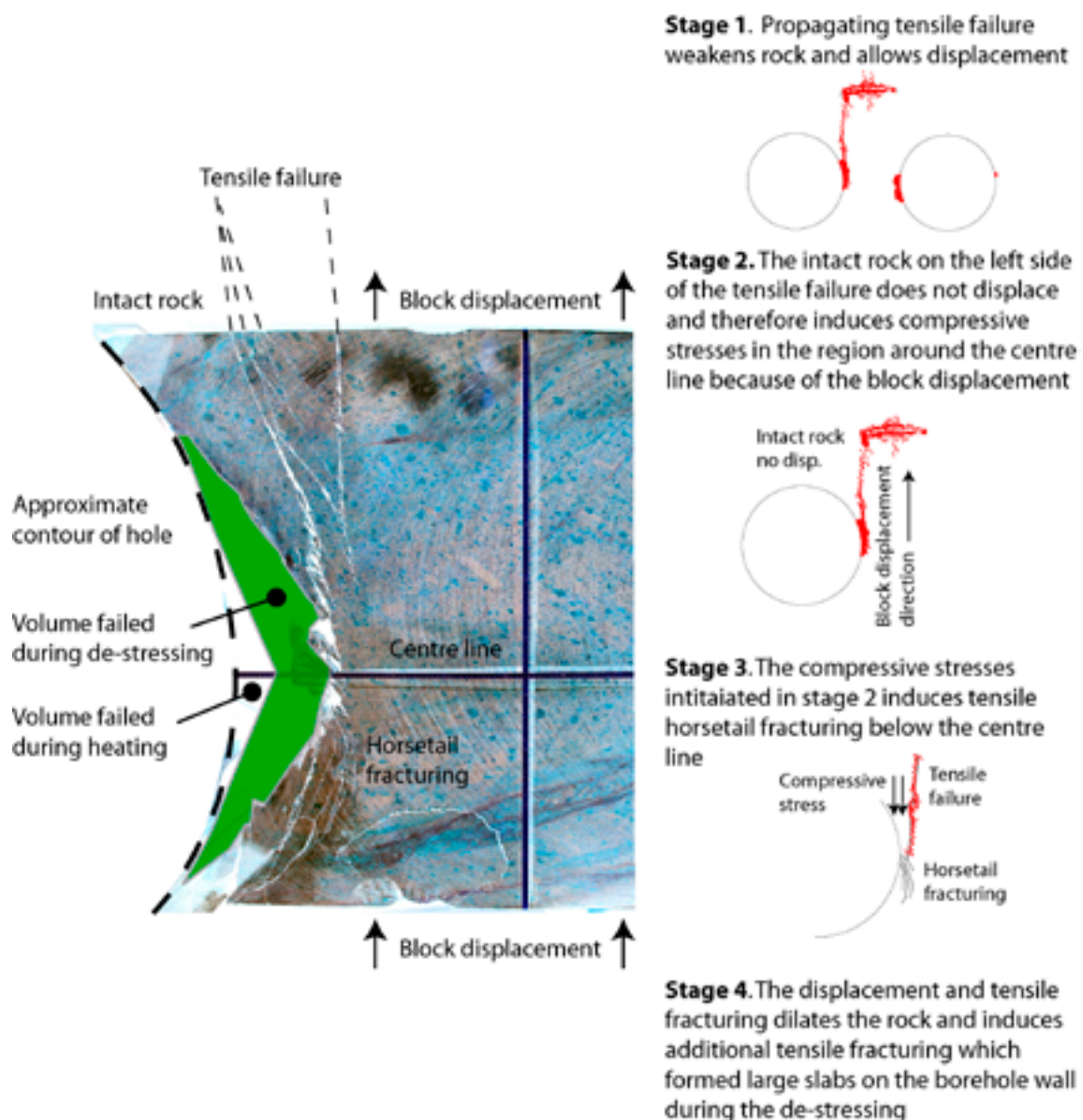
## 10.5 Discussion

It is clear that the Mohr – Coulomb models works quite well up to the stage when the failed zones had been developed (stage 20, Figure 10-22). After that more extensive yielding occurs in the model which not was observed in situ.

The Hoek – Brown model gives a poor representation of the field observations. The yielding in the model is initiated at earlier stages than observed and in the final model stages it indicates yielding of the entire pillar volume which clearly not is the case.

When yielding is initiated and the model applies the residual strength of the rock mass the results and the in situ observations starts to deviate. A conclusion is therefore that modelling results obtained after extensive yielding of the model are not reliable. Staging of the model is therefore important and the first indication of the failure geometry should be used because the understanding of the failure and the post failure processes in the rock is not very well known.

The studied stress paths indicate that the tensile stresses are very close to the tensile strength at yielding and it is assessed that the rock has primarily failed in tension. The failure was initiated close to the slot and propagated towards the pillar. The tensile failures weakened the rock until displacements in the shear direction could occur. This process created the shear band like formations seen in for example Figure 10-13. At the deepest part of the notch in Figure 10-14 the characteristics of the fractures are different and the observed horsetail fracturing is likely tensile fracturing. They may have formed as the shear displacements took place. It is likely that the slabs presented in Figure 10-5 formed then. A likely scenario for the forming of the horsetail fractures and the slabs is illustrated in Figure 10-33.

No natural fractures were included in the numerical models. The correlation between the observed displacements of fractures 08 and 14 during the de-stress drilling and the yielding in the Mohr – Coulomb model confirms the modelling results. As the pillar displaced towards the slot the nearby fractures were affected.

**Stage 1.** Propagating tensile failure weakens rock and allows displacement

**Stage 2.** The intact rock on the left side of the tensile failure does not displace and therefore induces compressive stresses in the region around the centre line because of the block displacement

**Stage 3.** The compressive stresses intitaiated in stage 2 induces tensile horsetail fracturing below the centre line

**Stage 4.** The displacement and tensile fracturing dilates the rock and induces additional tensile fracturing which formed large slabs on the borehole wall during the de-stressing

*Figure 10-33. Illustration of how the tensile failures induced the horsetail fractures and the additional yielding or the pillar wall during the de-stress drilling.*

The results presented in this chapter clearly illustrates that neither the Mohr – Coulomb or the Hoek – Brown failure criteria represent the behaviour of the rock at low compressive or tensile stresses accurately enough. For example: Hoek – Brown underestimates the rock mass strength as illustrated in Figure 10-27 and Mohr – Coulomb indicates a failed zone that not was observed in situ, Figure 10-20. It is however difficult to acquire the needed information about this process to enhance the model accuracy. The sample has to be subjected to both compressive and tensile stresses at the same time. New testing procedures are hence likely required.

138

# 11    Discussion and conclusions

The Äspö pillar stability experiment was carried out to examine the failure process in a heterogeneous rock mass when subjected to coupled excavation-induced and thermal-induced stresses. Prior to the APSE experiment stress-induced failure had only been observed at a few locations around the tunnels excavated at the Äspö HRL. Hence it was not known prior to the experiment the stress magnitudes required to cause failure. Because of this uncertainty the experiment was designed using the observational approach. This approach provided the flexibility required to modify the design if the design assumptions proved to be in error.

Extensive scoping calculations using two and three dimensional elastic stress analyses were carried out to: (1) reduce the uncertainty for the far-field in situ stresses, (2) establish the geometry for the access tunnel that would provide an elevated uniform stresses in the floor of the tunnel, and (3) the optimum width of the pillar. It was concluded based on the rock mass characteristics that a 1 m-wide pillar formed by two 1.75-m diameter boreholes would meet the design objectives. Thermal modelling showed that thermally-induced stresses in the pillar were adequate to elevate the pillar stresses above the stress magnitude expected to initiate failure. The failure stress was established from laboratory tests on intact rock and was expected to occur in the range from 80 to 135 MPa.

The rock mass yielding (spalling) strength for the Äspö diorite was calculated at 18 discrete points at the pillar wall and determined to be $(0.59 \pm 0.03)\sigma_c$. This value does though not apply to mylonitized or highly oxidized granitic rocks where the yielding strength was slightly lower than the yielding strength for fresh Äspö Diorite. The onset of crack initiation in uniaxial laboratory tests, determined from strain gauge data, was found to occur at approximately $(0.45 \pm 0.03)\sigma_c$ and with the AE method it was assessed to $(0.56 \pm 0.16)\sigma_c$. It was shown that that the onset of AE events in situ occurred when the tangential stress exceeded $0.43\sigma_c$. For sites with absence of in situ data it is recommended that the lower-bound value from the strain gauge method may be used for assessing the in situ rock mass spalling strength. The stress magnitude associated with on set of cracking in laboratory tests based on acoustic emission data is more difficult to assess.

The visual observation showed that the extent of spalling is sensitive to small changes in the stress magnitudes. It was determined using three dimensional modelling that changes in the tangential stress magnitude of only approximately 1 MPa was sufficient to cause yielding of the pillar to propagate. However, observations suggest that without this stress change yielding of the rock mass would not occur. In other words, there was essentially no evidence for time-dependent processes over the monitoring period used in the experiment.

The fractures formed during the yielding first forms as small chips tangential to the borehole wall underneath larger and larger chips are formed. The observations of the yielding process indicate that except from in the deepest part of the notch all fractures are formed in tension.

/Fairhurst and Cook 1966/ discussed rock splitting parallel to the direction of maximum compression in the neighbourhood of a surface. A modified Griffith theory /Griffith 1924/ was used to describe fracture initiation in a compressive environment. The tensile fractures are described to initiate in stress concentrations at the borders of flaws always present in a rock specimen. They then propagate parallel to the direction of the maximum compressive stress since the least amount of energy is required to propagate a fracture in this direction. Before the fracture can propagate the stress has to exceed the Griffith compressive strength. Additional stress is then required to propagate the fracture further.

The high tangential stresses acting at the boundary of the APSE pillar combined with the absent confinement at the boundary of the borehole wall results in high deviatoric stresses. When the stress exceeds the Griffith compressive strength the induced extensile force at the end points of the flaw induces a fracture that propagates and forms a slab (Figure 11-1). Because of the curvature of the boundary the slabs get a somewhat arched shape. When the first slab has formed the stresses are re-distributed and the stress at another flaw exceeds the Griffith strength and a new slab is formed. It is likely that the buckling process described by Fairhurst and Cook is what propagates the fractures to the boundary of the hole.

When flaws are initiated and fractures propagate deeper into the notch, the radii of the re-distributed stress path decrease. This has a self stabilizing effect because of increasing confining stress and because buckling is efficiently suppressed by the short fracture lengths. At this stage slabs can still form by the same process but this time along the notch's walls where high deviatoric stresses now are induced. This fracturing is however relatively soon suppressed by the increasing confining pressure and the complete notch is in a quasi state of equilibrium. As earlier described (Section 8.1.8) a distinct stress threshold value has to be reached before yielding is initiated or a previous yielded volume re-activated. This seems to correlate well with the theory that the Griffith strength has to be exceeded before fracture propagation is initiated. The conclusions by Fairhurst and Cook also correlate well with the step wise occurring displacements and AE activity.

A conclusion drawn is that the slabs formed during the experiment are initiated inside the pillar wall at the location of the maximum tangential stress and then grows towards the boundary of the hole as extension fractures. Buckling of the slabs may likely be what forces the fractures to grow to the boundary of the hole. The extremely thin chips/slabs that were the first ones to develop are an indication that there is no evidence of an excavation damaged zone that has re-distributed the stress at the boundary of the hole.

The conclusions from this experiment are very similar to the findings from the Mine by Experiment at URL in Canada both in terms of yielding strength and the fracture propagation during yielding. This confirms the validity of the APSE experiment results.
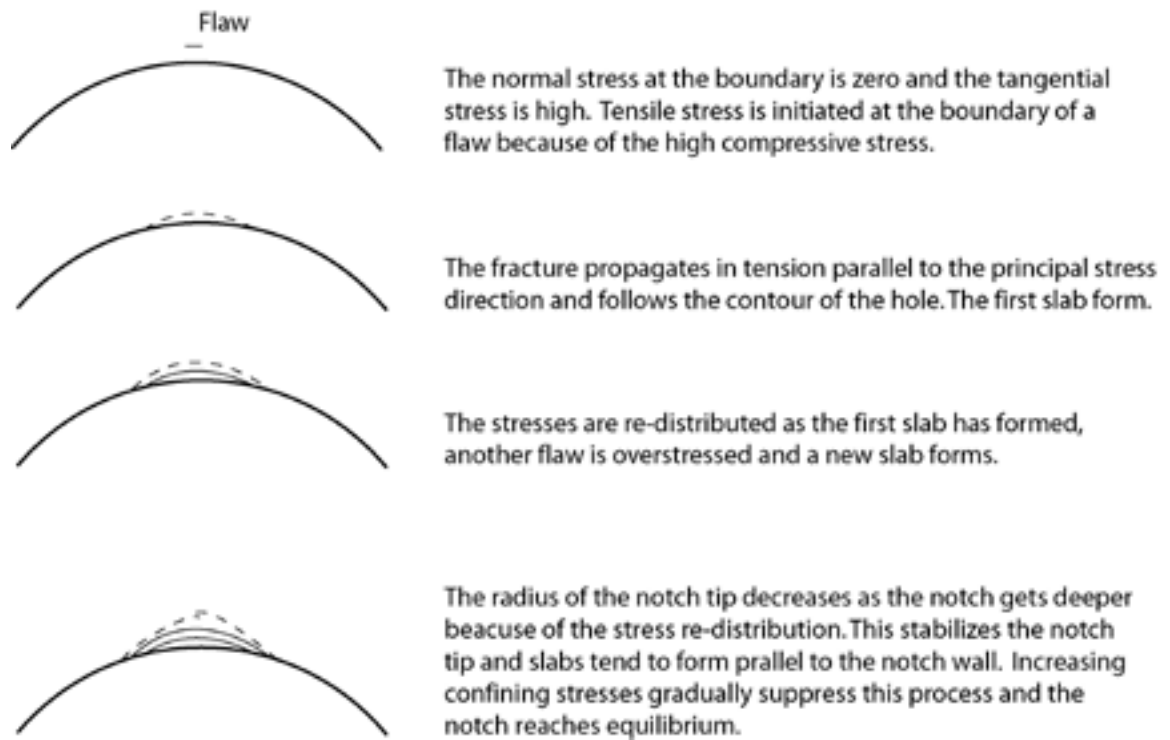
APSE results are also confirmed by case histories presented by /Edelbro 2006/. Data originating from sites with hard granitic rocks and limited fracturing has been taken from that report. The stress around the openings was back calculated and compared with the uniaxial compressive strength of the rock. The stress, strength ratios determined corresponds reasonably well with the ratio at which Äspö diorite yields. It should be noted that the in situ stress and the rock mass strength for the case histories has a large span.

The APSE results are confirmed by other experiments and observations but there are also cases where the results not apply. The results can hence not be applied to any granitic rock without studying the properties of the particular rock mass in detail.

It has been shown that the initiation of yielding is highly sensitive to low confinement pressures, a few hundred kPa.

Back calculations of the de-stress drilling of the pillar have indicated that it likely is a propagating tensile failure that has caused the failed zones in the blocks and the remaining pillar wall. The tensile fractures have weakened the rock and enabled displacements in the shear direction along the fracture planes. The resulting fracture pattern is very similar to a shear band indicating that many failures described as shear failures may have a tensile origin.

The modelling of the de-stress drilling clearly illustrates that neither the Mohr – Coulomb or the Hoek – Brown failure criteria represent the behaviour of the rock at low compressive or tensile stresses accurately enough. As presented in Chapter 10 the Hoek – Brown failure criterion underestimates the rock mass strength and the Mohr – Coulomb criterion indicates a failed zone that not was observed in situ. To enhance the model accuracy in this respect is difficult because laboratory testing at these stress regimes is difficult to perform. The sample has to be subjected to both compressive and tensile stresses at the same time which indicate the need for modified testing procedures.

**Flaw**

The normal stress at the boundary is zero and the tangential stress is high. Tensile stress is initiated at the boundary of a flaw because of the high compressive stress.

The fracture propagates in tension parallel to the principal stress direction and follows the contour of the hole. The first slab form.

The stresses are re-distributed as the first slab has formed, another flaw is overstressed and a new slab forms.

The radius of the notch tip decreases as the notch gets deeper beacuse of the stress re-distribution. This stabilizes the notch tip and slabs tend to form prallel to the notch wall. Increasing confining stresses gradually suppress this process and the notch reaches equilibrium.

*Figure 11-1.* *Illustration of the fracturing process in the Pillar Stability Experiment.*

# 12    Recommendations

The observations of the progressive yielding of the pillar should be studied in detail and compared with existing fracture mechanic theories. The information from this experiment is unique in its level of detail and can likely reveal new information of rock mass yielding.

The data set should be used to develop fracture mechanic codes that better captures the yielding processes for this type of loading. The codes generally indicate that the fractures are initiated and propagated in shear. The observations from the experiment indicate on the other hand that it is extensional fractures that are developing.

More work should be performed to study the radial expansion effect and the physics behind this observation.

It is important to better understand the absence of yielding in the confined hole as the confinement pressure was reduced. It could be investigated if it is induced micro fracturing that is a part of the explanation. This study should also look at the hole walls opposite to the pillar. These parts of the hole did not yield either even though they became highly stressed during the drilling of the de-stress slot.

Amplitude studies of the AE data set could be used to make an analysis of the failure mode of the recorded events. This study should in that case also include a detailed analysis of how the AE system should have been set up to capture the energy releases that occurred during the times of observed fracturing and displacements that did not trigger it.

Velocities for a number of ray paths between the transmitters and receivers were determined every night, with a few exceptions, throughout the experiment. This data set should be studied. A more detailed understanding about the yielding and micro fracturing in the pillar during the experiment can then likely be derived.

Drilling of a sub-horizontal core borehole in the rock volume between the de-stress slot and the pillar wall could be used to study the failed zones in more detail.

# 13 References

**Andersson J C, Johansson Å, 2002.** Boring of full scale deposition holes at the Äspö Hard Rock Laboratory. Operational experiences including boring performance and a work time analysis. SKB TR-02-26. Svensk Kärnbränslehantering AB.

**Andersson J C, 2003.** Äspö Pillar Stability Experiment, Summary of preparatory work and predictive modelling. SKB R-03-02. Svensk Kärnbränslehantering AB.

**Andersson J C, Martin C D, 2003.** Katsuhiko Sugawara and Yuozo Obara and Akira Sato (ed.) Stress variability and the design of the Äspö Pillar Stability Experiment. In the proceedings of the third international symposium on rock stress. RS Kumamoto '03, 4–6 November 2003, Kumamoto Japan, p 321–326.

**Andersson J C, Fälth B, Kristensson O, 2006.** Äspö Pillar Stability Experiment – TM back calculation. In the proceedings of GeoProc 2006. May 22-24, Nanjing, China.

**Backers T, Stephansson O, Rybacki E, 2002.** Rock Fracture Toughness Testing in Mode II – Punch-Through Shear Test. Int. J. Rock Mech. & Min. Sci, 39: 755–769.

**Barton N, 2003.** Äspö Hard Rock Laboratory. Äspö Pillar Stability Experiment. Q-logging of the TASQ tunnel at Äspö. For rock quality assessment and for development of preliminary model parameters. SKB report IPR-04-07. Svensk Kärnbränslehantering AB.

**Bergman S G A, Stille H, 1983.** Rock burst problem in a 2.6 million $m^3$ underground crude oil storage in granite. In the proceedings of the Fifth international congress on rock mechanics, Melbourne, Vicotria, Australia.

**Brace W F, Paulding B, Scholz C, 1966.** Dilatancy in the fracture of crystalline rocks. J. of Geophysical Research. 71: 3939–3953

**Brown E T, 1981.** Rock characterization, testing and monitoring. ISRM suggested methods. Pergamon Press, 107–127.

**Chang Y, 1994.** Tunnel Support with Shotcrete in Weak Rock. –A Rock Mechanics Study. Doctoral Thesis Division of Soil and Rock Mechanics. Royal institute of Technology. Stockholm, Sweden 1994.

**Christiansson R, Janson T, 2002.** Test with three different stress measurement methods in two orthogonal boreholes. In the proceedings of NARMS-TAC 2002. The 5th North American Rock Mechanics Symposium, Toronto, Canada July 7–11, 2002, p. 1429–1436.

**CIMNE, 2000.** CODE_BRIGHT. A 3-D program for thermo-hydro-mechanical analysis in geological media. Departemento de Ingeniería del Terreno; Cartográfica y Geofística, UCP, Barcelona, Spain.

**Donath B, 2002.** Stiffness of rock fractures – an experimental investigation. Diploma thesis. Technical University of Berlin.

**Edelbro C, 2006.** Strength of hard rock masses –a case study. Luleå University of Technology. Department of Civil and Environmental Engineering. Division of Geotechnical Engineering. 2006:13

**Eng A, Andersson J C, 2004.** Äspö Hard Rock Laboratory. Äspö Pillar Stability Experiment. Description of the displacement and temperature monitoring system. SKB R-04-15. Svensk Kärnbränslehantering AB.

**Eliasson T, 1993.** Mineralogy, geochemistry and petrophysics of red-coloured granite adjacent to fractures. SKB TR-93-06. Svensk Kärnbränslehantering AB.

**Eberhardt E, Stead D, Stimpson B, Read R, 1998.** Identifying crack initiation and propagation thresholds in brittle rocks. Can. Geotech. J. 35: 222–233.

**Fairhurst C, Cook N G W, 1966.** The phenomenon of rock splitting parallel to the direction of maximum compression in the neighbourhood of a surface. Proceedings of the 1st Congress of the International Society of Rock Mechanics, Lisbon 1966, pp. 687–692

**Fälth B, Kristensson O, Hökmark H, 2005.** Äspö Hard Rock Laboratory. Äspö Pillar Stability Experiment. Thermo-mechanical 3D back analyze of the heating phase. SKB report IPR-05-19. Svensk Kärnbränslehantering AB.

**Griffith A A, 1924.** Theory of Rupture, First Intern. Congr. Appl. Mech. (Delft) 1924, pp 55–63.

**Hakami H, 2003.** Äspö Hard Rock Laboratory. Update of the rock mechanical model 2002. SKB report IPR-03-37. Svensk Kärnbränslehantering AB.

**Hakkala M, Heikkilä E, 1996.** Summary report – Development of laboratory test and the stress – strain behaviour of Olkiluoto mica gneiss. Posiva report Posiva-97-04. ISBN 951-652-029-4.

**Haycox J R, Pettitt W S, Young R P, 2005.** Äspö Pillar Stability Experiment. Acoustic Emissions and Ultrasonic Monitoring. SKB R-05-09. Svensk Kärnbränslehantering AB.

**Hoek E, Brown E T, 1980.** Undergorund Excavations in Rock. Institute of Mining and Metallurgy, London, England.

**Holcomb D J, Martin R J, 1985.** Determining peak stress history using acoustic emissions. In the proceedings of the 26th U.S. Symp. on Rock Mechanics, Rapid City, USA. pp. 715–722.

**Itasca Consulting Group, Inc. 2002.** FLAC3D (Fast Lagrangian Analysis of Continua in 3 Dimensions). Version 2.1. Minneapolis. USA.

**Ivars D M, 2005.** Äspö Hard Rock Laboratory. Äspö Pillar Stability Experiment. Hydromechanical data acquisition experiment at the APSE site. SKB report IPR-05-21. Svensk Kärnbränslehantering AB.

**Lampinen H, 2005.** Äspö Hard Rock Laboratory. Äspö Pillar Stability Experiment. Detailed geological mapping of the pillar blocks. SKB report IPR-05-24. Svensk Kärnbränslehantering AB.

**Magnor B, 2004.** Äspö Hard Rock Laboratory. Äspö Pillar Stability Experiment. Geological mapping of tunnel TASQ. SKB report IPR-04-03. Svensk Kärnbränslehantering AB.

**Martin C D, Chandler N A, 1994.** The progressive fracture of Lac du Bonnet granite. Int. J. Rock Mech. Min. Sci. & Geomech. Abstr, 31, 643–659.

**Martin C D, Read R S, 1996.** AECL's Mine-by Experiment: A test tunnel in brittle rock. In the proceedings of NARMS 1996, Quebec, Canada.

**Martin C D, Read R S, Martino J B, 1997.** Observations of brittle failure around a circular test tunnel. Int. J. Rock Mech. Min. Sci. 34 (7), pp.1065–1073.

**Martin C D, 1997.** Seventeenth Canadian Geotechnical Colloquium: The effect of cohesion loss and stress path on brittle rock strength. Can. Geotech. J. 34 (1997) 698–725.

**Martin C D, Maybee W G, 2000.** The strength of hard-rock pillars. Int. J. Rock Mech. Min. Sci. 37, 1293–1246.

**Olsson M, Niklasson B, Wilson L, Andersson J C, Christiansson R, 2004.** Äspö HRL Experiences of blasting of the TASQ tunnel. SKB R-04-73. Svensk Kärnbränslehantering AB.

**Ortlepp W D, 1997.** Rock fracture and rock bursts, an illustrative study. The South African institute of mining and metallurgy, Johannesburg.

**Ouchterlony F, 1988.** Suggested methods for determining the fracture toughness of rock. Int. J. Rock Mech. Min. Sci. & Geomech. Abstr., 25: 71–96.

**Peck R B, 1969.** Advantages and limitations of the observational method in applied soil mechanics. Geotechnique, vol 19, no. 2, pp. 171–187.

**Pestman B J, Van Munster J G, 1996.** Microstructural analysis of uniaxially deformed sanstone-evidence of intergranular microcrack growth. Int. J. Rock Mech. Min. Sci. 34, 3, pp. 374.

**Rhén I, Gustafson G, Stanfors R, Wikberg P, 1997.** Äspö HRL – Geoscientific evaluation 1997/5. Models based on site characterization 1986–1995. SKB TR-97-06. Svensk Kärnbränslehantering AB.

**Read R S, 2004.** 20 years of excavation response to studied at AECL's Underground Research Laboraotry. Int. J. Rock Mech. Min. Sci. 41 (2004) 1251–1275.

**Rocscience. www.rocscience.com.**

**Shen B, Rinne M, Stephansson O, 2005.** FRACOD2D Users Manual ver 2.0 2005.

**Scholz C H, 1968.** Experimental study of the fracturing process in brittle rocks. J. Geophys. Res., 73, pp. 1447–1454.

**Stacey T R, 1981.** A simple extension strain criterion for fracture of brittle rock. Int. J. Rock Mech. Min. Sci. 18: 469–474.

**Staub I, Andersson J C, Magnor B, 2004.** Äspö Pillar Stability Experiment, Geology and mechanical properties of the rock in TASQ. SKB R-04-01. Svensk Kärnbränslehantering AB.

**Stille H, Groth T, Fredriksson A, 1982.** FEM-analys av bergmekaniska problem med JOBFEM. Report 307:1/82, Swedish rock engineering research, SveBefo, Stockholm.

**Wikman H, Kornfält K-A, 1995.** Updating the lithological model of the bedrock of the Äspö area. SKB PR-25-89-06. Svensk Kärnbränslehantering AB.

# 14 Published APSE reports and papers

**Andersson J C, 2003.** Äspö Pillar Stability Experiment, Feasibility Study. SKB IPR-03-01. Svensk Kärnbränslehantering AB.

**Andersson J C, 2003.** Äspö Pillar Stability Experiment, Summary of preparatory work and predictive modelling. SKB R-03-02. Svensk Kärnbränslehantering AB.

**Andersson J C, Martin C D, Christiansson R, 2004.** SKB's Äspö Pillar Stability Experiment, Sweden. In the proceedings of Gulf Rocks 2004, the 6th North American Rock Mechanics Symposium (NARMS), Houston, Texas, June 5–9, 2004.

**Andersson J C, Rinne M, Staub I, Wanne T, Stephansson O, Hudson J A, Jing L (ed), 2003.** The on-going pillar stability experiment at the Äspö Hard Rock Laboratory, Sweden. In the proceedings of GeoProc 2003, International conference on coupled T-H-M-C processes in Geo-systems: Fundamentals, Modelling, Experiments & Applications. KTH, October 13–15, 2003, Stockholm, Sweden, p. 385–390.

**Andersson J C, Martin C D, 2003.** Katsuhiko Sugawara and Yuozo Obara and Akira Sato (ed.) Stress variability and the design of the Äspö Pillar Stability Experiment. In the proceedings of the third international symposium on rock stress. RS Kumamoto '03, 4–6 November 2003, Kumamoto Japan, p. 321–326.

**Andersson J C, Eng A, 2005.** Äspö Pillar Stability Experiment. Final experiment design, monitoring results and observations. SKB R-05-02. Svensk Kärnbränslehantering AB.

**Andersson J C, 2005.** Äspö Pillar Stability Experiment. In the proceedings of the 40th Rock Mechanics Meeting, Stockholm March 14, 2005. Edited by SveBeFo, Swedish Rock Engineering Research.

**Andersson J C, Fälth B, Kristensson O, 2006.** Äspö Pillar Stability Experiment – TM back calculation. In the proceedings of GeoProc 2006. May 22–24, Nanjing, China.

**Andersson J C, 2007.** Rock Mass Response to Coupled Mechanical Thermal Loading. Äspö Pillar Stability Experiment, Sweden. Doctoral Thesis in Soil and Rock Mechanics. Royal Institute of Technology. Stockholm, Sweden 2007.

**Andersson J C, Martin C D.** The Äspö Pillar Stability Experiment: Part I – Experiment design. Submitted to: Int. J. Rock Mech. Min. Sci.

**Andersson J C, Martin C D, Stille H.** The Äspö Pillar Stability Experiment: Part II – Rock mass response to coupled excavation-induced and thermal-induced stress. Submitted to: Int. J. Rock Mech. Min. Sci.

**Barton N, 2004.** Äspö Hard Rock Laboratory, Äspö Pillar Stability Experiment, Q-logging of the APSE tunnel at Äspö, For rock quality assessment and for development of preliminary model parameters. SKB IPR-04-07. Svensk Kärnbränslehantering AB.

**Eng A, Andersson J C, 2004.** Äspö Pillar Stability Experiment. Description of the displacement and temperature monitoring system. SKB IPR-04-15. Svensk Kärnbränslehantering AB.

**Fransson Å, 2003.** Äspö Hard Rock Laboratory. Äspö Pillar Stability Experiment. Core boreholes KF0066A01, KF0069A01, KA3386A01 and KA3376B01: Hydrogeological characterization and pressure responses during drilling and testing. SKB IPR-03-06. Svensk Kärnbränslehantering AB.

**Fredriksson A, Staub I, Janson T, 2003.** Äspö Hard Rock Laboratory. Äspö Pillar Stability Experiment. Design of heaters and preliminary results from coupled 2D thermo-mechanical modelling. SKB IPR-03-03. Svensk Kärnbränslehantering AB.

**Fredriksson A, Staub I, Outters N, 2004.** Äspö Pillar Stability Experiment, Final 2D coupled thermo-mechanical modelling. SKB R-04-02. Svensk Kärnbränslehantering AB.

**Fälth B, Kristensson O, Hökmark H, 2005.** Äspö Hard Rock Laboratory, Äspö Pillar Stability Experiment. Thermo-mechanical 3D back analyze of the heating phase. SKB IPR-05-19. Svensk Kärnbränslehantering AB.

**Haycox J R, Pettitt W S, Young R P, 2005.** Äspö Pillar Stability Experiment. Acoustic Emission and Ultrasonic Monitoring. SKB R-05-09. Svensk Kärnbränslehantering AB.

**Lampinen H, 2005.** Äspö Hard Rock Laboratory. Äspö Pillar Stability Experiment. Detailed geological mapping of the pillar blocks. SKB IPR-05-24. Svensk Kärnbränslehantering AB.

**Magnor B, 2004.** Äspö Hard Rock Laboratory. Äspö Pillar Stability Experiment. Geological mapping of tunnel TASQ. SKB IPR-04-03. Svensk Kärnbränslehantering AB.

**Olsson M, Niklasson B, Wilson L, Andersson J C, Christiansson R, 2004.** Aspö HRL Experiences of blasting of the TASQ tunnel. SKB R-04-73. Svensk Kärnbränslehantering AB.

**Pöllänen J, Rouhainen P, 2002.** Äspö Hard Rock Laboratory. Difference flow measurements in boreholes KA3386A01, KF0066A01 and KKF0069A01 at the Äspö HRL. SKB IPR-02-55. Svensk Kärnbränslehantering AB.

**Pöllänen J, Rouhainen P, 2003.** Äspö Hard Rock Laboratory. Difference flow measurements in borehole KA3376B01 at the Äspö HRL. SKB IPR-03-07. Svensk Kärnbränslehantering AB.

**Rinne M, Baotang A, Lee H-S, 2003.** Äspö Hard Rock Laboratory. Äspö Pillar Stability Experiment. Modelling of fracture stability by Fracod. Preliminary results. SKB IPR-03-05. Svensk Kärnbränslehantering AB.

**Rinne M, Lee H-S, Shen B, 2004.** Äspö Pillar Stability Experiment, Modelling of fracture development of APSE by FRACOD. SKB R-04-04. Svensk Kärnbränslehantering AB.

**Sjöberg J, 2003.** Äspö Hard Rock Laboratory. Äspö Pillar Stability Experiment. 3D overcoring rock stress measurements in borehole KA3376B01 at Äspö HRL. SKB IPR-03-16. Svensk Kärnbränslehantering AB.

**Staub I, Janson T, Fredriksson A, 2003.** Äspö Hard Rock Laboratory. Äspö Pillar Stability Experiment. Geology and properties of the rock mass around the experiment volume. SKB IPR-03-02. Svensk Kärnbränslehantering AB.

**Staub I, Andersson J C, Magnor B, 2004.** Äspö Pillar Stability Experiment, Geology and mechanical properties of the rock in TASQ. SKB R-04-01. Svensk Kärnbränslehantering AB.

**Wanne T, Johansson E, 2003.** Äspö Hard Rock Laboratory. Äspö Pillar Stability Experiment. Coupled 3d thermo-mechanical modelling. Preliminary results. SKB IPR-03-04. Svensk Kärnbränslehantering AB.

**Wanne T, Johansson E, 2004.** Potyondy, D. Äspö Pillar Stability Experiment, Final Coupled 3D thermo – mechanical modeling. Preliminary Particle – mechanical modeling. SKB R-04-03. Svensk Kärnbränslehantering AB.

## Data filter time intervals

| Time turn OFF | Time turn ON |
|---|---|
| 2004-05-12;15:20:00 | 2004-05-12;16:00:00 |
| 2004-05-14;15:00:00 | 2004-05-14;16:20:00 |
| 2004-05-18;10:08:00 | 2004-05-18;11:28:00 |
| 2004-05-18;15:55:00 | 2004-05-18;16:35:00 |
| 2004-05-25;10:02:00 | 2004-05-25;11:31:00 |
| 2004-05-25;12:53:00 | 2004-05-25;14:42:00 |
| 2004-05-25;15:39:00 | 2004-05-25;17:16:00 |
| 2004-05-27;10:35:00 | 2004-05-27;11:30:00 |
| 2004-05-27;12:34:00 | 2004-05-27;15:12:00 |
| 2004-05-28;12:52:00 | 2004-05-28;14:11:00 |
| 2004-06-01;13:37:00 | 2004-06-01;15:25:00 |
| 2004-06-02;08:16:00 | 2004-06-02;09:30:00 |
| 2004-06-02;16:15:00 | 2004-06-02;17:10:00 |
| 2004-06-03;13:25:00 | 2004-06-03;16:30:00 |
| 2004-06-04;08:30:00 | 2004-06-04;09:11:00 |
| 2004-06-04;13:20:00 | 2004-06-04;13:37:00 |
| 2004-06-08;12:38:00 | 2004-06-08;13:26:00 |
| 2004-06-16;10:19:00 | 2004-06-16;11:21:00 |
| 2004-06-16;12:49:00 | 2004-06-16;14:00:00 |
| 2004-06-17;08:36:00 | 2004-06-17;12:00:00 |
| 2004-06-23;09:45:00 | 2004-06-23;11:30:00 |
| 2004-06-29;10:21:00 | 2004-06-29;11:30:00 |
| 2004-06-29;12:43:00 | 2004-06-29;14:24:00 |
| 2004-07-02;14:20:00 | 2004-07-02;15:20:00 |
| 2004-07-06;10:10:00 | 2004-07-06;11:30:00 |
| 2004-07-12;13:03:00 | 2004-07-11;14:45:00 |
| 2004-07-15;20:07:00 | 2004-07-15;20:22:00 |
| 2004-08-03;10:03:00 | 2004-08-03;11:11:00 |

## Temperatures

In this appendix the temperatures at the N and S positions in the large holes are presented. To ease the comparison with other data presented a conversion table between date and experiment day is given in Table A2a-1.

**Table A2a-1. Conversion table between date and experiment day.**

| Date, 2004 | Experiment day |
|------------|----------------|
| 5/14       | 0              |
| 5/24       | 10             |
| 07/6       | 24             |
| 21/6       | 38             |
| 05/7       | 52             |
| 19/7       | 66             |
| 02/8       | 80             |
| 16/8       | 84             |
| 30/8       | 98             |
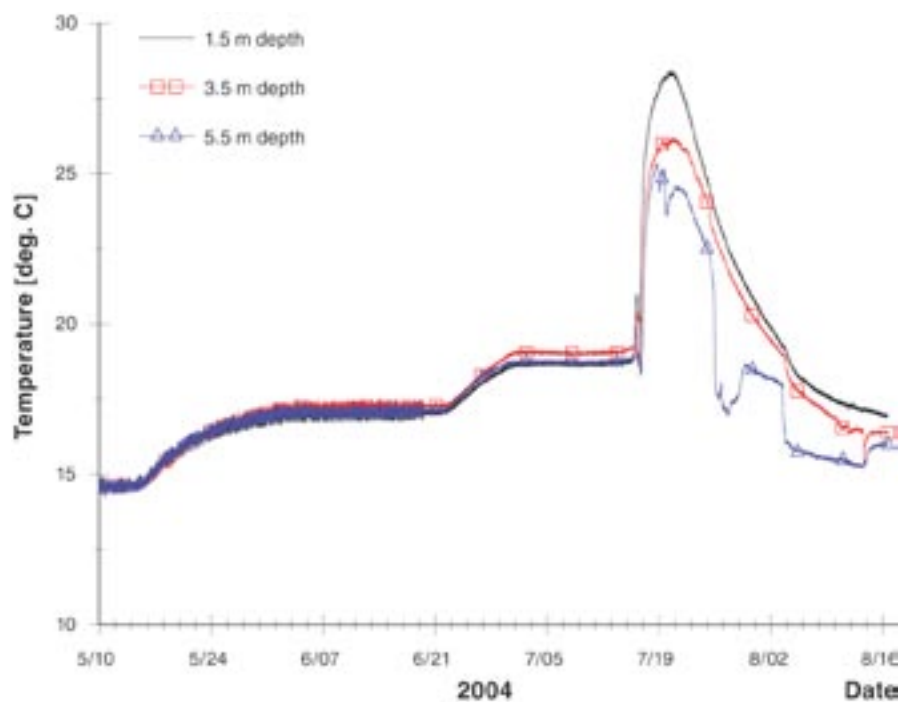


*Figure A2a-1.* *Measured temperatures in DQ0066G01 at position "N".*
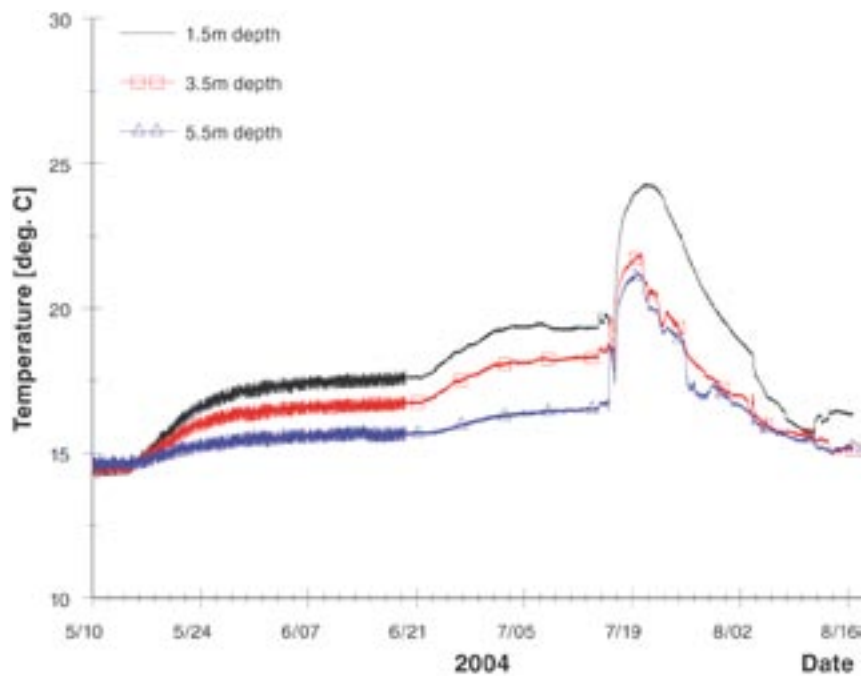
**Figure A2a-2.** *Measured temperatures in DQ0066G01 at position "S".*
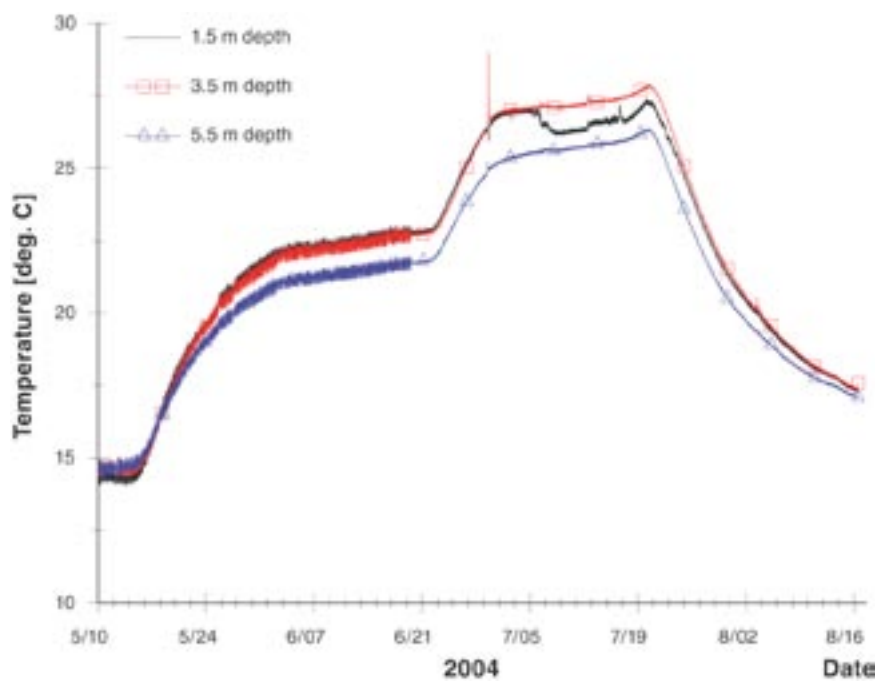


**Figure A2a-3.** *Measured temperatures in DQ0063G01 at position "N".*

154
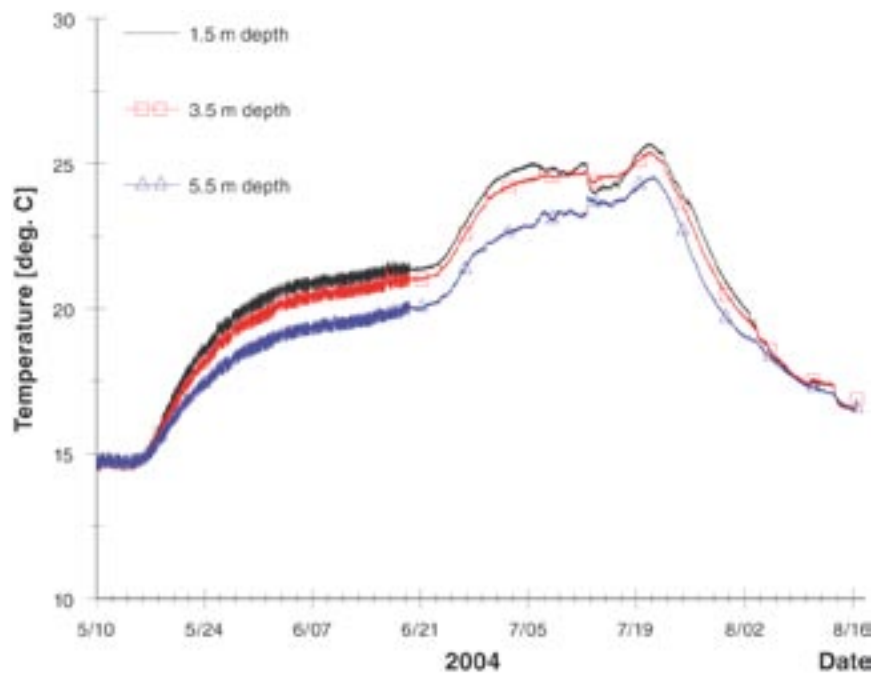
***Figure A2a-4.*** *Measured temperatures in DQ0063G01 at position "S".*

# Displacements

The monitored displacements for the individual transducers are presented in this appendix as well as displacements grouped on the left and right side of the centre pipe. An overview of the instrument position and numbers are given in Figure A2b-1, Table A2b-1 presents the exact depth and sensor type at each position. Figure A2b-2 to Figure A2b-23 includes displacement plots of each instrument position. On the three first instrument levels there are typically two instruments placed almost directly beneath each other at every measuring position, these are plotted together. The last set of figures (Figure A2b-24 to Figure A2b-27) present the deformations on the left and right side of the centre pipe.
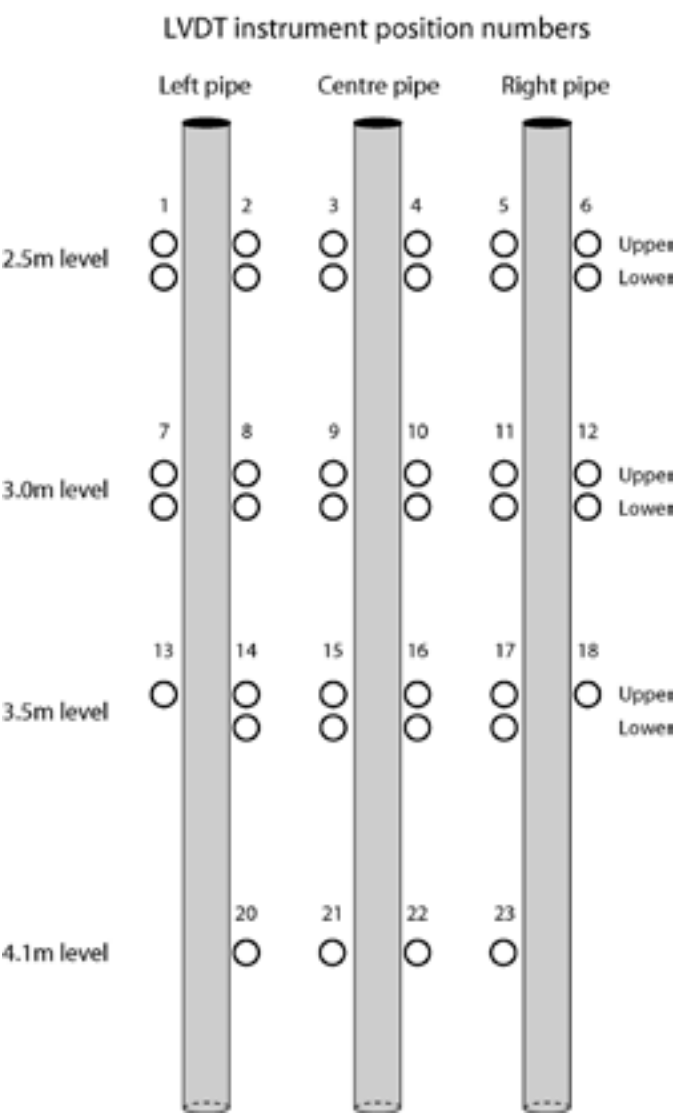


*Figure A2b-1.* LVDT positions and numbers.

**Table A2b-1.  Sensor row depths and type of sensors.**

| Level | Position # (from left) | Sensor type | Depth [m] (below −446.07 m) |
|---|---|---|---|
| 2.5 m upper | 1–6 | Long range | 2.46 |
| 2.5 m lower | 1–6 | Short range | 2.52 |
| 3.0 m upper | 2–12 | Short range | 2.99 |
| 3.0 m lower | 2–12 | Long range | 3.07 |
| 3.5 m upper | 13–18 | Long range | 3.50 |
| 3.5 m lower | 14–17 | Short range | 3.58 |
| 4.1 m upper | 20–23 | Short range | 4.10 |
| 4.1 m lower | – | Long range | Not installed |

A conversion table between date and experiment day is given in Appendix 2a.
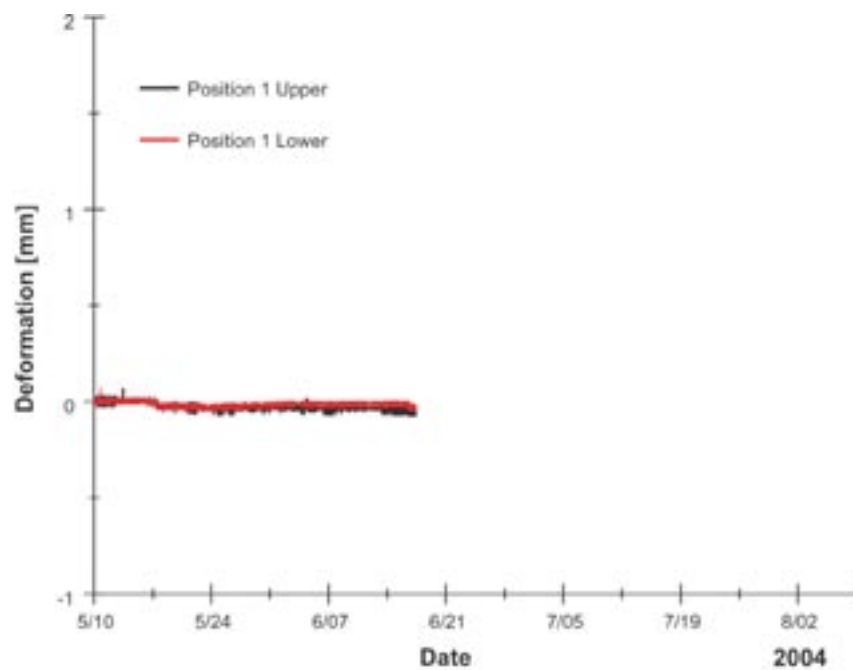


*Figure A2b-2.* *Deformations at instrument position 1.*

158
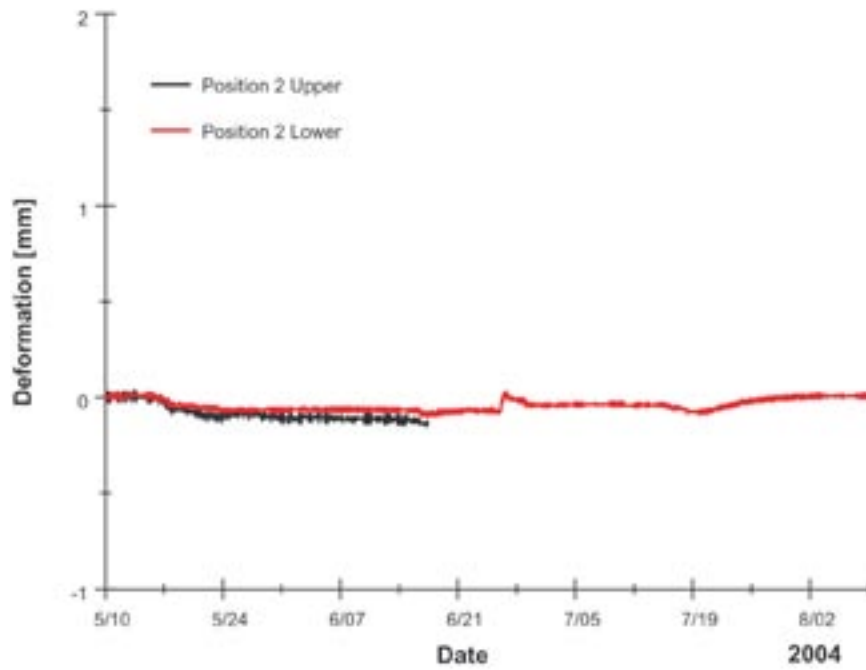
**Figure A2b-3.**  *Deformations at instrument position 2.*
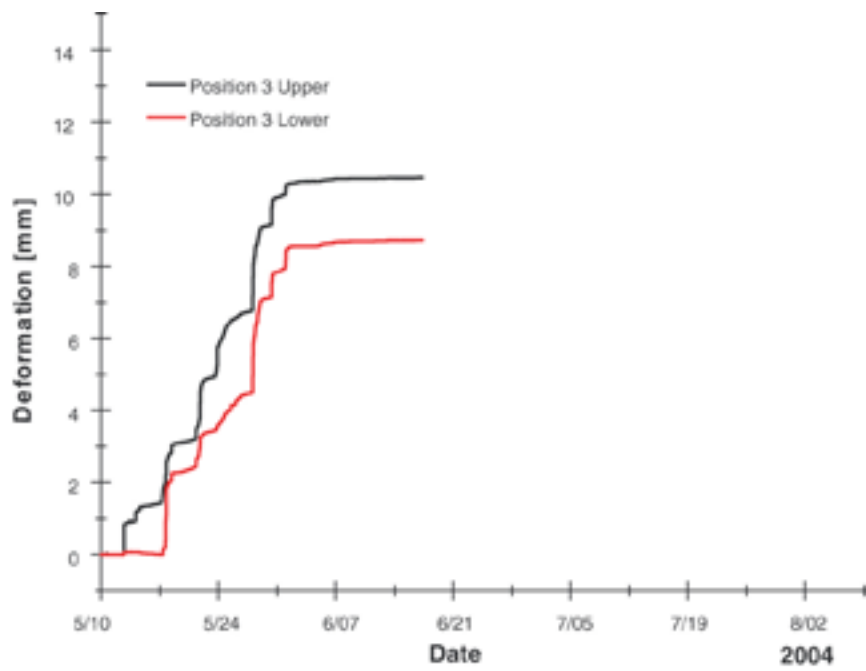


**Figure A2b-4.**  *Deformations at instrument position 3.*
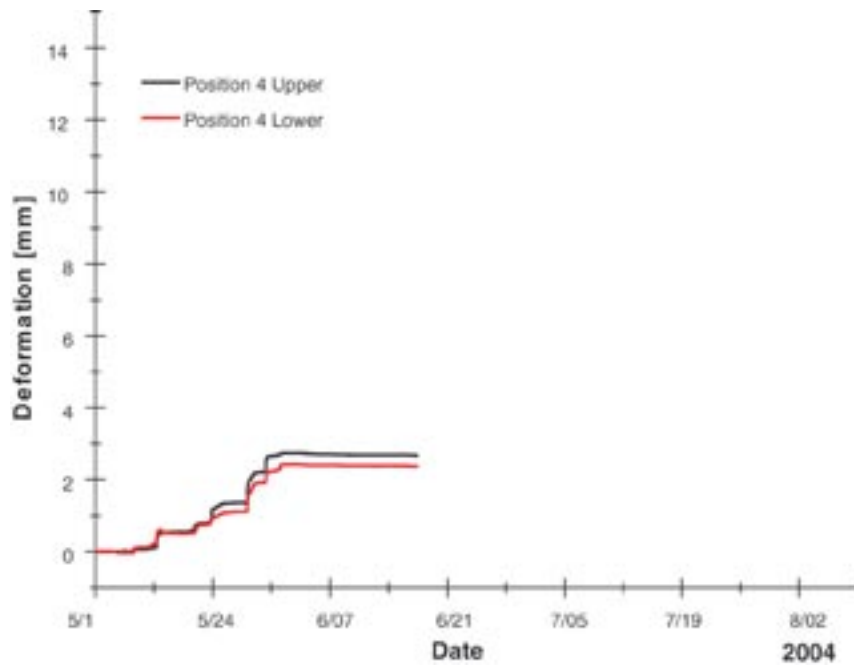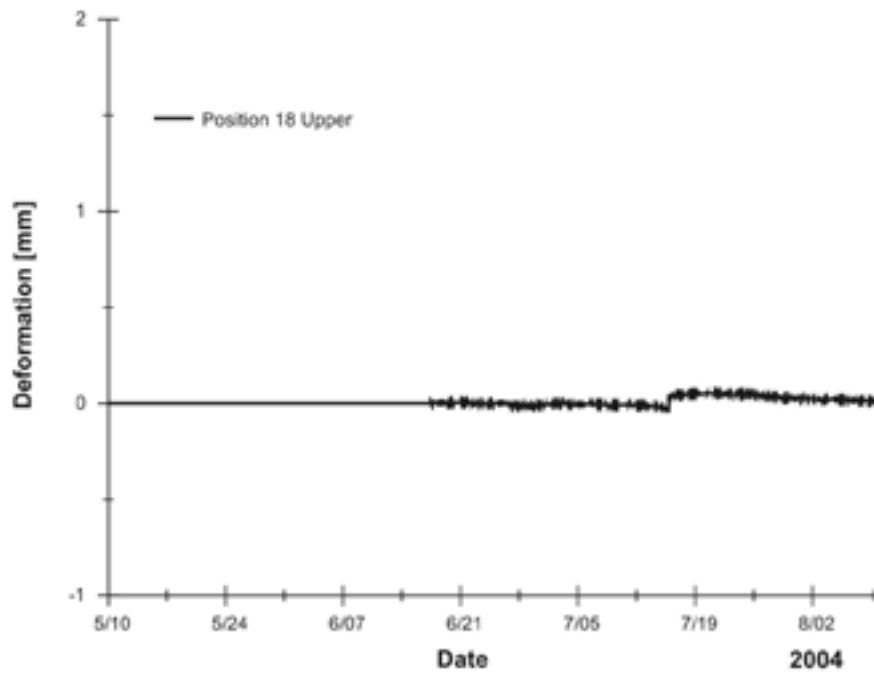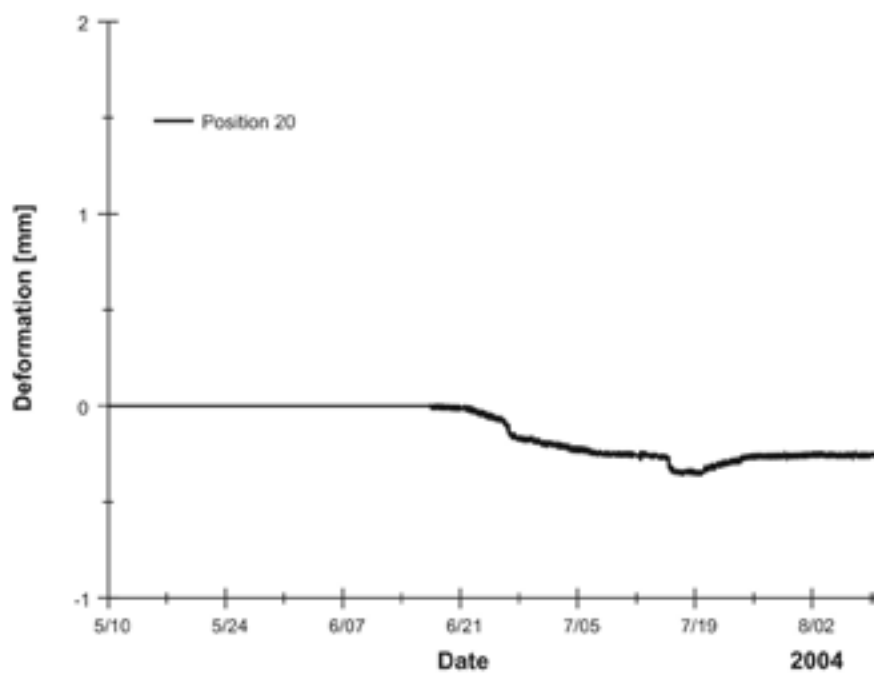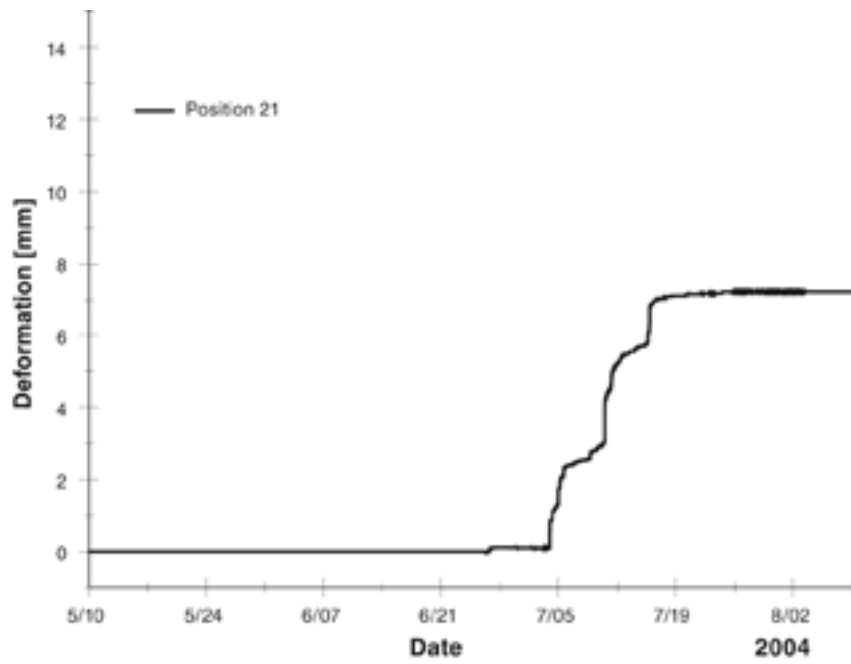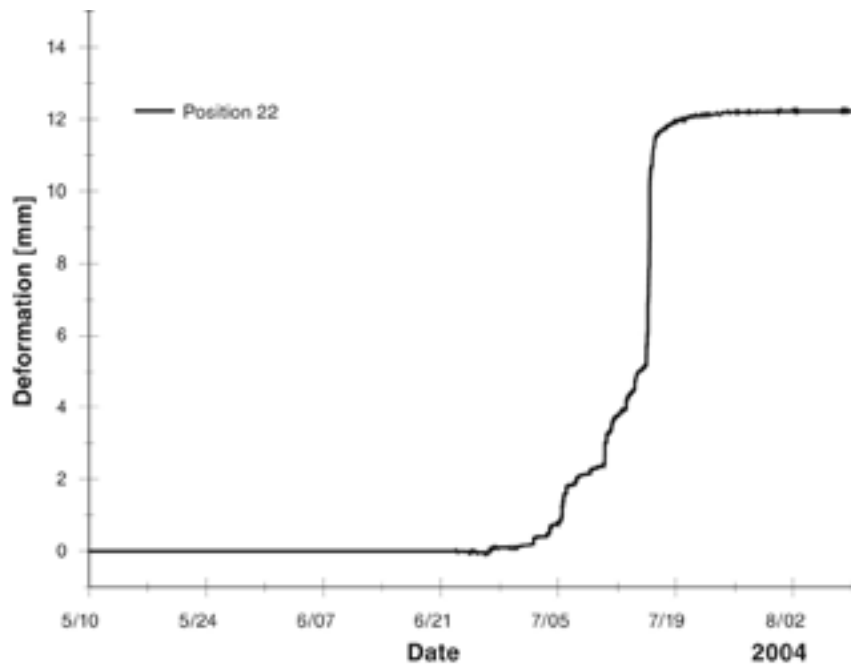
**Figure A2b-5.** *Deformations at instrument position 4.*
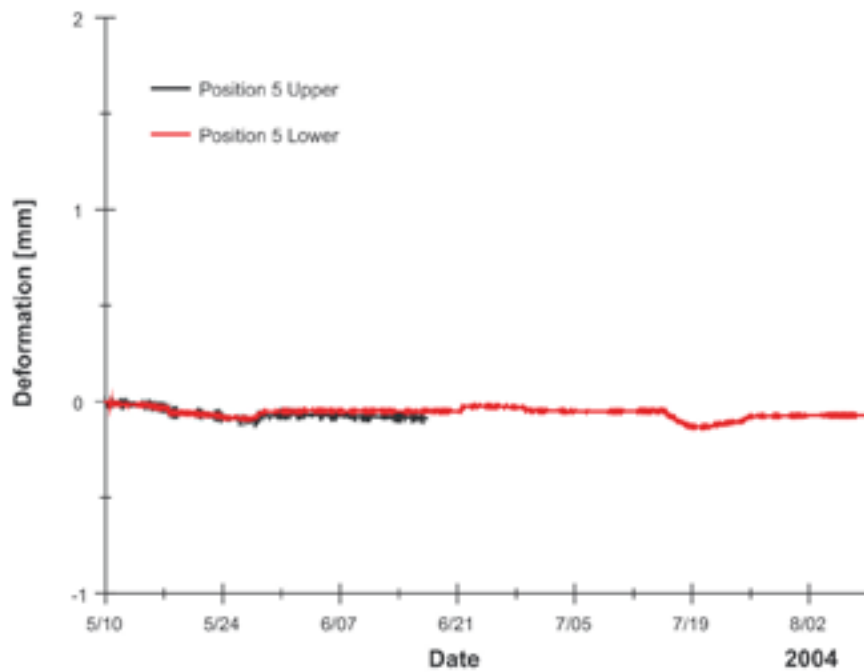


**Figure A2b-6.** *Deformations at instrument position 5.*

160
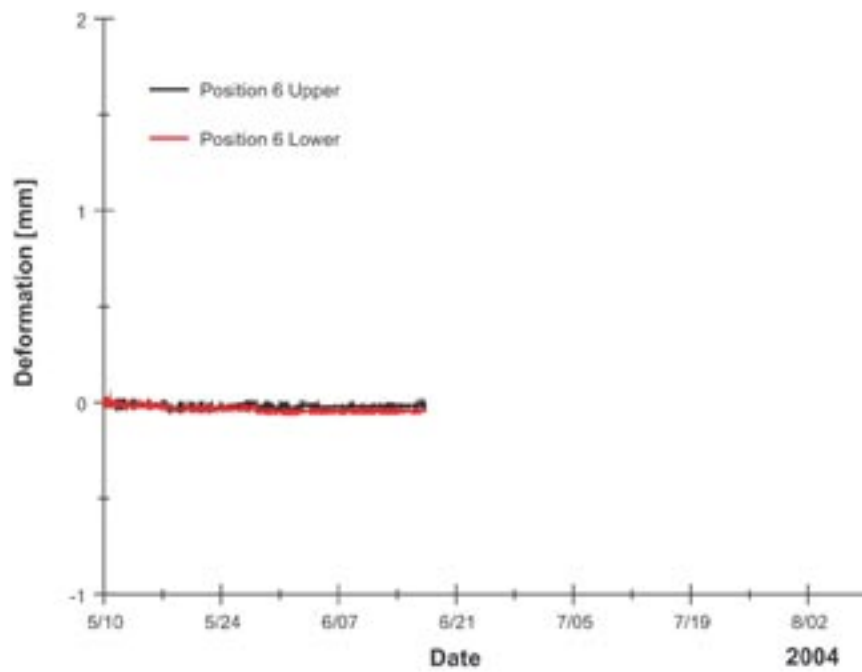
***Figure A2b-7.***  *Deformations at instrument position 6.*
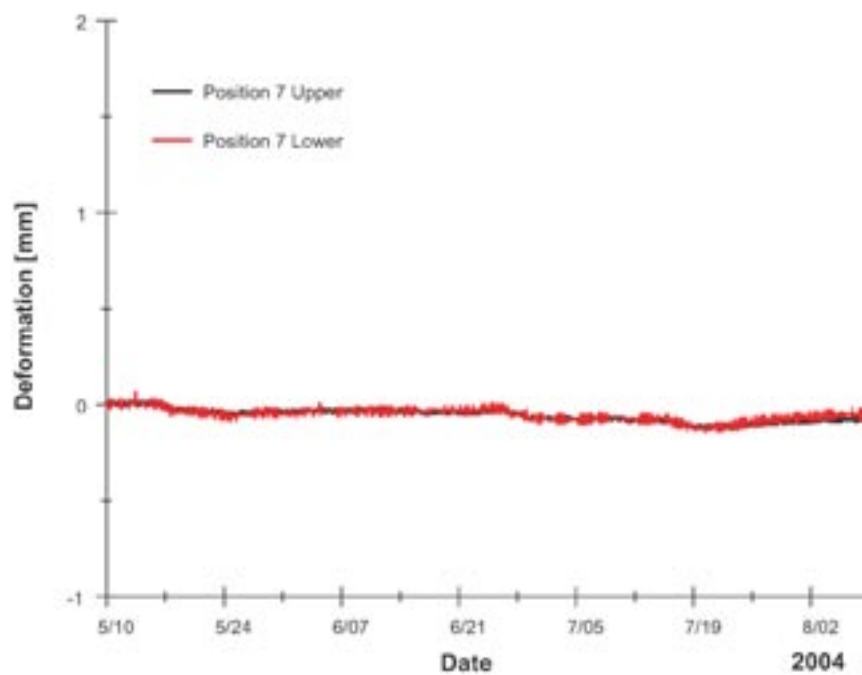


***Figure A2b-8.***  *Deformations at instrument position 7.*
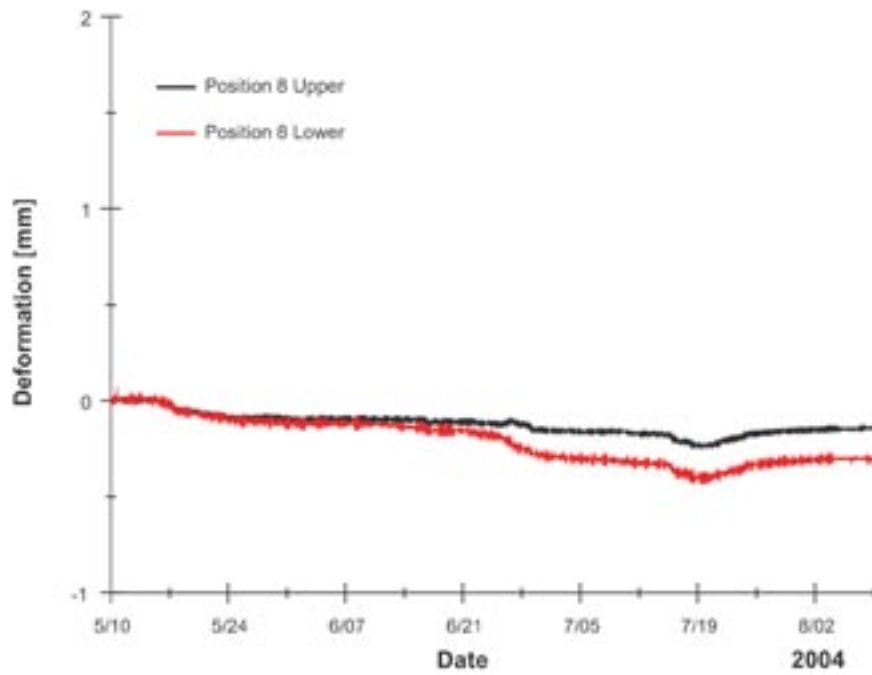
**Figure A2b-9.** *Deformations at instrument position 8.*
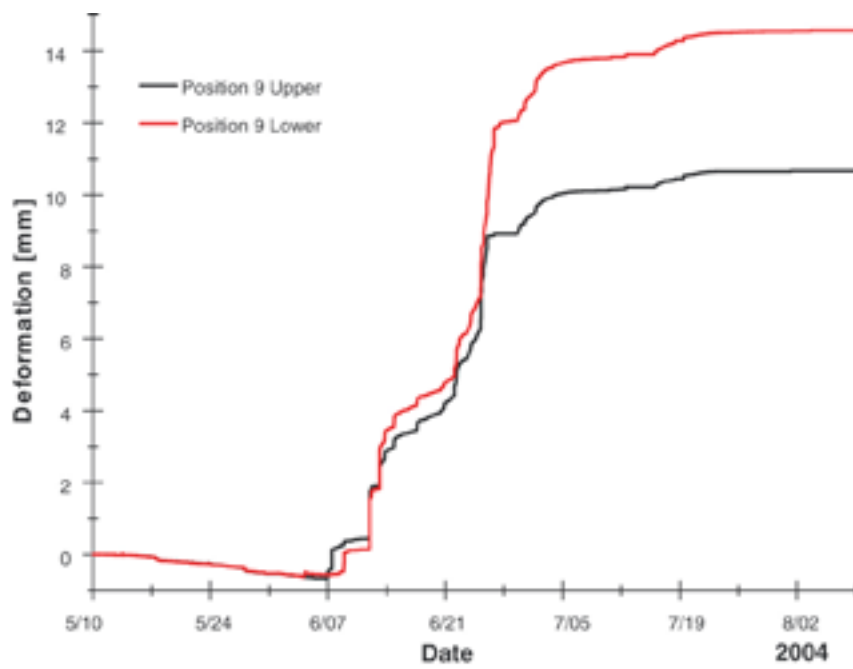


**Figure A2b-10.** *Deformations at instrument position 9.*
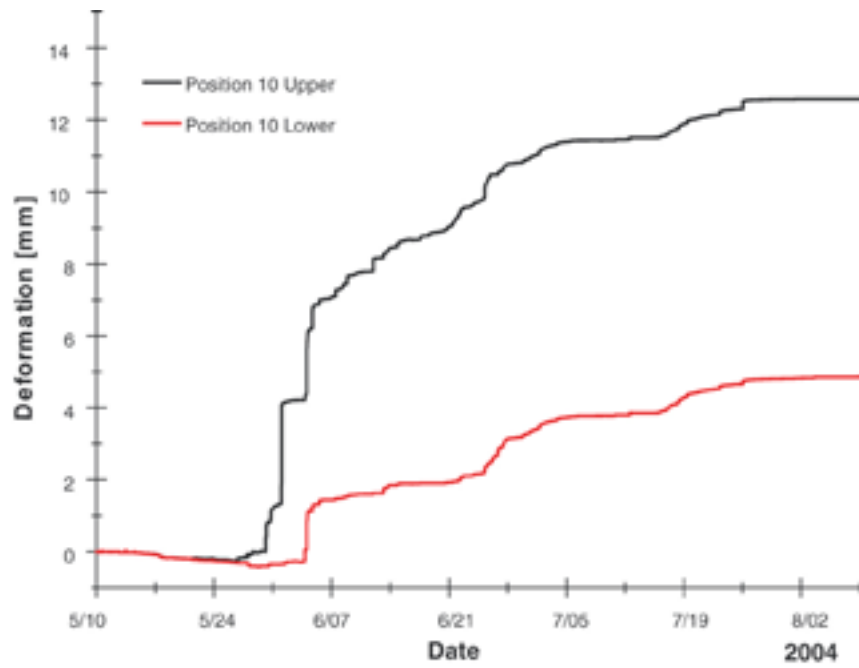
**Figure A2b-11.** *Deformations at instrument position 10.*
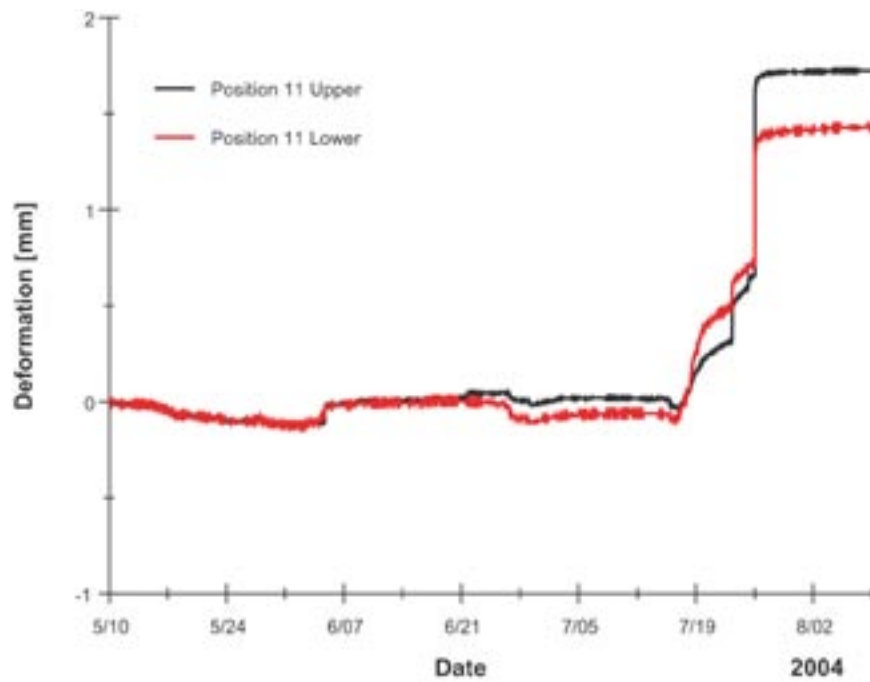


**Figure A2b-12.** *Deformations at instrument position 11.*

163
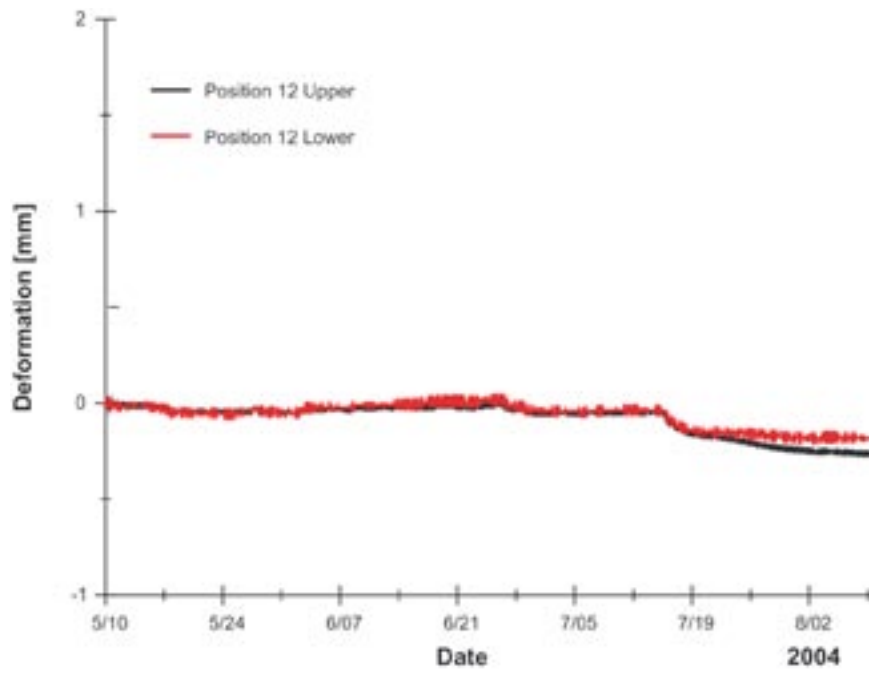
***Figure A2b-13.*** *Deformations at instrument position 12.*
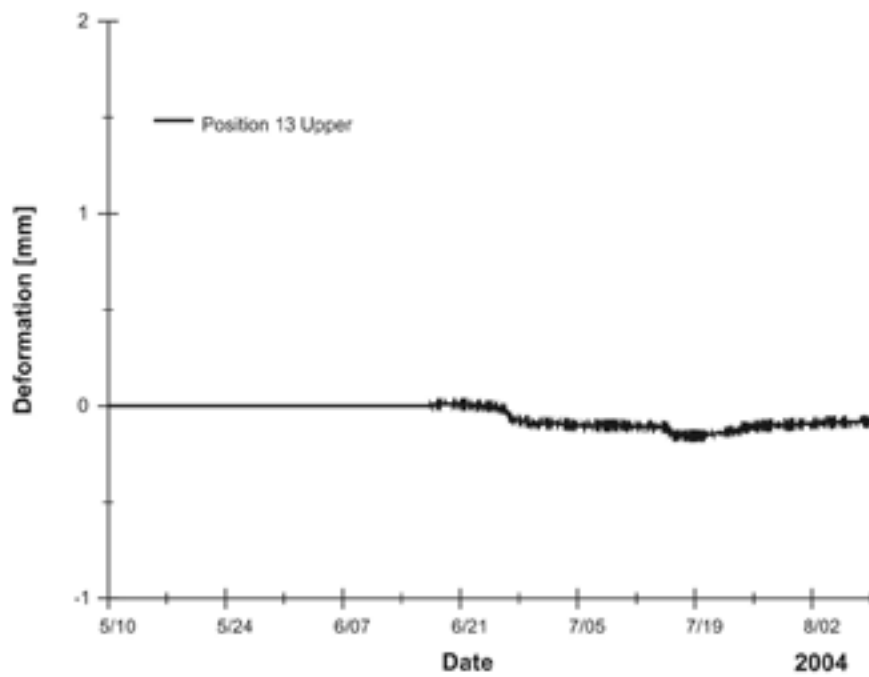


***Figure A2b-14.*** *Deformations at instrument position 13.*
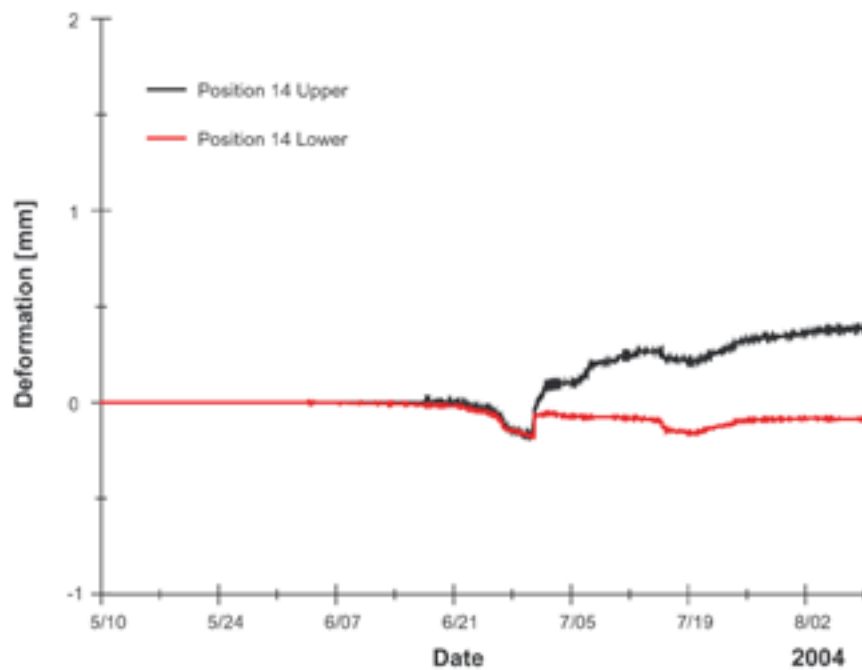
**Figure A2b-15.** *Deformations at instrument position 14.*
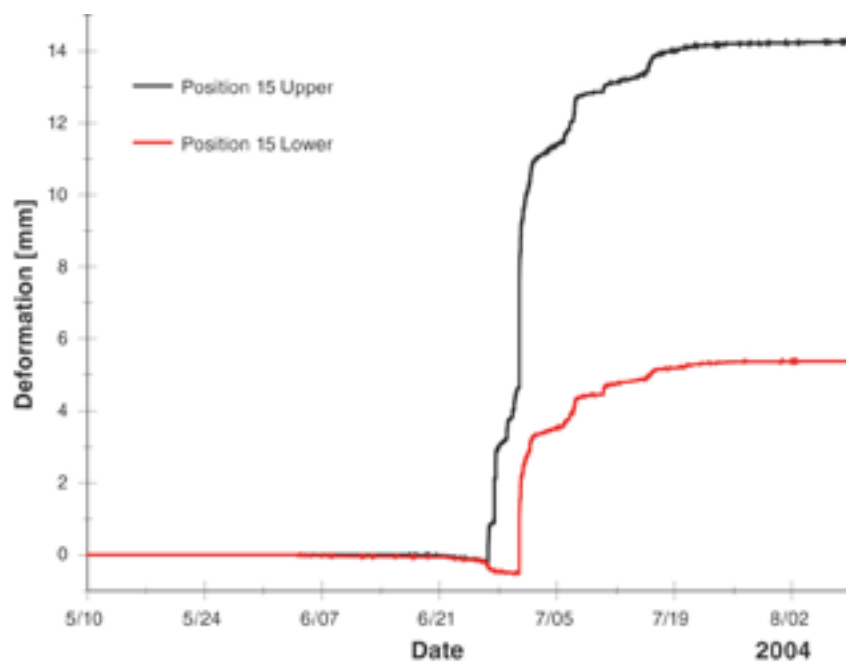


**Figure A2b-16.** *Deformations at instrument position 15.*
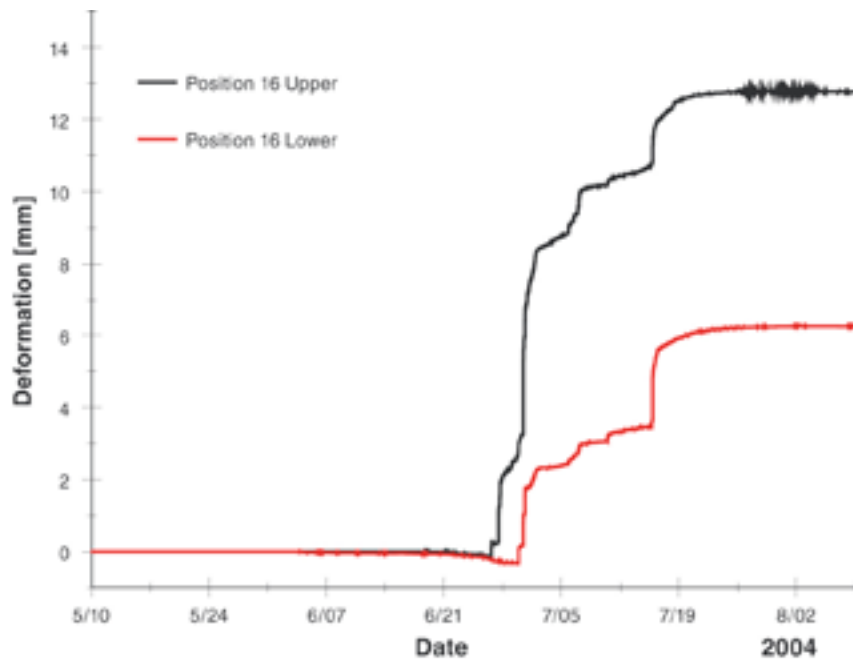
*Figure A2b-17.* *Deformations at instrument position 16.*
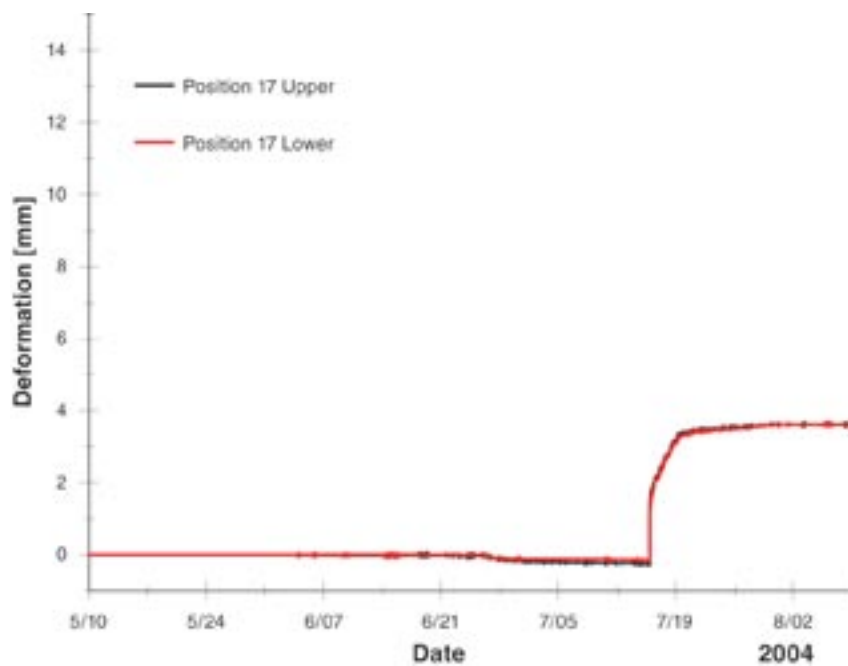


*Figure A2b-18.* *Deformations at instrument position 17.*

*Figure A2b-19.* *Deformations at instrument position 18.*



*Figure A2b-20.* *Deformations at instrument position 20.*

**Figure A2b-21.** *Deformations at instrument position 21.*



**Figure A2b-22.** *Deformations at instrument position 22.*

168
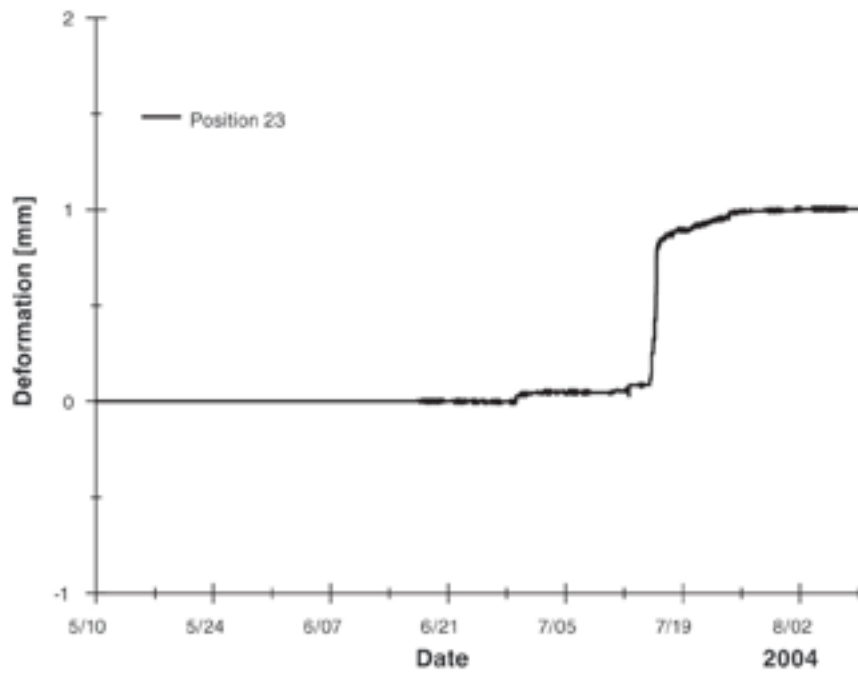
**Figure A2b-23.** *Deformations at instrument position 23.*

The displacements recorded with the transducers mounted on the left and right side of the centre pipe are presented in Figure A2b-24 to Figure A2b-27. The first two figures show plots for each of the instrument types on the left side, after which the plots from the right side are shown in the next two figures.
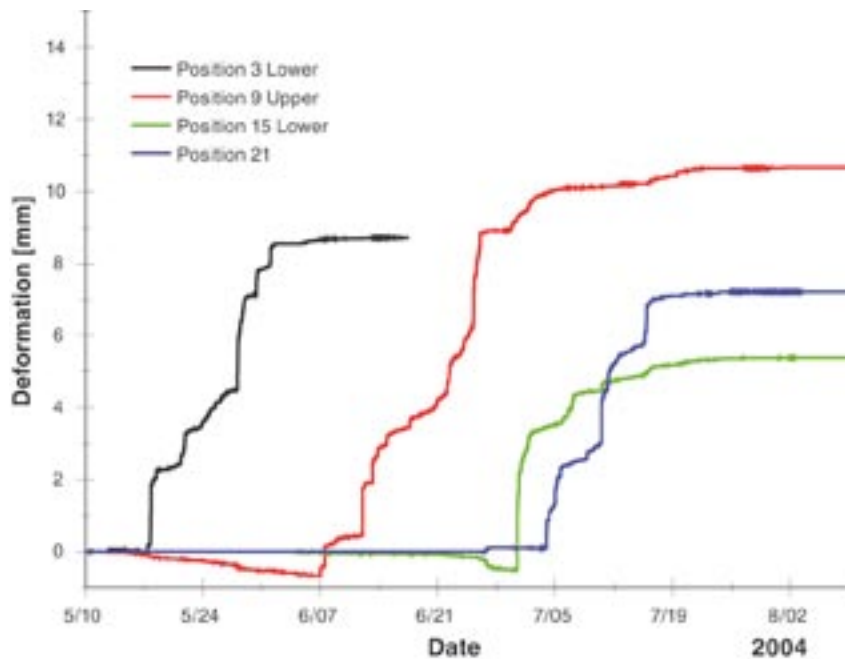


**Figure A2b-24.** *Deformation of the short-range sensors on the left side of the centre pipe.*

169
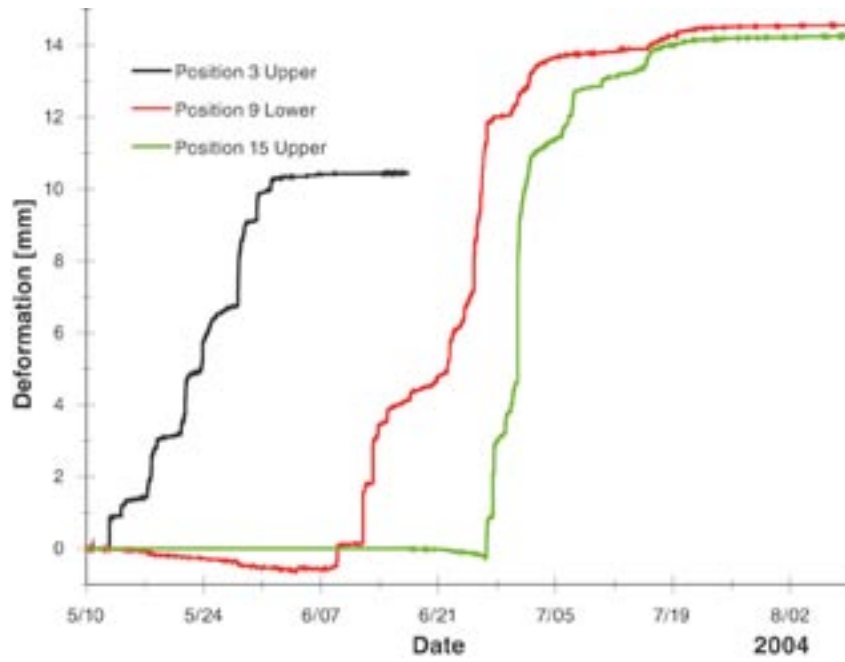
**Figure A2b-25.** *Deformation of the long-range sensors on the left side of the centre pipe.*
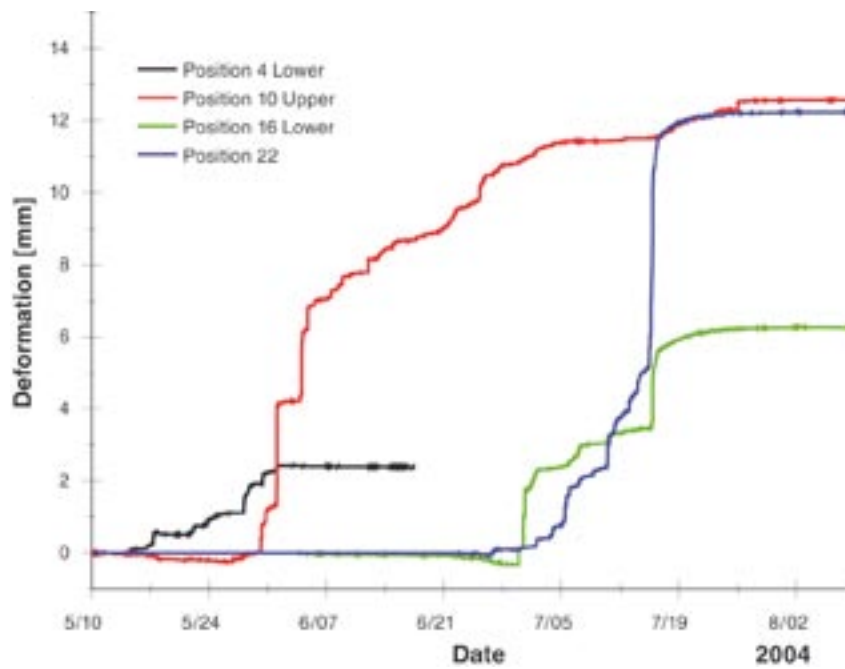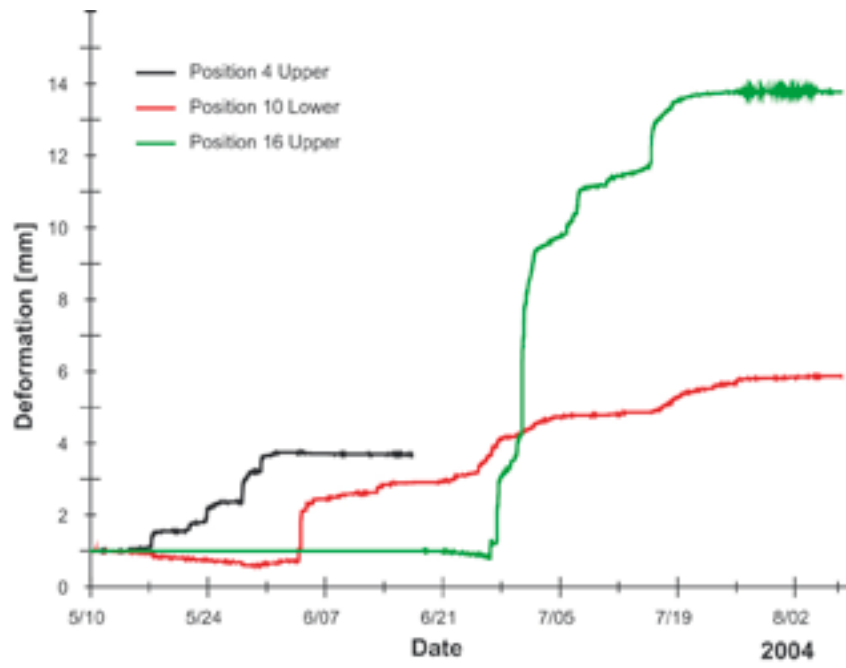


**Figure A2b-26.** *Deformation of the short-range sensors on the right side of the centre pipe.*

***Figure A2b-27.*** *Deformation of the long-range sensors on the right side of the centre pipe.*

## Verification of measured radial expansion

To verify that the small radial expansion displacement was real and not an effect of the transducers or the supporting system, two error sources have been identified and their possible effect assessed: I) pipe deflection and II) temperature effects. Cross correlations between the LVDTs and comparisons with analytical approximations have also been done to ensure the reliability of the measurements. The displacement data from the LVDTs at the 3.0 and 3.5 m levels during the periods of radial expansion are shown in Figure A2c-1 and Figure A2c-2. With few exceptions, all other transducers also indicate the radial expansion, but the displacements are very small. The indication itself is, however, evidence of the general occurrence of the radial expansion.

## A2c.1 Pipe deflection

The pipes were supported in the horizontal plane to prevent problems with deflections. To check deflection, the deformations monitored on the same pipe can be compared. If all LVDTs mounted on one pipe indicate displacements in the same direction simultaneously, there is reason to suspect that pipe deflection and not rock displacement is being monitored. The transducer positions on each pipe are presented in Appendix 2b.

Based on the observations presented below for the three pipes, it was found that pipe deflection did not occur during the times when radial expansion was measured.

### A2c.1.1 Observations left pipe

Positions 1 and 7 on the left side of the pipe are stable while positions 2 and 8 indicate displacements.

Positions 14 and 20 do not react at the same time. Position 20 also indicates larger radial expansion displacements even though it is closer to the firm horizontal support.
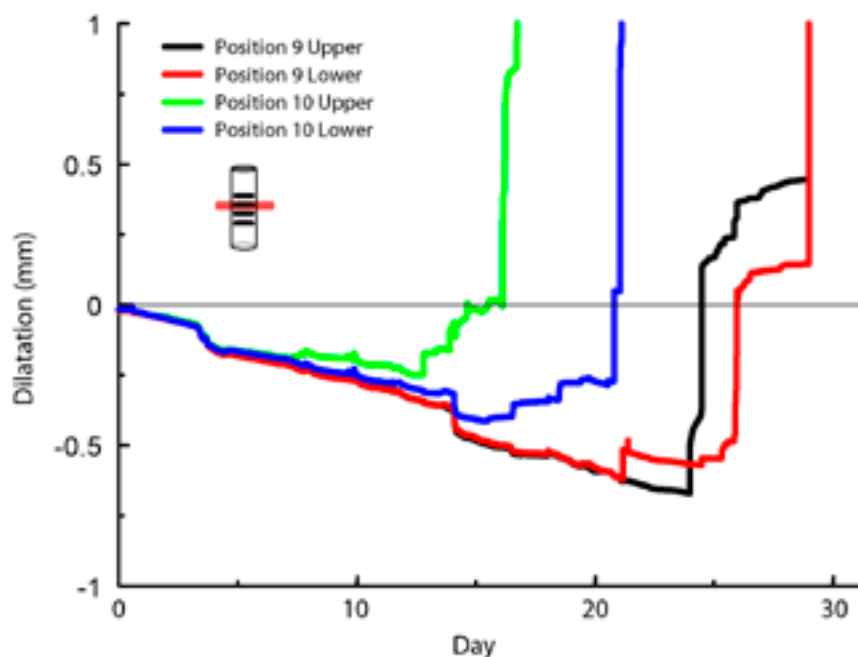


**Figure A2c-1.** *Detail of the displacements at the 3 m instrument level.*
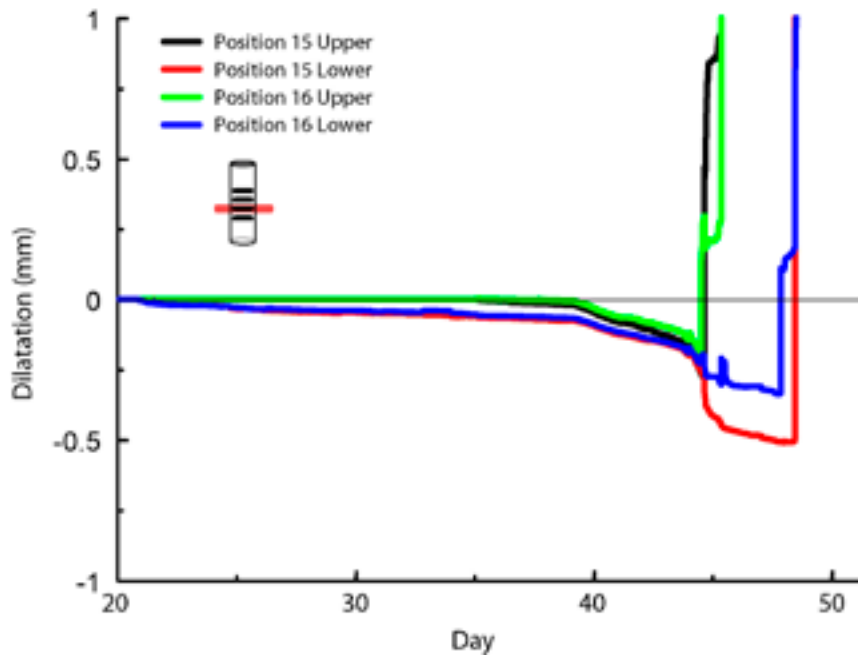
**Figure A2c-2.** *Detail of the displacements at the 3.5 m instrument level.*

## A2c.1.2 Observations centre pipe

Position 9 indicates much greater radial expansion that positions 15 and 16.

Positions 15 and 16, upper and lower, do not indicate radial expansion at the same time.

Positions 15 and 21 do not displace at the same time.

## A2c.1.3 Observations right pipe

Positions 5 and 11 indicate radial expansion displacements while positions 6 and 12 are stable.

Position 17 exhibits a different displacement pattern than position 23.

By combining the observations for pipes 1–3, it can be concluded that it is physically impossible for the radial expansion to be caused by deflection of the pipes.

## A2c.1.4 Temperature effects

Temperature effects on the monitoring results are discussed in Eng and Andersson (2005). All steel installations in the hole are affected by changing temperatures, including the LVDTs. The LVDTs have been calibrated for their temperature drift. The wide-range sensor with the largest drift changed 0.0106 mm/°C, while the short-range sensor with the largest drift changed 0.0022 mm/°C. The time period during which radial expansion takes place at each level is quite short, so the temperature increase is quite small. The temperature drift of the sensors is therefore not the cause of the measured radial expansion.

The steel plates that provide horizontal support are mounted so that when they expand due to temperature increase they push the pipes against the rock wall. The relative displacements monitored will be towards the hole and not indicated as radial expansion. The thermal expansion of the steel plates is 0.0094 mm per °C.

The final temperature effect that may have affected the monitoring of radial expansion is thermal expansion of the steel pipes on which the sensors are mounted. The vertical upward displacement of the pipe at the 2.5 m instrument level is 0.0495 mm/°C. It is highly unlikely that the vertical thermal expansion of the pipes is the cause of the measured radial expansion.

174

The sensors at positions 1–12 are all placed on small steel plates that were glued to the rock wall. The alignment of the plates was measured by moving the pipes vertically up and down while measuring horizontal displacements. It was found that the alignment lies in the range of 0 to 0.07 mm/mm pipe movement (absolute measures). It is important to note that the alignment was not in the same direction for the plates. In most cases, however, the sensors were compressed when the pipe was raised.

The LVDTs that were mounted directly on the rock wall were not tested with vertical pipe movements since they were mounted after heating had started. If pipe movement was the reason for the measured radial expansion for these transducers, they should all in that case have been mounted with the transducer point on the highest part of the rock in the vicinity. They would then all have slid into lower parts of the rock as the pipe displaces the transducer vertically up. It is more likely that the opposite is true. When the sensor is mounted and placed against the hole wall it slides down to the lowest part of the rock it is placed against. The transducer would then be compressed as the pipe moves vertically up.

When all temperature effects are combined, the wide-range transducer at position 15 upper displays the largest error, approximately 0.01 mm/°C. The sensor is compressed with increasing temperatures. The error thus reduces the effect of radial expansion rather than enlarging it.

The rock in the pillar itself expands into the hole due to the heating. The pillar volume is heated approximately 15 degrees, and the resulting expansion is judged to begin in the centre of the pillar and to be directed along the tunnel axis towards each of the large holes. The expansion coefficient of 7E–06 1/K gives an expansion of ~ 0.05 mm into the hole. The direction of this thermal effect is also opposite to the thermal expansion. One cannot simply add this value to the measured radial expansion and argue that it is larger due to the counter-effect of the rock expansion. The total rock expansion takes place during the entire experiment, while the radial expansion only occurs during a few weeks. The temperature increase in the pillar during this time is quite small, so the effect of the expansion of the rock is small.

## A2c.2 Comparisons of displacements at different levels

The transducers at positions 9, 10, 15 and 16 were used to perform the detailed study of radial expansion. The reason for this is that they indicated the largest displacements that are undoubtedly actual rock displacements. If the radial expansion signatures are compared for the two levels they are quite different. Transducers 9 and 10 at the 3 m instrument level indicate radial expansion for approximately three weeks. The sensors were mounted before the heating started and the propagation of the notch due to the stress increase occurred slowly. The transducers at position 15 and 16 at the 3.5 m instrument level indicate the radial expansion for a shorter period of time. This is probably due to the fact the stress increase levelled out and practically stopped for most of June. If the acoustic emission records are studied during that time, the events are seen to cluster close to, but not below, the 3.5 m level. When the temperature increases on June 21, the notch quickly propagates below the instrument level. Since the radial expansion follows in front of the notch it also has to appear during a shorter period of time.

The radial expansion is also indicated at the uppermost instrument level, at 2.5 m. The instruments were installed in the beginning of May very close to the notch and they almost instantly indicated radial expansion. It was observed that the radial expansion occurred during the installation work, but it was first thought that it was caused by slipping of the transducers in their fastenings. Most of them were therefore changed, but when the same phenomenon was later observed at the 3 m instrument level, it was concluded that the deformations were actual displacements of the rock.

## A2c.3 Conclusions

After the measured displacements have been studied and error sources associated with increasing temperature and pipe deflection have been compared, it can be concluded that the measured radial expansion is not due to a systematic temperature-induced error in the monitoring system. Nor has evidence been found that deflection lies behind the observations. It can be concluded that radial expansion is an actual phenomenon. An attempt has been made to simulate this by numerical modelling, and that work is presented in greater detail in Appendix 2d.

# Back calculation of radial expansion

The displacement measurements made during the heating phase indicated that the rock contracted, causing radial expansion, before the notch reached the transducers. The radial expansion was observed for the majority of the LVDTs but is greatest at the 3.0 m and 3.5 m instrument levels (Appendix 2c). As can be seen there, the displacements are small and lie between 0.2 and 0.6 mm.

The boundary element code Examine3D and the finite element code Phase2 have been used to try to simulate the observed behaviour of the rock. The results have also been compared with an analytical approximation of the deformations. An illustration of the conceptual model of the radial expansion used for the work is presented in Figure A2d-1. As the notch grows and migrates downwards, it is thought of as a spalled volume with a very low Young's modulus (modelled as a void) moving down the hole. The rock in the pillar is subjected to a very high horizontal stress and as a volume with low stiffness is introduced from above. The stresses are relieved by deformation of the rock towards the low stiffness volume.

The finite element code Phase2 was used to model a thin skin with a lower Young's modulus close to the hole wall. The skin can be regarded as an EDZ. The modulus in the skin was reduced to see what would happen with the displacements. Phase2 was also used to apply different boundary conditions and different stiffness properties to the pillar.

An analytical approximation resulted in displacements of the same order of magnitude as the numerical simulations.
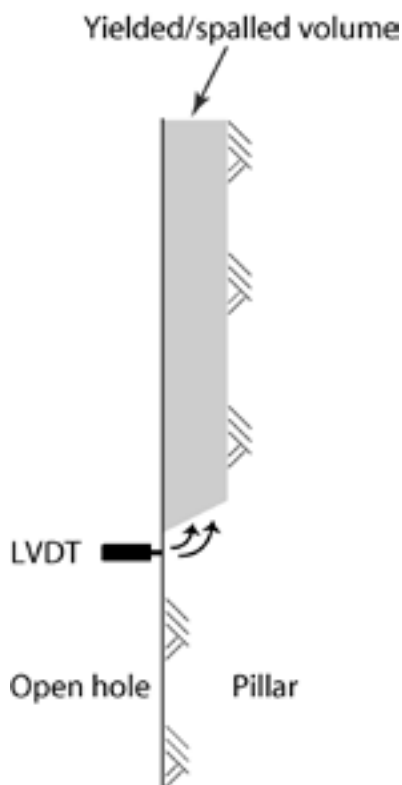


**Figure A2d-1.** *Conceptual model of the radial expansion of the pillar wall as the notch propagates towards the instrument level.*

## A2d.1  Model set-ups

### A2d.1.1 Examine3D geometries

The geometrical model in the Examine3D code used the tunnel and large-diameter borehole geometries as they were surveyed after the excavation. The exact geometry of the notch as it evolved during the spalling phase is not known, however. The results of the laser scanning of the boreholes performed after removal of the spalling slabs were used to make a best estimate of the geometry. A horizontal section located 2.58 m down the hole was used to represent the shape of the notch.

The hole wall was divided into four different sections as shown in Figure A2d-2. The four sections can be described as follows:

The upper 0.5 m of the pillar, which was not spalled at all during the experiment. This part of the pillar is therefore left with the standard hole geometry

A transition zone with an increasing notch depth until 1.5 m down into the hole, where the full depth of the notch is reached.

Approximately 1 m of the correct notch shape, which ends in…

...the notch tip, where the spalling is initiated. The tip was modelled with two shapes: 45 and 14 degrees inclination with respect to the horizon. Below section 4 the standard hole geometry is used.

The element size in sections 2 and 3 of the notch is approximately 4 cm. The notch tip section 4 has 2 cm elements. The element size of the hole is 10 cm except close to the notch tip, where the elements are 2.5 cm in length.

An Examine3D model with a standard hole geometry was also run. It was then possible to see the changes in displacements when the notch is introduced, which is exactly what happened during the experiment.
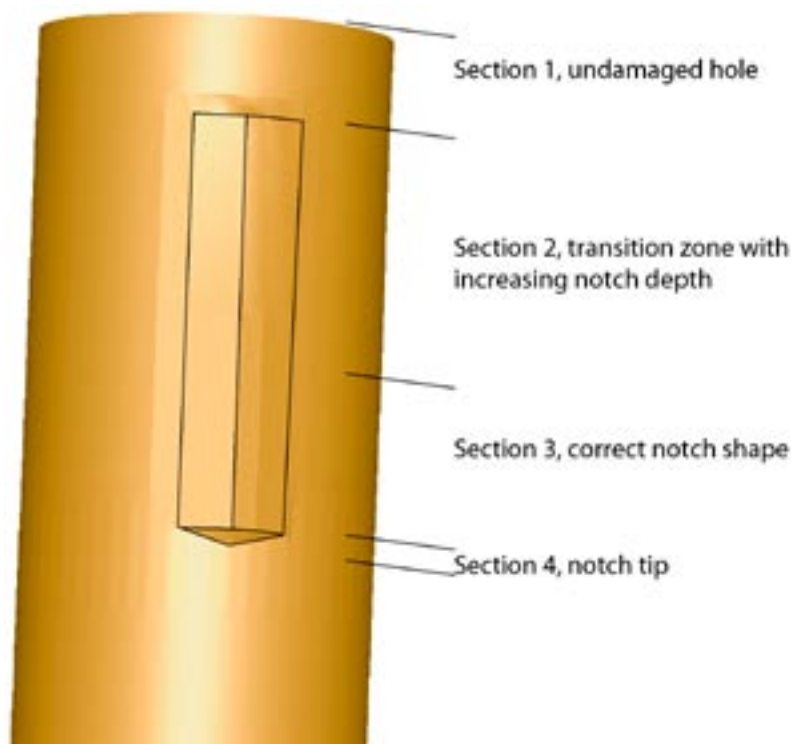


**Figure A2d-2.** *Examine3D model of the hole and the notch with its four parts.*

To enable the results to be plotted, data points were introduced in the model. The points cover the lower part of section 3, section 4 and the part of the hole with increased mesh density. The points are spaced 1 cm apart in vertical lines located every 5 degrees around the borehole periphery. Since the points are evenly distributed in the vertical direction, the results mirror what happens as the notch tip approaches. By plotting the results for one vertical line, the stresses and displacements due to an approaching notch tip can be studied. The points are located 4 mm into the hole wall.

## A2d.1.2 Examine3D alternative notch

An alternative notch model was also devised. The shape of the notch that was initiated during the drilling of the second hole was created using a simplified geometry. The notch was made triangular in shape with the same depth as the first type of notch, but symmetrical. The notch tip is pointed at an angle of 81 degrees from horizontal.

The results of the calculations of the pointed notch gave a less accurate approximation to the radial expansion than the other model that was used. The results from this alternative notch are therefore not included.

## A2d.1.3 Examine3D geotechnical parameters

Since a continuum 3D model was used, the only parameters that affected the results were stress, Young's modulus and Poisson's ratio. Young's modulus was set to 55 GPa and Poisson's ratio to 0.26 for all the Examine3D calcualtions. The stress field shown in Chapter 2 was used.

Elevated stresses due to the heating were not included in the model. A notch was formed down to a depth of 2 m during the drilling, and the modelled notch is placed at a depth of approximately 2.6 m. The stress in the model is therefore close to that which created the notch during drilling.

## A2d.1.4 Phase2 geometries

For the two-dimensional continuum modelling, five approaches were used to try to back-calculate the radial expansion.

1) Holes only.

2) Notch.

3) Ellipse.

4) Skin with reduced Young's modulus.

5) Boundaries.

The model with its different parts is shown in Figure A2d-3. The element size close to the hole boundary is approximately 2 cm. The confinement pressure did not affect the outcome of the models and was not included in the calculations.

## A2d.1.5 Phase2 geotechnical parameters

Since the problem is truly three-dimensional, the stress field has to be adjusted from the in situ values to get the tangential stresses. An upscaling of all stresses by a factor of 1.1 was found adequate to simulate the 3D stress field after excavation at a depth of approximately 3.5 m. To simulate the stresses at which yielding was initiated, the upscaling factor was approximately 1.37 times the in situ stress.

The models usually consisted of two stages. In the first stage the in situ stress was set to 1.1 and in the second stage to 1.37 times the in situ stress. The principal stress was inclined 96 degrees CCW from an axis through the centre points of the two holes. Since the tunnel were oriented 6 degrees from being perpendicular to the direction of the major principal stress, this had to be accounted for in the Phase2 model.

Young's modulus was set at 55 GPa and Poisson's ratio at 0.26 in the standard case. Variations were made which are discussed later in this appendix.
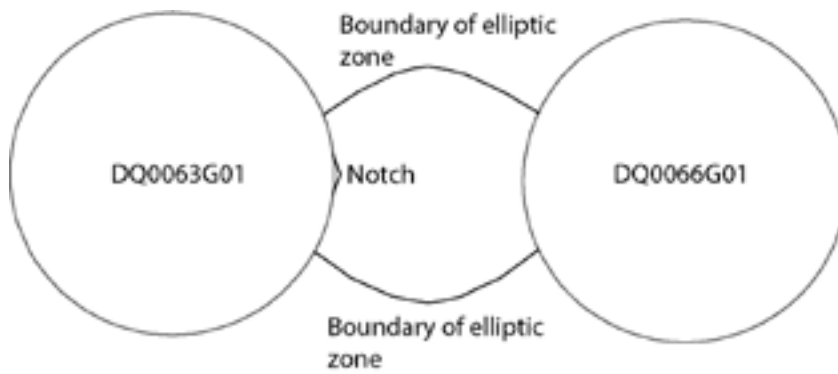
*Figure A2d-3.* *Phase2 model.*

## A2d.2 Examine3D modelling results

The majority of the result plots in this chapter were made with the results from the field point chains located 5 degrees to the left and right of the centre of the pillar. This is the approximate location of the LVDTs that measured the largest radial expansion magnitudes.

The model is oriented so that the tunnel axis corresponds to the north-south direction (the in situ stresses have been changed accordingly). A radial expansion is thus indicated by a positive north-ward displacement in the open hole DQ0063G01 (Figure A2d-4).
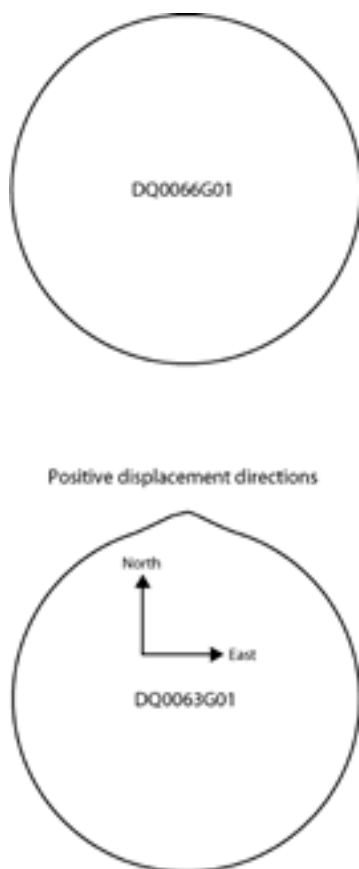


*Figure A2d-4.* *Definition of the direction of positive displacements in the Examine3D model of the radial expansion.*

180

Figure A2d-5 and Figure A2d-6 summarize the results for relative displacements in all three directions (north, up and east) for the monitoring points 5 degrees to the left and right of the pillar centre. All displacements in the two figures are compensated for the deformations due to the excavation of the holes. Consequently, only the deformations originating from the notch are accounted for. The displacements due solely to the excavations are shown in Figure A2d-7 for comparison.
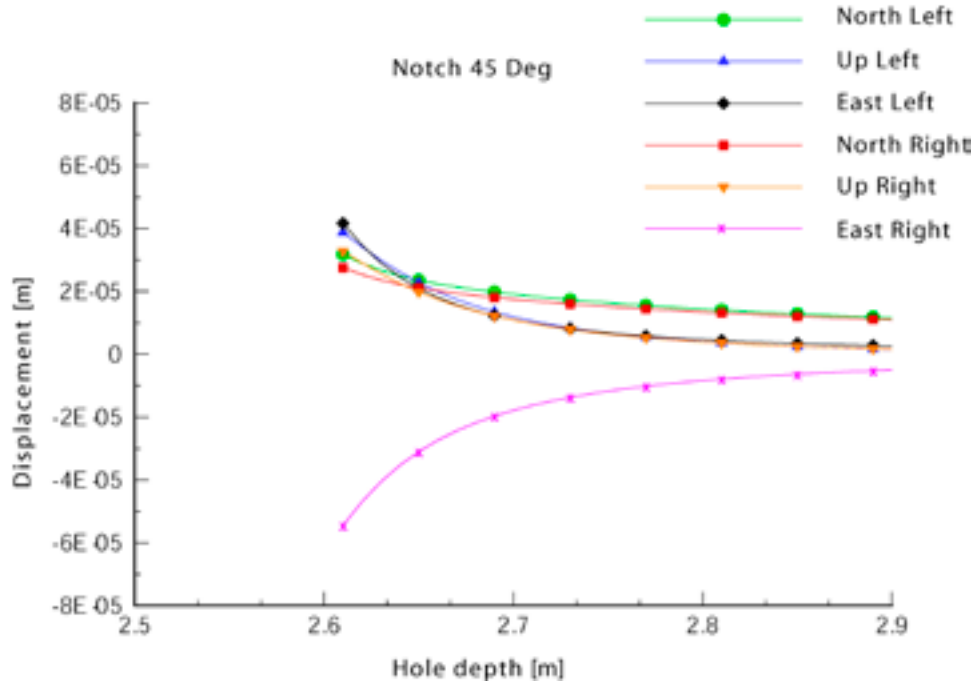


**Figure A2d-5.** *Relative orthogonal displacements with a notch tip angle of 45 degrees from horizontal.*
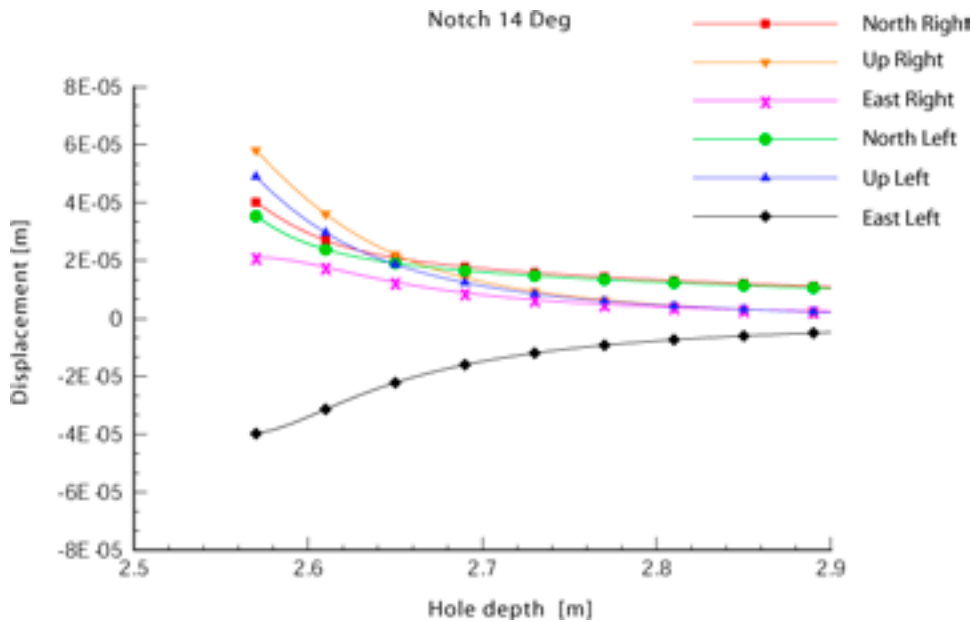


**Figure A2d-6.** *Relative orthogonal displacements with a notch tip angle of 14 degrees from horizontal.*
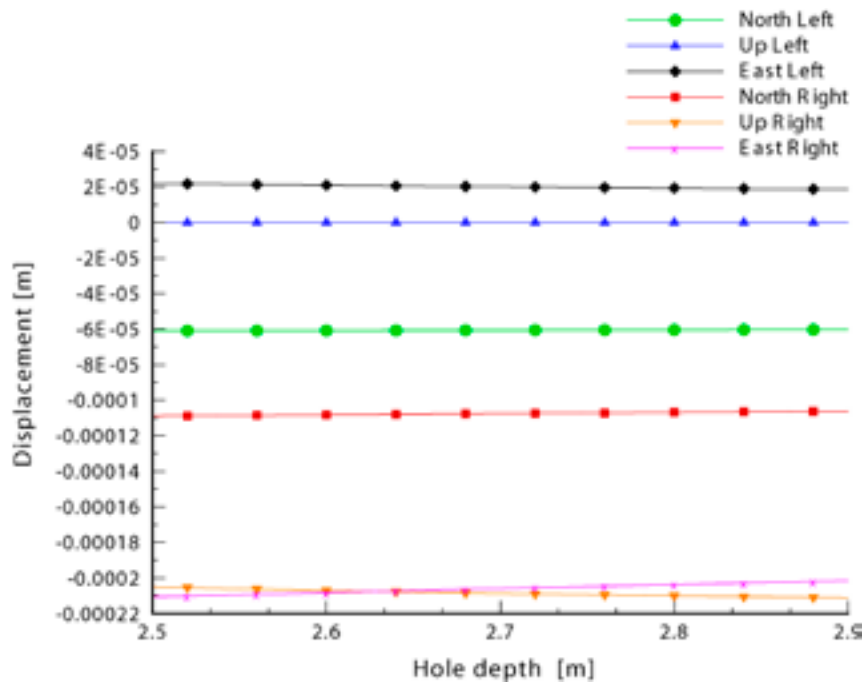
**Figure A2d-7.** *Orthogonal displacements due solely to the excavation of the holes.*

When studying the displacements, it should be borne in mind that they are all directed into the hole. The difference when the notch is introduced is that the displacements to the south are reduced and would be indicated as a radial expansion by the LVDTs.

The results indicate that the rock close to the pillar moves north and up and that the displacements are very small, approximately 0.04 mm. This represents the radial expansion, but only with one-tenth of the measured displacements. The difference between the different notch tip angles is very small (the displacements for the pointed notch were much smaller).

The LVDTs were fastened in a sturdy steel construction and could only measure N-S displacements. These displacements are presented in Figure A2d-8 and Figure A2d-9. The 5 degree difference between the true radial displacement and the modelled north one is not accounted for.
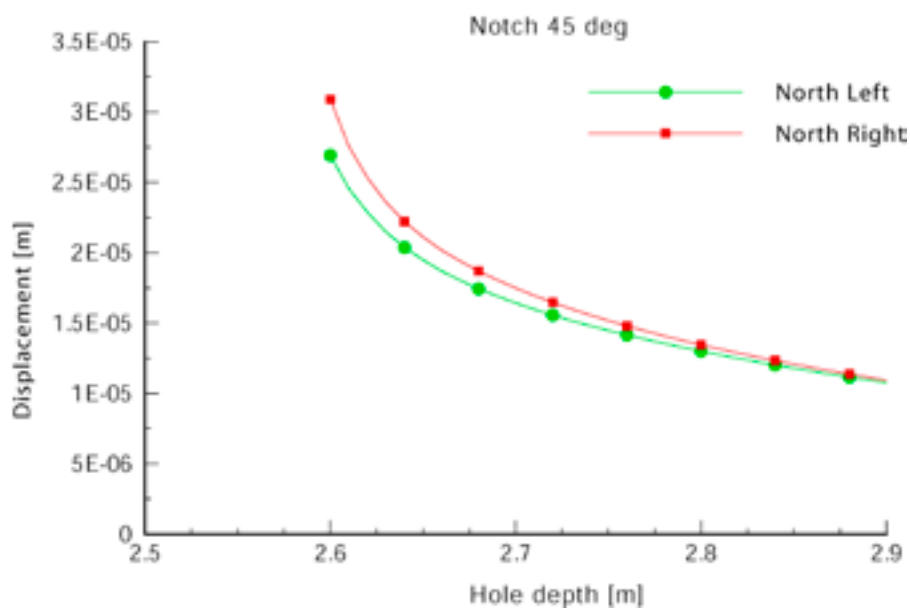


**Figure A2d-8.** *Relative northward displacements due to the notch 5 degrees to the left and right of the pillar centre. Notch tip angle 45 degrees.*
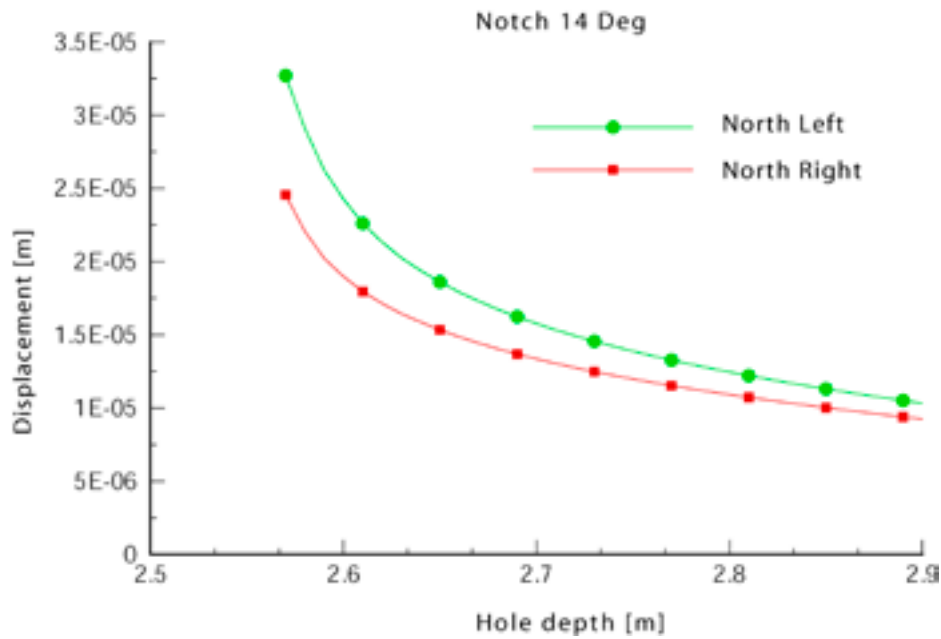
**Figure A2d-9.** *Relative northward displacements due to the notch 5 degrees to the left and right of the pillar centre. Notch tip angle 14 degrees.*
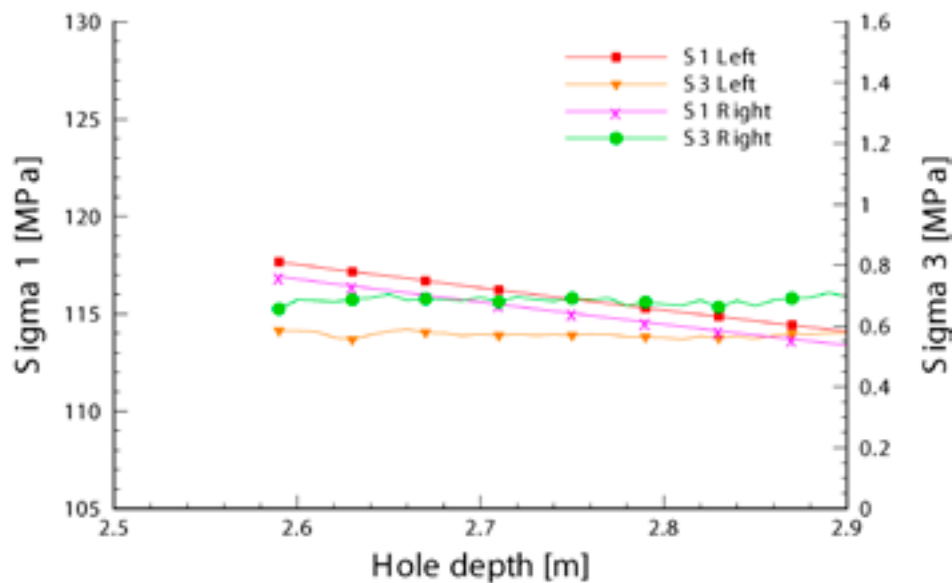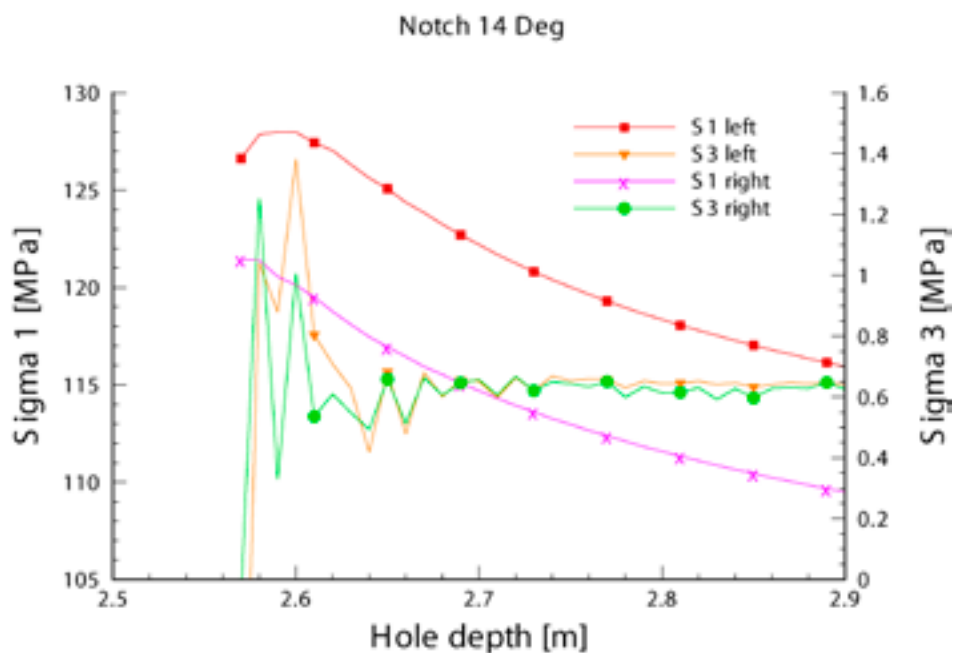


**Figure A2d-10.** *Holes only. Major and minor principal stresses five degrees left and right of the pillar centre.*

In Figure A2d-10 to Figure A2d-12, the major and minor principal stresses are plotted for the same geometries as the displacement plots. The 45 degree notch (Figure A2d-11) re-distributes the stresses so that they are elevated on both sides of the notch tip. The stress is elevated approximately 10 MPa compared with the stresses acting before the notch is introduced (Figure A2d-10). When the 45 degree notch (Figure A2d-11) and the 14 degree notch (Figure A2d-12) are compared, the difference in result is small. The near-horizontal 14 degree notch has slightly more elevated stresses on the right side, but for both notches the stresses decline evenly along the hole wall.

183
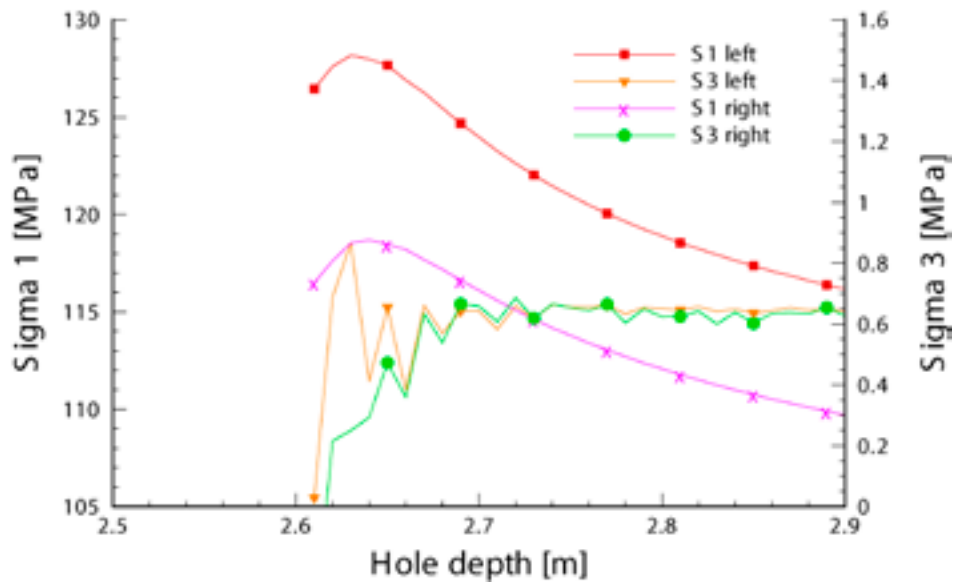
***Figure A2d-11.*** *Notch angle 45 degrees. Major and minor principal stresses five degrees left and right of the pillar centre.*

Notch 14 Deg



***Figure A2d-12.*** *Notch angle 14 degrees. Major and minor principal stresses five degrees left and right of the pillar centre.*

The stresses at the centre of the pillar, at the notch tip, are also of interest since this is where spalling was initiated in most cases. The major principal stress from the two different notch models as well as from the model with only the holes is shown in Figure A2d-13. Note the elevation of the stresses for the 45 degree notch.

For the 45-degree notch, the stresses have also been plotted in five degree increments (Figure A2d-14) starting with "0" at the pillar centre. Positive values are to the right (clockwise) and negative to the left of the pillar centre. In the figure one can see how the stresses decrease for each 5-degree increment. Approximately 20 degrees on each side of the pillar centre was spalled. The stress situation for the 14 degree notch is very similar.
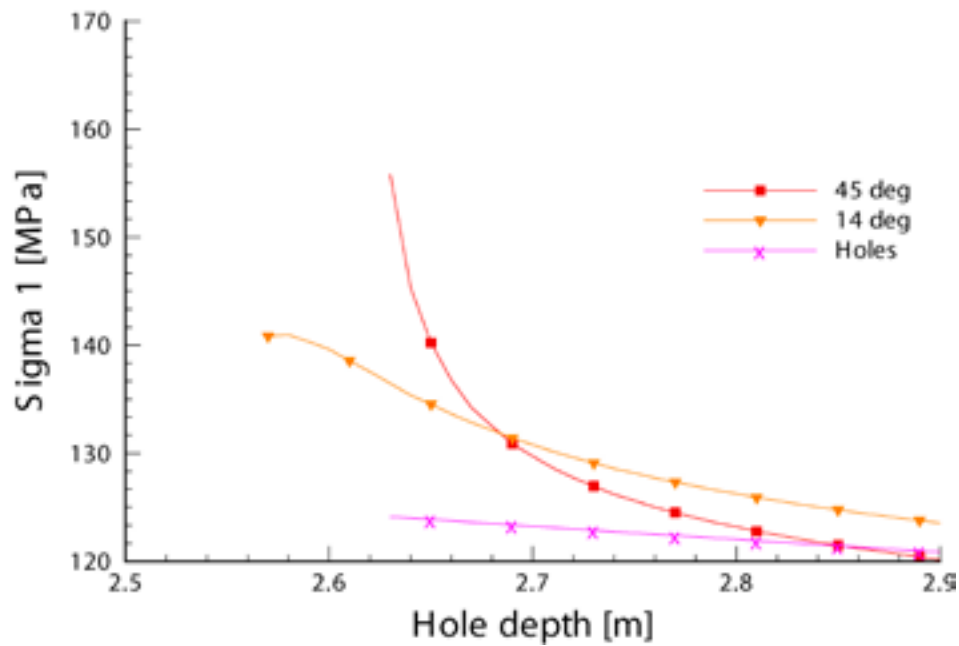
**Figure A2d-13.** *Major principal stress at the centre of the pillar for the two notch configurations and for the holes only.*

The northward displacements for the stresses plotted in Figure A2d-14 are given in Figure A2d-15. These results are interesting to compare with the monitored data. The outermost sensors at positions 1 and 6 (located at –30 and 30 degrees) indicate a radial expansion of approximately 0.03 to 0.04 mm during the first part of the experiment. These displacements are of the same magnitude as those modelled for the centre of the pillar. The displacements at –15 degrees are of the same order of magnitude (0.028 mm).
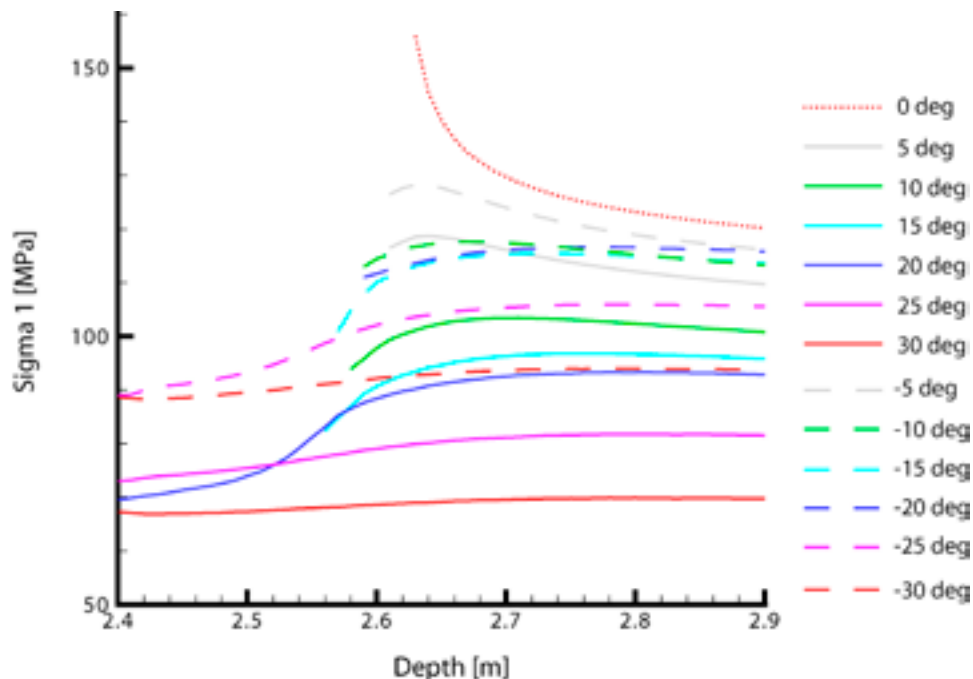


**Figure A2d-14.** *Stresses in five-degree increments left and right of the pillar centre. 0 deg is at the pillar centre and negative values to the left.*

185
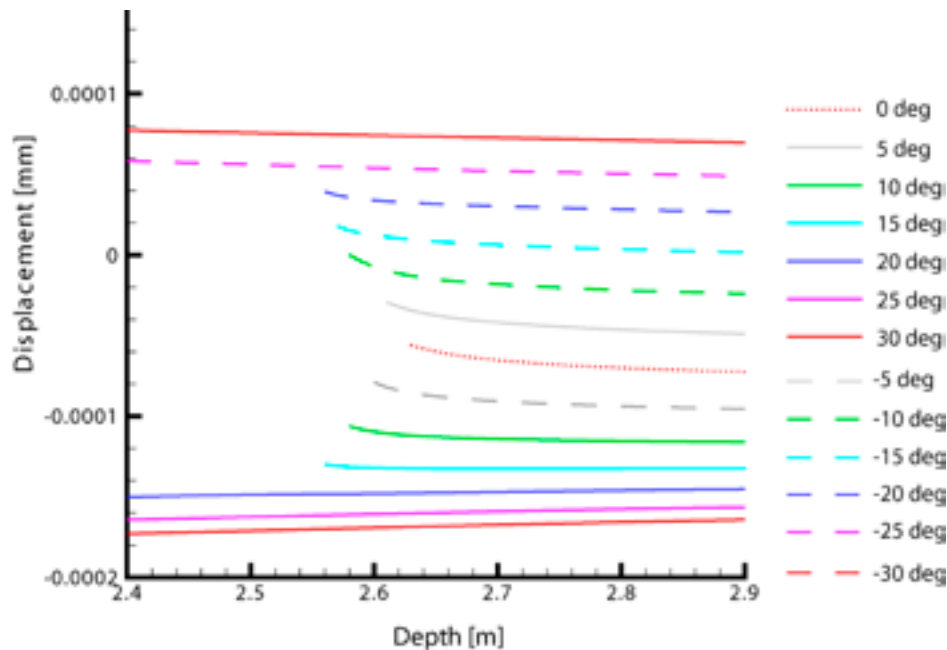
***Figure A2d-15.*** *Northward displacements in five-degree increments to the left and right of the pillar centre. 0 deg is at the pillar centre and positive values to the right.*

## A2d.3 Phase2 modelling results

As mentioned above, the Phase2 model was run in five major variations as described earlier. The results of the different variations of the model are presented in the following sections.

All models were run in two stages. The first stage simulated the stress on the boundary of the hole at a depth of approximately 3.5 m after excavation. In the second stage the stresses was raised to approximately 125 MPa at the most stressed locations in the hole. The stresses acting in the boundary at the yield strength of the rock were then simulated.

### A2d.3.1 Two holes only

The model that only included the two holes did not indicate the radial expansion in any way. The displacements into the hole increased with increasing stress.

### A2d.3.2 Notch in one hole

A notch approximately 3 cm deep and 20 cm wide was introduced in the open hole. Three models were run. I) the notch was introduced in the second stress stage; II) the notch was already present in the first stage; III) the notch was introduced in the second stage but the stresses were not increased after the first stage.

In model (I) where the notch was introduced in the second stage, the results indicated radial expansion at the notch tip. The deformations for the two stages at the approximate locations of the LVDTs in the open hole are shown in Figure A2d-16. Model III without the stress change but with the introduction of the notch in the second stage gave similar results as the first model. For both models, radial expansion is indicated at the centre. The model without the stress increase also indicates radial expansion at the approximate instrument positions 13 and 15.

Positive displacements are defined to the right in the figure. The change in displacement direction that can be seen is caused by the fact that the principal stress is inclined six degrees due to the alignment of the tunnel axis and the direction of the major principal stress.

186
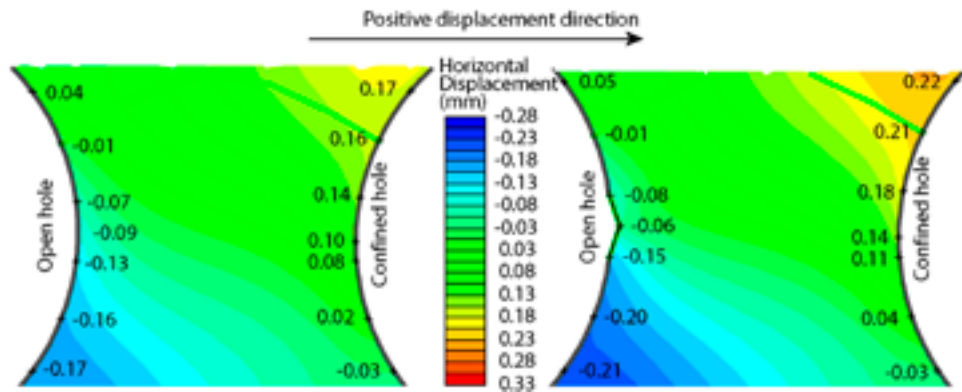
**Figure A2d-16.** *Displacements before and after the introduction of a notch and increase of the stress in the second stage. Positive displacements to the right.*

### A2d.3.3 Elliptic pillar centre

If stress is applied on the long sides of an elliptical body, the short sides will displace and stretch the body. An area in the pillar centre was given an elliptical shape as illustrated in Figure A2d-3. The area was assigned different properties in two different realizations. In one realization, Young´s modulus was set at 75 GPa, which is what has been measured on laboratory samples. In the other realisation, the modulus was reduced to 25 GPa. Both models were run in two stages, where the notch and increased stress were introduced in the second stage.

The change in modulus affected the total displacements, but the relative displacements between the first and second stage did not provide a better measure of the radial expansion than that provided by the models without the elliptical pillar centre. The stiffer model gave the better fit of the two.

### A2d.3.4 Skin with lower stiffness

Calculations were performed to determine whether a skin with a lower modulus simulating an excavation disturbance would effect the displacements and enhance the effect of the radial expansion observed in the other model runs. The skin was made three centimetres thick and given a Young´s modulus of 25 GPa, which is one-third of the modulus determined on core samples. As for several of the previous models, two stages were used. The notch and increased stresses were introduced in the second stage.

The effect of the skin was that the displacements increased but the relative displacements between the two stages in the model did not indicate the radial expansion any better than the other models used.

### A2d.3.5 Changed boundary conditions

A few realizations were made to study the effect of the boundaries. The changes made were that the vertical boundaries were set as roller boundaries in combination with fixed, roller and free horizontal boundaries. Distributed loads with the same magnitude as the major principal stress were also applied on the horizontal boundaries. The different boundary conditions did not give better simulations of the radial expansion.

## A2d.4 Analytical approximation

An analytical approach to the radial expansion has also been taken in an attempt to enhance conceptual understanding. The rock beneath the notch is approximated with a cubic block with 0.1 m sides. The side lengths are the approximate vertical distance between the LVDT transducers at the same level. The block was imagined to be located in the pillar with one vertical surface aligned with the hole wall. The approximation was done in two stages to make it as realistic as possible.

The first stage was to calculate the expansion of the cube into the hole before the notch is introduced. In this calculation it is assumed that the rock is able to constrain the vertical strain of the block.

The second stage was to assume that a slot with the same horizontal area as the block is cut into the top of the pillar. The vertical stress now has to become zero on the top of the block, but vertical strain is introduced. The horizontal expansion of the cube is calculated for this stage as well. By comparing the two results, it was possible to assess the horizontal deformation of the free vertical surface due to the approaching notch.

Hooke's generalized law was used to determine the strain. The parameters needed to solve the strain for a certain stress are Poisson's ratio ($v$) and Young's modulus (E). Hooke gives the strain by using the relationships:

Eq 1: $\varepsilon_x = 1/E \times (\sigma_x - v\sigma_y - v\sigma_z)$

Eq 2: $\varepsilon_y = 1/E \times (\sigma_y - v\sigma_x - v\sigma_z)$

Eq 3: $\varepsilon_z = 1/E \times (\sigma_z - v\sigma_x - v\sigma_y)$

Where z is the vertical direction, y is parallel to the major principal stress and x is parallel to the tunnel axis. Since the stress in the x direction is normal to the hole wall it is set to zero. Tensile stress is the positive direction in the equations. The compressive stresses acting on the block are therefore set to negative values. The equations can now be rewritten as follows:

Eq 4: $\varepsilon_{x1} = 1/E \times (-\sigma_x + v\sigma_y + v\sigma_z)$

Eq 5: $\varepsilon_{y2} = 1/E \times (-\sigma_y + v\sigma_x + v\sigma_z)$

Eq 6: $\varepsilon_{z3} = 1/E \times (-\sigma_z + v\sigma_x + v\sigma_y)$

In the first stage the cube is, as mentioned above, assumed to be located in intact rock with the assumption that vertical deformation is constrained. Equation 6 then has to be 0. This gives $\sigma_z = v\sigma_y$. Equation 4 is then rewritten as $\varepsilon_{x1.1} = 1/E \cdot (v\sigma_y + v^2\sigma_y)$.

In the second stage it is assumed that all rock on top of the cube is removed so that a horizontal free surface of 0.1×0.1 m² is created. The vertical stress then becomes zero. Equation 4 then gives $\varepsilon_{x1.2} = 1/E \cdot (v\sigma_y)$. Set $\Delta\varepsilon$ to the difference between $\varepsilon_{x1.1}$ and $\varepsilon_{x1.2}$, then: $\Delta\varepsilon = v^2\sigma_y/E$. Since $\Delta\varepsilon$ is positive, the relative displacement due to the free upper surface is directed into the pillar. An LVDT located on that point would therefore record a radial expansion of the hole.

To get numerical values of the radial expansion, a stress $\sigma_y$ of 125 MPa (approximately the spalling strength) along with a Poisson's ratio of 0.25 is assumed in Figure A2d-17 for stage 1 and the difference between stages 1 and 2. The radial expansion of the hole is shown in the figure as a function of Young's modulus. From the figure it can be concluded that it is not the effect of Young´s modulus that is the reason behind the indication of the radial expansion. The radial expansion was measured to be approximately 0.5 mm. To find that value in the graphs for stages 1–2, Young's modulus has to be set to 1.5 GPa, which is totally unrealistic. The modulus derived from core testing is 76 GPa and the rock mass modulus determined by convergence measurements is 55 GPa.

If the results for stage 1 in Figure A2d-17 are compared with Figure A2d-7, it can be concluded that the approximations made for the analytical solution and the results from the numerical model are of the same magnitude, which validates the results. However, the analytical model is very sensitive to the choice of cube length.

## A2d.5 Discussion

The 2D and 3D modelling of the pillar centre as the notch approaches indicates deformations in the same direction as the radial expansion. However, the deformations are only 10% of those measured in situ, so it cannot be argued that the models predicted the radial expansion, especially since the notch had to be introduced in the 2D model for the deformations to appear. In field, the LVDTs picked up the incoming notch before spalling was initiated at their location. A true 3-D problem.
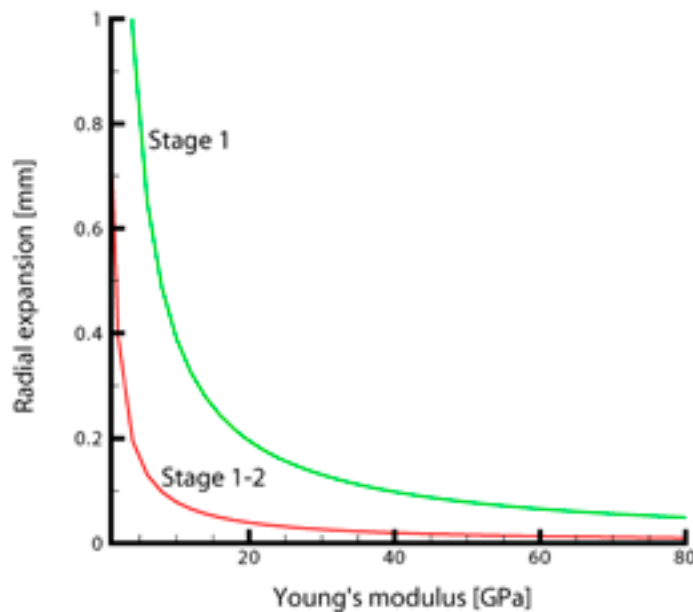
***Figure A2d-17.*** *Radial expansion as a function of Young's modulus for a cube located in the pillar. Stage 1 is the expansion of the cube into the hole before the notch is introduced. Stage 1–Stage 2 gives the displacement a LVDT would record when the notch has formed.*

When the deformations from the transducers located outside the spalled area were compared with modelled results, the measured displacements were of the same magnitude as those modelled close to the pillar centre. This can be seen as an indication of that the elastic modelling is probably quite close to what is actually happening, but that the complex geometry and stress situation inside the notch makes it impossible to model the situation exactly.

The 2D modelling clearly showed that the effect of a 3 cm thick EDZ is negligible when studying radial expansion.

The 3D notch models give similar results that can be interpreted as an indication of the radial expansion. Considering the geometry and the stresses, the observations made in the hole combined with the displacement monitoring indicate that the radial expansion is overtaken by brittle deformations as soon as the rock wall starts to chip. It was also observed that the spalling front quickly reached its full width of approximately 30 degrees (15 degrees on either side). These observations are similar to the constructed geometry of the 14- and 45-degree notches. The resulting stresses from both the 14- and 45-degree notches at –5 and 5 degrees are close to the spalling strength determined for the experiment. The stresses in the very centre are, however, higher for the modelled notches than what has actually been determined. Ten degrees from the pillar centre, the modelled stresses are lower than the spalling strength, approximately 5 to 10 MPa lower for the 45-degree notch. The back calculations in Chapter 8 have determined the yield strength of the rock to be ~ 125 MPa. The determined yield strength and the stress close to the notch are thus very close, and on that basis it could be argued that the notch propagates with that geometry. The observations in the hole indicate that the spalling starts with small chips forming on the rock wall, and that gradually larger chips form beneath these. The full width of the spalled area was reached close to the notch tip. The field observations and the results from the modelling make it likely that the actual shape of the notch is somewhere between the two models used.

The results presented here illustrate the complexity of modelling the problem. Different geometries have been been found to produce results that are generally comparable for some observations but not for others. The tools used are not adequate for simulating the problem, but it is uncertain whether more complex 3D codes could do a better job. Their major contribution would be their plastic analysis capabilities, combined with their ability to modify the material in the notch and model it as a material and not a void. That is probably not enough. The formation of the slabs with extensional fracturing is probably what controls the behaviour of the rock. The slabs beneath the hole surface are probably able to carry some load perpendicular to the tunnel axis, which makes the stress distribution in the notch very complex.

## Observations of fracturing and removal of slabs

The template used for the sketches of the spalling is presented in Figure A2e-1. The four instrument levels are indicated and each instrument position is marked with a black circle. Instrument positions 1 to 6 is at the 2.5 m level. Positions 7 to 12, 13 to 18 and 20 to 23 are found on the respective following levels. The grid is not included in all figures in this appendix in order to make them easier to read. The instrument position circles are though always included.

A conversion table between date and experiment day is given in Appendix 2a.
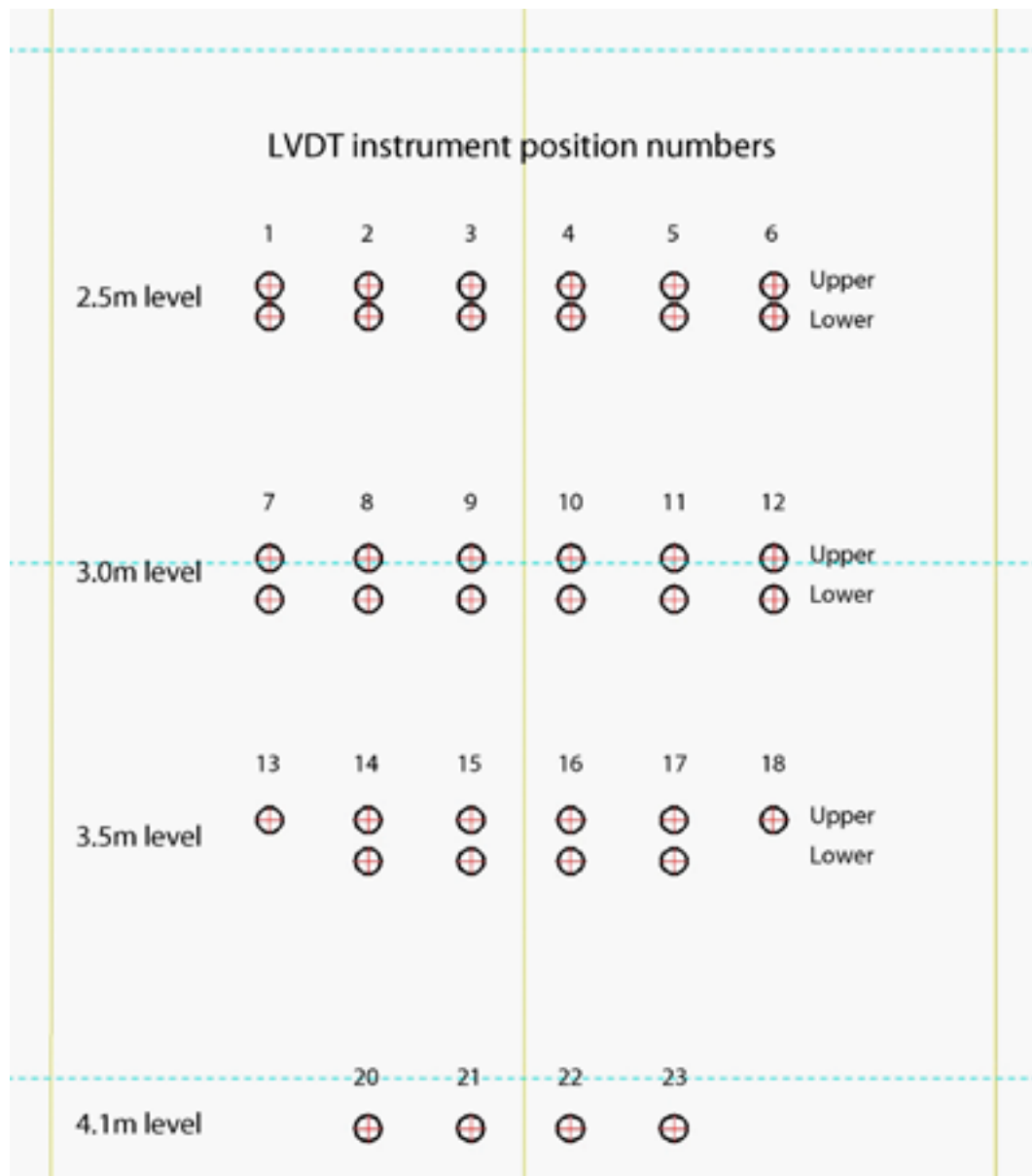


*Figure A2e-1.* *Template used for the spalling including the sensor positions. Grid spacing is 1 m.*

**April 26, 2004**

When the drilling of the large hole DQ0063G01was finished, spalling had propagated from 0.5 m down to 1.95 m from the borehole collar. Installation of the LVDTs and thermocouples was finished on April 28. During installation the spalling slowly propagated down the hole. On one occasion the popping sound of breaking rock was heard and a small cm-sized piece of rock was ejected. It is likely that the spalling propagation was due to the small temperature fluctuations in the hole originating from people working there. This indicates the delicate equilibrium at the notch tip which is further discussed in Chapter 8.

The first sketch of the spalling front was made on April 26. The spalling had then propagated close to the first instrument level.

**March 5, 2004**

During the weekend April 30 to May 3 spalling occurred and the notch moved down between the instrument positions 3 and 4. The spalling could be correlated with acoustic signals and with small deformations. It is clear that the extent of the spalling was affected by the force applied to the rock by the springs in the LVDT sensors. As can be seen in Figure A2e-2, the fracturing occurs around the steel plates. This is also the first time that small radial expansion displacements (contraction) directed into the pillar was noticed.

**May 12, 2004**

Practically no displacements or any acoustic events of importance took place from May 3 until May 12. In the afternoon May 12, the AE system started to pick up events and at the same time position 3 was displaced almost 1 mm. An inspection was therefore made in the hole and the new fracturing was sketched. The summary sketch in Figure A2e-2 shows that a small slab was created beneath the 3 instrument plate. The slab was terminated close to instrument plate 4 where the force from the LVDT spring was probably large enough to suppress the spalling.
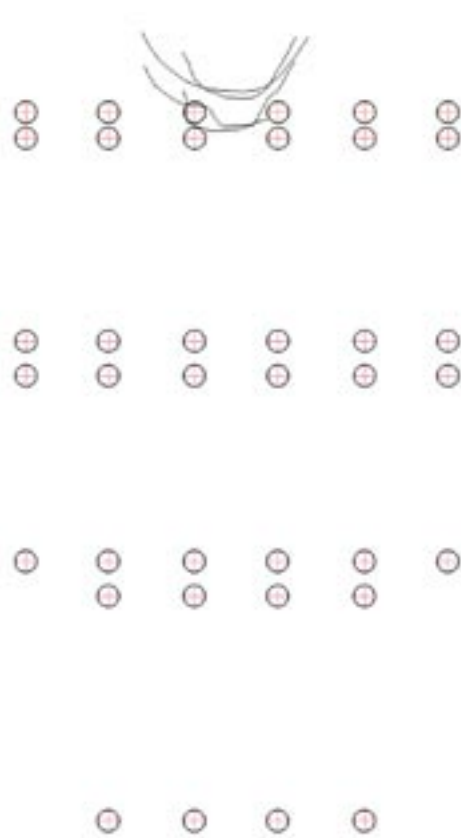


*Figure A2e-2. Summary sketch of the spalling observations between April 26 and May 14.*

**May 14, 2004**

In the early morning and early afternoon of May 14, acoustic events and displacements at position 3 were picked up again. No new fractures were observed in the hole, but an increase of the dilatation of the old slabs was clearly visible.

The sketches from April 26 to May 14 are summarized in Figure A2e-2 where it can be seen how the spalling front propagates downwards.

**May 18, 2004**

The acoustic activity picked up again May 17 and continued with quite a high event frequency until the beginning of June. This having been said, no general comments will be made on AE activity in the following sub-chapters.

In connection with the acoustic activity on May 17, displacement in the mm scale were observed with both sensor types at position 3. Displacements on the sub-mm scale were recorded with both of the sensors at position 4. The onset of negative displacements was monitored at positions 9 and 10.

Fracturing/slabbing associated with the other recordings includes a slab that was created beneath the short-range sensor at position 3. Fractures from that slab extended down the hole approximately 15 cm, where chipping occurred in a small mylonitized (dashed line) area. Still no fractures go past any of the sensors at position 4. The increasing dilation of the previously formed slabs is clearly visible. The dilatation of the fractures was approximately 1 to 2 mm.

The sketch from May 18 is shown in Figure A2e-3. The spalling propagation was photographed for the first time during this hole visit. Two of the photographs are shown in Figure A2e-4.
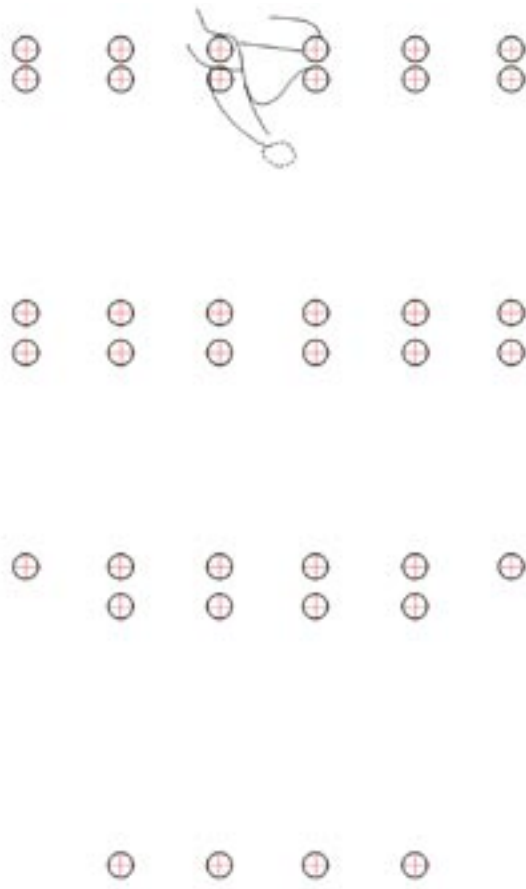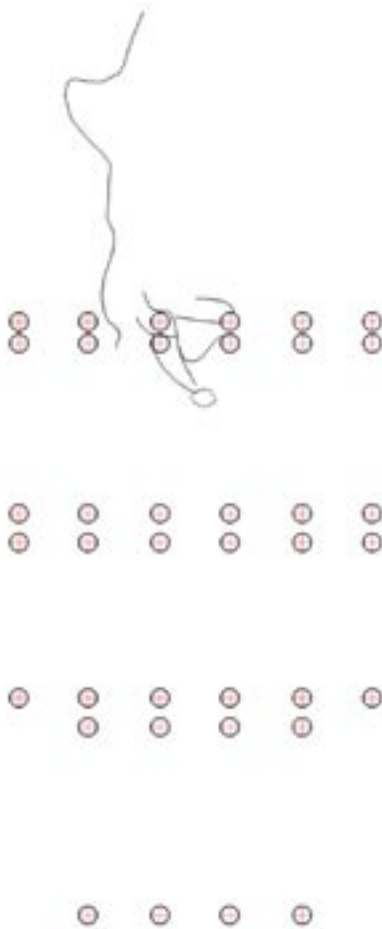


**Figure A2e-3.** *Spalling observations, May 18. Dashed line, chipping in mylonitized area.*

*Figure A2e-4.* *May 18. Photographs of the pillar wall. Left: close-up of position 3 (2.5 m level); the short-range LVDT is the lower one. Right: photograph from below along the centre of the pillar (pos. 3 to the left and pos. 4 right of the pipe).*

## May 25, 2004

The downward spalling propagation was very small on this date compared with the earlier observation dates. The slabs already formed continued to dilate, however, on May 25 a slab fell off the borehole wall. The upper part of the slab was fixed to the rock wall and the lower part was forced to dilate by the underlying slabs (the long line in Figure A2e-5). The edge of this slab was dilated between 10 to 20 mm. The slab was broken in a thin sub-horizontal pegmatite vein at the upper end of the long line.



*Figure A2e-5.* *Spalling observations May 25.*

When the hole was mapped that day, the increasing dilatation was obvious. Chipping continued in the thin mylonite band and the dilatation of the fractures from the rock wall was 5 to 10 mm. Figure A2e-5 presents the spalling observations and Figure A2e-6 shows photographs of positions 3 and 4.

## May 27–28, 2004

The hole was accessed again on the 27th to fit new sensor clamps. Mapping was done at the same time. Close to the instruments on the 3 m level there was chipping in the very centre of the pillar (dashed area). At one location along the mylonite band between the instrument levels, 1–2 mm thick chips were formed in the weaker mylonitized rock (oval area).

On May 28, displacements on the mm scale occurred at both the 2.5 and 3.0 m levels. A check was made in the hole but no new fractures were seen. There were some small additional chips between positions 9 and 10 (3 m level). Generally larger dilatation at almost all existing fractures was observed, Figure A2e-7. Photographs of position 3 is presented in Figure A2e-8.

## June 2, 2004

Chips had now formed around the centre instruments at the 3 m level between positions 9 and 10. Areas with small chips as well as increased dilatation in the pre-existing fractures were observed as well as drummy areas (inside dashed line) in Figure A2e-9. A sub vertical granite vein above position 4 is drummy and small chips is formed around it. The dilatation of the long fracture above position 2 is approximately 20 mm. The photographs in Figure A2e-10 shows the fracturing at position 10, which was not present at the previous hole visit. The figure also shows position 3.

## June 8, 2004

The spalling had now propagated below the instrument level at 3 m. A drummy area was formed between the 2.5- and 3-m instrument levels at (large dashed area). Chipping had occurred between the instrument positions 10 and 11 (small dashed ovals). Small chippings in a restricted area were observed at the centre of the pillar just below the 3 m instrumentation level (oval dashed area). The spalling is illustrated in Figure A2e-11 and photographs of the spalling at the 2.5 and 3 m levels are presented in Figure A2e-12.
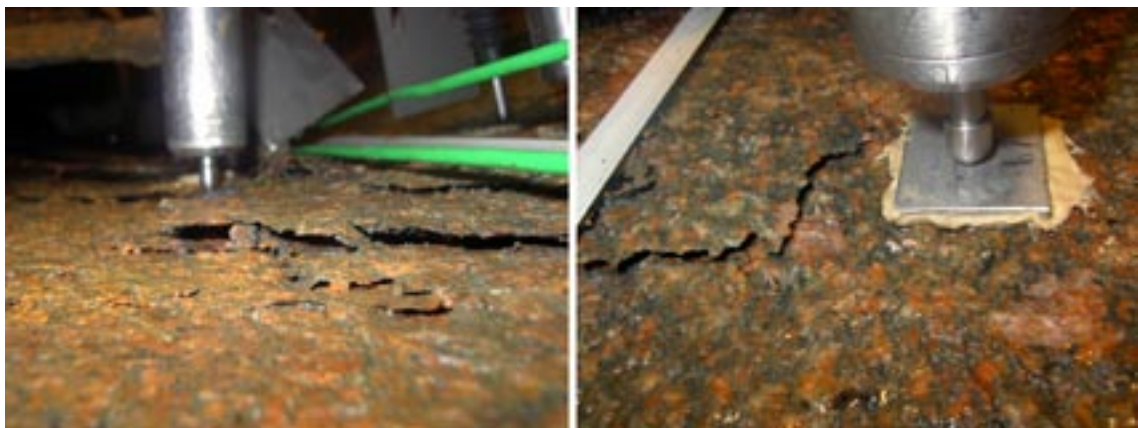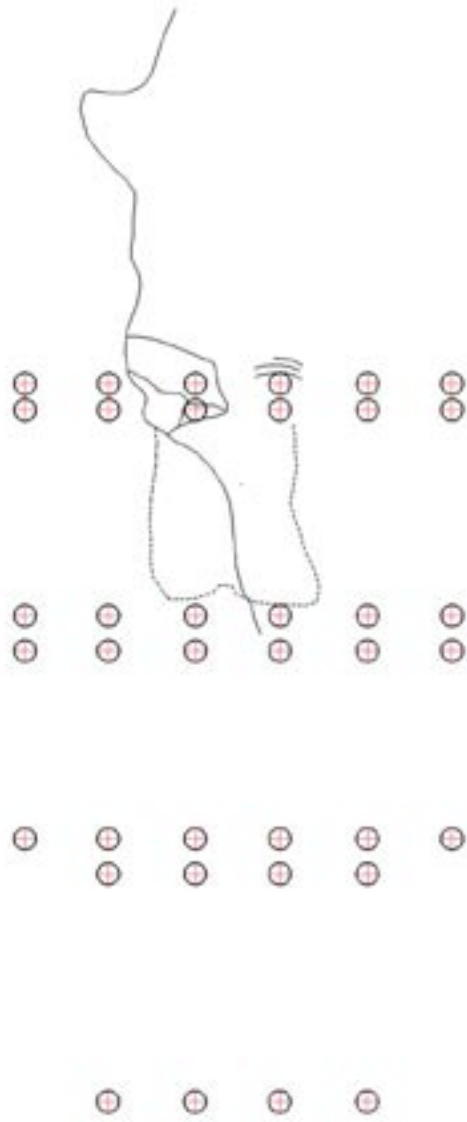


*Figure A2e-6. May 25. Photograph of the short-range sensors at positions 3 (left) and 4 (right).*
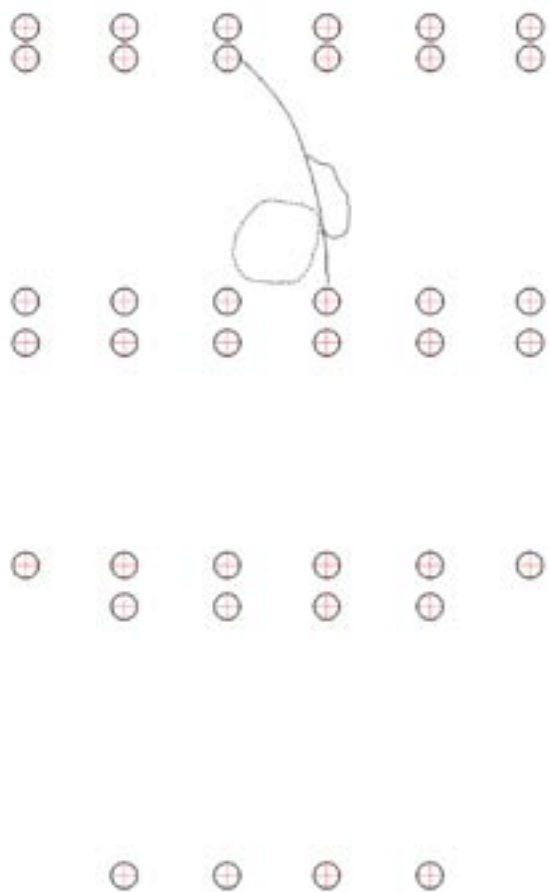
**Figure A2e-7.** *Spalling observations May 27. Dashed areas – chipping. Oval area – chips in mylonitized rock.*
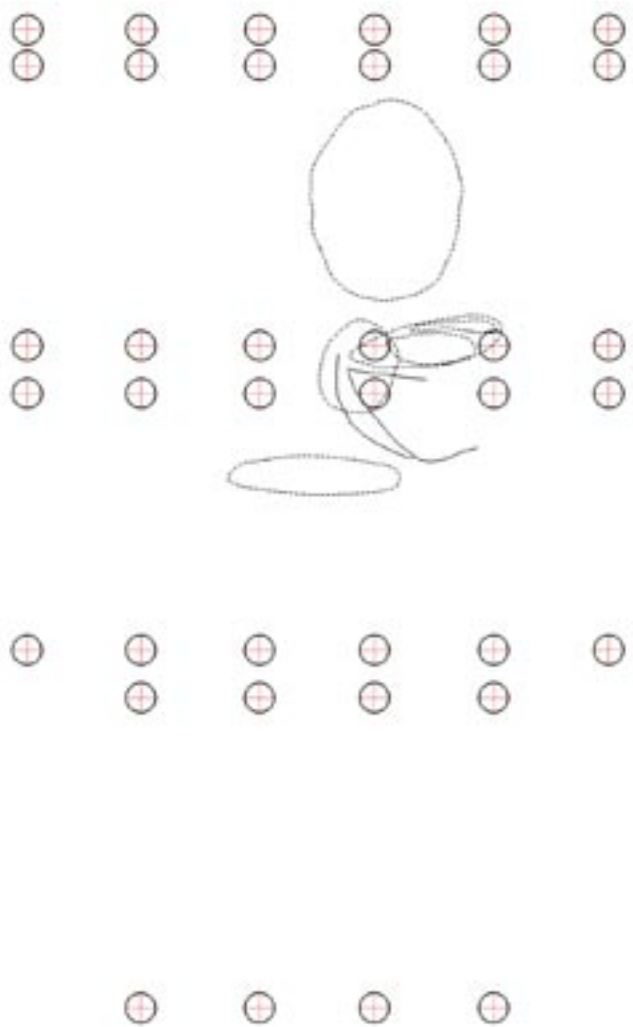


**Figure A2e-8.** *May 27. Photograph of position 3, left both sensors and right below the short range sensor.*

**Figure A2e-9.** *Spalling observations on June 2.*



**Figure A2e-10.** *June 2. Photograph of spalling/fracturing at positions 3 (left) and 10 (right).*

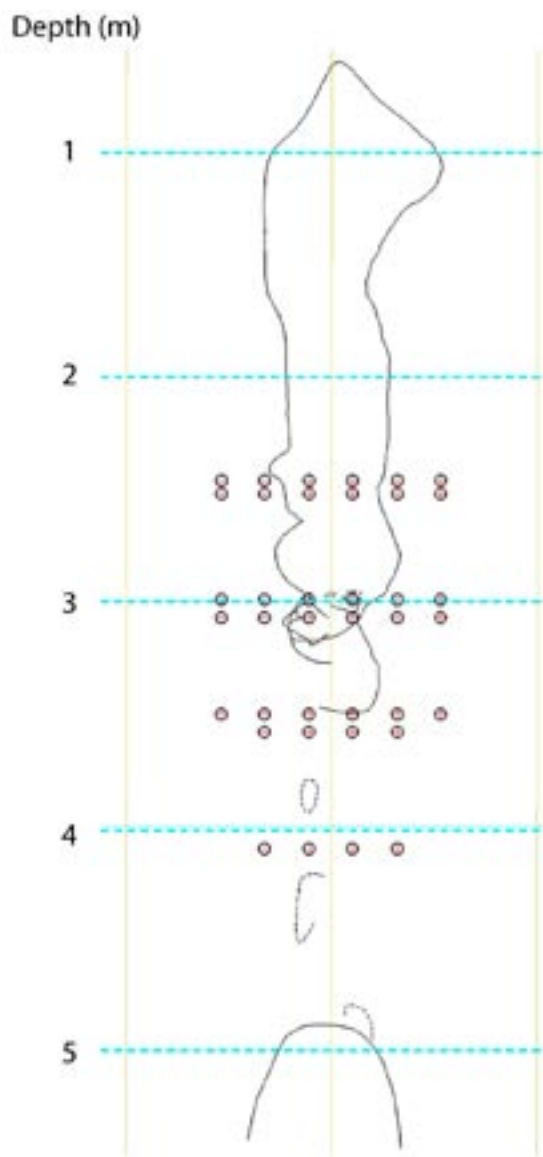**Figure A2e-11.** *Spalling observations on June 8.*



**Figure A2e-12.** *June 8. Photographs of spalling/fracturing at position 3 (2.5 m level) and between positions 9 and 10 at the 3 m level. In the right photograph position 9 is to the left.*

## June 16, 2004

The major difference since the last spalling observation was that at 3-m depth the spalled zone had widened in the horizontal direction. Thin finger nail sized chips were formed between the pillar centre and the long curved dashed line. Small areas with limited spalling were observed just above 4 m and at approximately 4.5 m depth (dashed lines). At 4.5 m the spalling was associated with an inclusion of greenstone. Just above 5 m depth spalling was initiated in mylonitized rock close to an existing fracture. The dilatation of the fractures above the 3 m instrument level lies between 10 to 20 mm. The spalling is illustrated in Figure A2e-13 and Figure A2e-14. Photographs of the spalling at the 2.5 and 3 m levels are shown in Figure A2e-15.

## June 23, 2004

Chipping had now occurred slightly to the left of the pillar centre at between the 2.5 and 3 m instrument levels in the area created by the lines. The chips there were thin with a size of approximately 5–10 times 10 centimetres. The dilatation of the fractures above the 3 m instrument level lies between 10 to 20 mm. The spalling is illustrated in Figure A2e-16 and photographs of the spalling at the 2.5 and 3 m levels are shown in Figure A2e-17.
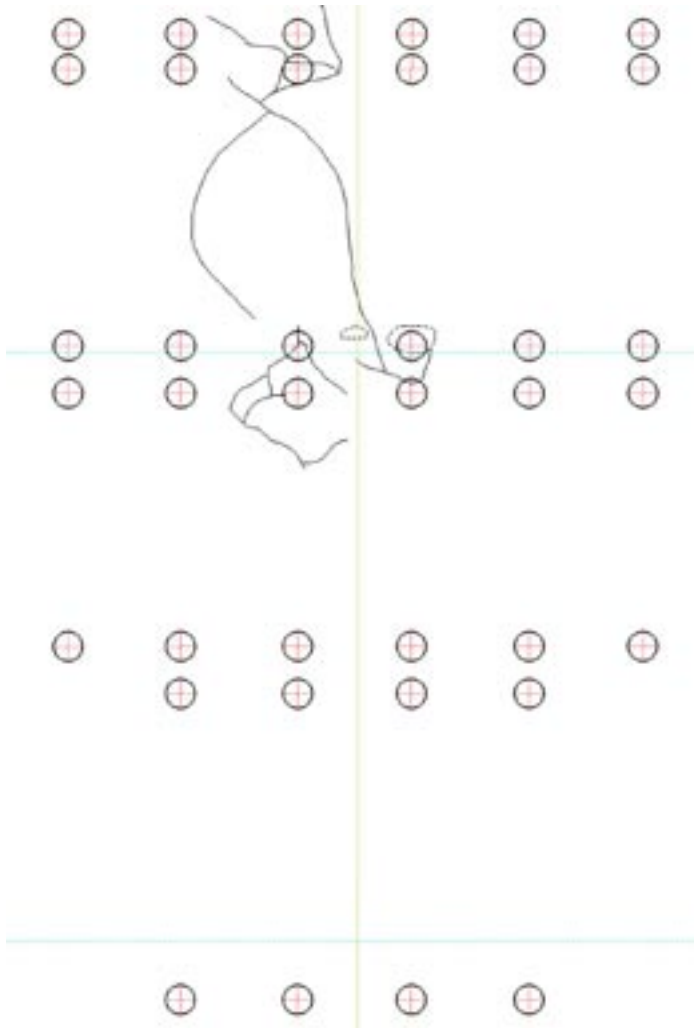


***Figure A2e-13.*** *General extent of spalling on June 16.*
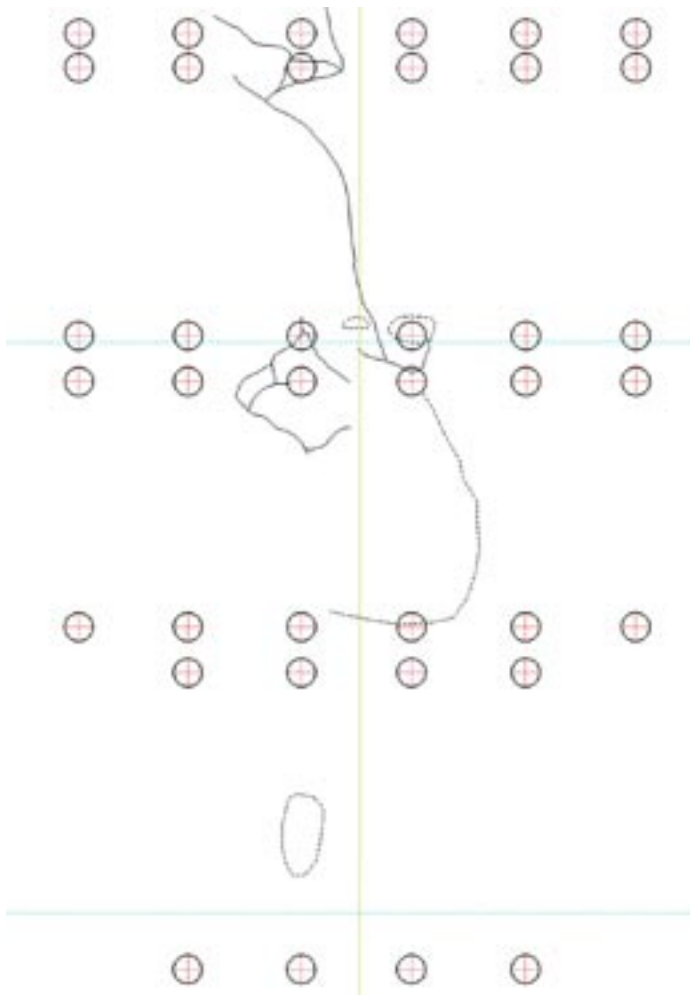
**Figure A2e-14.** *Detailed spalling observations on June 16. At 3 m depth a small rock fragment had fallen of at the very pillar centre (dashed oval).*



**Figure A2e-15.** *June 16. Photographs of spalling/fracturing at position 3 on the 2.5 m level (left) and at position 9 on the 3 m level (right).*
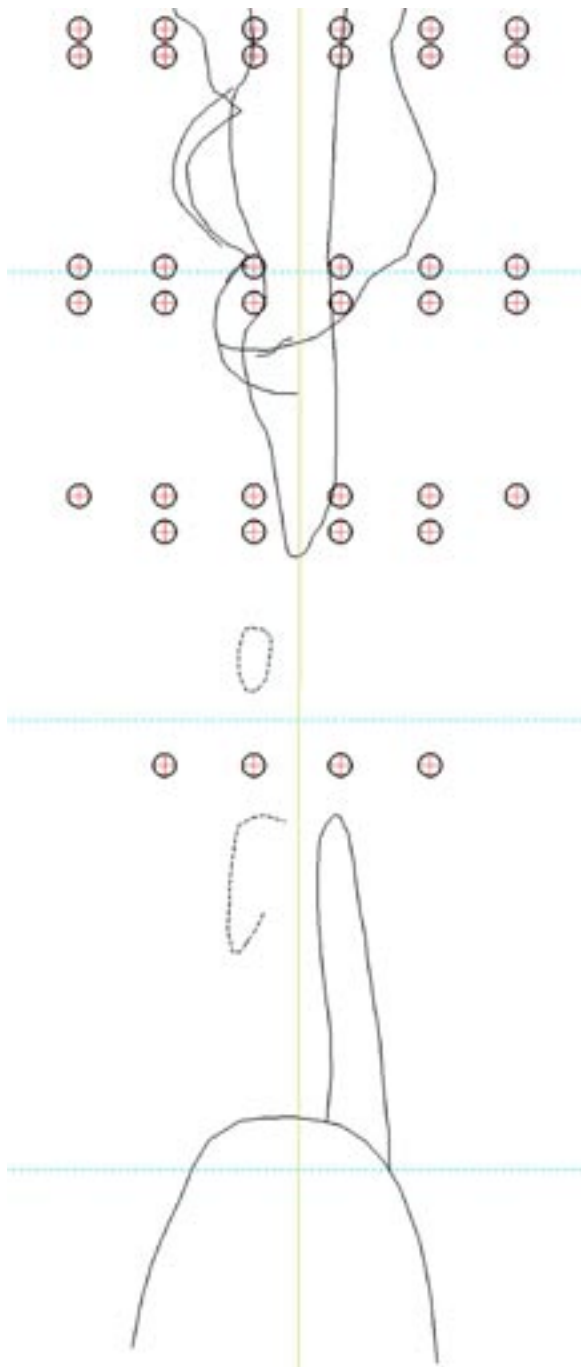
**Figure A2e-16.** *General extent of spalling on June 23.*



**Figure A2e-17.** *June 23. Photographs of spalling/fracturing at position 3 on the 2.5 m level (left) and at position 10 on the 3 m level (right).*

## June 29 2004

Now the spalling had propagated to the 3.5 m instrument level. The spalled zones at approximately 4 and 4.5 m had the same area but were more spalled. The oxidized and mylonitinized part of the pillar at approximately 5 m depth had continued to spall. The spalling had propagated upwards and had reached a hole depth of 4.2 m. The notches in the two spalling fronts seemed to be moving directly against each other. Quite a lot of small fractures are formed around instrument position 10 lower. The U-shaped dashed line at the 3.5 m instrument level contains thin chips from coin size and up. The spalling is illustrated in Figure A2e-18 and Figure A2e-19. Photographs of the spalling at the 2.5 and 3 m levels are shown in Figure A2e-20. Nothing seems to have happened in the upper part of the pillar.



**Figure A2e-18.** *General extent of spalling on June 29.*
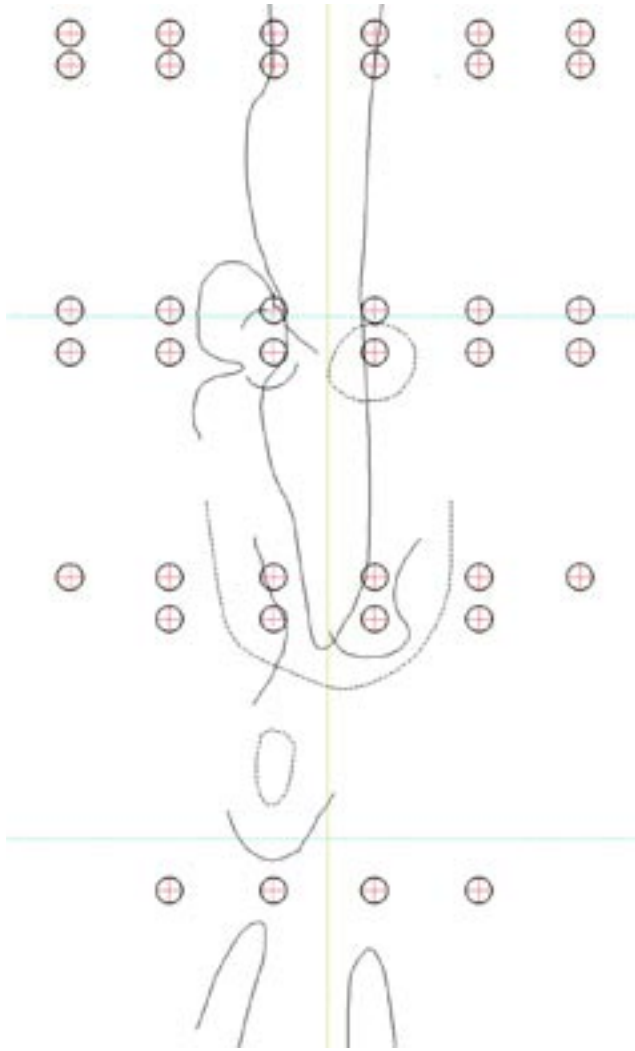
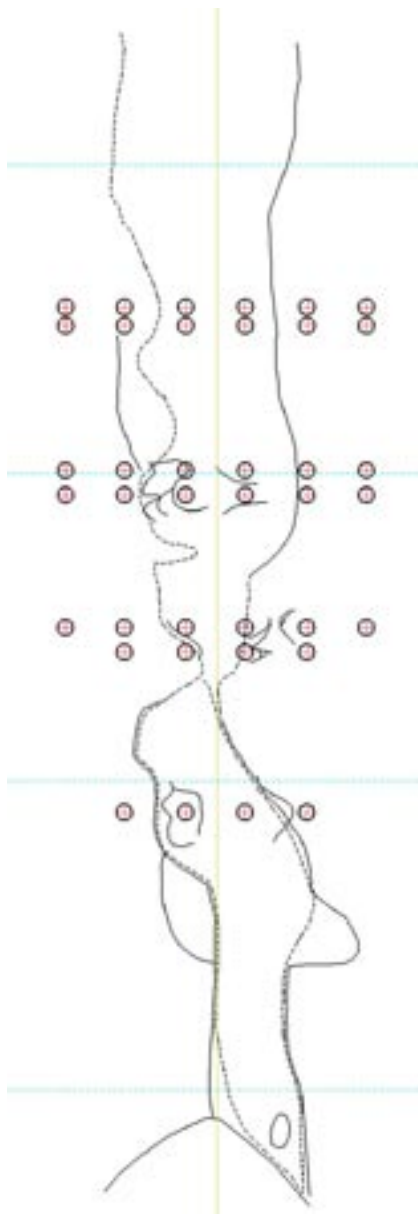**Figure A2e-19.** *Detailed spalling observations on June 29.*



**Figure A2e-20.** *June 29. Photographs of spalling/fracturing at position 9 at the 3 m level (left) and at position 15 at the 3.5 m level (right).*

## July 6, 2004

The upper and lower spalling fronts were now joined. Additional fracturing was observed at the 3, 3.5 and 4.1 m instrument levels as well as at a depth of 5 m close to a fracture trace. The spalling is illustrated in Figure A2e-21 and Figure A2e-22.

## July 12, 2004

A few new fractures were observed. Dilatation was increased at most locations, but fracture propagation had probably almost ceased due to the fact that the temperature was reaching a constant level and hence very small additional thermal stresses were being added. The spalling is illustrated in Figure A2e-24.
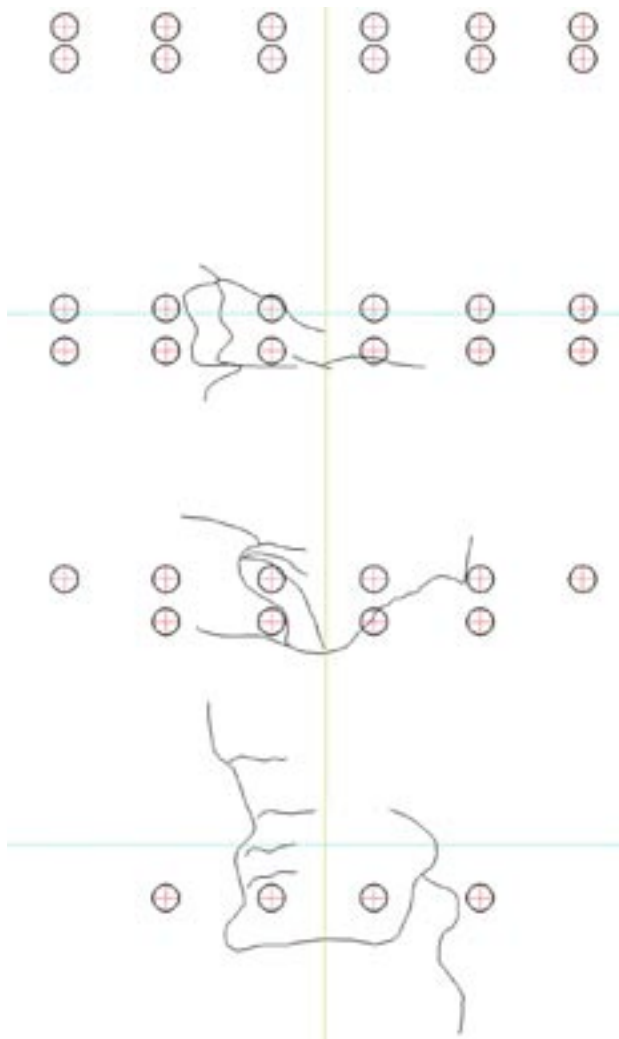


***Figure A2e-21.*** *General extent of spalling on July 6.*
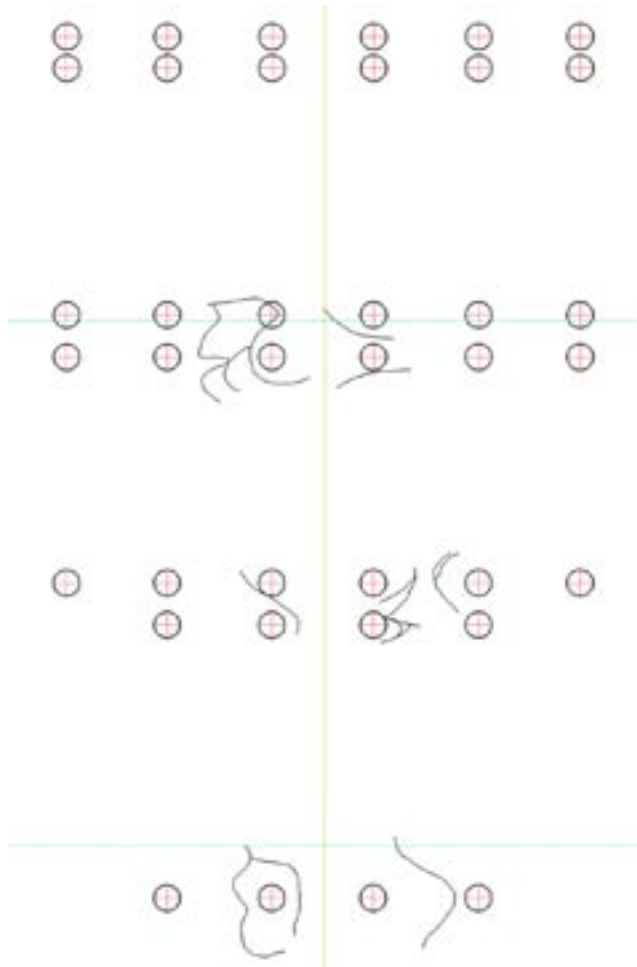
**Figure A2e-22.** *Detailed spalling observations on July 6.*



**Figure A2e-23.** *July 6. Photographs of position 10 (left) and position 16 (right).*

**Figure A2e-24.** *Spalling observations July 12.*

## Removal of spalled slabs

When the heaters had been turned off and the rock had cooled down, the slabs formed during the spalling process were removed. The observations made during this work are presented in this section. Since spalling was progressing downwards, the slabs were firmly attached at their upper end. The work of removing the slabs therefore started at the bottom of the hole. All the loose slabs were removed from an approximately 0.5 m long section before work started on the following 0.5 m section. The observations are therefore listed from the bottom of the hole and up.

The process of removing the slabs was quite easy. The tip of a flat screwdriver was carefully inserted in the opening between two slabs. The screwdriver was then turned to widen the gap between the chips. This was done until the slab could be gripped with the fingers and lifted into the plastic container.

### Depth 4.9–4.3 m

From 4.9 to 4.5 m the rock seemed to have displaced along an existing fracture and looked crushed. The chipping was more pronounced further up the hole, and between each of the larger slabs there was a thin zone with fractured rock. On the slab's surfaces there were many small thin chips on a mm scale. The slabs appeared to have been formed along invisible weakness planes. The surface was slightly undulating and the shape seemed to be determined by small-scale geology such as feldspar eyes etc.

A small pit with relatively small chips on a mm to cm scale was created at a depth of 4.2 m approximately 0.5 m to the left of the notch in a small body of fine-grained greenstone. It looks like the greenstone was stiffer than the surrounding rock mass and attracted stresses until it failed, Figure A2e-25.

Generally there are more small chips beneath and between the larger chips than could be seen from the surface. The chip size decreases closer to the notch. Its centre is quite crushed and consists of small fragments on a mm scale. The notch has followed an undulating path as it worked its way down the hole. This indicates that it followed the easiest way down. This is in itself an indication that the process has been quite slow since there has been time for the notch to move through the weaker parts of the rock instead of going the shortest way. That would probably have been the case if the process had been instantaneous.

All chips that were created in intact rock have very thin edges and are thicker in the centre. The thickness can be a few centimetres with edges thinner than half a millimetre. It is likely that the chips have been formed by pure normal displacement without shearing. The occurrence of shearing would probably have broken the thin edges of the chips/slabs.

No fractures could be found in the pillar wall after removal of the slabs. At some locations, pre-existing fractures have halted the growth of the spalling slabs. Where fracture growth has taken place in intact rock, a quite smooth and curved surface remains.

Another interesting phenomenon occurred at this level as well. Some weaker rock was located at a depth of approximately 5 m. Spalling was initiated there on around June 16 and propagated upwards in the hole. The major spalling front was then at a depth of approximately 3 m in the hole. The upward-moving spalling reached a depth of about 4.1 m, where it joined the major spalling front. It is interesting to note the formation of the chips in the upward-moving front. Their loose end points upwards, in the opposite direction of the other spalled areas. It can be concluded that the spalling direction determines the geometry of the chips, which is also logical. A photograph of these chips is shown in Figure A2e-26.



***Figure A2e-25.*** *The greenstone body that created a small pit in the rock wall.*

**Figure A2e-26.** *Photograph of the upward-pointing chips.*

## Depth 4.3 to 3.7 m

On the surface there are very loose small chips, and beneath those the slabs become quite large, Figure A2e-27. When a chip is removed one can see the typical small chips of mm scale that are present on almost all fracture surfaces. The chips in the notch are very small. The rock right next to it is however intact, which indicates that crushing in the notch and not pre-existing fracturing is the cause of the small chips. Another indication of crushing is grey dust in the centre of the notch. It is likely that this dust originates from a crushing process. It is very unlikely that the dust originates from drilling and has been transported there by water during the spalling process. The thin chips in the centre of the notch striking almost directly eastward in the Äspö 96 co-ordinate system or 45 degrees relative to the tunnel axis. The small chips are interlocked and quite difficult to remove.

At 4.2 m a chip with an arched shape was removed. This was the first chip of that shape that was found. The others have been flattish. If the remaining chips from 3.7 m and up are viewed from below, clear indications of arching can be seen. The displacement of the individual chips is also quite clear, Figure A2e-28.

## Depth 3.7 to 3.3 m

Here as well there are small mm-scale chips on top of larger chips at the surface. The geometry looks the same as in the lower part of the hole (except at the very bottom where more crushing occurred). Rock slabs are arranged like fish scales on top of one another. All the scales are attached at their upper end, and the lower end is normally displaced. All the way from the bottom of the hole the centre of the notch is coloured greyish by the crushed rock powder. There are sub-vertical fractures going straight into the pillar in parts of the section. They strike approximately N105E.

Quite a lot of chips were removed up to 3.2 m. There are sub-horizontal chlorite-filled fractures in the section. The chips broke along these fractures when they were subjected to a momentum during the removal. This determined their size in the longitudinal direction.

*Figure A2e-27.* *Photograph of rock wall at depth of approximately 4 m. The small cm-scale chips on top of the larger chips are clearly visible.*



*Figure A2e-28.* *Photograph taken from below of chips at 3.7 m and up. The dilatation and curvature of the slabs can be seen.*

When looking at the notch surface to the left and right of the centre at 3.7 m one can see the arching, the chips are small but they are arched. There is a distinct difference at the very centre of the notch. The chips there are very small, on a cm scale, interlocked and difficult to remove. The rock behind is drummy but the fracturing is behind the slabs that can't be removed (no fracture traces seen). The full extent of the spalling can therefore not be excavated. The notch at 3.4 to 3.5 m is not as crushed as it is below, instead the surface is smooth, Figure A2e-29. This might be due to the fact that the full extent of the spalling not has been excavated and that the crushed centre is somewhere beneath.

From lower parts of the spalling up to a depth of 4.1 m in the hole, the complete notch surface is quite smooth and arched, even in the very centre. Between 4.1 to 3.6 m (especially between 4.3 to 4.1 m) there are fractures in the notch centre. The fractures enter the notch from the left, striking N075E. Above 3.6 m the fractures have changed direction and now enter the notch from the right, striking N145E, almost perpendicular to the tunnel axis. This part of the rock is much more oxidized than the other parts.

The remaining chips from 3.3 m and up in the hole are dilated on their left side while the right side is attached to the rock wall, Figure A2e-30.

## Depth 3.3 to 2.7 m

Almost all of the slabs between depths of 2.7 and 3.3 m have a free left edge and are attached to the rock on the right side, just like in Figure A2e-30. The slabs also have a larger area then in the previous sections and there are fewer cm scale chips. The slabs are more interlocked here than in the previous sections. One has to work one's way up and down the section to remove one chip that locks other chips into place. The dust from the crushed rock is present in the centre of the notch.

Between 3 and 3.2 m, the fractures entering the notch centre strike approximately N125E, almost parallel to the major principal stress direction. These fractures disappear above 3 m.



**Figure A2e-29.** *Photograph of the smooth arched notch at a depth of 3.7 m.*

***Figure A2e-30.*** *Photograph of the slabs with a free left surface and the right side attached to the rock wall. The depth at the bottom of the photograph is 3 m.*

The steel plates glued to the rock wall for the LVDTs at the 3 m instrument level were removed. The upper plate in position 9 was attached to a chip covering its entire back surface. The chip thickness was a few mm. A diagonal fracture divided the chip below the lower plate into two pieces. The right part of the chip was still glued to the plate and its thickness was about 15 mm.

The upper plate at position 10 fell down almost by itself. The back of the plate was covered with thin rock fragments. The lower plate at the same position also came down very easily. A thin rock chip was still attached to the entire back of the plate.

Both of the plates at position 11 were located at the same chip, whose thickness was about 10 mm.

Between 2.8 and 2.9 m, the slabs increase in thickness quite rapidly. The left edge is very thin and the right side, which is attached to the rock wall, is about 20 mm thick.

The notch surface between 3.2 to 2.7 m is quite smooth, Figure A2e-31, especially above 3 m, and arching of the chips is visible. The slabs closest to the hole surface are the largest, after which the slabs decrease in size only to increase again at the notch bottom. It is mainly the slabs closer to the tip of the notch that are arched. As the 2.5 m instrument level is approached, an excellent view is obtained of the slabs beneath instrument position 3, Figure A2e-32.

The slabs on the right side of the pillar centre at a depth of approximately 2.6 m and higher up have a larger area and are more tightly interlocked. The left side was therefore removed first, since it was easier to remove. On the right side there was one obvious difference compared with the other sections observed. The very small chips that have been present on the hole surface are not there and the usual cm-scale chips are very few in number. It would appear that the larger slabs were created instantaneously with no time for the small chips to grow in an increasing stress environment.
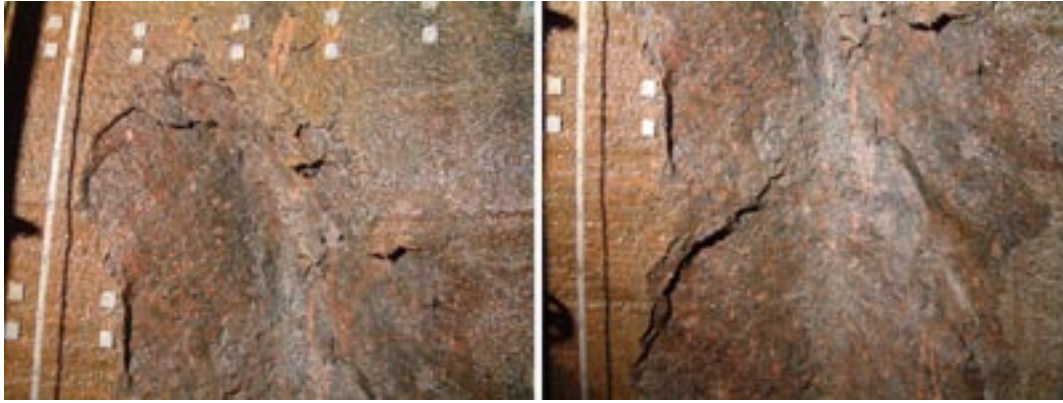
*Figure A2e-31. Photographs of the smooth notch surface. The upper two rows of steel plates in the left photograph are from the 2.5 m instrument level.*
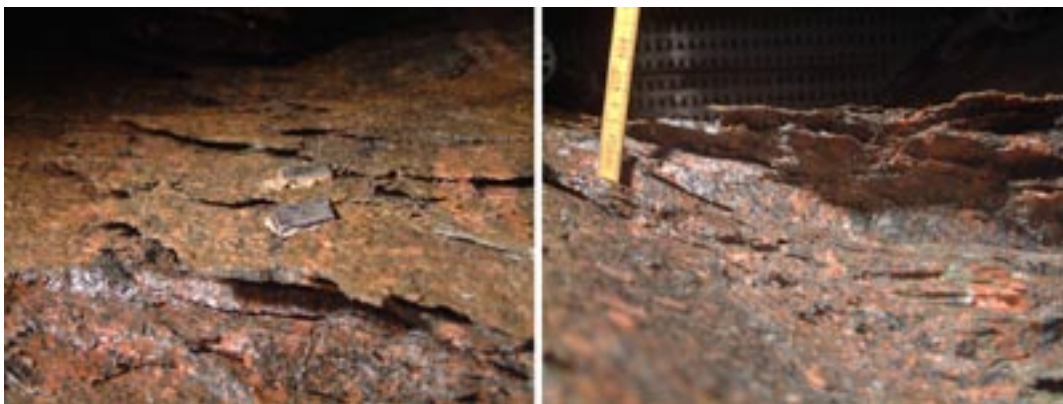


*Figure A2e-32. Photograph of the steel plates at instrument position 3 and a photograph taken from below of the slabs beneath the same plates.*

## Depth 2.7 to 2.1 m

In this section the fracture pattern becomes quite different from what has been seen deeper down in the hole. Fractures come in from the left with a large angle in relation to the tunnel axis. The slabs created become curved when they approach the centre of the pillar. In the deepest part of the notch the fracturing is very intense, and mostly cm-sized rock fragments were removed. Almost no slabs could be removed from the right side of the pillar, and the slabs on the left side were quite inter-locked, Figure A2e-33.

The slab to which the upper and lower steel plates at position 2 were glued was removed. The boundary fracture for the slab was beneath the centre of the upper plate and to the left of the lower plate. The lower plate fell off when the slab was removed. The rock behind the slab was not drummy. That slab is probably the only one that is formed at position 2.

The upper steel plate in position 3 was attached to quite a large slab. The slab is approximately 20 cm long and 15 cm wide with an oval shape. The slab's thickness is 15 to 20 mm. The steel plate at position 3 lower came loose with a chip of approximately the same size as the plate. The chip was wedge-shaped and had a thin point ending about 1 cm above the plate. The chip's base was located at the lower end of the chip. The base thickness was approx. 5 mm.

***Figure A2e-33.*** *Photograph at depth of approximately 2.5 m showing the right side of the pillar, where almost no slabs could be removed.*

The same pattern regarding the distribution of the chip sizes is evident here as well. Beneath the larger slabs located closest to the hole periphery there is a zone with more intensely fractured rock (smaller chip size). Deeper into the notch the chip size then increases again.

The upper steel plate at position 4 fell down during work on nearby slabs. The plate was attached to a very thin chip. The lower plate at position 4 was easy to remove from the rock wall and it was drummy underneath.

## Depth 2.1 to 1.6 m

This section enters the part of the hole that was spalled during the drilling. The initial spalling reached a depth of 1.95 m and is illustrated by the photograph in Figure A2e-34.

The angle of the fracture entering the pillar from the left is now smaller, and the fracture strikes N080E. The right side of the pillar is drummy, but no rock fragments could be removed. The curvature of the slabs is more pronounced here. A beautifully arched chip from the centre of the notch was retrieved between 2 and 1.6 m, Figure A2e-35.

While a chip close to 1.6 m was being removed, a number of large slabs between 1.6 to 1.1 m fell down to the bottom of the hole.
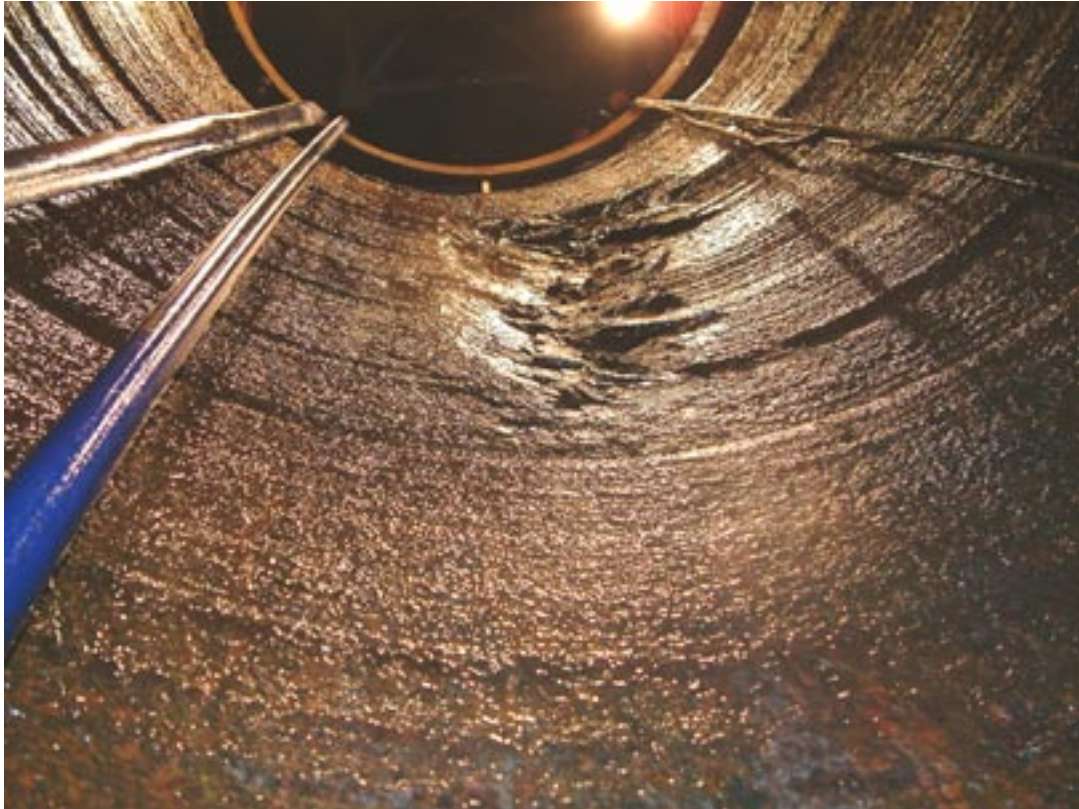
**Figure A2e-34.** *Photograph of the initial spalling in DQ0063G01 that occurred during the drilling.*



**Figure A2e-35.** *Photograph of the location of the arched chip and the chip itself.*

***Figure A2e-36.*** *Photograph of the fractures and slabs between 1.6 and 1.1 m.*

### Depth 1.6 to 1.1 m

Like at 3.6 m, the fracturing angle is larger and more perpendicular to the tunnel axis. The complete spalled volume cannot be excavated, Figure A2e-36. There seem to be fractures behind the wall, indicated by drumminess. The opposite edge of these fractures cannot be seen. They may, however, originate from a depth of 2.5 m, where fracture traces are visible that could continue behind the rock wall up to this level. The notch is located in a local inclusion of greenstone. The powder probably originating from crushed rock is clearly visible.

### Depth 1.1 to 0 m

From the beginning of the hole and down to 0.7 m, no spalling has occurred. The reason is probably softening of the rock mass in the floor from the excavation (Excavation Damaged Zone) as well as displacement along the ductile shear zone at the top of the pillar. Between 0.7 and 1.1 m, very little spalled rock was removed. However, the total volume of spalled rock in that region due to the drilling is in the same range as for the lower parts of the hole, where thermal effects triggered the spalling.

## Acoustic emission in pre-existing fractures

It was important to be able to determine the boundary conditions of the pillar so that appropriate numerical models could be used for the back calculations. Geological mapping (Chapter 2) of the pillar site indicated that especially one fracture (fracture 08) was intersecting the pillar. If it displaced during the experiment it could re-distribute the stress field in the pillar and it would be difficult to back calculate the stresses acting in the pillar.

The location of the water bearing fracture 08 is presented in Figure A2f-1. It is visible in the bottom of block 5 and on the left wall where it disappears at approximately 3 m depth. On the right wall the fracture is continuous to 3 m depth where it intersects the large hole and leaves the pillar.

During the drilling of the first hole there was practically no response from inside the pillar (Figure A2f-2). The source locations in the pillar all origins from localized yielding of the rock in fracture intersections and areas with rock weakened due to alteration.
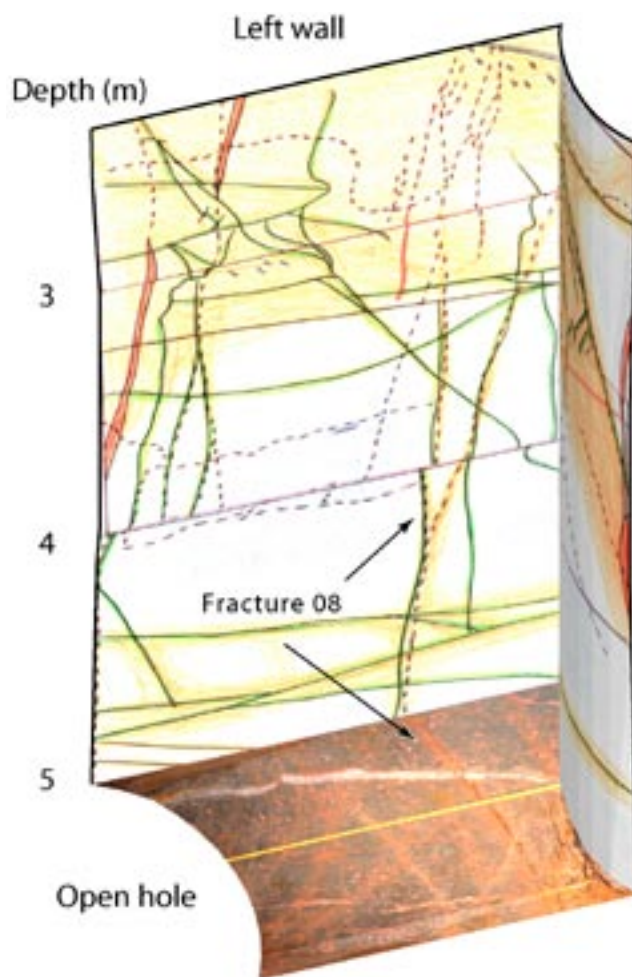


*Figure A2f-1.* *The location of the water bearing fracture 08 as it intersects the pillar.*
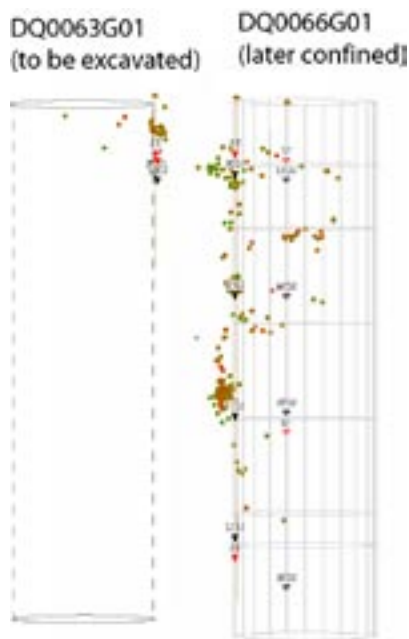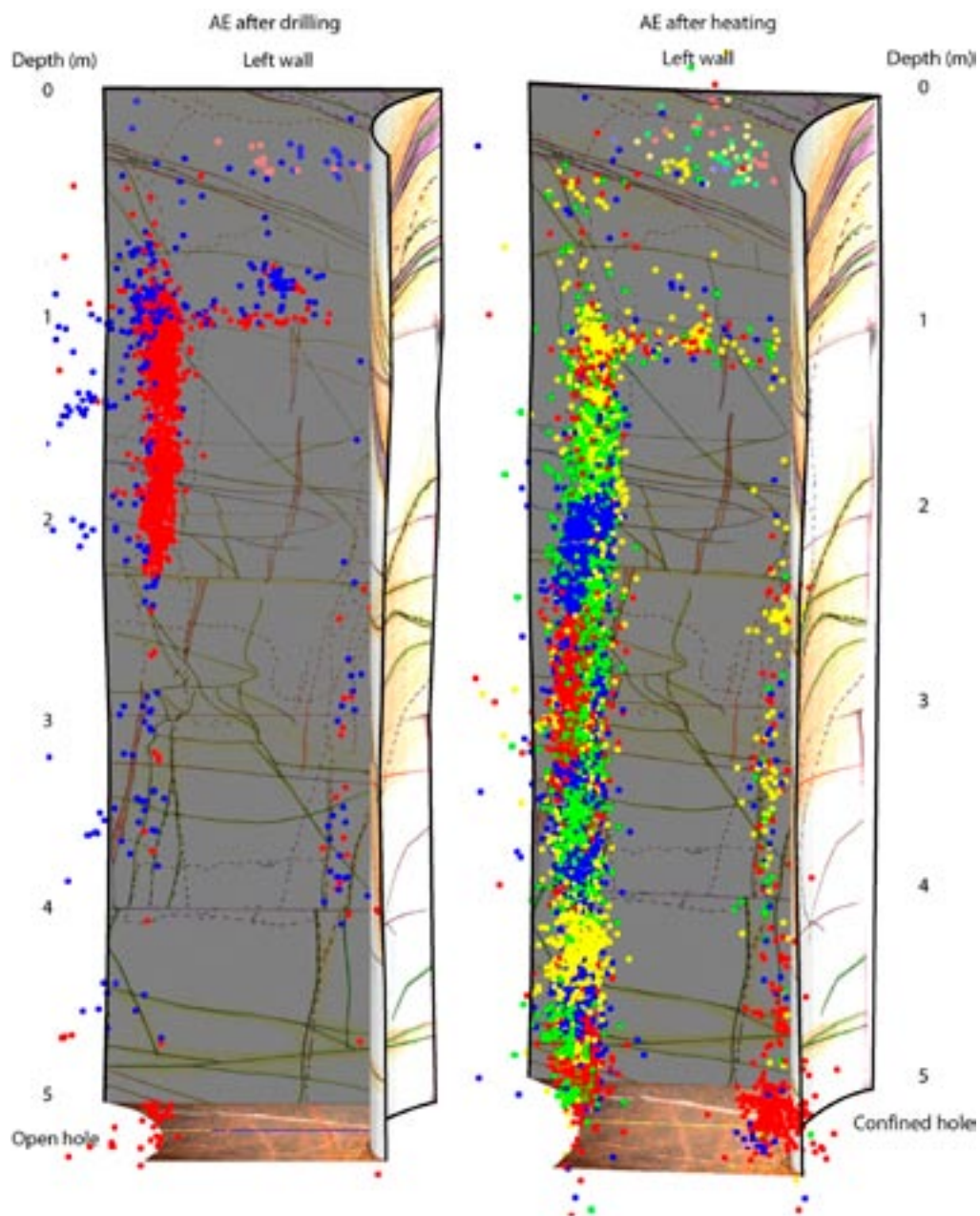
**Figure A2f-2.** *Accumulated source located events during the drilling of the first large hole (DQ0066G01).*

During the drilling of the second hole there are events that likely are located at the fracture 08 plane as is illustrated in Figure A2f-3. The events are very few and do not indicate that there should be any displacement along the fracture's surface. It is most likely yielding of asperities in the fracture plane that is recorded.

Also during the heating phase there are events recorded most likely located in the fracture 08 plane (Figure A2f-3). The largest cluster at almost 5-m depth occurred instantly one evening in June 25. At the same time as the AEs were recorded there was a sudden increase of the confinement pressure. Water was released to restore the confinement pressure and after the bladder was removed at the end of the experiment the hole wall was examined at that location. Minor yielding of the rock was found adjacent to one fracture. The rock close to the fracture had yielded during the drilling of the first hole and those parts were covered by steel plates. The largest AE cluster on the confined side is hence not associated with fracture 08. The other events are also in this case quite few and do not likely depend on displacement of the fracture surface.

Acoustics are located in the shear zone as it intersects the pillar and also where it intersects with the tunnel floor (Figure A2f-4). Deformation of the shear zone was recorded as presented in Chapter 6. The small deformation and the few acoustic events do however not indicate that the general stress situation in the pillar was affected by deformations in the shear zone.

After studying the acoustic records there are no indications of displacements in fracture planes that could distort the stress distribution in the pillar. Elastic analysis of the stress situation is therefore an appropriate approach to determine the stresses in the pillar.

***Figure A2f-3.*** *Accumulated source located AE events during the drilling of the second large borehole DQ0063G01 (left) and during the heating (right).*
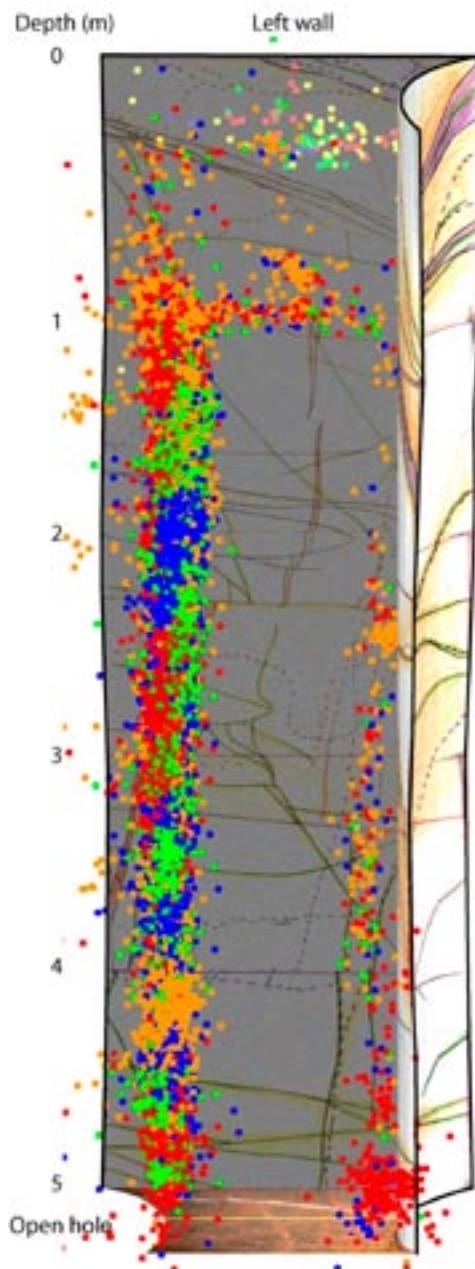
***Figure A2f-4.*** *All source located AE events during the drilling and heating of the pillar. Acoustics during the release of the confinement pressure are not included.*